ENABLING LOCAL-TO-GLOBAL BEHAVIORS IN COLLECTIVES ACROSS LENGTH SCALES

A Dissertation

Presented to the Faculty of the Graduate School

of Cornell University

in Partial Fulfillment of the Requirements for the Degree of

Doctor of Philosophy

by

Steven Ceron

August 2022

ENABLING LOCAL-TO-GLOBAL BEHAVIORS IN
COLLECTIVES ACROSS LENGTH SCALES

Steven Ceron, Ph.D.
Cornell University 2022

Collectives in nature demonstrate behaviors that extend far beyond the capabilities of any single agent. Social slime mold, for example, has thousands of cells that aggregate and form mobile and immobile nutrient-searching structures as a function of the chemical signaling between cells and their interactions with the surrounding environment. This species embodies many features that swarm roboticists wish to incorporate in self-reconfigurable robot collectives: emergent complexity, plasticity, and scalable constituents. This thesis argues that regardless of the length scale, we can implement some of the same principles and features to exploit robot morphology, physical interactions among agents, and low-level coordination mechanisms to enable diverse collective behaviors for useful applications across fields.

In this thesis, I present novel emergent behaviors through physical robot collectives at the macro- and micron length scales and virtual collectives and explain how each behavior arises as a function of agents interacting with other agents, agents interacting with or reacting to their environment, and agents exploiting their environment to better influence other agents.

I expand the relatively new field of mobile coupled oscillators. Specifically, I present a new iteration of the swarming coupled oscillator (swarmalator) model, which enables many new emergent collective behaviors in addition to those already shown in the literature. It also replicates many behaviors of

natural and artificial collectives even though the detailed physical interactions are not taken into account. This abstract model has the potential to inform on the coordination mechanisms possible at different length scales. At the macro-scale communication-constrained coordination may serve as a fall-back, and at smaller length scales it may reveal some collective behaviors that are possible with agents that cannot currently have on-board processing.

At the macro-scale, I present soft modular robot collectives that exhibit embodied intelligence by exploiting a tight coupling between sensing and actuation to enable reconfiguration, locomotion, and strain-based consensus among other collective behaviors. I have contributed to the development of various soft actuators, a sensor, and two different types of soft robot collectives with differing capabilities, and have studied these collectives using both physical hardware and simulations.

At the micron scale, I present novel behaviors through magnetic microrobot collectives that use physical interactions between agents and their surrounding environment to enable the collective to perform on-demand reconfiguration of various functions and morphologies and manipulate passive objects in the surrounding environment. The microrobot collective behaviors are further studied through a physical model and a swarmalator model.

The diverse collective behaviors presented in this thesis hold many potential applications in swarm robotics, self-reconfigurable modular robots, and small-scale manufacturing; additionally, they hold great value for fundamental scientific research in self-assembly, self-organization, and emergent complexity. This thesis expands the fields of soft robotics, microrobotics, and coupled oscillators and demonstrates the potential to unlock many new emergent collective behaviors by exploiting low-level sensing, actuation, and coordination mechanisms.

BIOGRAPHICAL SKETCH

Steven Ceron attended the University of Florida for his Bachelor of Science in Mechanical Engineering and then completed his Ph.D. in the Collective Embodied Intelligence Lab under the direction of Professor Kirstin Petersen at Cornell University. He focuses on low-level coordination mechanisms that enable diverse emergent collective behaviors at the macro-scale and micron scale. He is interested in enabling robots with limited actuation, sensing, and processing capabilities to seamlessly work in teams by exploiting their morphology and the physical interactions with each other and the environment to carry out complex functions that would otherwise be difficult or impossible with a single agent. His major research topics include soft robotics, microrobotics, swarm intelligence, and coupled oscillators. His work has been highlighted in multiple media outlets including National Geographic and IEEE Spectrum. He is the recipient of the Fulbright Germany Scholarship, the Cornell Colman fellowship, and the National Science Foundation graduate research fellowship.

Dedicated to my loving and supportive family.

ACKNOWLEDGEMENTS

First and foremost, I would like to thank my family, especially my mom, dad, and grandmother, who have been supportive throughout my endeavors and have given me a great example of hard work, dedication, and love through their own lives. I am lucky to be their son and am grateful for the lessons and advice they have given me to live my best and fullest life.

I appreciate Robert Shepherd, Hadas Kress-Gazit, and Itai Cohen for being my PhD committee and for giving me great advice throughout my Ph.D. I would also like to thank Metin Sitti for letting me work in his lab during 2021; it was an incredible experience that introduced me to many talented individuals and expanded my research vision.

I would also like to thank my fellow lab members for making the lab such a fun place. Haron and Nialah are graduating with me, and I am sure they will continue to their next projects with the same talent and dedication they have shown throughout the past couple of years. Danna, Sadie, Jiahe, Jonathan, Alli, and Jake are amazing people and incredibly talented; I am sure the lab will continue to grow with them, and I hope they can achieve all of their professional and personal desires.

I would also like to acknowledge and thank two individuals who I was lucky to work with: Kevin O'Keeffe and Gaurav Gardi. Kevin is an applied mathematician that is a lot of fun to work with and has helped me in my work on swarming coupled oscillators and has expanded my research vision on modeling and studying collectives at different length scales. Gaurav is the Ph.D. student in Metin's lab that I worked with to realize the diverse microrobot collective behaviors; he was a lot of fun to work with and he taught me the basic intuitions behind micro-scale systems. Beyond being a great collaborator and

significantly expanding my research vision, he is an amazing friend that I hope I can work with again to realize many of the project ideas we have discussed.

I would like to give a big thanks to my advisor and friend, Kirstin Petersen, who has guided me throughout my PhD and helped me gain many new technical skills during the past couple of years. I am very happy that I was able to be a part of your lab, Kirstin. You are an amazing engineer, scientist, writer, advisor, mentor, and professor; I am very excited to see the projects you will lead your lab towards in the coming years and the awesome papers that will result. Thank you for making my PhD experience an incredible one through the opportunities you opened for me, and for being such a great mentor at all stages of my projects. I hope we can work together again in the future.

Finally, I would like to thank all my friends who I have been lucky to meet. Carlos Diaz-Ruiz, Ronald Heisser, and Philip Bedoukian are just some of the great friends I have met throughout graduate school and that I share great memories with of the last five years. Everyone has been an incredible support through the different stages and have all led me to this amazing moment.

TABLE OF CONTENTS

LIST OF TABLES

LIST OF FIGURES

CHAPTER 1

INTRODUCTION

Natural collectives, like foraging honey bees or mound-building termites, have inspired algorithms and mechanisms for robot swarms to accomplish remarkable tasks beyond the ability of the individual robots [221, 147, 163]. In natural and artificial micro-scale and macro-scale collectives, when multiple agents coordinate and work together, it becomes possible for the group to exhibit functions or properties that were previously not present or possible with single agents [98, 228]; this emergent, complex behavior has the potential to drastically increase the collective's capabilities. The swarm robotics field holds promising potential for large groups of robots that can efficiently change their collective morphology and behaviors to accomplish diverse tasks like shape formation [163], object manipulation [162], and collective locomotion [98]. By enabling these collective behaviors, groups of robots may accomplish much more than what a single robot can do, like redundancy / fault tolerance, coverage, adaptability. There are many challenges in this pursuit, including the coordination mechanisms to enable the behaviors, communication across the collective, and how to design systems which are tolerant to internal errors and external perturbations. This thesis focuses on addressing some of the challenges related to coordination mechanisms among collectives from the micro- to macro- length scales.

There are two main approaches to achieving collective behaviors; one is a high-level coordination approach and the other is a low-level coordination approach. In this thesis, the first approach means the collective is composed of "intelligent" and "capable" agents, and in the second, and are limited in their

perception and communication range. The high-level coordination approach means each robot in the collective is composed of sensors, actuators, and processors onboard that allow it to move through its environment and / or manipulate its surroundings, make sense of its own state and its surroundings, and plan its next course of action given some current state. In many ways, this approach is desirable because it means that each agent can accomplish much on its own and could possibly "figure out" how to get out of situations that are undesirable for itself and / or the collective. At the macro length scales, individuals' sophistication means it is harder to scale up the number of agents in the collective because of the resources and cost associated with computation, coordination, and motion. At the micro-scale, there are currently limitations on the amount of on-board processing possible, which means it is not possible right now to enable high-level coordination for collective behaviors at this scale.

The second coordination approach enables us to address some of these issues by using low-level cues like strain and chemical signaling that do not necessarily require the agent to "understand" much about its own state or its surroundings, yet the collective is still able to achieve diverse collective behaviors. Social slime mold, is especially interesting because it embodies many features that would enable a robot collective to omit the need for sophisticated actuation, sensing, and processing capabilities and instead exhibit emergent complexity which can enable the collective to complete diverse tasks. These features include: low-level communication, plasticity, and simple agents.

Social slime mold exhibits these features as it transitions through several collective formations throughout its life span [85]. When there is an abundance of nutrients, thousands of cells are dispersed throughout an area. When starva-

tion begins, however, they begin to aggregate and form loose, interconnected clusters. As that starvation period lengthens, the clusters tighten and eventually transition to a plasmoid, or slug-like, stage. The slug-like formation is composed of thousands of aggregated cells and a gel that encapsulates them; through distributed low-level coordination, the cells within the slug enable it to move through the surrounding environment while searching for nutrients. If the starvation period extends for long enough, the slug transitions into a fruiting body where the cells along the stalk region self-sacrifice for the good of the collective and the cells at the top are released as spores into the air in search of nutrients elsewhere.

The whole time there is no high-level coordination, and no "thinking" involved, since no cell has neurons. The collective is composed of agents that can only sense and communicate locally, and are each only capable of moving through various mediums, yet simply through chemical and strain signaling, the group can shape-shift and reconfigure into different forms to fulfill different functions. Although the collective begins to act as a single body or entity, especially at the slug and fruiting body stages, it is important to remember that it is a collection of cells giving rise to different emergent behaviors based on the local interactions between agents and their surrounding environment.

Beyond the micro-scale, there are examples of other natural collectives at larger length scales that exhibit robust collective behavior and reconfiguration as a result of low-level coordination mechanisms. For example, at the millimeter-scale army ant collectives build bridges and rafts with their own bodies by exploiting their collective entanglement and the physical forces between agents [110]. At a larger length scale, schools of fish combine visual observation

and sensing of hydrodynamic effects to stay together as a group and move away from predators [15].

Throughout these examples, the collectives are solving different types of problems, and given their size, morphology, and surrounding environment, they develop different methods of coordination, and sometimes that method of communication can exploit the surrounding environment. It is not intuitive that each collective behavior should be possible, given that the individuals are so simple. In some cases, the collective behaviors are mainly possible because of each agent's morphology; in other cases it is because of the specific physical interactions between agents. When the agents have a greater sense of their own state, their neighbor's states, and the surrounding environment, the collective behaviors might be possible because of high-level coordination between agents. In many cases, the collective behaviors result from a combination of these different features. For swarm roboticists that take inspiration from nature, the challenge is to boil down the essentials and pick the most important coordination mechanisms that will enable these behaviors to be realized in robot collectives composed of simple and scalable agents.

To enable various robot collective behaviors at different length scales, we have to first consider what are the fundamental types of interactions taking place across all of these systems. The first type of interaction is how agents interact with each other (agent-agent interaction), the second is how agents interact with or react to their surrounding environment (agent-environment interaction), and the third is about how agents may exploit their surrounding environment to better influence other agents and produce new collective behaviors (agent-environment-agent interaction), Fig. 1.1. Each of these mechanisms will

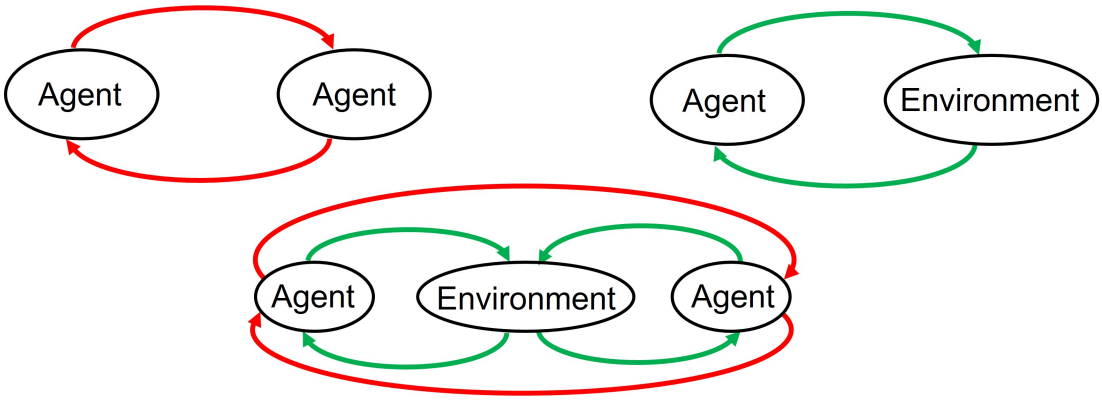

Figure 1.1: Three basic forms of interaction in a swarm: (top left) agent-agent interaction, (top right) agent-environment interaction, and (bottom) agent-environment-agent interaction.

be different depending on the size and morphology of the agents, the composition of their surrounding environment, and the task they are performing. The fundamental question overarching my work in this thesis is: how can we exploit these interactions through low-level actuation, sensing, and coordination mechanisms to enable diverse emergent collective behaviors across length scales? I address this through contributions to the fields of soft robotics, coupled oscillators, and microrobotics.

Cross-Scale Coordination Mechanisms: Chapter 2 in this thesis details a low-level coordination mechanism useful for studying and implementing emergent collective behaviors at different length scales. We use the swarming coupled oscillator, swarmalator [138], model to enable diverse emergent collective behaviors that replicate many real world natural and artificial collective systems. The swarmalator model was originally introduced in 2017 Kevin O'Keeffe, Hyunsuk Hong, and Steven Strogatz [138]; it combined two related fields of self-organization which previously had mostly remained separate, the spatial [156, 208] and temporal [91, 188] self-organization fields.

The spatial self-organization field studies how collectives of natural or artificial agents can produce emergent unified motions through space by exploiting simple local interactions. Two outstanding developments in this field are Craig Reynold's boid algorithm [156] and the Viscek model [208]. The boid algorithm was introduced in 1987 and it changed the way researchers thought about the unified motion of flocks of birds and schools of fish. It summarized the motion of each agent in those collectives as a balance between spatial separation and cohesion with neighbors while also trying to align its direction with that of its neighbors. With these three simple rules, the algorithm demonstrated the emergence of uniform motion among many agents even though there was no central coordination. The Viscek model was introduced in 1995, and became widely popular in the physics community for studying the behaviors of natural and artificial collectives composed of self-propelling constituents across all length scales. The model summarized the motion of each agent in a collective as an average of the motion of its neighbors. The model is dependent on the following three parameters: the density of particles, the noise in the system, and radius of agent-agent interaction. By varying these parameters, the emergent collective behavior could switch between general states like aggregation, disorder, and flocking.

The temporal self-organization field studies how a collective's internal state changes over time as a result of local interactions between the constituents. Although there are many different methods in which agents may affect each other's internal state and produce some collective results, here we focus on temporal self-organization through collectives of stationary phase coupled oscillators. This field was first introduced in 1967 through the Winfree model [224], which studied the emergent behaviors of biological oscillators like fireflies and

circadian rhythms. The Kuramoto model came later in 1975 and simplified the Winfree model to an exactly solvable form and has been studied with many variations including multi-dimensional networks [12], incorporation of noise [133], time delays [103] and many other parameters of interest. These two fields of self-organization have found applications across physics [159, 59], biology [18, 29], and engineering [197, 117].

When the swarmalator model was introduced in 2017 [138], the spatial and temporal self-organization fields were connected by enabling phase coupled oscillators to move as a function of the phase interaction with their neighbors, and to change their phase as a function of their relative spatial position to other agents. The original study demonstrated that the model could arrive at five different states. The collective could aggregate and synchronize or move towards asynchrony, it could self-reconfigure into a static or dynamic ring-like formation organized by phase, or it could split into petal-like formations organized circumferentially by phase. Other work has been introduced that explores the emergent collective behaviors when there is local coupling [74], an external periodic stimulus[105], and when the motion is confined to a ring [134]. Others have shown that the behaviors transfer to a robot collective system with terrain and aerial drones [11].

Although the original study was instrumental in introducing a new field of research, the model made several assumptions that make it slightly non-realistic. Among those assumptions was that the collective had global coupling and that all agents share the same natural frequency. We address some of those assumptions in our work and find many new states that can help in characterizing micro-scale natural and artificial collectives, or could be used to en-

able macro-scale robot collectives to reconfigure into many different formations through low-level signaling between agents. We further demonstrate how a collective of mobile coupled oscillators may behave when agents can move along one dimension or when the environment is laden with static coupled oscillators. This mathematical framework is powerful since it can be used throughout so many systems. We demonstrate in later chapters that a phase coupled oscillators approach is useful for generating several emergent behaviors in a soft robot collective and that the swarmalators approach can be used to replicate some of the behaviors in a magnetic microrobot collective.

Macro-Scale Robot Collectives: Chapters 3-8 summarize my work on actuator, sensor, robot / system integration, and algorithm development for macro-scale soft robot collectives. The swarm robotics field is interested in realizing behaviors like collective locomotion, object manipulation, and self-reconfiguration through robotic agents that can be easily scaled to large numbers. The soft robotics field offers a way of fabricating large numbers of robots that can easily deform, adapt their shape to their environment, and exploit low-level sensing and actuation mechanisms (i.e. strain and inflation) to make sense of their surroundings and produce diverse collective behaviors. I explore several methods for actuation that could be used in a scalable soft robot collective and then implement one of the forms of actuation on one of the soft robot collectives. On the sensor side, I present a novel strain sensor with scalable and accessible fabrication methods that can be used for exteroception and proprioception; I implement this sensor on one of the robot collectives and demonstrate that it can simultaneously supply information about the robot's own state and its surroundings. Finally, I present work on hardware and software development for two soft robot collectives that may use deformation and compliance to make

sense of their own state, their surrounding environment, and coordinate with neighboring agents to produce new collective behaviors.

The two soft robot collectives demonstrate how we can tightly couple sensing and actuation mechanisms on macro-scale robots to exploit information through passive deformation and physical perturbations. Although these robot collectives are not meant to be used in industrial settings, they are useful for studying reconfiguration schemes in cluttered environments [223], how passive deformation can be used to make sense of the surroundings [27], how coupled oscillatory physical perturbations can be used as low-level coordination mechanisms [25], and to study how strain may propagate through a collective of soft active agents [132]. These collectives are essentially a distributed sensor/actuator network that communicates through locally induced strain similar to slime mold and epithelial tissues [8, 85].

The soft robotics field has experienced major progress in actuation, sensing and control, fabrication, and energy storage mechanisms during the past decade [165, 71, 48]. Soft robots can exhibit large strain and have open-loop control that enables the robot to passively conform to the surrounding environment [173]. They also have scalable fabrication procedures and work has begun on coupling actuation and powering mechanisms to make these robots more energy dense [10]. The field has had many developments in various drivers of actuation including pneumatic [131], light-driven [30], dielectric [72], temperature-sensitive [226, 26], and magnetic mechanisms [47]. Throughout my work, I exploit pneumatic and magnetic actuation mechanisms that enable the robots to move, change size, and deform around surrounding objects.

In this thesis, each soft robot collective is composed of identical agents that

individually have limited actuation, sensing, and communication capabilities. Each collective stems from the self-reconfigurable modular robotics field, which holds the promise of extreme versatility and adaptability across diverse environments [237]. The self-reconfigurable modular robotics field aims to develop robot collectives that can shape-shift on-demand to complete any task required, like navigate through a cluttered environment [223], manipulate an object [41], or move through different terrains [172].

Related to the physical design of these robots, the following are several of the long-standing challenges must be addressed: (1) scalable fabrication, (2) successful reconfiguration, and (3) low maintenance, including low mechanical wear. To have modular robots that reconfigure between different morphologies and functionalities there needs to be many robotic modules. Therefore, there needs to be fabrication procedures that enable the production of many modules in a short amount of time. Modules must be able to attach and detach along each other's perimeters to reconfigure between different configurations and while they perform these docking maneuvers the physical components must be able to withstand mechanical fatigue so that these critical functions do not suffer over a short period of time. The self-reconfigurable modular robotics field has explored docking mechanisms that rely on mechanical coupling [43], temperature sensitive materials [195], and magnetic interactions [86]. electropermanent magnets and electromagnets have been used in past self-reconfigurable modular robotic systems to enable robots to dock onto each other [42, 41].

I co-designed a new platform named the 'Donuts' [223] to address these three challenges listed above by using a compliant PCB as the body of the robot, which holds all components for actuation, sensing, and processing on it, and

enables fast and inexpensive fabrication. The 'Donuts' use simplified electropermanent magnets to enable modules to move about each other's perimeters to attach at designated sites without any moving components. Most self-reconfigurable modular robots have been composed of rigid agents; however, by introducing soft materials we can exploit their high deformation and compliance to overcome issues related to mechanical tolerance. With soft materials, modules can have higher mechanical tolerance and do not have to be perfectly aligned with each other to successfully dock in place.

The second platform I developed, the 'Foambots', consists of cylindrical polymer modules that can dock to neighbors via passive magnets embedded in their perimeter. Individual modules can change diameter by inflation, and many coupled modules can shape morph and move through synchronized inflation/deflation cycles. We further exploit the soft aspect of these modular robot collectives by studying how strain sensors onboard each type of module can be used to make a sense of the surroundings through passive deformations and physical perturbations.

Another significant challenge in modular robots is distributed algorithms used to explore how passive deformation of the modules can be used to estimate the shape of nearby objects. With the Foambots, we use one of the strain sensors we have developed [107] to estimate surrounding modules' behavior and use a coupled oscillator approach to switch between different collective behaviors. The strain sensors onboard the Foambots enable each module to tightly couple its sensing and actuation mechanisms. By employing coupled oscillator theory, each module can use radial oscillations to perturb and infer neighbors' state to enable synchrony, traveling waves, and asynchrony to enable collective

functions like synchronized force exertion, tuning of mechanical properties like stiffness and porosity, locomotion, and dispersion.

Micro-Scale Robot Collectives: Chapter 9 focuses on a magnetic microrobot collective exhibiting various emergent behaviors as a result of local interactions. Robot collectives at the small scale have also had many developments during the last decade. There are two main approaches for driving the behavior of these small-scale robotic systems: direct actuation of each microrobot or a global signal that affects the response of the entire robot collective. Systems with local actuation may use a directed signal that actuates individual agents in a collective. For example, one of the smallest microrobots currently in existence functions as an optical wireless integrated circuit [123, 102, 38]. When a laser beam is focused on one of the microrobot's photovoltaic cells, a certain portion of it actuates which allows it to move along a fluid or substrate medium. Systems with global actuation use an external signal that affects all agents in the collective at once; because of their local physical interactions, various collective behaviors can be achieved when the signal is changed. Various types of signals, like magnetic [228], electric [248], and light [126], have been used to elicit collective modes like vortex-like formations [104], chains [241], gas-like states [247]. Most systems have been shown to elicit only one or a few collective behaviors in the presence of an external field. The magnetic microrobot collective in this thesis demonstrates more behaviors than any other system currently in the literature and uses the different behaviors to execute different functions like object manipulation, collective locomotion, and dispersal.

The microrobot collective in this thesis remains at the fluid-air interface throughout the studies and its behaviors are the result of two perpendicular

oscillating magnetic fields that change how each agent spins or oscillates about its own center of mass and disturbs the surrounding fluid medium which influences the motion of surrounding agents and / or passive objects; the global signal affects the relative strength of the local agent-agent interactions that enable different collective behaviors. I demonstrate that collectives can reconfigure on demand between different behaviors, functions, and morphologies. I also show that the microrobots can perform internal and external actuation on surrounding passive structures to drive small mechanisms. All of these are emergent behaviors resulting from the individual microrobots' response to the global magnetic field. Rather than relying on any type of processing to react to their neighbor's behaviors, these agents rely on their physical composition and its response to an external field to drive their individual behavior and its interactions with other agents and the surrounding environment, and thus to realize the different collective behaviors. These micro-robots are as simple as can be; there is no onboard computation, sensing, or actuation, but emergent complexity is still possible because there are many, and they leverage agent-agent, agent-environment, agent-environment-agent interaction

1.1 Thesis Organization

- Chapter 2: We study the emergent behaviors of a population of swarming coupled oscillators, dubbed 'swarmalators'. Previous work considered the simplest, idealized case: identical swarmalators with global coupling. Here we expand this work by adding more realistic features: local coupling, non-identical natural frequencies, and chirality. This more realistic model generates a variety of new behaviors including lattices of vortices,

beating clusters, and interacting phase waves. Such behaviors are found across natural and artificial micro-scale collective systems, including social slime mold, spermatozoa vortex arrays, and Quincke rollers. Our model may aid characterization and understanding of natural swarms, as well as design of complex interactions in collective systems from soft and active matter to micro-robotics.

- Chapter 3: Natural organisms use a combination of contracting muscles and inextensible fibers to transform into controllable shapes, camouflage into their surrounding environment, and catch prey. Replicating these capabilities with engineered materials is challenging because of the difficulty in manufacturing and controlling soft material actuators with embedded fibers. In addition, while linear and bending motions are common in soft actuators, rotary motions require three-dimensional fiber wrapping or multiple bending or linear elements working in coordination that are challenging to design and fabricate. In this work, an automatic embroidery machine patterned Kevlar™ fibers and stretchable optical fibers into inflatable silicone membranes to control their inflated shape and enable sensing. This embroidery-based fabrication technique is simple, low cost, and allows for precise and custom patterning of fibers in elastomers. Using this technique, we developed inflatable elastomeric actuators embedded with a planar spiral pattern of high-strength Kevlar™ fibers that inflate into radially symmetric shapes and achieve nearly 180° angular rotation and 10 cm linear displacement.
- Chapter 4: A key advantage to Fluidic Elastomer Actuators (FEA) is that they permit easy fabrication of robots capable of sophisticated manipulation and mobility. This advantage arises primarily from the continu-

ous stretching and relaxation of elastomeric material that defines an active degree of freedom (DOF), prescribed during the manufacturing process. While the low elastic moduli of the soft material allows for infinite passive DOFs, each active DOF typically requires a valve and/or pump. Onboard valving adds weight and size to the robots, and off-board valving requires tubing that imparts resistance to flow and requires higher pressure differentials for reasonable actuation velocities. In contrast to these methods, the work presented here exploits fluidic resistance in poroelastic foam actuators to create a traveling wave using only a single valve and pressure inlet. This concept is evaluated with respect to foam volume and fluid viscosity, and further demonstrated in a three-legged robot capable of millipede-inspired locomotion. The robot is capable of traveling at 1.1 mm/s, with individual legs (closest to the inlet) extending 41.28, 27.36, and 12.95 mm. These results represents an important step towards increasingly complex behavior in soft robots that remain simple to fabricate and control.

- Chapter 5: Shape reconstruction by soft sensors may be useful in applications ranging from precision agriculture to haptics and factory automation due to the potential for low-cost fabrication, durable operation, and safe and compliant interaction. Current prevalent techniques, however, require expertise, expensive materials, and high-end processing equipment which limits both their transition to practice and their accessibility to researchers. To address this issue, we present easily accessible, low-cost, and rapid fabrication techniques for soft and resistive carbon composite sensors. We characterize their repeatability and durability in response to stretch up to 135%. We further show how this fabrication technique may

be easily customized to two different applications, including a stretchable, tactile interface for passive sensing, and an active, soft pneumatic gripper that can fully encompass an object to reconstruct its shape. We complement these with simple control and analysis, and show how to achieve high relative accuracy, despite the high manufacturing tolerances of the sensors.

- Chapter 6: A major goal of autonomous robot collectives is to robustly perform complex tasks in unstructured environments by leveraging hardware redundancy and the emergent ability to adapt to perturbations. In such collectives, large numbers is a major contributor to system-level robustness. Designing robot collectives, however, requires more than isolated development of hardware and software that supports large scales. Rather, to support scalability, we must also incorporate robust constituents and weigh interrelated design choices that span fabrication, operation, and control with an explicit focus on achieving system-level robustness. Following this philosophy, we present the first iteration of a new framework toward a scalable and robust, planar, modular robot collective capable of gradient tracking in cluttered environments. To support co-design, our framework consists of hardware, low-level motion primitives, and control algorithms validated through a kinematic simulation environment. We discuss how modules made primarily of flexible printed circuit boards enable inexpensive, rapid, low-precision manufacturing; safe interactions between modules and their environment; and large-scale lattice structures beyond what manufacturing tolerances allow using rigid parts. To support redundancy, our proposed modules have on-board processing, sensing, and communication. To lower wear and consequently

maintenance, modules have no internally moving parts, and instead move collaboratively via switchable magnets on their perimeter. These magnets can be in any of three states enabling a large range of module configurations and motion primitives, in turn supporting higher system adaptability. We introduce and compare several controllers that can plan in the collective's configuration space without restricting motion to a discrete occupancy grid as has been done in many past planners. We show how we can motivate redundant connections to prevent single-module failures from causing collective-wide failure, explore bad configurations which impede progress as a result of the motion constraints, and discuss an alternative "naive" planner with improved performance in both clutter-free and cluttered environments. This dedicated focus on system-level robustness over all parts of a complete design cycle, advances the state-of-the-art robots capable of long-term exploration.

- Chapter 7: Modular self-reconfigurable robots have the ability to change their connection topology to form large networks of distributed sensors and actuators, for example to reason about gradients in the environment or the geometry of their surroundings. Past work has focused on distributed algorithms to compute the intrinsic shape of the robot. Here, we instead focus on distributed algorithms that permit planar modular robots to compute the shape of external objects in 2D. Grounded in characterization of physical sensors, we simulate shape estimation by modular robots for increasing object size and complexity. Specifically, we compare the use of connectivity and IR sensors which are commonly available on modules, and demonstrate what may be gained from deformable modules with integrated strain sensors. The algorithms we present are dependent only on

motion constraints and may generalize to a wide set of modular platforms.

- Chapter 8: Many modular robots and active matter platforms are inspired by natural aggregates of single-celled organisms that exhibit complex emergent behaviors far beyond the capability and range of individuals. These behaviors stem primarily from short range chemical and mechanical interactions. Past work has focused largely on wireless communication akin to chemicals, however, physical interactions require a shift from rigid to soft, durable robots capable of inducing and measuring strain. Here, we present a platform to support such studies. The hardware consists of stand-alone, soft, pneumatic robots capable of radial expansion and contraction. The robots are cheap and fast to produce; they have 3 directional strain sensors, and 6 magnet pairs to loosely couple with their neighbors.We characterize force profiles, sensors, elastic modulus, magnetic interaction, as well as exploratory aggregate motions. Finally, we demonstrate their ability to synchronize, locomote, and fracture in a complimentary quasi-static simulator, with a coupled oscillator model, and discuss evaluation metrics. We hope that this platform will serve to further insights on how simple physical interactions between locally informed agents may lead to complex emergent behaviors.
- Chapter 9: Mobile microrobots, which can navigate, sense, and interact with their environment, could potentially revolutionize biomedicine and environmental remediation. Many self-organizing microrobotic collectives have been developed to overcome inherent limits in actuation, sensing, and manipulation of individual microrobots; however, reconfigurable collectives with robust transitions between behaviors are rare. Such systems that perform multiple functions are advantageous to operate in com-

plex environments. Here, we present a versatile microrobotic collective system capable of on-demand reconfiguration to adapt to and utilize their environments to perform various functions at the air-water interface. Our system exhibits diverse modes ranging from isotropic to anisotrpic behaviors and transitions between a globally driven and a novel self-propelling behavior. We show the transition between different modes in experiments and simulations, and demonstrate various functions, using the reconfigurability of our system to navigate, explore, and interact with the environment. Such versatile microrobot collectives with globally driven and self-propelled behaviors have great potential in future medical and environmental applications.

1.2 Collaborations

The highly interdisciplinary work in this thesis resulted in collaboration with individuals from several different departments and research groups.

- Chapter 2: The work in this chapter resulted from collaboration between myself and Kevin O'Keeffe (former postdoc at the Senseable City Lab).
- Chapter 3: The work in this chapter resulted from a collaboration between myself, Prof. James Pikul (University of Pennsylvania) when he was a post-doc in Prof. Itai Cohen's lab (Cornell University) and Prof. Robert Shepherd's lab (Cornell University), as well as Prof. Cindy Harnett (University of Louisville) when she was a visiting researcher in Prof. Shepherd's lab.

- Chapter 4: The work in this chapter resulted from a collaboration between myself, an undergraduate student, Chaim Futran, and a graduate student, Benjamin MacMurray, in Prof. Robert Shepherd's lab.
- Chapter 5: The work in this chapter resulted from a collaboration between myself, another graduate student, Danna Ma, and an undergraduate student, Gregory Kaiser, in Prof. Kirstin Petersen's lab.
- Chapter 6: The work in this chapter resulted from a collaboration between myself, another graduate student, Nialah Wilson-Small, and three undergraduate students, Logan Horowitz, Claire Chen, and Daniel Kim, in Prof. Kirstin Petersen's lab.
- Chapter 7: The work in this chapter resulted from a continued collaboration between myself, Nialah Wilson-Small, and Logan Horowitz.
- Chapter 8: The work in this chapter resulted from a collaboration between myself, an undergraduate student, Marta An Kimmel, and a post-doc, Alexandra Nilles, in Prof. Kirstin Petersen's lab.
- Chapter 9: The work in this chapter resulted from a collaboration between myself, a graduate student, Gaurav Gardi, in Prof. Metin Sitti's lab (Max Planck Institute for Intelligent Systems), and Prof. Wendong Wang (University of Michigan-Shanghai Jiao Tong Joint Institute).

1.3 Associated Papers

- Chapter 2: The work in this chapter is currently under journal review; the work presented here is also featured in the submitted paper and is currently being revised.

- Chapter 3: The work in this chapter resulted in a journal publication in *Biomimetics*. Chapter 5 is adapted from this paper, the work presented also featured in the paper [22].
- Chapter 4: The work in this chapter resulted in a conference publication in *IEEE International Conference on Soft Robotics*. The work presented here is also featured in the paper [55].
- Chapter 5: The work in this chapter resulted in a journal publication in *IEEE Robotics and Automation Letters*. Chapter 8 is adapted from this paper, the work presented here is also featured in the paper [107].
- Chapter 6: The work in this chapter resulted in a journal publication in *Frontiers in Robotics and AI* and a conference publication in *International Symposium on Multi-Robot and Multi-Agent Systems (MRS)*. The work presented here is also featured inthe paper [223].
- Chapter 7: The work in this chapter resulted in a conference publication in *International Symposium on Multi-Robot and Multi-Agent Systems (MRS)*. The work presented here is also featured in the paper [27].
- Chapter 8: The work in this chapter resulted in a journal publication in *IEEE Robotics and Automation Letters*. The work presented here is also featured in the paper [**?**].
- Chapter 9: The work in this chapter resulted in a journal publication in *Nature Communications*. The work presented here also presented in the paper [56].

CHAPTER 2

DIVERSE BEHAVIORS IN NON-UNIFORM CHIRAL AND NON-CHIRAL SWARMALATORS

Synchronization (self-organization in time) and swarming (self-organization in space) are present in many natural and artificial systems. Sync occurs in flashing fireflies [124], firing heart cells [122], spiking neurons [18, 109], and chorusing frogs [4]. Swarming, on the other hand, is seen in cell collectives that migrate in response to external signals [180, 8], flocks of birds that seamlessly change collective flight direction [17], and schools of fish that coalesce and move together to the collective's advantage [146].

A combination of sync and swarming also occurs in diverse contexts, from biological micro-scale collectives [157, 152] and chemical micromotors [126, 191], to magnetic domain walls [75] and robotic drones [182]. In spite of its ubiquity, a theoretical understanding of this interplay between sync and swarming is lacking. Sync research has, broadly speaking, focused on oscillators which may synchronize in time, but not move around in space [224, 91, 1, 188]. Swarming research has done the reverse; it has studied units moving through space [208, 206] that may synchronize external spatial variables like orientation, but do not synchronize with respect to an internal phase variable in time. As such, the interplay of sync and swarming defines a new kind of collective dynamics about which little is known.

The first steps to explore this new terrain were taken a few years ago by Igoshin et al. [77] and Tanaka et al. [198, 79]; they derived models of chemotactic oscillators with diverse behaviors. Later O'Keeffe et al [138] proposed a generalized Kuramoto model of 'swarmalators' (short for "swarming oscil-

lators") whose states have been seen in natural [180, 157, 152, 193] and artificial [191, 229, 68, 247, 202] micro-scale collectives and is now being implemented on robotic swarms [11]; many researchers are now extending this swarmalator model [135, 74, 119, 105].

This paper continues swarmalator research by further exploring the model introduced by O'Keeffe et al. [138]; our motivation is to comprehensively map out the space of emergent behaviors the model generates. In the original work, for simplicity's sake, the swarmalators were identical, non-chiral, and globally coupled. Here, we relax these idealizations and consider swarmalators which are non-identical, chiral, and locally coupled. The inclusion of these realistic features enhance the model's descriptive power and enable many new behaviors including interacting phase waves, vortices, concentric phase self-organization, and radial oscillation. Many of these behaviors resemble those displayed by vortex arrays of sperm [206], the flocking patterns of Quinke rollers [68, 247], the various life stages of slime mold [180], spatiotemporal waves of cellular self-organization related to embryology [205, 204, 203], and the radial oscillation of phototactic micromotors [126]. Additional states shown in this paper, such as bouncing and revolving clusters, do not to our knowledge have any natural counterparts, but could be useful as inspiration for an applied context. For example, artificial swarmalator systems such as aerial or marine drone collectives could use periodic orbits to maximize surveillance [70] or information-sharing between agents that do not always remain close to each other. Colloids could also be designed to exhibit these emergent behaviors so they can be used in high-precision medicine [183]. We hope this work will inspire new studies on swarmalators, and be useful in the characterization and control of natural and artificial collective systems.

2.1 The Model

Swarmalators have a position x_i and a phase θ_i which evolve according to equations (2.1) and (2.2). As per equation (2.1), each oscillator i has an inherent velocity (v_i), a spatial attraction to all other agents defined by a unit vector between agents' positions and a positive coefficient ($A = 1$), a spatial phase interaction term with a coefficient ($J \in [-1, 1]$), and a global repulsive term defined by a power law and a positive coefficient ($B = 1$). In equation (2.2), each agent has a natural frequency (ω_i), a coupling factor (K), and an inverse dependence on the distance between agents.

$$\dot{\mathbf{x}}_i = \mathbf{v}_i + \frac{1}{N}\sum_{j\neq i}^{N}\left[\frac{\mathbf{x}_j - \mathbf{x}_i}{|\mathbf{x}_j - \mathbf{x}_i|}\left(A + J\cos\left(\theta_j - \theta_i - Q_{\dot{x}}\right)\right) - B\frac{\mathbf{x}_j - \mathbf{x}_i}{|\mathbf{x}_j - \mathbf{x}_i|^2}\right] \tag{2.1}$$

$$\dot{\theta}_i = \omega_i + \frac{K}{N}\sum_{j\neq i}^{N}\frac{\sin\left(\theta_j - \theta_i - Q_{\dot{\theta}}\right)}{\left|\mathbf{x}_j - \mathbf{x}_i\right|} \tag{2.2}$$

In the original model, all (uncoupled) swarmalators moved in the same direction with $|\mathbf{v}_i| = v_0$, and v_0 was set to zero via a change of reference. Here we modify this by setting $v_i = c\frac{\mathbf{n}_i}{|\mathbf{n}_i|}$, where ($c = |\omega_i|R_i = 1$) is a product of the natural frequency (angular velocity) (ω_i) and the inherent radius of revolution (R_i), so that swarmalators are now chiral. When ω_i is positive, the agent moves in counterclockwise (CCW) revolutions while a negative value indicates clockwise (CW) revolutions. Equation (2.3) specifies the agent's instantaneous direction of motion so that θ_i cycles between 0 and 2 and is defined by an agent's position within its circular orbit in the global reference frame. We also include new phase offset terms, $Q_{\dot{x}}$ and $Q_{\dot{\theta}}$, defined in equations (2.4) and (2.6) , which enable a kind of 'frequency coupling'. The motivation here is to increase the attraction

between agents with opposing signs for their natural frequency; this enables more realistic emergent behaviors reminiscent of hydrodynamically and mechanically coupled systems. Supplementary Discussion 1 and Supplementary Fig. 2.8 further discuss the phase offset terms and their effect on the collective's oscillatory behavior.

$$\mathbf{n}_i = \begin{bmatrix} \cos(\theta_i + (\frac{\omega_i}{|\omega_i|}\frac{\pi}{2})) \\ \sin(\theta_i + (\frac{\omega_i}{|\omega_i|}\frac{\pi}{2})) \end{bmatrix} \tag{2.3}$$

$$Q_{\dot{x}} = \frac{\pi}{2}\left|\frac{\omega_j}{|\omega_j|} - \frac{\omega_i}{|\omega_i|}\right| \tag{2.4}$$

$$Q_{\dot{\theta}} = \frac{\pi}{4}\left|\frac{\omega_j}{|\omega_j|} - \frac{\omega_i}{|\omega_i|}\right| \tag{2.5}$$

Finally, we consider swarmalators with natural frequencies ω_i drawn from four different distributions:

- $(F1)$ All swarmalators have $\omega = \Omega$.
- $(F2)$ Exactly half of the swarmalators have $\omega = \Omega$ and the other half have $\omega = -\Omega$.
- $(F3)$ All swarmalators have ω $U(0, \infty)$.
- $(F4)$ Exactly half of the swarmalators have ω $U(0, \infty)$ and the other half have ω $U(-\infty, 0)$.

where $\delta(\cdot)$ is the dirac delta function. More details on the natural frequency distributions used for this study can be found in Supplementary Discussion 2.

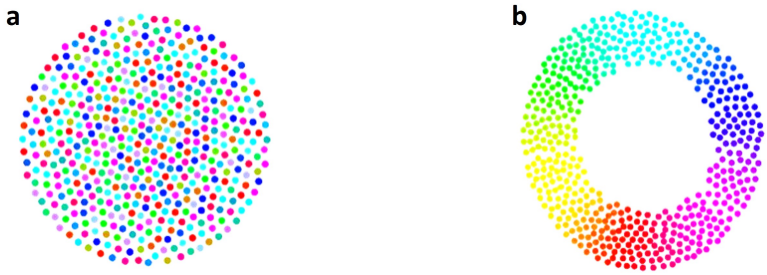

Figure 2.1: Spatial-phase organization order parameter. Two of the five emergent behaviors in the original swarmalator study. (a) Static async ($S \approx 0$). (b) Static phase wave ($S \approx 1$).

To catalog the various collective states of our model, we use the order parameter introduced in Ref. 24:

$$S_{\pm} = \frac{1}{N} \sum_{j=1}^{N} e^{i\phi_j \pm \theta_j} \tag{2.6}$$

Here, ϕ_j is an agent's angular position with respect to the collective centroid $\phi_j = arctan(\frac{y}{x})$ and θ_j its phase; this measures a kind of circumferential 'space-phase order' in the system. When there is no correlation between the angular position and phase, as in Fig. 2.1a, $S_{\pm} = 0$; when there is maximal correlation, as in Fig. 2.1b, $S_{=1}$. Throughout our work, we will refer to $max(S_+, S_-)$ as S and use heat maps of the order parameter in $K - J$ parameter space to draw out the approximate locations of the different emergent states.

2.2 Non-Chiral Swarmalators

We begin our exploration with the simplest case of non-chiral swarmalators with no frequency coupling: $c = 0$, $Q_{\dot{x}} = 0$, and $Q_{\dot{\theta}} = 0$. We numerically simulated Eqs. (2.1) and (2.2) using an Euler method with step size $dt = 0.1$ for

$T = 1000$ time units at which steady states were achieved. We scanned over the state space $J \in [-1, 1]$ and $K \in [-1, 2]$. We use the same numerical scheme and parameter regions in K and J space throughout our work. Numerics revealed a zoo of convergent self-organization behaviors; some stationary, some dynamic. Some of the most interesting are depicted in Fig. 2.2, the full set are reviewed and shown in Supplementary Discussions 3-4 and Supplementary Figs. 2.9-2.17. We discuss in detail the properties of each the most interesting states when $F1$ and $F2$. Results regarding the emergent collective behaviors when $F3$ and $F4$ are in the supplementary material.

2.2.1 Discrete Set of Natural Frequencies

The heat map in Fig. 2.2a shows the general locations of the emergent collective behaviors within $K - J$ parameter space when $F1$, while Fig. 2.2b refers to systems where $F2$. Static async (Fig. 2.2c) is found through much of negative K - space and phase waves (static, active, and splintered) appear when K is negative and J is positive. This is clear from the bright triangular region in Fig. 2.2a which indicates there is high circumferential phase organization. Note that S shows very little difference between the region of static phase wave and splintered phase wave, but dips slightly at low K and high J where the active phase wave emerges. As opposed to previous studies where the static phase wave remained static in space and phase, the phase wave shown in Fig. 2.2d has a static annulus formation and a circumferentially traveling phase wave. When there are several natural frequency groups, however, the number of phase waves change and they become significantly more dynamic. Fig. 2.2e shows two interacting phase waves, each composed of agents with the same natural frequency;

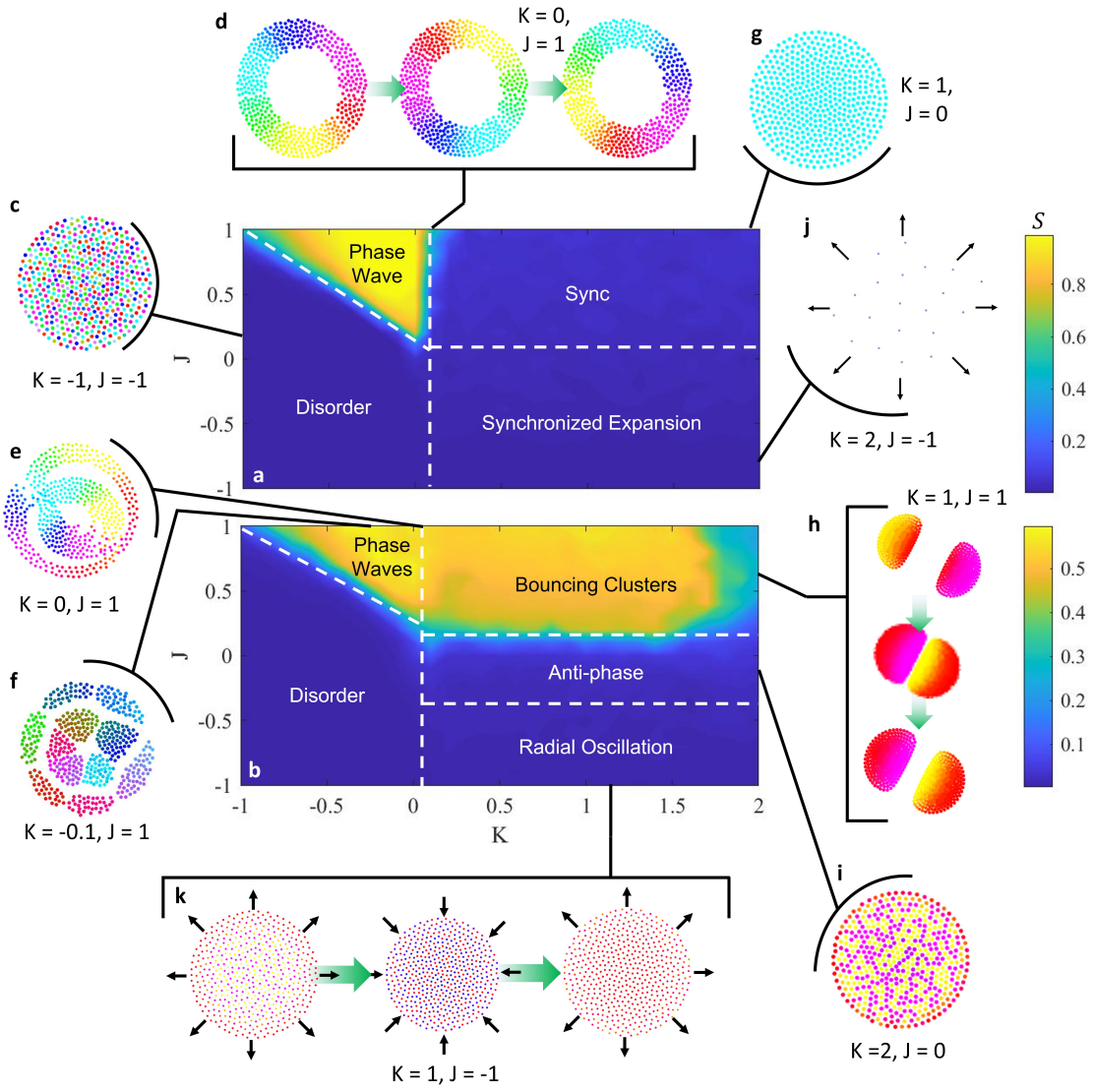

Figure 2.2: Non-Chiral swarmalators with no natural frequency spread. Heat maps of S across K-J parameter space are shown for test cases with (a) $F1$ and (b) $F2$. (c) Static async. (d) Phase wave traveling circumferentially across static agents. (e) Double interacting phase waves. (f) Double interacting splintered phase waves. (g) Static sync. (h) Periodic bouncing clusters. (i) Static anti-phase. (j) Expanding synchronized collective. (k) Periodic radial oscillation.

the two annulus formations oscillate in place as each of their phase waves travels around the circular border and interacts with the opposing group's phase wave. The two phase waves shown here are concentric, but it is worth noting that the collective can also settle on an inter-locked ring formation where either of the natural frequency groups can be closer to the collective centroid. Regardless of whether the phase waves are concentric or inter-locked, they remain circumferentially ordered by phase, which enables a high S value along negative K and positive J, as shown in Fig. 2.2b.

At $K \approx -0.1$, the collective forms a single splintered phase wave when all agents share the same natural frequency, but then display concentric splintered phase waves that rotate about the collective centroid in opposing directions (Fig. 2.2f). Collectives with more than two natural frequency groups also have multi-layer concentric formations, but the spacing between the groups is not clean and there is no clear direction of rotation in each layer of the formation. The splintered phase waves with multiple natural frequency groups are shown in Supplementary Fig. 2.13.

We also observe the static sync state when there is only one natural frequency (Fig. 2.2g); however, the collective behavior is significantly more dynamic when $F2$ because two clusters form and synchronize within themselves, but do not synchronize with the opposing cluster (Fig. 2.2h). Their inability to synchronize causes the collective to enter a bouncing cluster state where each natural frequency group oscillates between attraction and repulsion with the other group, and the two produce symmetric, periodic oscillations about their mutual centroid. The oscillatory behavior is due to the clusters having equal and opposite natural frequencies; this means one group moves about the phase unit circle

in the CW direction while the other moves in the CCW direction. Since both groups have the same absolute natural frequency value, they move about the phase unit circle at the same rate, share the same phase, and are offset by two times per phase cycle. This means the two groups oscillate between having no phase difference and the maximum phase difference and produce periodic attraction and repulsion to each other. Notice in Fig. 2.2b that S remains high around low positive K, but dips slightly at very high K. There is relatively high spatial-phase order for bouncing clusters since the two groups independently synchronize and remain symmetric about an axis running through the collective centroid; however, at high K, the collective eventually transitions from the bouncing cluster state closer to a static sync state, which lowers S because there is no longer circumferential phase organization. The bouncing cluster behavior becomes even more interesting when there are more than two natural frequency groups, a greater number of bouncing clusters form, but their behavior is no longer symmetric about a single axis. Supplementary Fig. 2.14 shows and characterizes bouncing cluster collectives when there are more than two natural frequency groups.

At high K and $J = 0$, collectives with $F2$ create circular formations and enter static anti-phase states (Fig. 2.2i); agents synchronize within their own natural frequency group, but remain offset from the opposing group. Since there is no spatial attraction between like-phased agents, there is a fairly uniform distribution of agents from both groups across the circular formation. Once the collective aggregates into a stable circular shape, agents remain fixed and their interaction distance, which still affects their phase coupling behavior, does not change. Some effects of this can be picked out at lower K: agents are unable to synchronize and as a result phase waves are seen traveling radially. Agents in

the center couple more easily to all other agents, than those close to the boundary; as a result they are able to lead the phase waves within each natural frequency group. As K gets closer to 2, agents begin to freeze their phase behavior; the two natural frequency groups synchronize within their own group, but maintain a constant phase offset with the opposing group; K is high enough that the two groups phase lock.

Finally, we observe a sync state in collectives with a single natural frequency that drives the collective to a circular formation that then proceeds to expand ($K > 0$,$J < 0$), shown in Fig. 2.2j. In this case, agents synchronize and then repel from similarly phased agents; since all share the same phase, the repulsion leads to uniform expansion. Supplementary Discussion 4 and Supplementary Fig. 2.16 address the expansion behavior for various values of J and find that at J=-1, the collective expands indefinitely. The same region of $K - J$ parameter space for $F2$ reveals a radial oscillation state, where the collective evenly distributes agents from both natural frequency groups across a circular formation and proceeds to periodically expand and contract (Fig. 2.2k). The phase interaction behavior is similar to when there are bouncing clusters; the two groups oscillate between attraction and repulsion, but instead of splitting into multiple clusters, agents coalesce in one so they are close to agents from the opposing group. As the two groups' phase difference decreases, agents repel each other and the collective expands, but as their phase difference reaches its maximum, attraction occurs and the group contracts.

2.3 Chiral Swarmalators

Chiral swarmalators' motion and phase coupling behavior is defined by Eqs. (1) and (2) when $c = 1$ and $Q_{\dot{x}}, Q_{\dot{\theta}} = 0$; each agent's natural frequency is defined according to one of the four distributions discussed in the previous section. An overview of the chiral swarmalators' behaviors when there is no frequency coupling is further reviewed in Supplementary Discussions 5-6 and characterized in Supplementary Figs. 2.18-2.21. Results regarding the emergent collective behaviors when $F2$ and $F1$ are reviewed in Supplementary Discussion 5.

2.3.1 Natural Frequency Spread

Chiral collectives composed of agents revolving in the same direction, but with a spread of revolution radii between 0 and 1 are summarized in Fig. 2.3. The S heat maps are shown for collectives with equal and opposite revolution directions in Figs. 2.3a and b, respectively. Both heat maps demonstrate relatively high circumferential phase order across the $K-J$ parameter space and especially high S triangular regions spanning positive and negative K and J. Disordered phase waves are also found with natural frequency spread (Fig. 2.3c) at low K; ordered phases waves lie in the triangular regions. As opposed to most previous phase wave formations where an annulus formed, the frequency spread enables agents to revolve at different inherent radii and form a vortex formation like the one shown in Figs. 2.3d-e; the vortex in Fig. 2.3d looks marginally more organized since all agents revolve in the same direction.

The single and multiple sync revolving clusters are also found at high K and

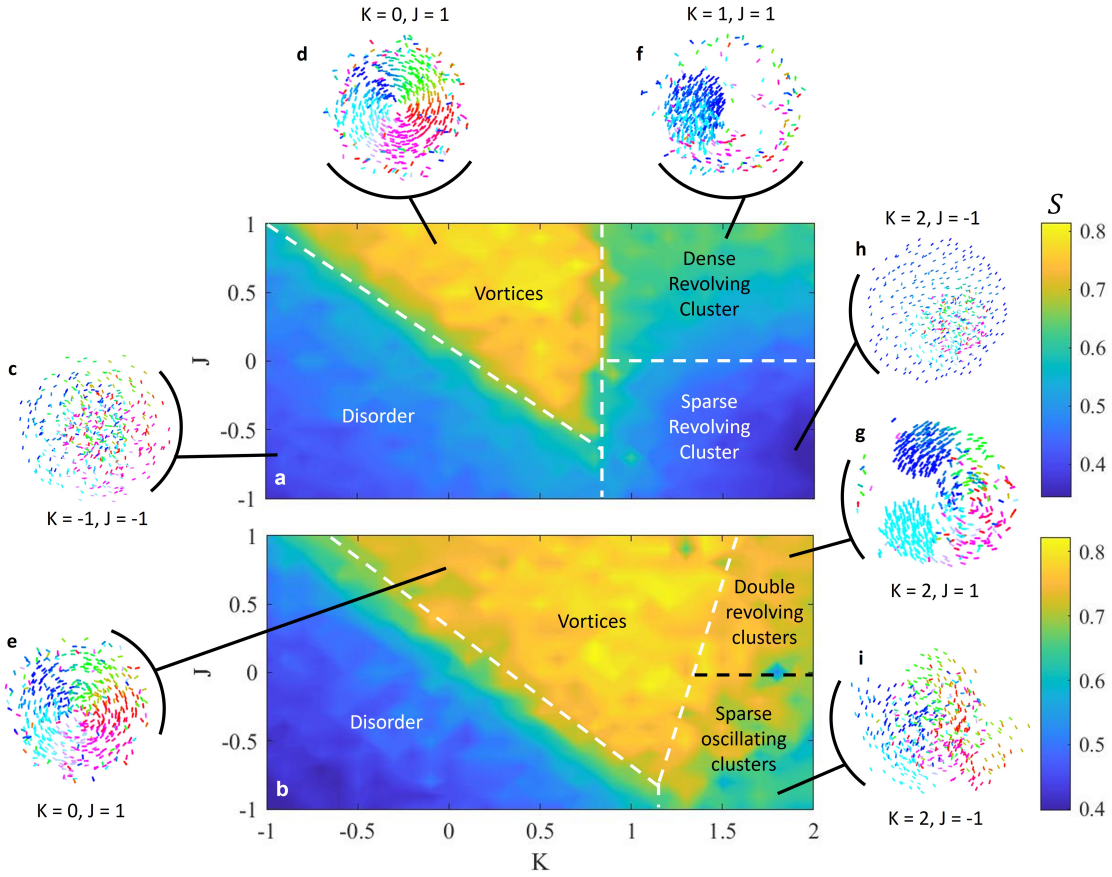

Figure 2.3: Chiral swarmalators with a natural frequency spread. Heat maps of S across K-J parameter space are shown for test cases with (a) $F3$ and (b) $F4$. (c) Disorder. (d-e) Vortex. (f-g) Dense revolving clusters. (h-i) Sparse revolving clusters.

J (Figs. 2.3f-g); the main difference is that a subset of the population remains outside of the clusters. Fig. 2.3f shows a revolving cluster with a ring of asynchronous agents along its trajectory; the agents on the ring have a higher natural frequency and a lower revolution radius. Rather than traveling along the ring, these agents complete small circular motions while repelling away from the cluster and other agents on the ring because of their phase interactions. Fig. 2.3g shows a disordered cluster at the center while the two revolving clusters move around it; a small set of agents remain along the outer ring. This general revolving cluster behavior persists through negative J as well, the main differ-

ence is that the clusters become much sparser (Figs. 2.3h-i). The S value also dips at high K and low J because the synchronized clusters become so sparse that they occupy wide angular regions of the circular trajectory so the circumferential phase organization decreases.

2.4 Frequency-Coupled Chiral Swarmalators

Frequency-coupled chiral swarmalators (FCCS) affect each other's motions similar to the way counter revolving agents might locally affect each other through physical interactions in a real-world setting. In equations (2.1) and (2.2), $Q_{\dot{x}}$ and $Q_{\dot{\theta}}$ are defined by equations (2.4) and (Qtheta); therefore, the natural frequency sign difference between two agents plays an important role in how they will affect each other's motion and phase coupling. Because the spatial and temporal interactions are altered by the sign difference between agents' natural frequencies, we only show results for the distributions $F2$ and $F4$; the emergent behaviors of FCCS when $F1$ and $F3$ are the same as regular chiral swarmalators with the same natural frequency distributions. The emergent behaviors of FCCS are summarized in Fig. 2.4 and further discussed and shown in Supplementary Discussion 6 and Supplementary Figs. 2.22-2.23.

When the collective is split into two equal and opposing natural frequencies, behaviors emerge that appear similar to those from the regular chiral swarmalators; increased repulsion between agents with opposite natural frequency signs, however, enables the collective to split into different clusters and minimize trajectory intersection along several regions of the $K - J$ parameter space, shown in Figs. 2.4a,b. This is not always the case; for example, when $F2$ and there is

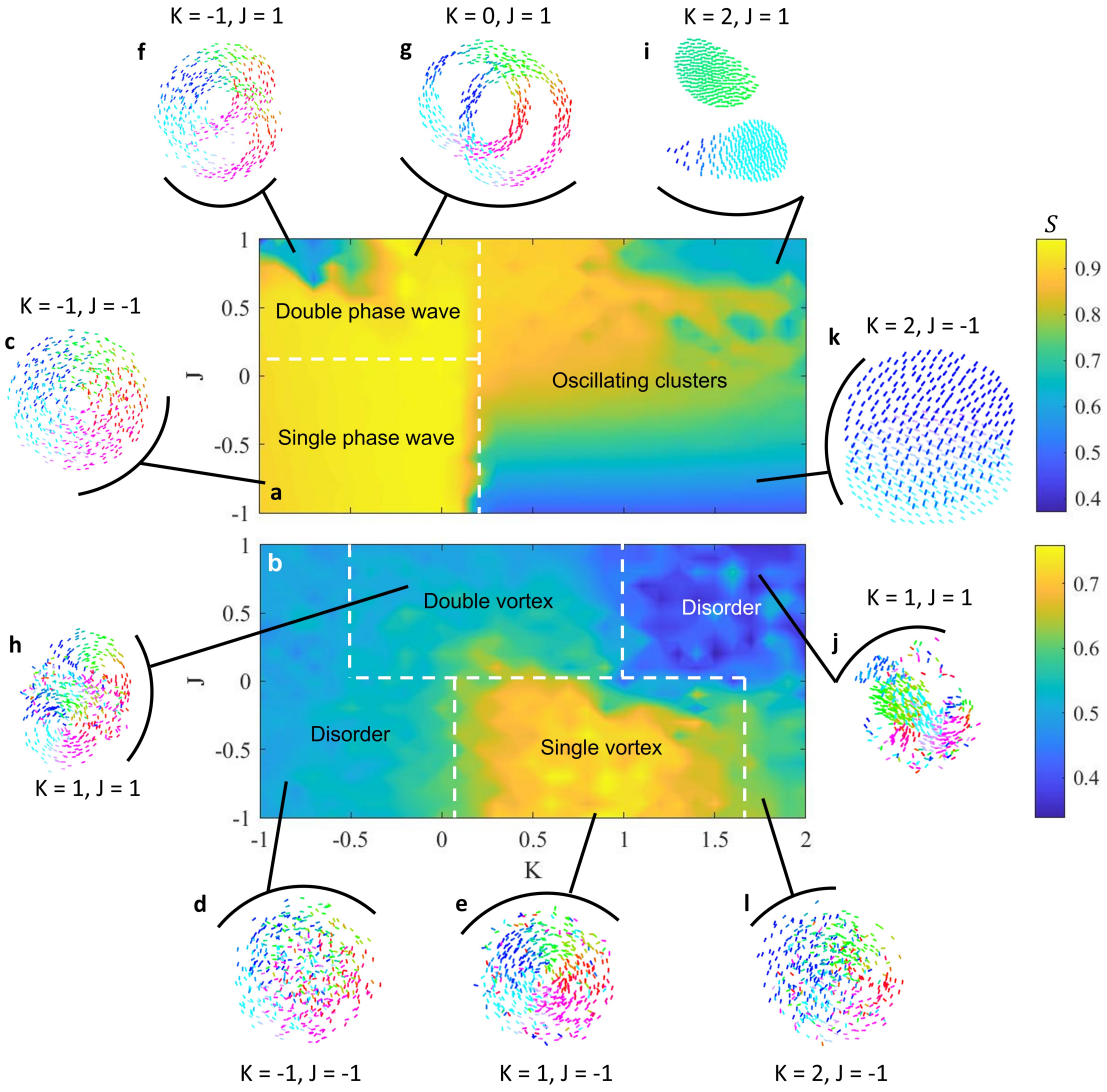

Figure 2.4: Frequency-coupling chiral swarmalators. Heat maps of S across $K-J$ parameter space are shown for test cases with (a) $F2$ and (b) $F4$. (c) Disorder. (d) Phase wave. (e) Double Vortices. (f-g) Double phase waves. (h) Disorder. (i) Dense revolving clusters. (j) Vortex. (k) Disorder. (l) Sparse revolving clusters.

low K and J, an annulus forms with agents from both natural frequency groups moving close to each other (Fig. 2.4c). The same region of $K - J$ parameter space when $F4$ yields high mixing and high disorder (Fig. 2.4d); the disorder most likely occurs because of the large spread of natural frequencies. The bright rectangular region in the lower half of Fig. 2.4b is indicative of a single vortex emerging with high mixing between agents with opposite signs of natural frequency (Fig.2.4e).

The first demonstration of high repulsion between counter-revolving agents is shown in Figs. 2.4f-h. Figs. 2.4f-g show two interacting phase waves that intersect each other when $F2$; the regular chiral swarmalators also exhibit interacting phase waves, but are sometimes difficult to distinguish since they are concentric. The phase wave intersection is caused by the phase shift terms $Q_{\dot{x}}$ and $Q_{\dot{\theta}}$ which enable agents with opposite revolving directions to repel similar phases. At very low K, the phase waves become counterrotating ellipses, which decreases the circumferential phase organization of the whole colletive and lowers S (upper left region of Fig. 2.4a); when K is close to zero, the collective maintains circular double phase waves. When there is a frequency spread, the collective forms two vortices that intersect similarly to the double phase waves; in addition to the vortices, however, there are loose agents around the intersection region that have a high natural frequency and are unable to join the organized formations.

Double revolving clusters are also observed when $F2$ (Fig. 2.4i-j); however, FCCS inhibit trajectory intersection for high K and J. Rather than follow the same circular trajectory in opposite directions, each cluster follows a fairly circular trajectory, but repels away from the opposing cluster as soon as they begin

to intersect. This behavior is much less evident at low J because the clusters become sparser so they can intersect more without being close to other agents. Two clusters also emerge along the same regions when there is a frequency spread, but the behavior is much noisier because of agents with a high natural frequency (Figs. 2.4k-l).

2.5 Comparison to Real World Swarmalators

We demonstrate that locally coupled collectives composed of chiral and non-chiral swarmalators enable new emergent behaviors that closely mimic some natural and artificial swarms. The local coupling instance of the chiral swarmalator model is defined by Eqs. (9)-(11); agents only sense other agents within a set radius (σ), which is tested for values between $\sigma = 0.8R_{max}$ and $\sigma = 2R_{max}$, where R_{max} is the maximum radius of revolution in the collective and has a value of 1 for this study. While the convergent behavior is qualitatively similar, the quantitative behavior of the locally coupled swarmlators are affected by their starting condition. Figs. 2.5-2.7 show several of the emergent behaviors for locally coupled swarmalators that imitate real collective systems including slime mold, vortex arrays of spermatozoa, rotating magnetic colloids, and Quincke rollers. We demonstrate some quantitative and qualitative results that replicate the behaviors of the real collective systems and show more emergent formations in Supplementary Figs. 2.24-2.31.

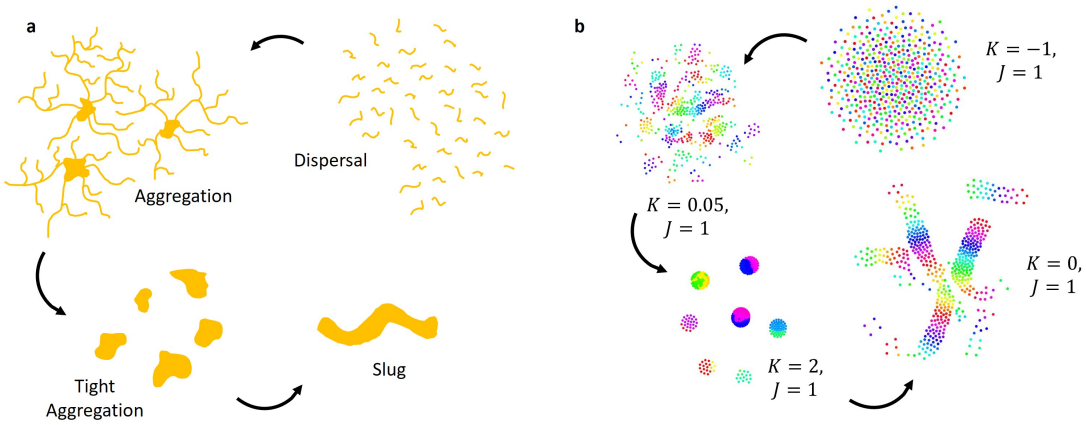

Figure 2.5: Non-chiral swarmalators resembling slime mold. (a) Graphical representation of slime mold life stages. (b) Stages from (a) reproduced by non-chiral swarmalators when $\sigma = 1.4R_{max}$.

2.5.1 Non-Chiral Swarmalators

Social slime mold has various life stages that consist of aggregation, collective motion, and dispersal [180, 45]. Here, we demonstrate that locally coupled non-chiral swarmalators can reproduce these four general life-stages of the multicellular amoebae. Fig. 2.5a shows the various life stages for Dictyostelium Discoideum where thousands of cells begin to aggregate through starvation; as the starvation period continues, prolonged aggregation enables tight clusters that can then combine to form a plasmodium or "slug". This formation enables cells to move together even though there is no brain within the collective; the slug moves around the environment until it finds nutrients and the collective disperses. Fig. 2.5b shows the swarmalators' version of the general behaviors graphically represented in Fig. 2.5a. The non-chiral swarmalators in Fig. 2.5b change K and J and have $F2$ and $\sigma = 1.4R_{max}$. The sparse clusters when $K = 0.05, J = 1$ result from agents that partially synchronize within small groups; when $K = 2, J = 1$, the collectives form tighter clusters. The slug stage is achieved by setting $K = 0, J = 1$; this turns off phase coupling while enabling

attraction between agents with a similar phase. A set of phase wave ribbons form instead of the annulus since agents can only sense locally. We have not done an exhaustive exploration of state transitions, but we did find that clusters are harder to form when there is high dispersion.

2.5.2 Frequency-Coupled Chiral Swarmalators

Fig. 2.6 highlights some of the similarities between spermatozoa vortex arrays and the swarmalators when multiple phase waves emerge. Fig. 2.6a shows a graphical representation of the spermatozoa vortex arrays shown by Reidel et al. [157], where the vortices are tightly packed. In their paper, the authors provide a histogram of the sperm head orientation versus position about their circular trajectory; this concept is depicted in Fig. 2.6b where each dot represents an agent, its color the phase (θ_i) or position about the circular trajectory, and the orientation is ϕ_i. We show a similar plot (Fig. 2.6c) and find that the general trend remains similar for swarmalators. This is powerful because we can use this model to replicate some of the emergent collective behaviors of a natural system without taking into account the specific hydrodynamic coupling mechanisms that occurs in the real system. Fig. 2.6d shows similar packing of the ring-like formations; although, as shown by the trajectories in Fig. 2.6e, the swarmalator vortices are in square grids across all rather than hexagonal grids like those depicted in Fig. 2.6a. The FCCS have a strong attraction between agents with differing natural frequency when their phase is offset by π, so agents from opposing natural frequency groups will actually have a stronger attraction than agents from the same group.

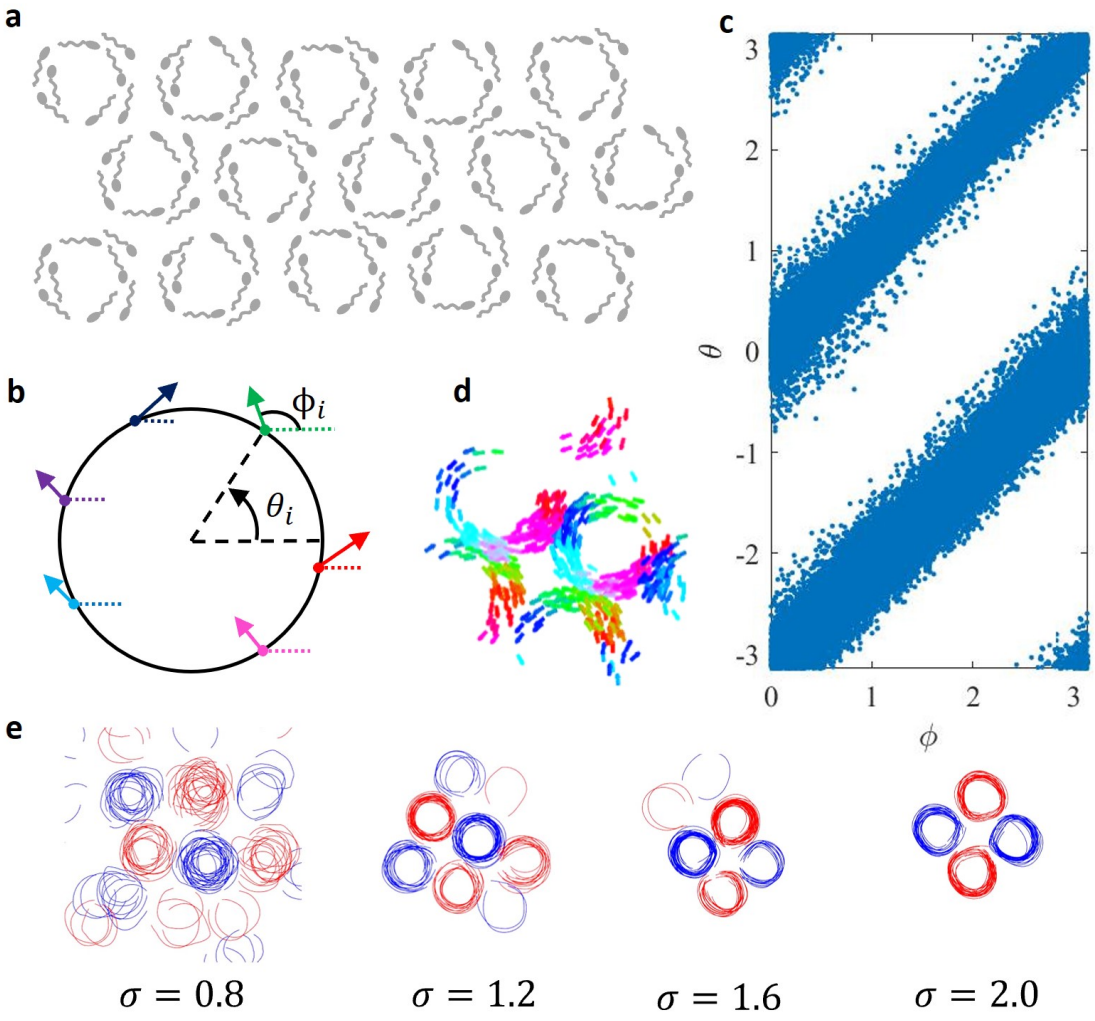

Figure 2.6: FCCS resembling spermatozoa. (a) Graphical representation of sperm vortex arrays. (b) Head orientation vs. position along circular trajectory. (c) Plot of head orientation vs. angular position similar to the one shown in Ref. 10. (d) Snapshot of swarmalators demonstrating this behavior when $K = 0$,$J = 1$,$\sigma = 1.2$, and $F2$. (e) Trajectories of swarmalators with sperm-like collective behavior at various σ (Blue trajectories correspond to swarmalators with inherent circular motion in the clockwise direction, and red correspond to counter clockwise).

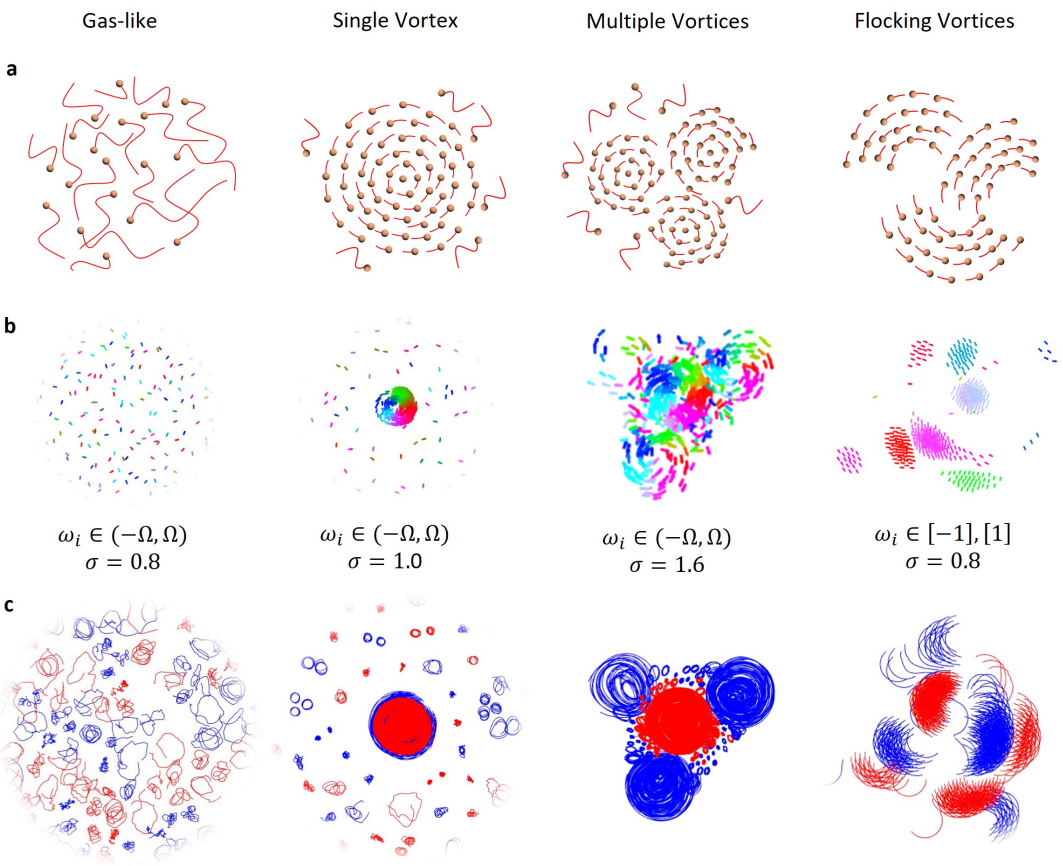

Figure 2.7: FCCS resembling Quincke rollers. (a) Graphical representation of Quincke rollers exhibiting four distinct states. (b) Swarmalator behaviors that closely match the behaviors seen in Refs. 28 and 29;the cases for the natural frequencies from left to right are $F4$, $F4$, $F4$, and $F2$. (c) Trajectories of swarmalator collectives shown in (b). Blue trajectories correspond to agents with a negative natural frequency and red trajectories to a positive natural frequency.

Finally, we compare the swarmalators to Quincke roller collectives [68, 247], which exhibit different formations including gas-like, single vortex, multiple vortices, and flocking vortices; these states are graphically depicted in Fig. 2.7a. Figs. 2.7b,c show sample emergent formations and the corresponding trajectories of swarmalators exhibiting those states when we vary values for σ, K, J, and the natural frequency distribution. Each of the trajectory snapshots shown was chosen to replicate some of the formations shown in Refs. [68] and [247]. There is a vast literature on the emergent behaviors of Quincke rollers with many more

behaviors that would be worth exploring to see if the swarmalators can reproduce those behaviors as well.

2.6 Discussion of Results

We explored non-chiral and chiral swarmalators across various natural frequency distributions and found a zoo of emergent behaviors. Non-chiral swarmalators have no inherent motion, yet their temporal behavior drives them towards dynamic behaviors like radial oscillation, synchronized expansion, bouncing clusters, static anti-phase states, concentric phase self-organization, and many variations of phase waves, sync, and partial sync states. Chiral swarmalators couple spatial and temporal behavior by adding an inherent circular motion to each agent; the emergent behaviors follow similar trends to the non-chiral swarmalators in the $K - J$ parameter space, but demonstrate that the circular motion enables higher levels of spatial-phase order even when there is little or no phase coupling. Some of the most interesting emergent behaviors include single and multiple vortices and phase waves, along with dense and sparse revolving clusters. Throughout the non-chiral and chiral swarmalators, global and local coupling illuminates the effect of distance on the emergent self-organization occurring for different values of K and J. The emergent behaviors mimic a wide variety of collective systems including slime mold, spermatozoa, magnetic colloids, and Quincke roller collectives.

Past work on swarming systems includes several models similar to the Viscek model [208], which demonstrates that collectives can transition from disordered states to flocks by modifying individual agents' behavior according to

their neighbors' motion and orientation. Modified Viscek models defined the agents' motion as inherent revolutions; this led to a breadth of states including revolving flocking patterns [96, 97], vortices, and active foams [206]. These models address emergent swarming states in the presence of noise and agent-to-agent coupling; however, if inherent motion is removed, many of the behaviors cease to exist. With our iteration of the swarmalator model, we seek to present some of the emergent behaviors that result when the inherent motion is turned on or off. The strength of the swarmalator model lies in the fact that it can represent inherently mobile agents where the phase is correlated to orientation, as was the case in the previously mentioned works [208, 206, 96, 97], as well as collectives where there is no inherent motion and the phase is an internal property.

Since our iteration of the swarmalator model enables us to mimic many behaviors found in chiral and non-chiral biological and artificial collectives; we posit that it could be used as a 'toy model' to advance studies in many fields given the universality of phase dependence and circular motion. We also hope this encourages a line of fundamental studies on the emergent behaviors that result from an interdependence between time-domain and spatial-domain-specifc parameters; we believe this could bring strong contributions to the active matter field. Finally, the model demonstrates a wide variety of self-organization patterns that result from low-level coordination; applications could be found in macro-scale robot swarms with constituents that travel in periodic orbits across large distances [243] or have limited information and sensing relative to the span and task of the collective, as well as micro-scale robot collectives that rely almost soley on local interactions among robots and their environment to produce robust and adaptive collective behaviors.

2.7 Materials and Methods

2.7.1 General Simulation Parameters

All numerical studies were run on Matlab using Euler integration, 500 agents, a time step size of $dt = 0.1$, and a final time step of $t_f = 1000$. Simulations for the S order heat maps were run for 10 trials.

2.7.2 Degree of Synchrony

The degree of synchrony holds a value between zero and one, and measures how close a set of agents' phases are to each other. Equation (2.7) is used to calculate the degree of synchrony, Z_G, for a whole collective with N agents. Equation (2.8) is used to calculate the average degree of synchrony within the collective when there are multiple natural frequency groups. In equation (2.8) there are n agents within a natural frequency group and m agents in another group. The degree of synchrony for the collective is the average of the degree of synchrony within each group. In this study we look at the average degree of synchrony within groups when there are two natural frequency groups.

$$Z_G = \frac{1}{N}\sum_{j=1}^{N} e^{i\theta_j} \tag{2.7}$$

$$Z_{FG} = \frac{1}{2}\left(\frac{1}{n}\sum_{j=1}^{n} e^{i\theta_j} + \frac{1}{m}\sum_{j=1}^{m} e^{i\theta_j}\right) \tag{2.8}$$

2.7.3 Local Coupling Model

The local coupling model uses step functions to determine whether agents affect each other's motion and phase behavior. The maximum distance for coupling is defined by the variable which is varied between 0.8 and 2 throughout the simulations.

$$\dot{\mathbf{x}}_i = \mathbf{v}_i + \frac{1}{N}\sum_{j\neq i}^{N}\left[\left(\frac{\mathbf{x}_j - \mathbf{x}_i}{|\mathbf{x}_j - \mathbf{x}_i|}\left(A + J\cos\left(\theta_j - \theta_i - Q_{\dot{x}}\right)\right) - B\frac{\mathbf{x}_j - \mathbf{x}_i}{|\mathbf{x}_j - \mathbf{x}_i|^2}\right)H(\sigma - \left|\mathbf{x}_j - \mathbf{x}_i\right|)\right] \tag{2.9}$$

$$\dot{\theta}_i = \omega_i + \frac{K}{N}\sum_{j\neq i}^{N}\left(\frac{\sin\left(\theta_j - \theta_i - Q_{\dot{\theta}}\right)}{\left|\mathbf{x}_j - \mathbf{x}_i\right|}\right)H(\sigma - \left|\mathbf{x}_j - \mathbf{x}_i\right|) \tag{2.10}$$

$$H\left(\sigma - \left|\mathbf{x}_j - \mathbf{x}_i\right|\right) = \begin{cases} 1, & \sigma - \left|\mathbf{x}_j - \mathbf{x}_i\right| 0 \\ 0, & \sigma - \left|\mathbf{x}_j - \mathbf{x}_i\right| \leq 0 \end{cases} \tag{2.11}$$

2.8 Supplementary Materials

2.8.1 Discussion 1. System Oscillation Characterization

This discussion reviews the oscillatory behavior in attraction and repulsion across various phase interaction parameter spaces. The plots in Supplementary Fig. 2.8 show why oscillation in attraction and repulsion occurs as the agents' phases vary. Supplementary Fig. 2.8a shows a heat map of the spatial phase interaction term in equation (2.1) from the main text; when the two agents' phases

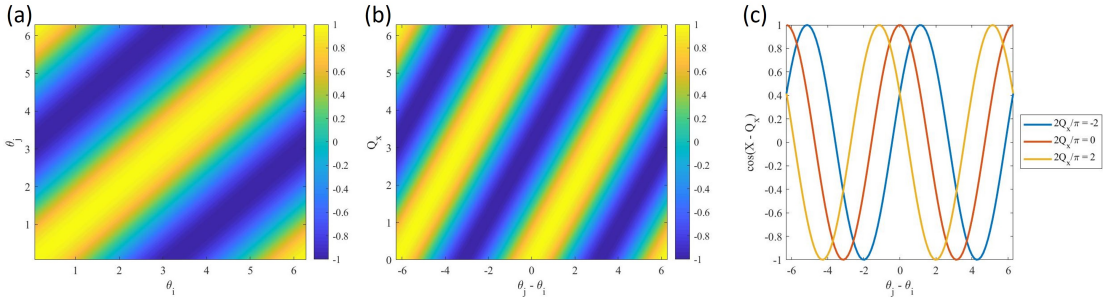

Figure 2.8: Phase-interaction parameter space. Value given by the spatial phase interaction term in equation (2.1): (a) Cases explored for $Q_{\dot{x}} = 0$ and different phase values. The color bar is defined by $cos(\theta_j - \theta_i)$. (b) Cases explored for a constant phase shift value $Q_{\dot{x}}$ and different phase differences $(\theta_j - \theta_i)$. The color bar is defined by $cos(\theta_j - \theta_i - Q_{\dot{x}})$. (c) Oscillation behavior of the phase coupling-induced motion term in $\dot{\mathbf{x}}_i$.

are used as coordinates to plot a point in $\theta_i - \theta_j$ space, we can determine whether that point lies along attraction or repulsion regions. If the point lies close to the line $\theta_j = \theta_i$, then it lies within the yellow region which indicates a positive value for the spatial phase interaction; this enables attraction. When the point lies close to either of the lines $\theta_j = \theta_i - \pi$ or $\theta_j = \theta_i - \pi$, then the spatial phase interaction is negative, which enables repulsion. If agents vary their phases at the same rate, they will maintain the same phase difference over time and according to the phase distribution they will maintain a constant amount of attraction or repulsion over time. However, with natural frequency distributions the phase difference changes over time and the (θ_i,θ_j) point moves through attraction and repulsion regions over time. Supplementary Fig. 2.8b shows the effect of a phase offset on the spatial phase interaction term. Here, the space is defined by the phase difference running between -2π and 2π and a fixed phase offset $(Q_{\dot{x}})$ running between 0 and 2; the trend shown continues over larger ranges. In supplementary Fig. 2.8a there were two bands of repulsion and one band of attraction; however, the phase offset enables two additional bands, three bands of repulsion and two bands of attraction. The more complex space means that

agents are more prone to switch between attraction and repulsion when their phase difference changes over time. Supplementary Fig. 2.8c shows the spatial phase interaction value when $Q_{\dot{x}}$ is defined by equation (2.4) from the main text. Here, the three possible values for $Q_{\dot{x}}$ are $-\pi$, 0, and π. The frequency dependence is relevant when modeling physical systems, where agents with the same direction of motion will tend to align and repel agents that are revolving in the opposing direction. The three lines show the phase shifts along positive and negative phase differences that occur with frequency coupling. Future swarmalator studies with different natural frequency distributions may find the ideal spatial phase interaction space that leads to specific static or dynamic formations that are dependent on phase interactions. Further research along these lines may find that macro-scale robot collectives can be made to move in specific ways and self-organize into any formation by simply communicating some phase value to surrounding agents and reacting to the neighbors' phase through a programmable spatial phase interaction.

2.8.2 Discussion 2. Natural Frequency Distributions

This discussion reviews the methods used for generating the four natural frequency distributions used in this study. The swarmalators' natural frequency distributions were generated using the following uniform distribution: $R_i \in (0, 1]$. Each agent's natural frequency was computed through $\omega_i = \frac{c}{R_i}$.

- When the collective shares the same natural frequency ($F1$), $c = 1$ and $R_i = 1$.
- When the collective is split into two natural frequency groups ($F1$), half of

the collective's natural frequency is computed with $c = 1$,$R_i = 1$ and the other half with $c = -1$,$R_i = 1$.

- When there is a spread of natural frequencies across only positive values so that $F3$, the natural frequencies are computed with $c = 1$ and $R\ U(0, 1)$.
- When there is a spread of natural frequencies across positive and negative values so that $F4$, the natural frequencies are computed with $c = 1$ for one half, $c = -1$ for the other half, and $R\ U(0, 1)$.

For regular chiral swarmalators and frequency-coupled chiral swarmalators (FCCS) this ensures that agents have a negative or positive sign to their natural frequency / inherent angular velocity which determines their direction of motion. For chiral swarmalators, R_i is a physically relevant term since it defines an agent's revolution radius; for non-chiral swarmalators it is simply a mechanism for generating a wide natural frequency distribution. Although non-chiral swarmalators have no revolution radius, the same distribution between 0 and 1 is used so that the natural frequency distributions for the non-chiral, chiral, and frequency-coupling chiral swarmalators remain the same throughout the study. Since R_i always holds a value between 0 and 1, the minimum $|\omega_i|$ is 1 and the maximum is indefinite. Although the presence of agents with a very high natural frequency may cause some concern over the reproducibility of the different emergent behaviors when there is a frequency spread, simulations across the $K - J$ parameter space showed reproducible trends in behaviors that could be explained by the coupling values and the natural frequency distribution. Moreover, this enabled us to find additional behaviors throughout the $K-J$ parameter space. If all natural frequencies were low, the collective would eventually settle down to the behaviors found when the collective was split into discrete natural

frequency groups. With the large spread, we were able to study how a collective might behave when there are very diverse agents with very large natural frequencies or very small revolution radii. This diversity essentially served to incorporate noise into the system and observe the different emergent behaviors.

2.8.3 Discussion 3. Non-Chiral Swarmalators with a Natural Frequency Spread

This discussion presents some of the most interesting emergent collective behaviors when there is a natural frequency spread for non-chiral swarmalators. Supplementary Figs. 2.9a-b show that disorder lies throughout much of the $K - J$ parameter space and an example formation is shown in Supplementary Fig. 2.9c. At higher values of K and J, however, clusters of agents with lower $|\omega_i|$ begin to synchronize while agents with higher $|\omega_i|$ remain asynchronous and at the outer edges of the collective. Supplementary Fig. 2.9d shows the first instance of partial synchronized collectives with a positive natural frequency spread; at $K = 1$, the collective begins to couple and initially a small, synchronized cluster forms in the center of a ring of asynchronous agents, much like the one in Supplementary Fig. 2.9e. Over time, agents from the asynchronous group begin to couple more closely with the cluster and therefore move towards the center. The agents joining the center cluster have a higher natural frequency; therefore, it is difficult for the group to remain synchronized and an elongated phase wave forms along an axis. Agents from the outer boundary coalesce at one end of the phase wave and begin to enter the phase wave; agents at this end have a lower natural frequency than the ones extending further out.

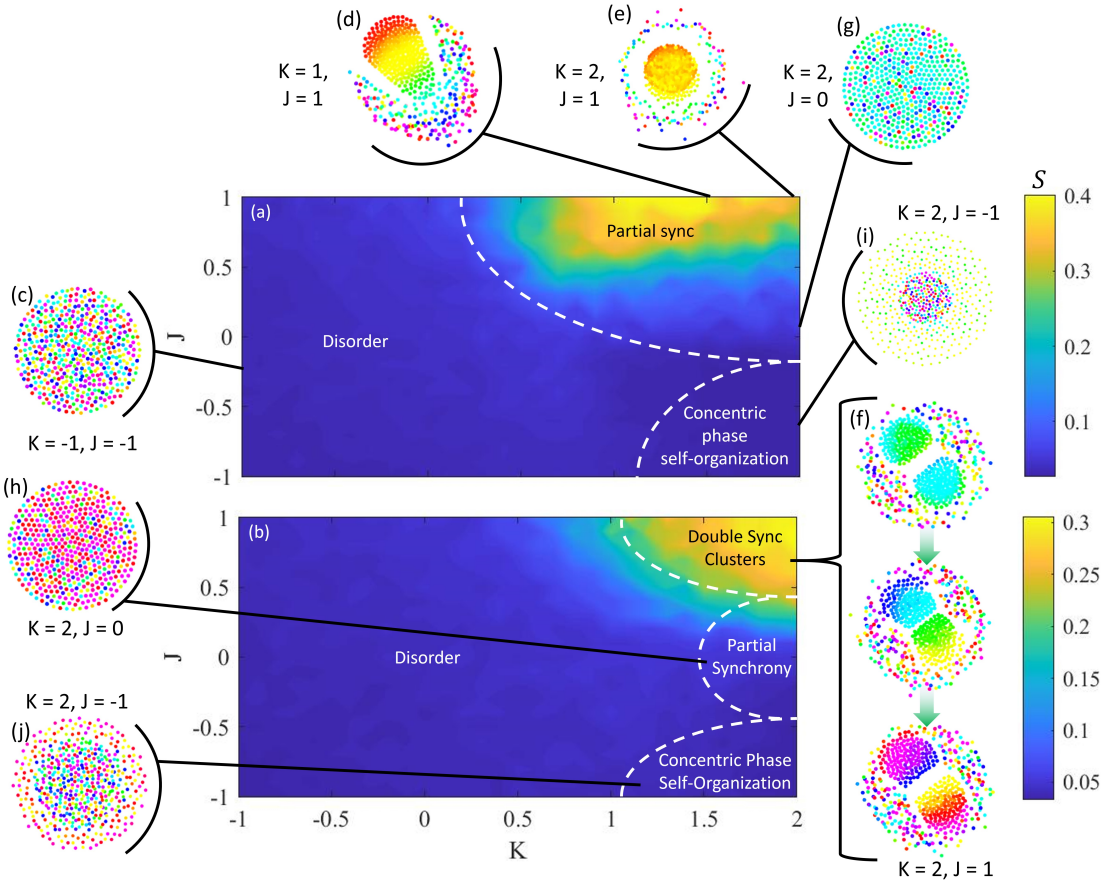

Figure 2.9: Non-chiral swarmalators with a natural frequency spread. Heat maps of S across $K - J$ parameter space is shown for test cases with (a) $F3$ and (b) $F4$. (c) Static async. (d) Partial sync with phase wave along an axis. (e) Partial sync with synchronized cluster forms at the center. (f) Periodic bouncing of partial sync clusters. (g-h) Partial sync within a circular formation. (i-j) Concentric phase self-organization.

Supplementary Fig. 2.9e also shows partial synchronization; however, K is high enough that the center cluster remains mostly synchronized while a thin outer ring of asynchronous agents with high natural frequencies remains on the outskirts and radially oscillate. The radial oscillation is asynchronous and results from fluctuating phase interactions with the center cluster. Similar behaviors occur when the natural frequency spread is across positive and negative values, except two sync clusters form since agents with the same sign of natu-

ral frequency can synchronize more easily. As shown in the sequential images in Supplementary Fig. 2.9f, two clusters periodically bounce from each other's boundary because of oscillatory attraction and repulsion and are surrounded by a cloud of agents with higher natural frequencies. The mechanisms of phase interaction here are like those underlying the behavior in main text Fig. 2.9g, but the spatial oscillation amplitude remains much lower because of the many agents along the border that are unable to join one of the synchronized clusters. Another partial synchronization state emerges at high K when $J = 0$ for both natural frequency distributions; agents coalesce into a circular formation and many of them synchronize (Supplementary Figs. 2.9g-h). A static sync state remains difficult to achieve here because of those agents with a high natural frequency.

Finally, a state emerges at high K and low J; agents self-organize concentrically by phase and an asynchronous cluster forms at the center. When $J < 0$, agents with a high $|\omega_i|$ spatially attract since their phase difference is large much of the time, thus a cluster forms. Conversely, agents with a lower $|\omega_i|$ synchronize more easily and repel each other because of the low phase difference; this drives them to form a sparse cloud around the center cluster (Supplementary Figs. 2.9i-j). A greater fraction of the collective forms the sparse cloud in Supplementary Fig. 2.9i than in Supplementary Fig. 2.9j because all agents have natural frequencies distributed across positive values, which enables a greater fraction to have low $|\omega_i|$ and synchronize more easily. When $K = 1$, $J = 1$, and there is a frequency distribution $F2$, there is slight radial oscillation; however, we classify these as separate states because (1) the radial oscillation is almost insignificant, (2) much of the collective remains clustered and is not expanding, and (3) the perimeter cloud of agents has a noticeable concentric phase wave

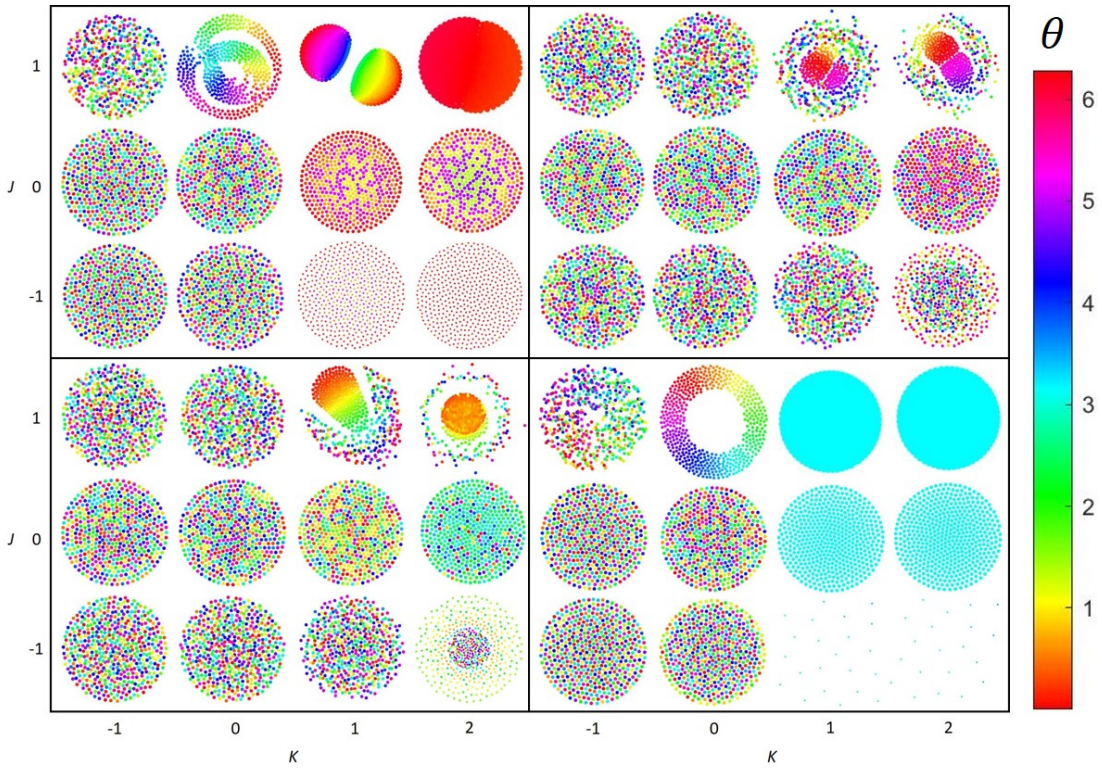

Figure 2.10: Collective behaviors of non-chiral swarmalators with no frequency coupling. $g(\omega) = \frac{1}{2}(\delta(-\Omega) + \delta(\Omega))$ (Upper left). $g() = Uni(-\Omega, \Omega)$ (Upper right). $g(\omega) = Uni(1, \Omega)$ (Lower left). $g(\omega) = \delta(\Omega)$ (Lower right).

traveling from the center out that is not as obvious in the radially oscillating collective from Fig. 2.2j.

2.8.4 Discussion 4. Overview and Characterization of Non-Chiral Swarmalators

This discussion reviews the collective behaviors exhibited by non-chiral swarmalators with no frequency coupling. The behaviors achieved by swarmalators when $c, Q_{\dot{x}}, Q_{\dot{\theta}} = 0$ for integer values of K and J are shown for the four natural frequency distributions in Supplementary Fig. 2.9. The formations shown here

have only scratched the surface of what emerges when the coefficients within $\dot{\mathbf{x}}_i$ and $\dot{\theta}_i$ are varied. The formations shown in Supplementary Fig. 2.11 correspond to swarmalators with discrete natural frequencies; Supplementary Figs. 2.11a-g help the reader visualize each of the corresponding behavioral characterizations that are relevant in Supplementary Figs. 2.11h-n. The first behavior shown and characterized in Supplementary Figs. 2.11a and 2.11h is the interacting phase waves formation that results from half of the collective having $\omega_i = -1$ and the other half, $\omega_i = 1$. The mean speed and S order are plotted for the range of K when $J = 1$. Throughout most of the cases in which $K > 0$, the collective holds a stable mean speed between 0.1 and 0.15; however, around the point where two interacting phase waves emerge ($K \approx 0$), the collective increases its mean speed because of the increased oscillation that occurs when the agents spread out along rings and are each closer to agents from the opposite natural frequency group. When K,$J > 0$, two clusters form that oscillate between attraction and repulsion; this enables the entire collective to be in constant motion, and after each natural frequency group synchronizes within itself, the speed remains constant ($K \approx 0.3$). At these higher values of K, the cluster formation ensures that each agent's motion is affected mainly by two values at any point in time: the average phase within its own natural frequency group and the average phase of the opposite group. When the ring formations emerge, the global spatial-phase order decreases because of the presence of two natural frequency groups, but the concurrent interaction between so many different phases enables each agent to oscillate in place more quickly.

In Supplementary Fig. 2.11i the local coherence measures the average phase coherence of each agent with neighbors that are within a distance of 0.15. The static anti-phase locked state occurs when $J = 0$; when $K < 0$, the local coher-

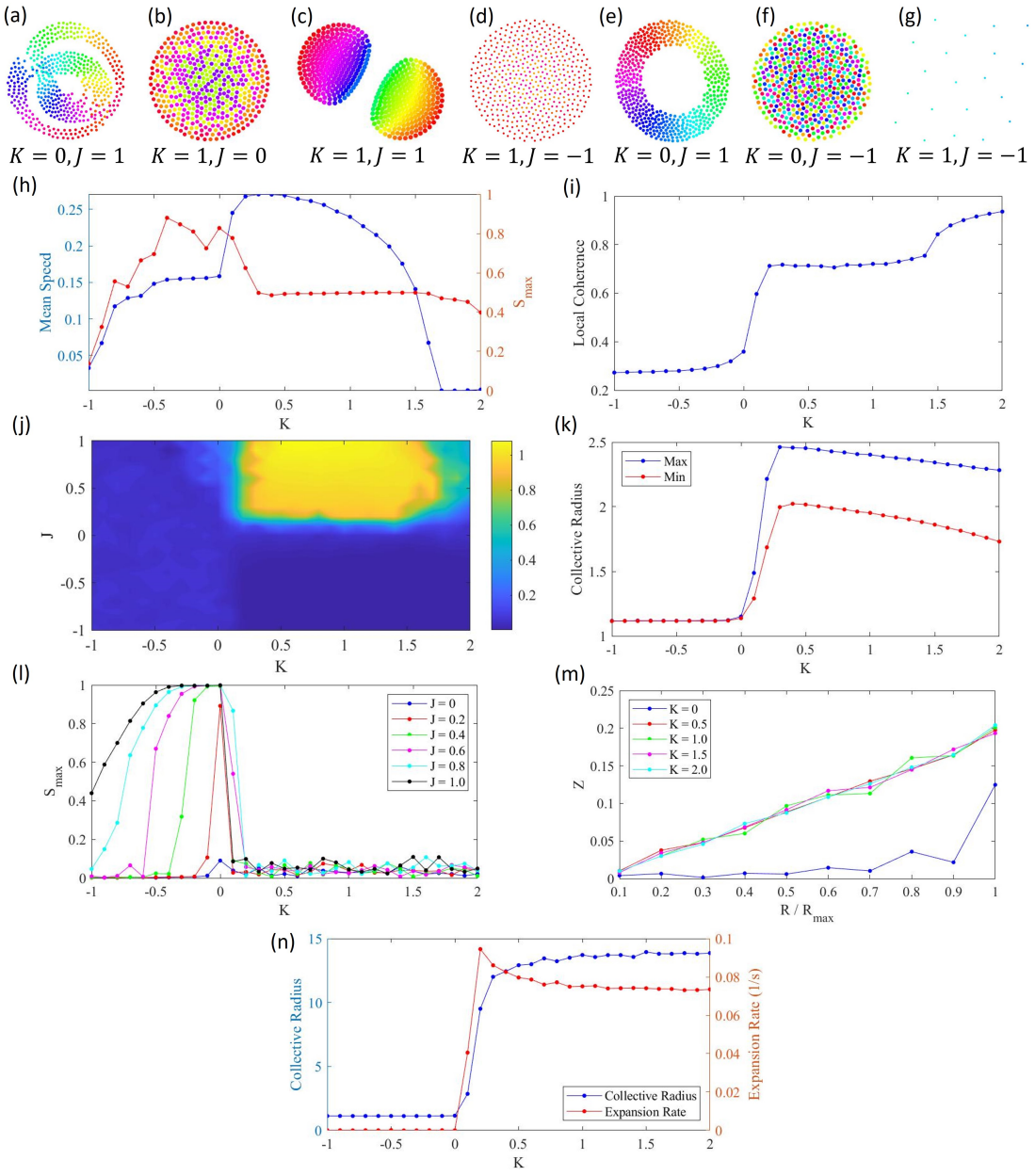

Figure 2.11: Characterization of collective behaviors in non-chiral swarmalators with no frequency coupling and discrete natural frequencies. (a-g) Various emergent configurations of non-chiral swarmalators. (h-k) Collective behavior characterizations for the same distributions listed in (a-k), respectively. (a) $F2$; (b) $F2$; (c) $F2$; (d) $F2$; (e) $F1$; (f) $F1$; (g) $F1$. (h) Mean speed and S order when $J = 1$; (i) Max distance between the two natural frequency group centroids; (j) Local coherence with neighboring agents when $J = 0$; (k) collective radius at peak expansion and contraction when $J = -1$; (l) S order for various values of J and K; (m) phase coherence as a function of distance from the collective's centroid when $J = -1$; (n) collective radius and expansion rate when $J = -1$.

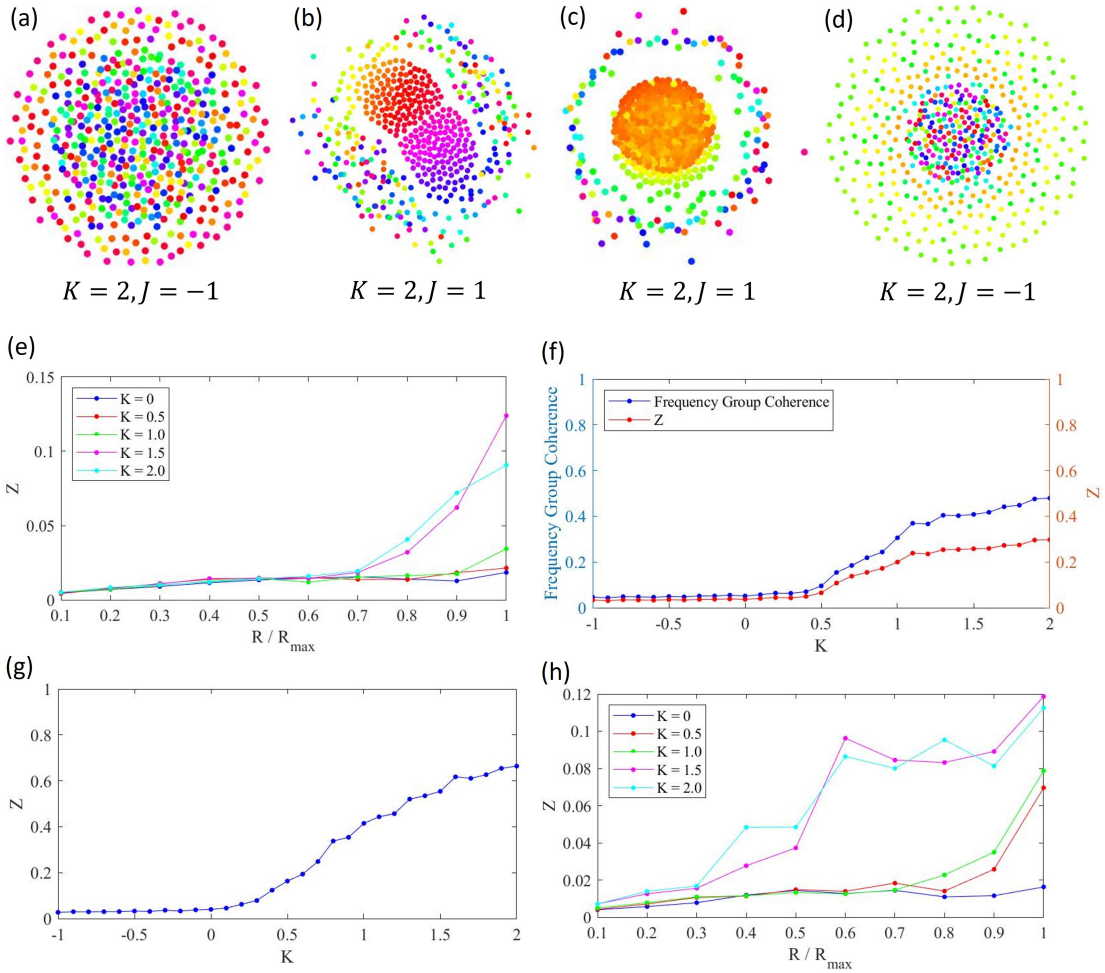

Figure 2.12: Characterization of collective behaviors in non-chiral swarmalators with no frequency coupling and a natural frequency spread. (a-d) Various emergent configurations of non-chiral swarmalators. (e-h) Collective behavior characterizations for the same natural frequency distributions listed in (a-d), respectively. (a) $F4$; (b) $F4$; (c) $F3$; (d) $F3$. (e) Natural frequency group and global phase coherence when $J = 1$; (f) phase coherence as function of distance from the collective centroid when $J = -1$; (g) phase coherence when $J = 1$; (h) phase coherence when $J = -1$.

ence remains at a very small value and then spikes up as soon as it is positive. Another increase in phase coherence occurs when $K > 1.5$; here, the agents synchronize with most other members within the same natural frequency group.

Supplementary Fig. 2.11j shows the amplitude of the distance between the centroids of the two natural frequency groups throughout $K - J$ space. The

amplitude is highest when two clusters form and "bounce" off each other's circumference (K,$J > 0$). At high values of K, ($K \approx 2$) the whole collective begins to synchronize which halts the bouncing cluster behavior and forms the sync state that has been observed in earlier works25. We have run longer simulations with lower values of K for this natural frequency distribution and have found that the bouncing clusters continue oscillating about their common centroid with the same amplitude. We demonstrate that clustering also occurs when there are more than two natural frequency groups. A collective of 500 agents with random phases are evenly divided among the following five natural frequencies: -1, -0.5, 0, 0.5, and 1. When K, $J = 1$, five independently synchronous clusters form that oscillate between attraction and repulsion with the surrounding clusters; the five separate clusters in Supplementary Fig. 2.14a. Supplementary Figs. 2.14b-f show the oscillation between each natural frequency group's centroid as it oscillates between attraction and repulsion with each of the other groups. Since there are more than two groups, the oscillation is noisy as the frequency groups in the center are squeezed out of the visible range of the axis along which the groups align. We also show images of collectives with three, four, five, and nine natural frequency groups in Supplementary Fig. 2.14g-j. We believe this emergent behavior could be especially relevant to robot collectives at the macro scale that can separate and cluster into distinct groups simply by changing their natural frequencies.

The expanding and contracting collectives are analyzed in Supplementary Fig. 2.11k where the collective's radii is recorded for the peak minimum and maximum as it oscillates. When $K < 0$,$J = -1$, agents cannot synchronize and as a result there is minimal repulsion across the collective since few agents share the same phase. As soon as $K > 0$, the collective increases its degree of syn-

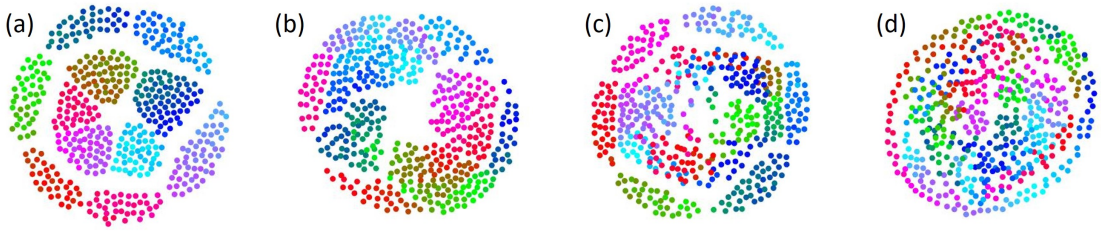

Figure 2.13: Splintered phase waves. Images of collectives with different numbers natural frequency groups when c,$Q_{\dot{x}}$, $Q_{\dot{\theta}} = 0$,$K = -0.1$,$J = 1$. (a) $\omega_i \in [-1], [1]$. (b) $\omega_i[-1], [0], [1]$. (c) $\omega_i \in [-1], [-0.5], [0.5], [1]$. (d) $\omega_i \in [-1], [-0.5], [0], [0.5], [1]$.

chrony within each natural frequency group, and agents repel each other when they share the same phase. Agents with $\omega_i = -1$ are essentially traveling about the phase unit circle in the clockwise direction while the agents with $\omega_i = 1$ are traveling in the counterclockwise direction. Since both groups are traveling at the same rate about the phase unit circle in opposite directions, they exhibit the same phase two times for each phase oscillation cycle. The repulsion between the two groups is highest when the whole collective shares the same phase, which results in the maximum point for the radial oscillation cycle. The greatest attraction occurs when the phases of the two natural frequency groups are at opposite ends of the phase unit circle; this results in the minimum collective radius for the radial oscillation cycle. Supplementary Fig. 2.11e shows the phase wave behavior that results when $g(\omega) = \delta(\Omega)$ and $K = 0$,$J = 1$. This is very similar to what was shown in 2017 by O'Keeffe et al [138]. with the difference that although each agent remains essentially unmoving once the phase wave formation is reached, the whole collective oscillates in place so that a uniform phase wave oscillates circumferentially about the annulus formation. In the original swarmalator study, the collective was shown either in a static phase wave state where the agents' motion and phase remained static, or in an active phase wave state where their phase and motion was dynamic. The phase wave

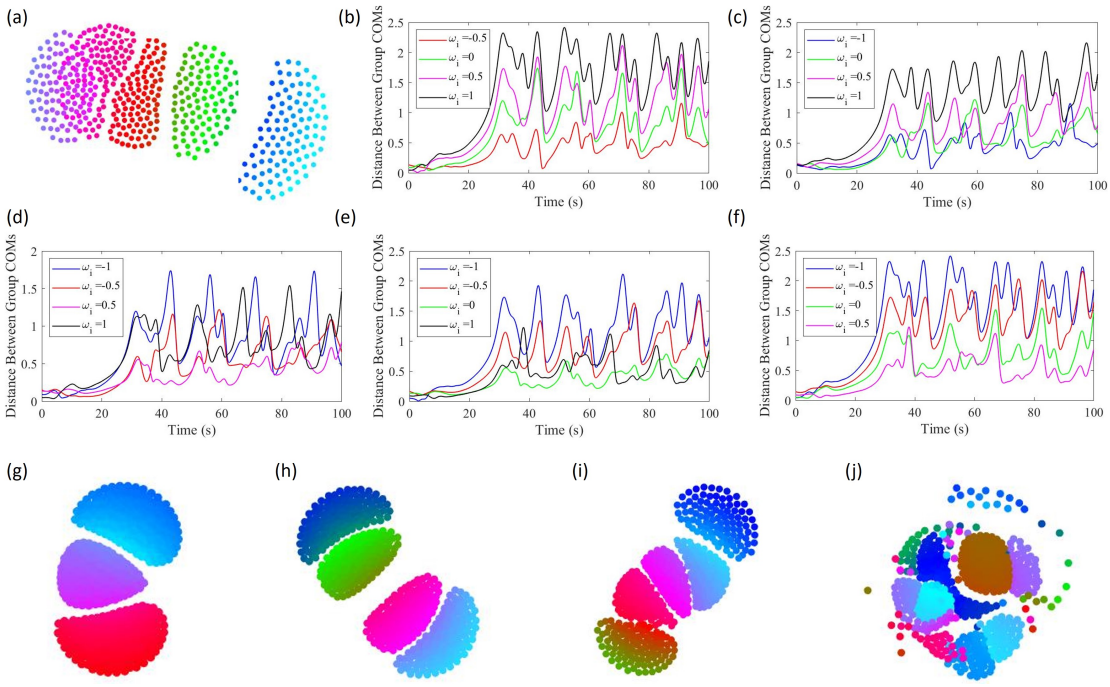

Figure 2.14: Frequency group separation. (a) A collective with five natural frequency groups ($\omega_i \in [-1], [-0.5], [0], [0.5], [1]$) when $c = 0$, and K,$J = 1$. (b-f) The distance between each natural frequency group's center of mass and all other frequency groups' center of masses over time. Distance from the center of mass of the group of agents with a natural frequency of (b) $\omega_i = -1$, (c) $\omega_i = -0.5$, (d) $\omega_i = 0$, (e) $\omega_i = 0.5$, (f) $\omega_i = 1$. (g-j) Collectives with differing numbers of natural frequency groups shown after 775 time steps. (g) $\omega_i \in [-1], [0], [1]$. (h) $\omega_i \in [-1], [-0.5], [0.5], [1]$. (i) $\in [-1], [-0.5], [0], [0.5], [1]$. (j) $\omega_i \in [-4], [-3], [-2], [-1], [0], [1], [2], [3], [4]$.

state achieved in our study results from the fact that the natural frequency for all agents is much higher than what is needed for phase-coupling-induced motion given by the spatial phase coupling term in $\dot{\mathbf{x}}_i$. If we had chosen a lower natural frequency, we would have also observed the active phase wave state. Supplementary Fig. 2.11l shows the spatial-phase order throughout the collective for different values of K and J; these results allow us to get a closer look at the behavior of the order parameter S throughout $K - J$ parameter space than what is shown in the main text.

The collective reaches another state where degree of synchrony increases

with distance from the collective's centroid when $F1$ and $K = 0, J = -1$, as shown in supplementary Figs. 2.11f and 2.11m. As opposed to exponential-like and step-like behavior in degree of synchrony as a function of increasing distance from the collective centroid seen for collectives with $F3$ and $F4$, the plot shown in supplementary Fig. 2.11m shows a very linear behavior. The linear behavior is the same when $K = 0.5, 1, 1.5$, and 2, and reaches a maximum degree of synchrony value of ~ 0.2. From supplementary Fig. 2.11f we can distinctly see a ring of agents with similar phases lining the circular boundary of the collective.

Supplementary Fig. 2.11g shows an expanding collective when $F1$ and K=2,J=-1; since J is negative, agents with similar phases will repel and expand the radius of the collective. Supplementary Fig. 2.11n shows the rate of expansion and the final radius (after 500 time steps) for different values of K when $J = -1$. After K reaches a high enough value to synchronize agents' phases, radial repulsion begins, and the collective maintains the same rate of expansion and final radius after 500 time steps. Supplementary Fig. 2.14 explores the expansion behavior across 1000 time steps for different values of J; this plot demonstrates that when $0 > J > -1$, the collective expands and reaches a steady collective radius at which it remains. When $J = -1$ the collective continues expanding and does not seem to stop; this is reasonable since the phase coupling-induced motion in $\dot{\mathbf{x}}_i$ is defined by a unit vector and the coefficient for global attraction (A) has a value of 1. When $J = -1$ and all agents are synchronized, the unit vector term in $\dot{\mathbf{x}}_i$ is cancelled out and only the power law repulsion term remains active; thus, all agents repel each other slightly and the collective expands indefinitely.

When $F4$, the collective has a uniform distribution of natural frequencies

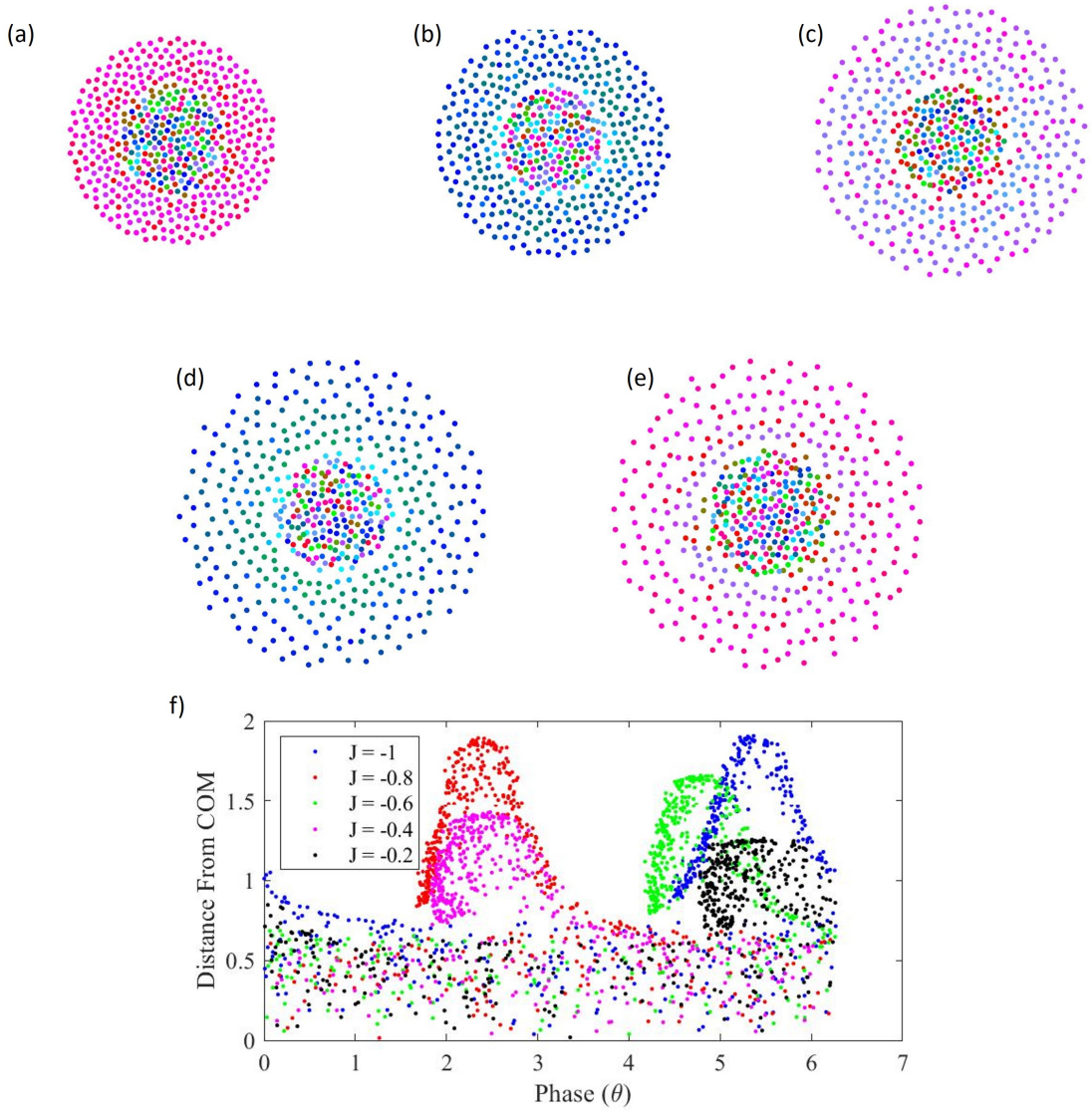

Figure 2.15: Concentric phase self-organization. (a-e) Collectives with $F4$ and different negative values of J that self-organize concentric rings of agents with similar phases. (a) $J = -0.2$, (b) $J = -0.4$, (c) $J = -0.6$, (d) $J = -0.8$, (e) $J = -1.0$. (f) Plot of agents' distance from collective centroid as a function of phase demonstrates that after a certain distance there is distance-based phase self-organization.

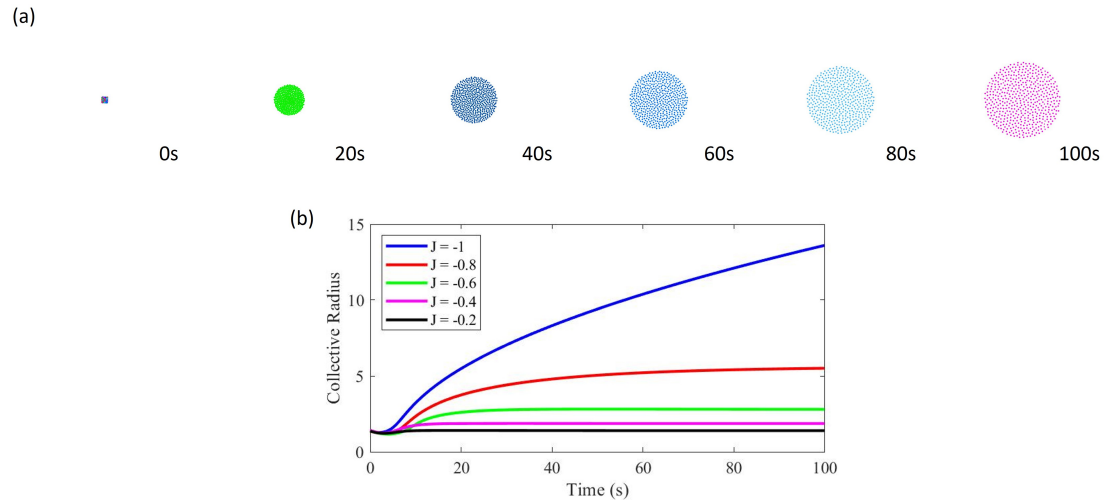

Figure 2.16: Collective expansion. (a) Collective expanding indefinitely when $c = 0$, $F1$, $K = 1$, and $J = -1$. (b) Collective radius plotted as a function of time for various value of J.

across positive and negative values. This ensures that agents with the same sign of natural frequency will not synchronize as easily as when $F2$. The emergent behaviors for collectives with natural frequency distributions are shown in Supplementary Figs. 2.12a-d and characterized in Supplementary Figs. 2.12e-h. The first emergent collective behavior presented for this natural frequency distribution is shown in Supplementary Fig. 2.12a ($K = 2$,$J = -1$), where a cluster of phase-disordered agents forms at the center and is surrounded by rings of agents with greater phase synchrony. Supplementary Fig. 2.12e explores the phase synchrony behavior as a function of distance from the collective's centroid for different positive values of K. At $K = 0$,0.5, and 1, the degree of synchrony remains below 0.05 across all distances from the centroid. Once $K \approx 1.5$, there is a jump in the degree of synchrony at about $0.7R_{max}$ and which increases with distance from the collective centroid. These periodic rings of higher synchrony occurs because of the spread in natural frequency; agents with a higher $|\omega_i|$ will have a harder time synchronizing their phase with their neighbors. Since J is negative in these cases, agents with greater phase differences will tend to

attract to each other and cluster closer to the collective centroid. Agents with a lower$|\omega_i|$ will synchronize more easily with other agents that share the same sign for their natural frequency; this means that these agents will repel each other more and move towards the collective's boundary where they will have the greatest distance from similarly phased agents. Agents with positive and negative natural frequencies will have high phase differences which enables greater attraction. As a result, although the degree of synchrony increases the collective boundary, it does not surpass 0.15 because agents with differing phases attract and sometimes occupy the same annulus regions used for the measurements in this plot.

Supplementary Fig. 2.12b ($K = 2$,$J = 1$) shows two clusters of synchronized agents form close to the collective centroid while a ring of phase-disordered agents encapsulate the clusters. Fig. 2.12f shows how the degree of synchrony for the whole collective and within each natural frequency group increases with K. This shows that higher values of K are needed to fully synchronize each group and the whole collective. Similar bouncing cluster behavior is also observed for K,$J > 0$; however, the clusters do not repel each other at such great distances as was the case when $F2$ since there is greater phase disorder resulting from the spread of natural frequencies.

When $g(\omega) = Uni(1, \Omega)$, the collective has a uniform distribution between 0 and 1 for the agents' natural frequencies. Supplementary Fig. 2.12c shows the collective almost forming a sync state when $K = 2$,$J = 1$; however, a tight ring of asynchronous agents encapsulate the center cluster. The outer agents have higher natural frequency which makes it more difficult for them to synchronize with the center agents. Since J is positive, agents with similar phases attract to

each other; therefore, the outer agents tend to radially oscillate as their phase difference with the center cluster increases or decreases. In supplementary Fig. 2.12g, we show that the collective synchrony increases with K, but only reaches about 0.6 because of the spread in natural frequency. When $K = 2$,$J = -1$ (Supplementary Fig. 2.12d), the collective exhibits a more organized version of what emerges at the same values of K and J when the natural frequency is spread across negative and positive values. A tight cluster of phase disordered agents forms at the center while rings of more coherent agents encapsulate it. The agents along the boundary have a lower natural frequency than those in the cluster and thus synchronize more easily. Supplementary Fig. 2.12h shows how the coherence within concentric rings increases with distance from the collective's centroid. Starting at about $K = 1.5$ the degree of synchrony begins to rise at a distance of ~ 0.4 from the collective centroid. Since all agents share the same sign for their natural frequencies, there are lower phase differences between agents with a lower$|\omega_i|$ which enables greater spacing between the phase-ordered agents and thus a larger region of phase-ordered agents than when $F2$. This is clearly shown for different J in Supplementary Fig. 2.15, which shows a plot of agents' distance from the collective centroid plotted as a function of phase, to clearly show agents' concentric phase self-organization behavior.

2.8.5 Discussion 5. Chiral Swarmalators with Discrete Sets of Natural Frequencies

This discussion reviews the chiral collective's behavior when all agents revolve in the same direction at the same rate and when half revolve clockwise (CW)

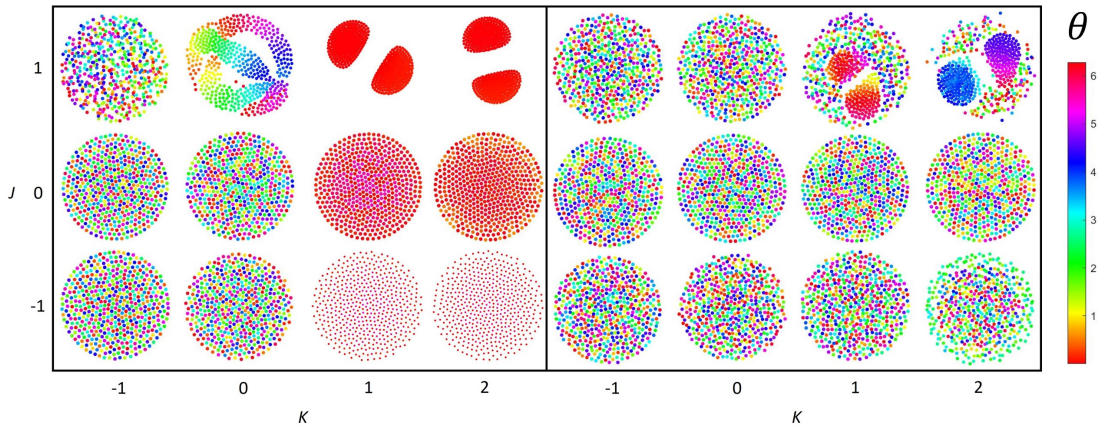

Figure 2.17: Collective behaviors of non-chiral swarmalators with frequency coupling. $Q_{\dot{x}} = \frac{\pi}{2}\left|\frac{\omega_j}{|\omega_j|} - \frac{\omega_i}{|\omega_i|}\right|$, $Q_{\dot{\theta}} = \frac{\pi}{4}\left|\frac{\omega_j}{|\omega_j|} - \frac{\omega_i}{|\omega_i|}\right|$. $F2$ (Left). $F4$ (Right).

and the other half counterclockwise (CCW) at the same rate. The emergent formations across K and J in the four natural frequency distributions is shown in Supplementary Fig. 2.18; however, only the upper left and lower right quadrants of the figure relate to this discussion. A summary of the most interesting behaviors and the S order heat maps across $K - J$ parameter space is shown in Supplementary Fig. 2.19. Supplementary Figs. 2.19a-b shows that S remains relatively high even when K and J are negative; a very disordered phase wave forms along this region (Supplementary Fig. 2.19c) with high spatial-phase order at the outer boundary and low order towards the center. The circular motion and negative K drives agents to follow circular paths that will intersect where the phase difference is greatest. Agents on opposite sides of the collective, revolving in the same direction, minimize the distance between each other when they are offset by π along their circular trajectories, and the emergent formation in Supplementary Fig. 2.19c results.

Disordered phase waves also exist at low J and high K; Supplementary Fig. 2.19d shows a phase wave along an axis that results from a rotating ellipse

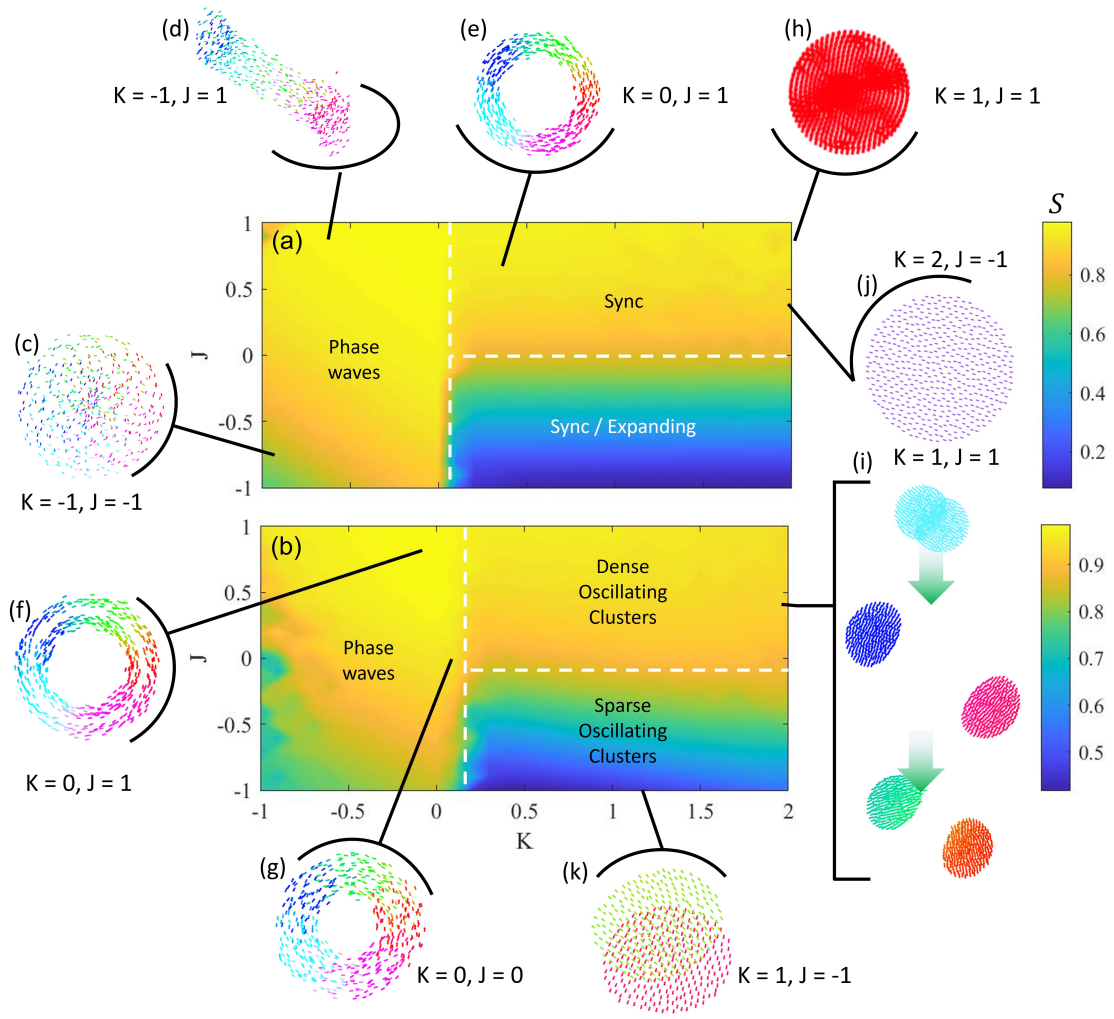

Figure 2.18: Collective behaviors of chiral swarmalators with no frequency coupling. $F2$ (Upper left). $F4$ (Upper right). $F3$ (Lower left). $F1$ (Lower right). Quiver plots are shown here instead of instantaneous positions because chiral swarmalators have an inherent motion driving them.

formation that steadily increases its major axis over time. In this case, similar phases spatially attract but temporally repel; instead of moving towards synchrony, agents anti-couple and become asynchronous. This enables the formation to slowly stretch out over time. Similar ellipse formations are observed when the collective has two natural frequency groups; however, the two ellipses that emerge rotate about a common center in opposite directions and maintain relatively constant major axes over time. The equal and opposite natural fre-

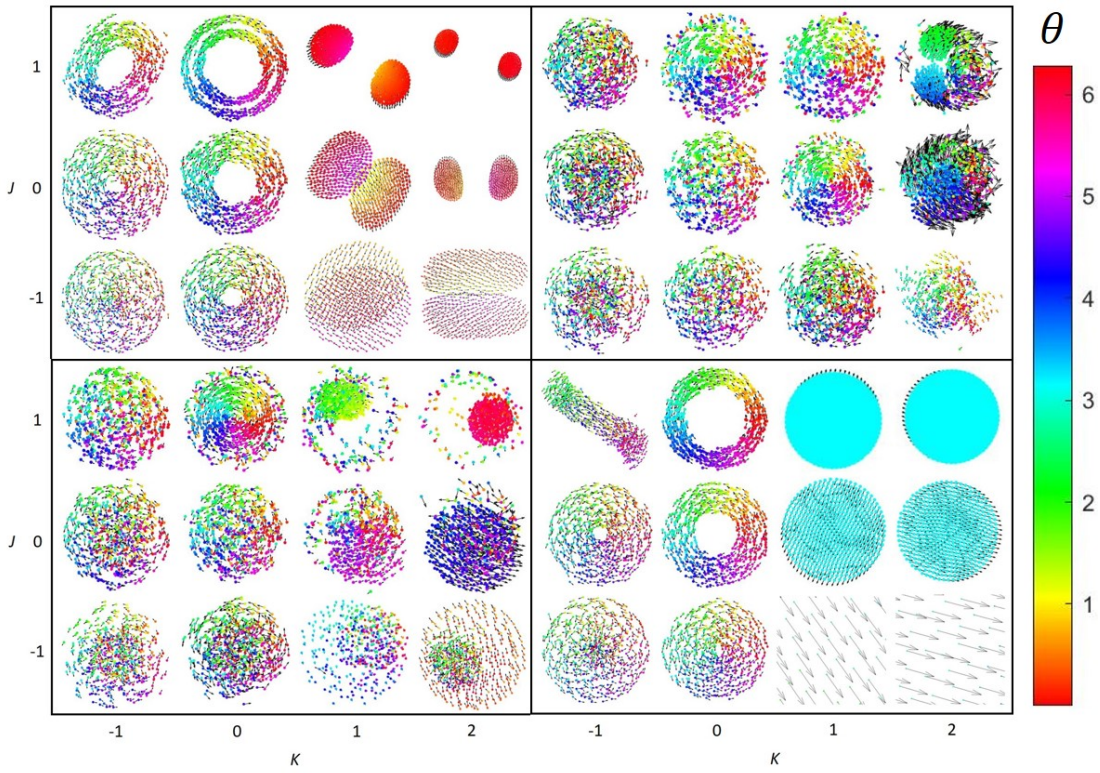

Figure 2.19: Chiral swarmalators with no natural frequency spread. Heat maps of S across $K - J$ parameter space is shown for test cases with (a) and (b) $F2$. (c) Phase wave. (d) Phase wave along a slim ellipse. (e) Phase wave. (f) Concentric double phase waves. (g) Phase wave. (h) Synchronized cluster. (i) Dense revolving clusters. (j) Expanding synchronized revolving cluster. (k) Sparse oscillating clusters.

quencies inhibit perfect anti-coupling, so the collective maintains a steady rotating formation over time.

Like the non-chiral swarmalators, distinct phase waves emerge when $K = 0$ (Supplementary Figs. 2.19e-g. With two natural frequency groups, $K = 0$,$J = 1$ enables agents to separate into concentric, counterrotating groups that each oscillate between being on the inside and being on the outside (Supplementary Fig. 2.19f). This is driven by their spatial repulsion and their attempt to each settle at the same revolution radius. A phase wave also forms when there is no spatial or temporal coupling (Supplementary Fig. 2.19g), the collective forms

an annulus because of the agents' inherent circular motion with equal radii, their spatial attraction through the unit vector model, and repulsion through a power law model. All agents maintain the same radius of revolution but switch between the inner and outer boundaries of the annulus.

Sync states are also observed at positive K and J when the collective revolves in the same direction (Supplementary Fig. 2.19h); and a high S is maintained because the collective maintains high circumferential phase order about its time-average centroid. Similar behavior is observed when there are two natural frequency groups; two clusters independently synchronize and revolve along the same circular trajectory in opposite directions (Supplementary Fig. 2.19i). Contrary to the bouncing clusters observed for the non-chiral swarmalators, these collectives maintain a steady trajectory and pass through each other two times per phase cycle because of their inherent circular motion. Their inherent motion inhibits synchronization since agents from opposite natural frequency groups have a harder time clustering. Finally, expanding synchronized collectives are also found for chiral swarmalators when the collective has uniform revolution behavior (Supplementary Fig. 12.19j) and sparse revolving clusters when there are two natural frequency groups (Supplementary Fig. 2.19k). The sparse revolving clusters are very similar to the dense revolving clusters, except that there is much higher neighbor spacing. Each cluster size also remains relatively constant, as opposed to constant expansion (Supplementary Fig. 2.19j) or radial oscillation (main text Fig. 2.2k), because of the inherent circular motion that inhibits much of the phase interaction effects between the two groups.

2.8.6 Discussion 6. Overview and Characterization of Chiral Swarmalators

This discussion reviews the collective behaviors of regular and frequency-coupled chiral swarmalators. The behaviors of collectives composed of chiral swarmalators with no natural frequency coupling ($c = 1$,$Q_{\dot{\mathbf{x}}}$,$Q_{\dot{\theta}} = 0$) when there are integer values for K and J and different natural frequency distributions are shown in Supplementary Fig. 2.19. Supplementary Figs. 2.20a-e show many of the emergent behaviors when the collective has discrete natural frequencies and each behavior is characterized in Supplementary Figs. 2.20f-j.

Supplementary Fig. 2.20a highlights chiral swarmalators' emergent behaviors when there is no phase coupling and only global attraction enabled by a unit vector model and repulsion through a power law. The phase wave formation results from the fact that all agents have the same angular velocity and thus the same radius of revolution; half have an inherent clockwise motion and the other half a counterclockwise motion. Since K,$J = 0$, there is no phase coupling behavior and agents simply revolve about the same centroid. The plot of S in supplementary Fig. 2.20f shows a clearer view of the spatial-phase order when J=0 than the heat map shown in the main text. As opposed to non-chiral swarmalators, which maintain a low spatial-phase order when the spatial phase coupling term is zero in $\dot{x}_i$, the chiral swarmalators naturally self-organize into a phase wave formation with an even distribution of phases across the collective. The high value for S when $K > -0.9$ is a direct result of each agent's inherent circular motion and each collective starting with a uniform distribution of phases, meaning the agents' orientations are spread across 0 and 2π. Even when agents anti-couple ($K < 0$), the inherent circular motion ensures that a single spinning

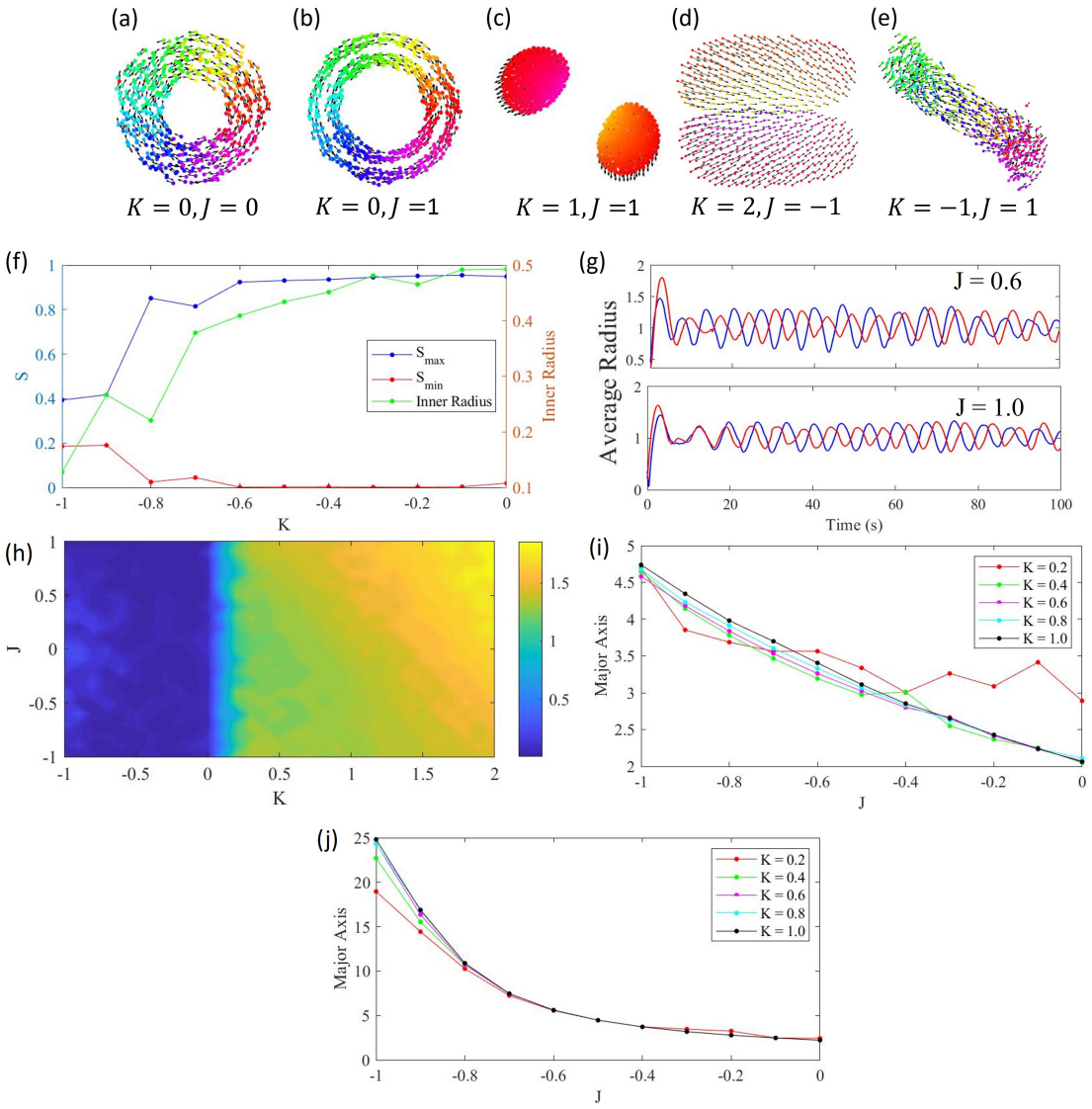

Figure 2.20: Characterization of collective behaviors in chiral swarmalators with no frequency coupling and discrete natural frequencies. (a-e) Various emergent configurations of chiral swarmalators. (f-j) Collective behavior characterizations for the same ω distributions listed in (a-e), respectively. (a) $F2$; (b) $F2$; (c) $F2$; (d) $F2$; (e) $F1$; (f) S_{max}, S_{min}, and inner ring radius when $J = 0$; (g) average radius of each natural frequency group over time when $J = 0.6$, 1; (h) max distance between the two clusters; (i) major axis length for different K; (j) major axis length when $K = -1$.

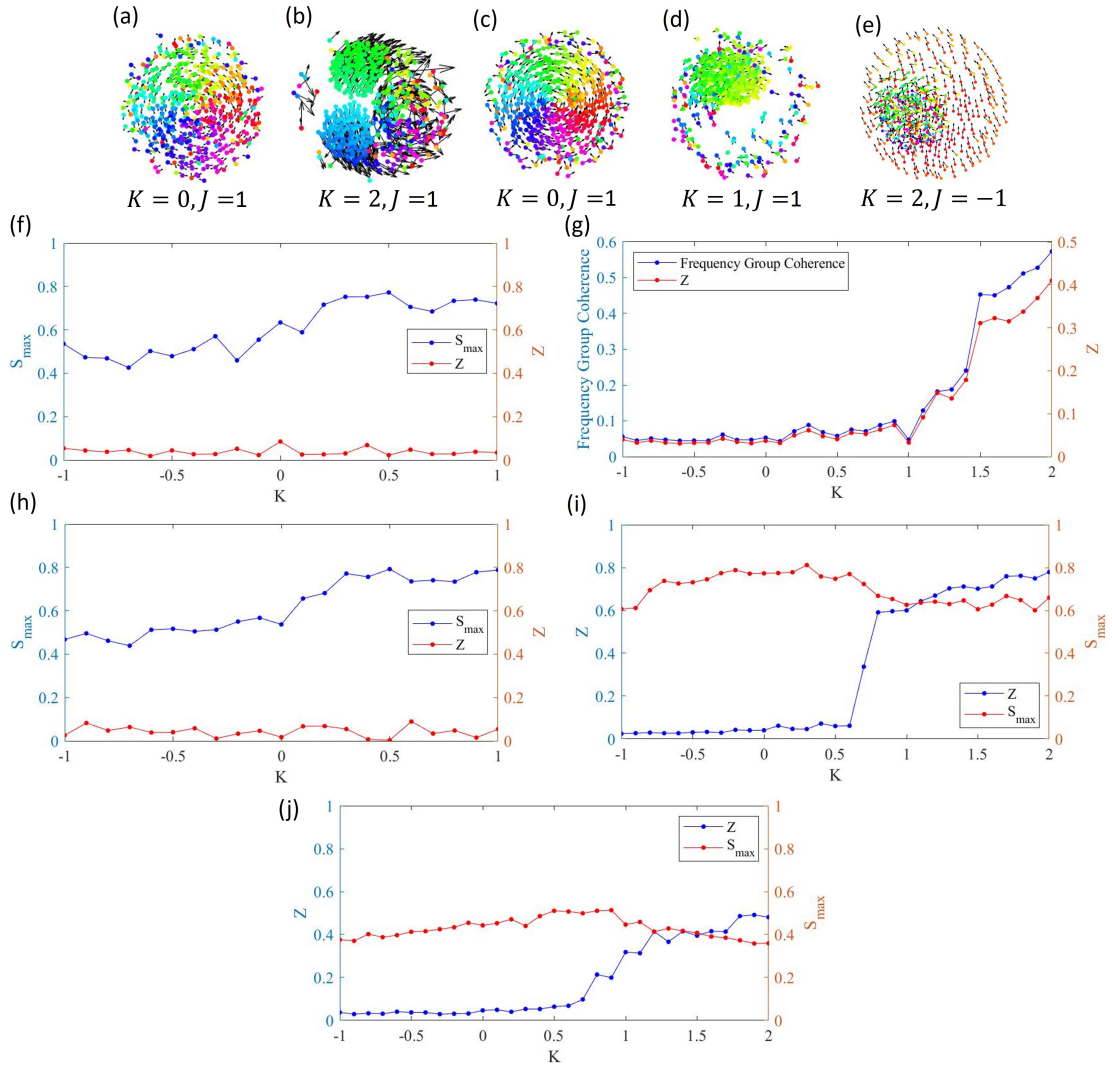

Figure 2.21: Characterization of collective behaviors in chiral swarmalators with no frequency coupling and a natural frequency distribution. (a-e) Various emergent configurations of chiral swarmalators. (f-j) Collective behavior characterizations for the same ω distributions listed in (a-e), respectively. (a) $F4$; (b) $F4$; (c) $F3$; (d) $F3$; (e) $F3$. (f) S order and phase coherence when $K = 0$; (g) Natural frequency group and global phase coherence when $J = 1$; (h) S order and phase coherence when $K = 0$; (i) S order and phase coherence when $J = 1$; (j) S order and phase coherence when $J = -1$.

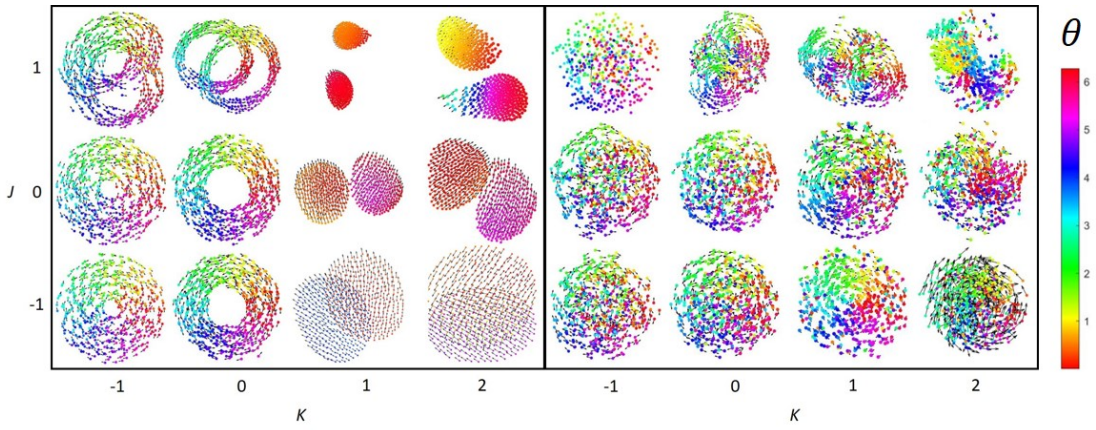

Figure 2.22: Collective behaviors of frequency-coupled chiral swarmalators. $Q_{\dot{x}} = \frac{\pi}{2}\left|\frac{\omega_j}{|\omega_j|} - \frac{\omega_i}{|\omega_i|}\right|$, $Q_{\dot{\theta}} = \frac{\pi}{4}\left|\frac{\omega_j}{|\omega_j|} - \frac{\omega_i}{|\omega_i|}\right|$, $F2$ (Left). $F4$ (Right).

vortex will form. We also note that the trend in inner radius of the collective decreases with K, this results from the fact that as K decreases, agents will tend to phase couple more easily with other agents with whom they have a phase difference closer to π; this will drive the collective to lower the inner radius since this is the point at which agents with a phase difference of π will be closest to each other.

The two concentric ring formations shown in Supplementary Fig. 2.20b happen when $F2$ and $K = 0$,$J = 1$. Each ring is formed by a natural frequency group and the two are composed of agents revolving in opposite directions. As shown in supplementary Fig. 2.17bii, the average radius of each frequency group oscillates over time, and this behavior persists even when the collectives run for longer simulation times. The radial oscillation occurs because each natural frequency group has equal and opposite angular velocities that are paired with the phase behavior. As agents minimize their phase difference with agents from the other natural frequency group, which happens twice for each phase cycle, the attraction between these agents maximizes so that a single ring ap-

pears. Since the phase difference between agents is continuously increasing or decreasing, the two ring formations quickly separate back into concentric formations. Supplementary Fig. 2.20g shows that the two groups oscillate between being outside and inside. This most likely occurs because each group has a natural revolution radius of 1 and it is easier for each agent to continue traveling along the direction closest to their instantaneous direction of travel when the attraction between the two groups begins to decrease. This means that agents from the outer ring, which were moving towards the center as their attraction with agents from the other natural frequency group grew, will continue traveling towards the collective centroid once the attraction begins to decrease. It is interesting to note that while the frequency of radial oscillation remains about the same throughout time, the amplitude changes a good amount; this could be due to slightly non-uniform distributions in the agents' x, y, and θ values at the beginning of the simulation. The slightly non-uniform distributions could drive each group to reach variable maximum and minimum radii; however, the average radius remains the same over time and equal to each group's inherent revolution radius.

The dense clusters observed for non-chiral swarmalators are also seen for positive values of K and J with the chiral swaramalators (Supplementary Fig. 2.20c). The general revolving cluster behavior, however, persists throughout negative J as well for the chiral swarmalators when $F2$ as shown by the heat map of maximum distance between the centroid of the two natural frequency groups in Supplementary Fig. 2.20h. The densest clusters are formed at high K and J since this enables agents from the same natural frequency group to synchronize and cluster with similarly phased agents. As J decreases, each natural frequency group cluster becomes sparser and forms an ellipse-like formation that

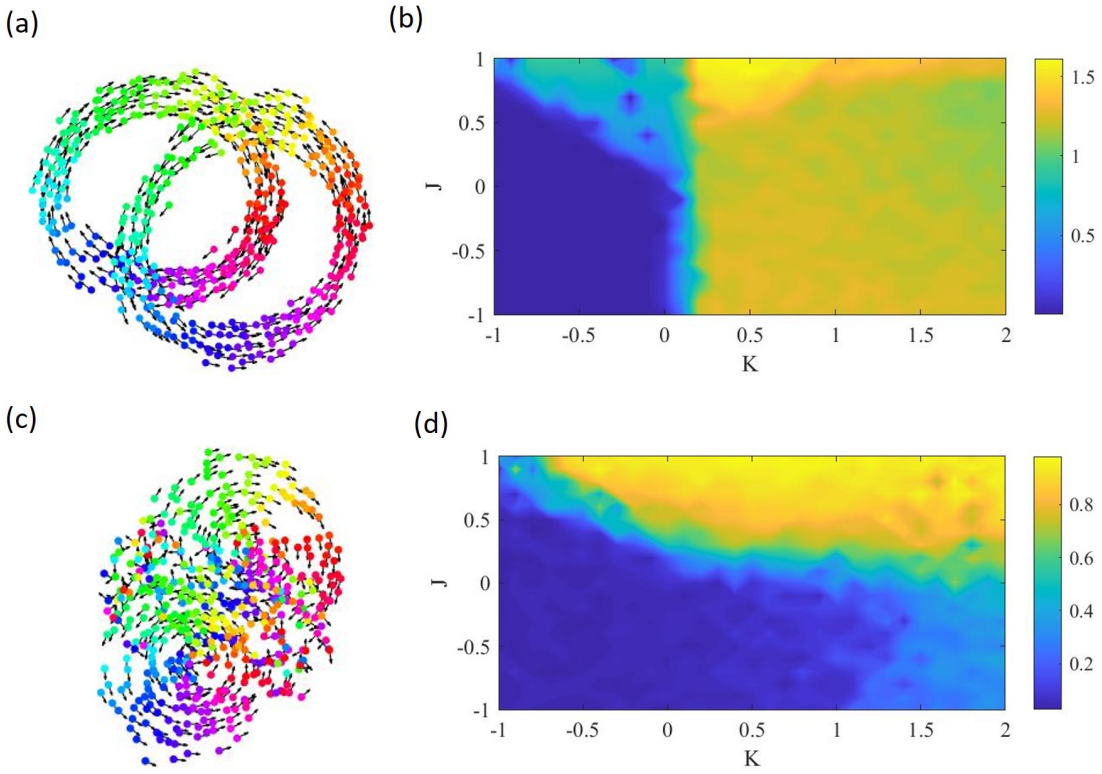

Figure 2.23: Characterization of collective behaviors in frequency-coupled chiral swarmalators. (a) $K = 0$,$J = 1$,$F2$. (c) $K = 0$,$J = 1$,$F4$. (b,d) Average distance between the natural frequency groups' centroids for (a) and (c), respectively.

oscillates in attraction and repulsion to the other cluster. When $J < 0$, lower J enables agents within the same natural frequency group to increase their neighboring spacing since they synchronize their phases and repel each other more strongly. The inherent circular motion of the agents, however, induces clustering since they share the same phase within each natural frequency group. Agents from opposite natural frequency groups still undergo oscillatory spatial attraction and repulsion two times per phase cycle (revolution cycle). This induces agents from opposite natural frequency groups to have high attraction and repulsion through each revolution; an ellipse-like formation enables agents from each group to balance the time-varying attraction / repulsion forces that drive each agent to (1) maintain its inherent circular motion, (2) increase its spac-

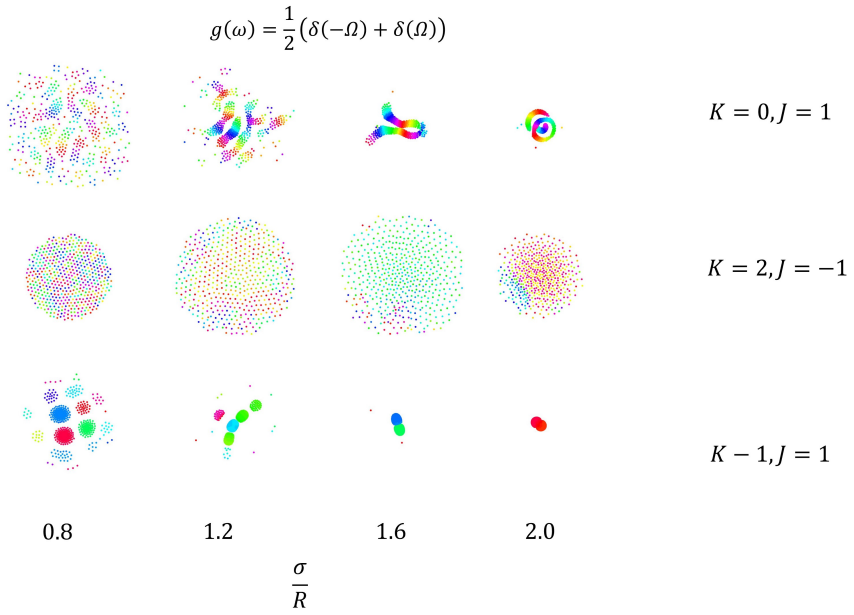

Figure 2.24: Collective behaviors of locally coupled non-chiral swarmalators with no frequency coupling and no natural frequency spread. The x-axis increases the coupling distance (σ) and is normalized by the maximum radius of revolution ($R = 1$). (Top) $K = 0$,$J = 1$. (Middle) $K = 2$,$J = -1$. (Bottom) $K = 1$,$J = 1$.

ing from similarly phased agents, and (3) move towards or away from agents in the opposing natural frequency group (Supplementary Fig. 2.20d). Supplementary Fig. 2.20i shows that the major axis of each natural frequency group increases as J becomes lower, which agrees with the statements above.

The image shown for Supplementary Fig. 2.20e shows the collective with $F1$, $K = -1$,$J = 1$ at the end of a simulation; during the simulation the collective starts out in a phase wave formation and over time begins to elongate into a rotating ellipse until the collective forms an ellipse with a very small minor axis (essentially a line) as shown in the image. The behavior repeats itself across different values of K and the ellipse's major axis increases dramatically as J approaches -1, as shown in Supplementary Fig. 2.20j.

When $F4$, half of the collective has an inherent circular motion in the clock-

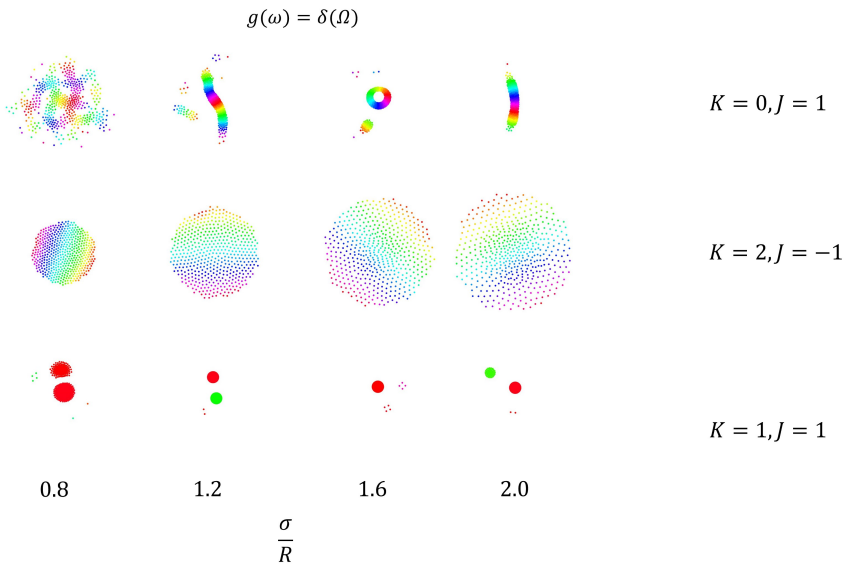

Figure 2.25: Collective behaviors of locally coupled non-chiral swarmalators with no frequency coupling and one natural frequency. The x-axis increases the coupling distance (σ) and is normalized by the maximum radius of revolution ($R = 1$). (Top) $K = 0$,$J = 1$. (Middle) $K = 2$,$J = -1$. (Bottom) $K = 1$,$J = 1$.

wise direction, and the other half the counterclockwise direction; agents have an uniform distribution of revolution radii between 0 and 1. Supplementary Figs. 2.21a-e shows some of the most interesting behaviors when there is a natural frequency spread and their corresponding characterization in Supplementary Figs. 2.21f-j. The global attraction between agents and their inherent circular motion enables the collective to form a single vortex when $K = 0$,$J = 1$ (Supplementary Fig. 2.21a); a small ring of phase-disordered agents on the boundary of the collective keeps the collective from having as high of a value for S as when $F2$. The agents on the boundary each have a very small revolution radius and high natural frequency; this prohibits them from matching the phase of nearby agents and causes them to be repelled to the outer region of the collective. Supplementary Fig. 2.21f also shows that the degree of synchrony also remains low even with positive K because of the spread in natural frequencies across negative and positive values. Supplementary Fig. 2.21b shows two revolving clusters with a

group of phase-disordered agents that remains around the centroid of the collective while the two clusters revolve about it at an average radius of 1. The plot shown in Supplementary Fig. 2.21g shows that the collective's and each natural frequency group's degree of synchrony significantly increases at $K \approx 1.5, J = 1$ but remains relatively low because of the natural frequency spread.

Supplementary Fig. 2.21c results from $F3$, $K = 0$, $J = 1$ and shows a very similar vortex to the one shown in Supplementary Fig. 2.21a. The trends for spatial-phase order and degree of synchrony shown in Supplementary Fig. 2.21h also closely resemble those in Supplementary Fig. 2.21f; this demonstrates that even though the whole collective has an inherent circular motion where agents travel in the same direction, the uniform distribution for the natural frequencies keeps the agents from reaching a very high degree of synchrony when $K < 1, J = 1$.

A revolving synchronized cluster with a ring of phase-disordered agents is shown in Supplementary Fig. 2.21d; the agents forming the outer ring of the collective each have a small revolution radius and a high natural frequency. As shown in Supplementary Fig. 2.21i, the spatial-phase order remains above ~ 0.5 when $-1 < K < 1$ because the synchronized cluster is traveling in a circular trajectory around the collective's centroid. Even though there is no instantaneous distribution of phases about the centroid as was the case when the collective formed a vortex, most agents are synchronized and have a position about the centroid that is phase-correlated. The spatial-phase order cannot be higher because of the phase-disordered agents that remain even when K is positive.

When $J < 0$, agents with similar phases repel each other; as shown in Supplementary Fig. 2.21e, agents with a larger revolution radius and thus a lower natural frequency tend to synchronize more easily and form a large revolving

orb. Agents with a low revolution radius and a high natural frequency are unable to synchronize and thus attract to each other to form a cluster of phase-disordered agents closer to the collective's centroid. Supplementary Fig. 2.21j shows that order remains relatively constant at a low value across negative and positive values of K since the collective either has high phase disorder ($K < 0$) or has partial synchronization ($K > 0$) at which point agents with the same phase are evenly distributed circumferentially about the collective's centroid. In both cases there is low opportunity for the collective to achieve circumferential phase organization. The degree of synchrony, however, begins to increase to a higher value when $K \approx 0.7$; this enables the collective to partially synchronize and encapsulate a tight cluster of phase-disordered agents.

An overview of the chiral swarmalators' emergent behaviors with natural frequency coupling is shown in Supplementary Fig. 2.22 and the characterization of some of the emergent behaviors is shown in Supplementary Fig. 2.23. Supplementary Fig. 2.23a shows the emergent formation when $F2$,$K = 0$,$J = 1$; two non-concentric phase waves with counterrotating agents form side by side. The non-concentric formation occurs because of the phase shift in $Q_{\dot{\mathbf{x}}}$ and$Q_{\dot{\theta}}$ determined by the agents' natural frequency. The distance between the centroids of the two natural frequency groups is shown by the heat maps in Supplementary Fig. 2.23b, with a maximum occurring around $0.2 < K < 1$ and $J \approx 1$. The distance between the group centroids is non-zero for almost all positive values of K. The natural frequency dependence on coupling enables the current model to produce behaviors very similar to spermatozoa vortex arrays when there is local coupling.

When $F4$, the collective begins to mix more easily because the natural fre-

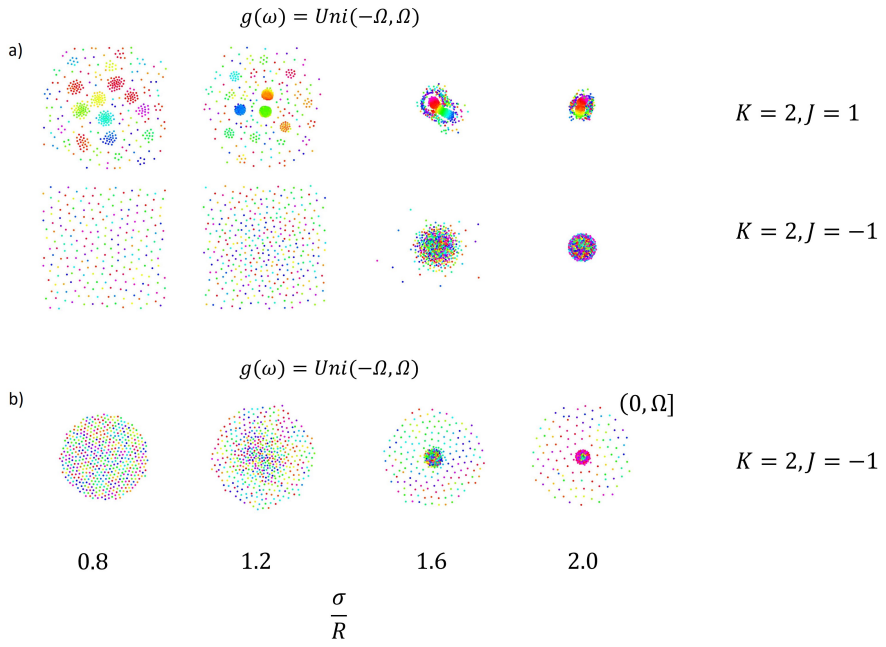

Figure 2.26: Collective behaviors of locally coupled non-chiral swarmalators with no frequency coupling and a natural frequency spread. The x-axis increases the coupling distance () and is normalized by the maximum radius of revolution ($R = 1$). (a) $F4$. (Top) $K = 0$,$J = 1$. (Bottom) $K = 2$,$J = -1$. (b) $F3$. $K = 2$,$J = -1$.

quency distribution prevents each group from synchronizing within itself and producing strong oscillatory attraction and repulsion with the opposing group, which is the case when $F2$. The double vortex formation is shown in supplementary Fig. 2.23c, where two vortices form next to each other because of the phase shift in $Q_{\dot{\mathbf{x}}}$ and $Q_{\dot{\theta}}$. The heat map in Supplementary Fig. 2.23d shows that the greater distance between the centroids of the two natural frequency groups occurs when $J > 0$ and $K > 0$. This is reasonable since these are the regions of the $K - J$ parameter space in which the clusters are most likely to enable coupling between agents with a similar sign for their natural frequency and thus enable some oscillatory attraction and repulsion with agents from the other natural frequency group.

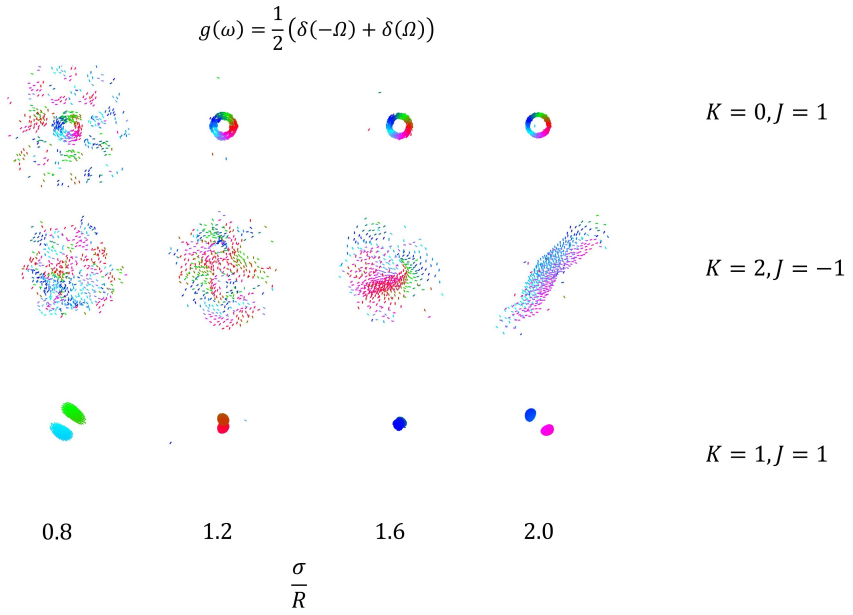

Figure 2.27: Collective behaviors of locally coupled chiral swarmalators with no frequency coupling and no natural frequency spread. The x-axis increases the coupling distance (σ) and is normalized by the maximum radius of revolution ($R = 1$). (Top) $K = 0$,$J = 1$. (Middle) $K = 2$,$J = -1$. (Bottom) $K = 1$,$J = 1$.

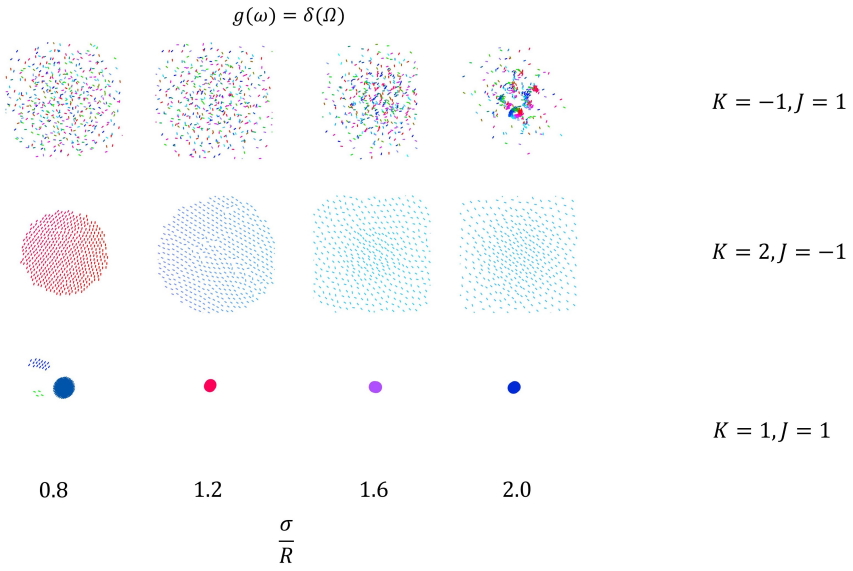

Figure 2.28: Collective behaviors of locally coupled chiral swarmalators with no frequency coupling and one natural frequency. The x-axis increases the coupling distance (σ) and is normalized by the maximum radius of revolution ($R = 1$). (Top) $K = -1$,$J = 1$. (Middle) $K = 2$,$J = -1$. (Bottom) $K = 1$,$J = 1$.

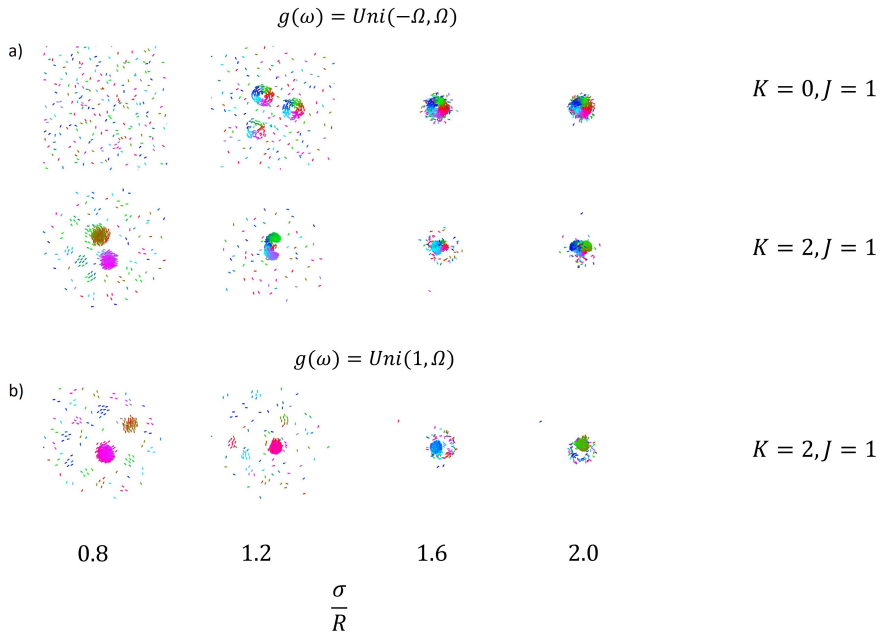

Figure 2.29: Collective behaviors of locally coupled chiral swarmalators with no frequency coupling and a natural frequency spread. The x-axis increases the coupling distance (σ) and is normalized by the maximum radius of revolution ($R = 1$). (a) $F4$. (Top) $K = 0$,$J = 1$. (Bottom) $K = 2$,$J = 1$. (b) $F3$. $K = 2$,$J = 1$.

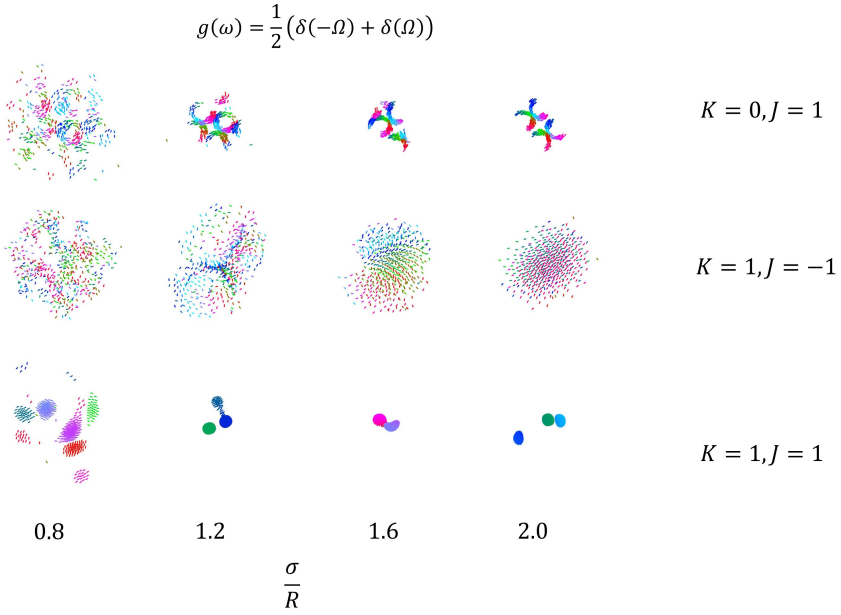

Figure 2.30: Collective behaviors of locally coupled frequency-coupled chiral swarmalators and no natural frequency spread. The x-axis increases the coupling distance (σ) and is normalized by the maximum radius of revolution ($R = 1$). (Top) $K = 0$,$J = 1$. (Middle) $K = 1$,$J = -1$. (Bottom) $K = 1$,$J = 1$.

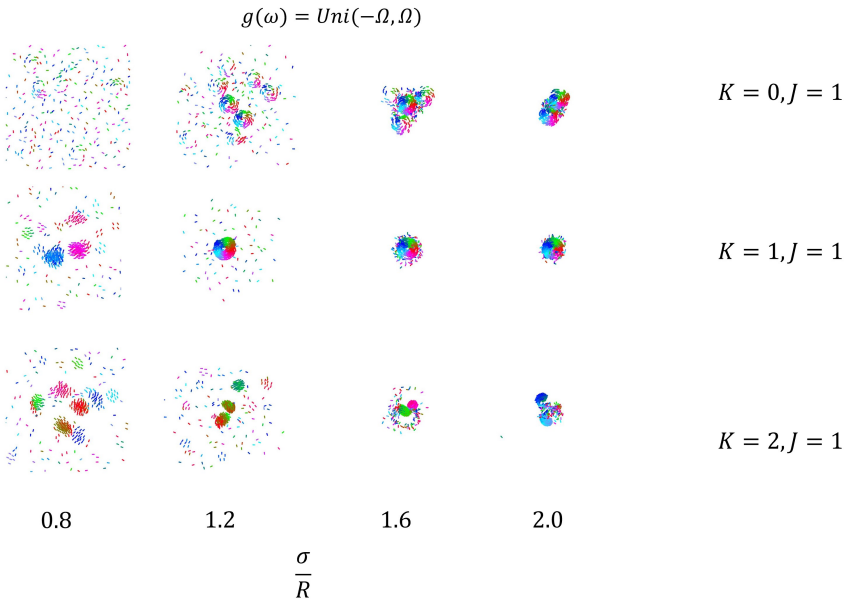

Figure 2.31: Collective behaviors of locally coupled chiral swarmalators with frequency coupling and a natural frequency spread. The x-axis increases the coupling distance (σ) and is normalized by the maximum radius of revolution ($R = 1$). (Top) $F4$. (Top) $K = 0$,$J = 1$. (Middle) $K = 1$,$J = 1$. (Bottom) $F3$. $K = 2$,$J = 1$.

CHAPTER 3

FIBER EMBROIDERY OF SELF-SENSING SOFT ACTUATORS

Protrusible muscular organs, like a frog's tongue or squid's tentacle, use a combination of constricting muscles and inextensible fibers to rapidly elongate soft tissue appendages and catch prey [64]. A Loligo pealei squid's tentacle can elongate by up to 80% in 40 milliseconds, while changing the tip trajectory to adjust for prey movement [92, 83]. The bending, twisting, and elongation of a tentacle are controlled by tentacle extensor fibers, which are inextensible fibers arranged in circumferential and perpendicular arrangements relative to the tentacle's long axis.

Twisting and rotation are essential for endpoint control, working around obstacles, and carrying out rotating operations with objects like doorknobs and screwdrivers. Researchers have previously achieved rotation by inflating compliant materials that are more akin to soft tissue than to axles and wheels. The collapse of coupled soft structures produced local rotation [230], the unfolding of creases during inflation led to combined twisting and rotation of origami cylinders [232], and radial arrays of soft bending actuators were sequenced for continuous rotation [5]. Even closer to structures found in nature, lightweight and inherently safe robotic tentacles and limbs capable of rotation have been previously constructed from fabrics, with endpoint rotation achieved by bending inflated fabric tubes at joints. Approaches to bending joints include using a polymer mesh to control local stiffness [186, 185], changing the fabric tension with cables on either side of the joint [210], and using gussets to vary the fabric extensibility on one side of the tube for a continuous tentacle-like limb [99]. Another broad category of fiber-based inflatable actuators is the McKibben ac-

tuator (reviewed in [201]), which uses fibers wrapped around cylindrical elastomeric tubes to control the degree of contraction or elongation of the actuator during the inflation of the elastomeric chamber. McKibben actuators have long been used as artificial muscles in robotic arms. McKibben tubes have also been embedded within a membrane for contractile motion and twisting motion of up to 30° to assist the pumping of animal hearts [158]. Not only can these devices work as linear actuators, but the spacing between fibers, their relative angle, and the elastomer stiffness can be adjusted to cause bending or twisting [219, 36]. The fiber angle and elastomer stiffness determine the degree of actuator twist [36]. However, the fabrication process for realizing twisting is difficult because the fibers are helically wound by hand around an elongated, elastomeric chamber.

The key difference between the above inflatable actuators and the rotating membrane presented in this work is that our fiber patterns are fabricated in a plane rather than on a cylinder or other three-dimensional (3D) structure. Planar fabrication makes high speed assembly, alignment, and cutting operations possible without the need to grasp and orient a complex shape; it is the foundation of both the semiconductor and garment assembly industry. Textile equipment for sewing, weaving, knitting, and embroidery produces objects from fibers at high-speed and at low enough cost to satisfy a price-sensitive market. With fabric clamped in a planar format, industrial embroidery machines typically insert 20 stitches per second, while consumer-grade machines do 5–10 stitches per second. Merging soft, inflatable fiber-reinforced actuator functionality [173] with textile fabrication methods enables rapid soft actuator fabrication with a diverse range of functional fibers and fabrics. In one such example, yarn coated with an electroactive polymer was custom-knitted into

textiles and inserted in an electrolyte solution, producing localized fabric contractions [115]. In another, our team showed that patterned cutouts from inextensible fiber sheets embedded in silicone membranes could control the 3D shape of inflated silicone structures [149].

Machine embroidery solves the problem of orienting fibers in complex, reproducible two-dimensional (2D) patterns for transfer into other materials. In this work, we have developed actuators that reversibly twist and transform from a 2D plane into axisymmetric 3D shapes upon inflation. The silicone disc actuators are embedded with Kevlar™ fibers spirally patterned by a computer-automated embroidery machine. Silicone disc actuators with spiral patterns have previously achieved dome-like bending using spiral air chambers [199] and self-sensing using a spiral-patterned liquid metal resistive/capacitive sensor [232]. They have also been proposed as a way to change the handedness of spiral microantennas [51]. While those works did not investigate in-plane twisting of the discs during inflation, they were similar to our work in that the spiral-patterned materials (air, liquid metal, and a thin metal film, respectively) had a different modulus than the elastomer. The Kevlar™ polyaramide fibers in this paper have a high tensile strength (3620 MPa) thanks to hydrogen bonds between adjacent polymer chains. The fiber patterns controlled the final inflated shapes and maximum rotations, up to 170° for the inflated membranes shown in Fig. 3.3. The fabrication process was simple, fast (2–3 min to form the fiber pattern), and used water-soluble thread and stabilizer to lock complex fiber shapes into solution-cured elastomers. Additionally, by placing stretchable optical waveguides over the inflating elastomeric discs, we were able to sense the optical signal output corresponding to the degree of rotational actuation of specific fiber-patterned membranes. These actuators present a new approach

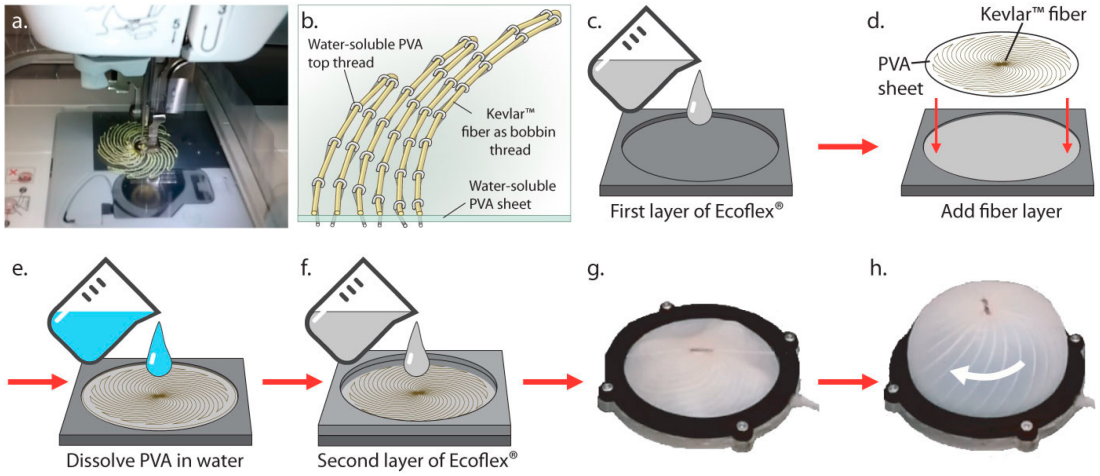

Figure 3.1: A pattern of inextensible fibers made in a water-soluble plastic sheet using (a,b) an embroidery machine (c–f) is embedded in a silicone membrane (g,h) causing vertical and rotational displacement. PVA: Poly(vinyl alcohol).

for the scalable fabrication of synthetic skins that combine local actuation and sensing.

3.1 Materials and Methods

This study focused on spiral fiber patterns that could be parametrized by a few variables. Threads radiating in a spiral from the center of an inflatable membrane can be expected to induce twisting, because when the threads are inextensible compared with the elastomer, they must straighten out, untwisting the spiral, in order to reach the center of the membrane as it rises.

3.1.1 Spiral Pattern Design for Embroidered Actuators

Spiral patterns were created with parametric Equations (3.1) and (3.2) that consider k, the number of times each spiral wraps around the center, and n, the total number of spirals emanating from the center. Both r (Equation (3.1)) and θ (Equation (3.2)) increase linearly as the parameter t ranges from 0 at the center to 1 at the edge, forming a family of interleaved Archimedes spirals,

$$r(t) = r_{max}t \tag{3.1}$$

$$\theta(t) = 2\pi kt + \frac{2\pi(m-1)}{n} \tag{3.2}$$

where r_{max} is the outer radius of the pattern, and $\frac{2\pi(m1)}{n}$, where m ranges from 1 to n, is the angular offset of the m^{th} spiral to achieve equal angular spacing.

The embroidery machine sewed each pattern with one continuous thread, using the x,y coordinates generated by the parametric Equations (3.3) and (3.4). We obtained the best performance by joining pairs of spirals across the center. There were even numbers of spirals in each pattern, and we wrote the coordinates in a sequence that connected each spiral with the one on the opposite side,

$$x(t) = r_{max}tcos\left(2\pi kt + \frac{2\pi(m-1)}{n}\right) \tag{3.3}$$

$$y(t) = r_{max}tsin\left(2\pi kt + \frac{2\pi(m-1)}{n}\right) \tag{3.4}$$

The coordinates for the embroidery design were generated in MATLAB (MathWorks, Inc., Natick, MA, USA) to conform to the EXP embroidery file format. Embird conversion software (Balarad, S. R. O., Prešov, Slovakia) translated the EXP file format to the PES file format required by the embroidery machine.

3.1.2 Membrane Fabrication

The procedure for fabricating a fiber-embedded elastomer is shown in Fig. 3.1. A water-soluble poly(vinyl alcohol) (PVA) sheet (Ultrasolvy stabilizer, Sulky of America, Inc., Punta Gorda, FL, USA) was embroidered with a spiral fiber pattern (Brother PE-525 embroidery machine, Brother Industries, Ltd., Nagoya, Aichi, Japan) using water-soluble PVA thread (Wash-A-Way, YLI Corp., Rock Hill, SC, USA) in the needle, and 23 lb Kevlar™ fiber (0.0081 inch diameter, The Thread Exchange, Weaverville, NC, USA) as bobbin thread (Fig. 3.1a,b). The process also worked using 100% polyester sewing thread as the needle thread, instead of Wash-A-Way. A two-part liquid-cure silicone (Ecoflex® 00-10, Smooth-On, Inc., Macungie, PA, USA) was chosen for the stretchable membrane material, because it was soft enough to achieve maximum rotation at low (¡3 psi) pressures that did not cause leaking around the seal. Equal amounts of Ecoflex® 00-10 (A) and (B) were thoroughly mixed, and 20 g of the mixture was poured into a plastic mold with a 90 mm diameter and 2 mm depth (Fig. 3.1c). The silicone was degassed in a vacuum chamber. The fiber pattern was embedded Kevlar™ side down into the still-uncured Ecoflex® 00-10 (Fig. 3.1d). A similar method has been used by others to insert fine wires into elastomer castings using a sewing machine without a programmable path [154]. In our work, the machine guided the thread to each x,y coordinate as shown in Fig.

3.1a. The silicone was then cured in a 70 °C oven for 30 min. After curing, the water-soluble plastic was washed away in smooth-running tap water (Fig. 3.1e) with care to avoid displacing the embedded fibers. In the final step, the embedded Kevlar™ fibers were covered with a top layer of silicone by pouring a second 20 g layer of Ecoflex® 00 – 10 over the mold (Fig. 3.1f), degassing it for five minutes, and then curing it again in the oven. At the end of the process, the fiber pattern was embedded at the mid- thickness of a 3 mm thick, ≈ 90 mm diameter Ecoflex® circle. Optionally, after curing the top Ecoflex® layer, a stretchable optical fiber [69] was placed across the spiral pattern through its center. Ecoflex® was dispensed on top of the fiber in a thin layer and cured to attach it to the surface. Thread-embedded silicone membranes were removed from the mold and clamped for testing. Fig. 3.1 shows one of the actuators before (Fig. 3.1g) and after (Fig. 3.1h) inflation. Inflation produces both rotational and vertical displacement of the membrane.

3.1.3 Testing Methods

We used an image analysis program (Adobe Photoshop, Adobe Systems, Inc., San Jose, CA, USA) to measure the rotational motion and 3D deformations induced by the thread pattern and inflation pressure; specifically to measure angles and *x*,*y* coordinates in images. The actuators were characterized by maximum degrees of rotation, torque output, and shape profile. A membrane with an embedded optical fiber was also investigated as a rotation sensor toward a control system for actuation.

3.1.4 Measuring Inflation of Soft Actuators

A pressure-regulated pump (EFD Inc., East Providence, RI, USA) was used to inflate the soft membranes throughout the experiments. Prior to inflation, an actuator was placed on top of a piece of laser-cut acrylic with an inner chamber of approximately 2 mm in depth. A second piece of acrylic with a $\approx$ 90 mm diameter hole in the middle was placed on top of the membrane. The two pieces of acrylic were screwed together around the membrane edge to create enough clamping force to inflate the membrane. The pressure differential (P) between the inner bladder and atmosphere could be set in the range $\Delta P = 0$ to $\Delta P = 3$ psi without leaking.

3.1.5 Rotational Motion Measurements

Prior to inflating a soft actuator, a line $\approx$ 3 cm long was drawn at the center of the membrane with a marker. During inflation, a digital camera (EOS Rebel T3i, Canon Inc., Tokyo, Ota, Japan) recorded top-view videos over the center of the membrane to capture the actuator's twisting motion, and then the first and final frames of each recording were isolated and analyzed to measure the total twisting angle.

3.1.6 Shape Characterization

We also recorded the membranes' inflations using side-view video, and 10 evenly spaced frames from the recording were isolated for image analysis. For

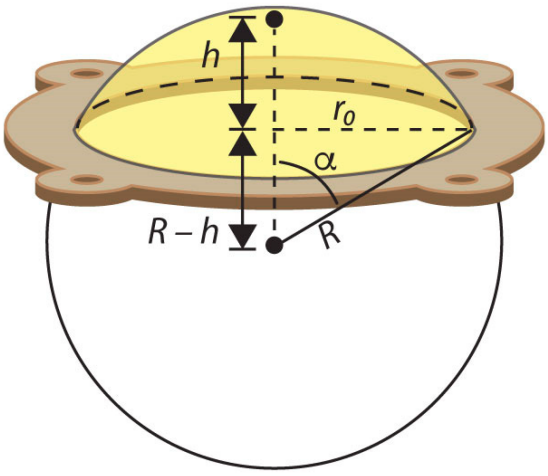

Figure 3.2: Spherical cap coordinate system used in energy balance model for an inflating silicone membrane (yellow region). h: Center height; R: Radius of the spherical cap; r_0: Base radius of the membrane; α: Zenith angle.

each frame, we selected ten approximately evenly spaced points along an inflated membrane's left half surface and used their locations with respect to the highest point at the center of the membrane. These ten points were used to characterize how closely the shape of each membrane matched the spherical cap model illustrated in Fig. 3.2; we determined the radius R of a spherical cap matching the membrane's base radius, r_0, and its measured center height h. A polygon-based shape metric (see Supplementary Methods, Equation (3.14)) was used to compare the measured profile shape to the corresponding spherical cap.

3.1.7 Torque Measurements

Torque was measured using a 14 cm long, flat, lightweight ($\approx$ 0.4 g) wooden stick glued with Loctite® 404 to the center of the actuator (Supplementary Fig. 3.8). The end of the stick was pressed down on a scale to measure the torque produced at increasing angles at pressures up to 3 psi.

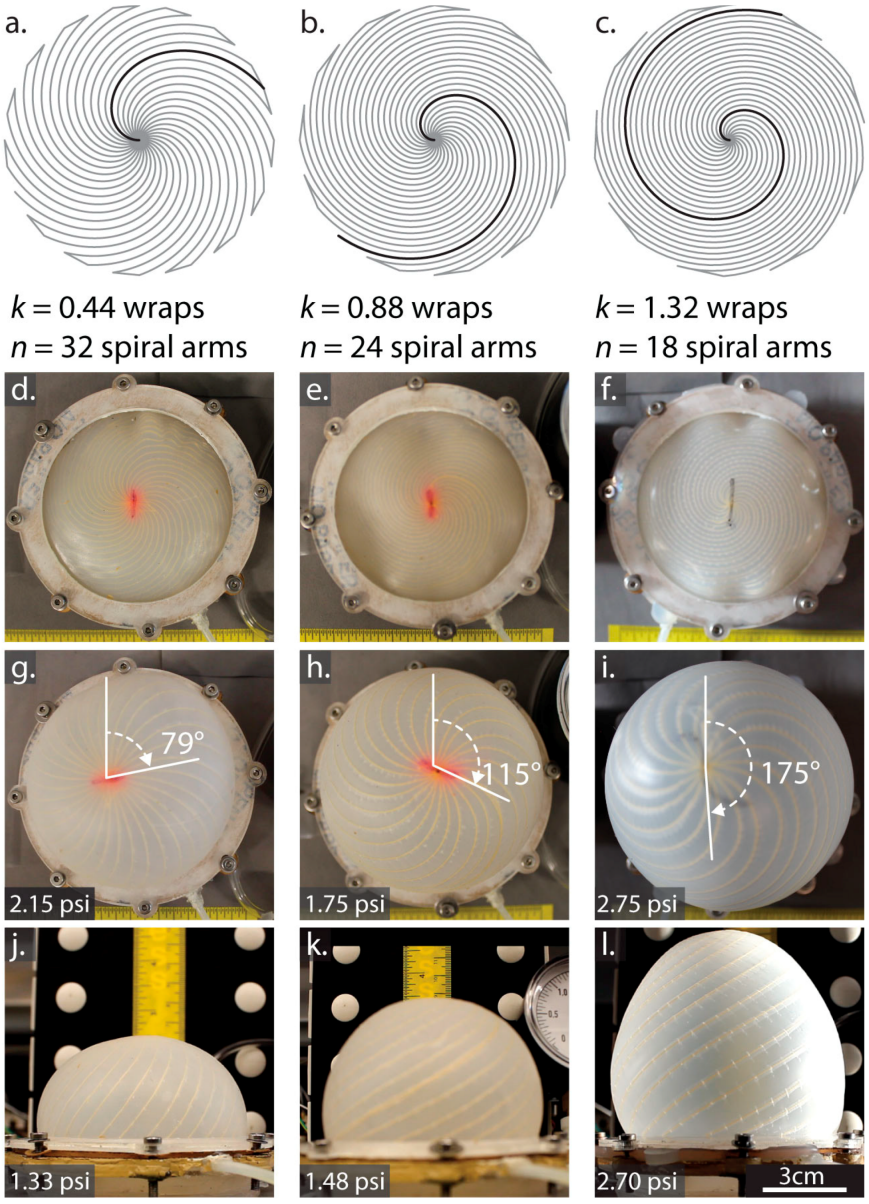

Figure 3.3: Layout and implementation for three different spiral designs (a–c) Embroidery layout for spiral patterns with three different wrap numbers k and similar thread densities. (d–f) Uninflated top views. (g–i) Inflated top views near the maximum rotation value for each actuator. (j–l) Side views used for comparing inflated shapes to the spherical cap model. These three designs were fabricated and inflated. As pressures increased, the membranes approached a maximum rotation angle (Table 1) determined by the wrap number k.

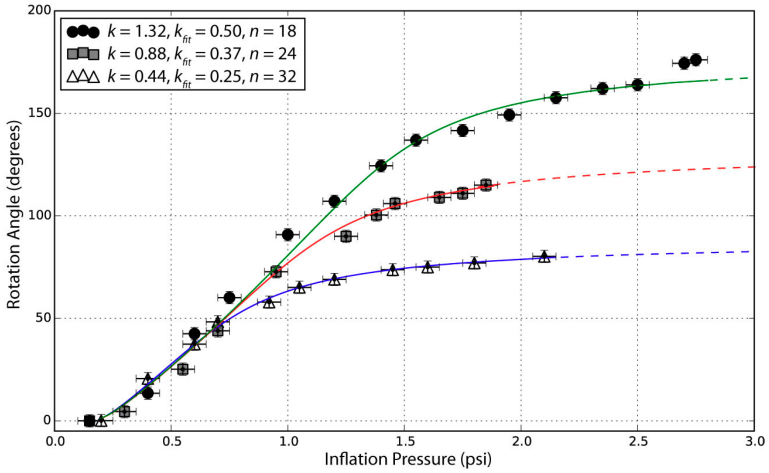

Figure 3.4: Rotation vs. pressure for an individual test of each of the three spiral designs in Figure 3, along with the spherical cap energy–balance model using torsional spring constant $\kappa = 0.06Nm$, strain energy coefficient $\gamma = 30Jm^2$, and base radius $r_0 = 0.038$ m. Dashed lines indicate where the model extends beyond measured inflation pressures.

3.1.8 Fiber Optic Lamination and Testing

A stretchable fiber optic waveguide (for details, see Supplementary Information in [69]) was placed across an embedded fiber pattern, and then cast under a poured layer of Ecoflex® 00 – 10. Fiber ends were connected to an infrared light-emitting diode (LED) and an amplified photodiode (TSL-12, ams-Taos Inc., Plano, TX, USA).

3.2 Actuator Model

We used the energy balance between the pressurized gas and membrane strain to predict the inflated membrane shapes. The inextensible fibers force the membrane to only stretch in the direction perpendicular to the fiber alignment. The fibers can bend freely and, when they unwind, the compliance allows the cen-

ter of the membrane to rise up. At a given pressure, the energy stored in the stretched and sheared silicone balances the energy lost by the gas as the volume increases. The membrane minimizes the amount of stored strain energy in the system by finding a shape with the smallest amount of surface area (stretch) and rotation (shear) that will enclose the volume, subject to the constraint that the Kevlar™ threads cannot stretch. Our semi-empirical model approximates the shape of the membrane as a spherical cap, finds the radius that achieves the energy balance at each pressure, and links the twist angle to the radius using the geometry of the spiral projected onto the spherical cap.

3.2.1 Energy Balance

The energy stored in the system can be modeled as

$$U = \gamma A\left(\frac{A - A_0}{A_0}\right) + \frac{1}{2}\kappa\theta^2 - PV, \tag{3.5}$$

where γ is a strain energy coefficient having units of Jm^2, A is the surface area of the inflated thin membrane, A_0 is the surface area of the flat membrane, κ is a torsional spring constant for the membrane, θ is the rotation angle, P is the inflation pressure, and V is the enclosed volume. Because the membrane takes on a rotation angle θ that minimizes the total energy at a given pressure P,

$$\frac{dU}{d\theta} = \gamma\left(\frac{2A}{A_0} - 1\right)\frac{dA}{d\theta} + \kappa\theta - P\frac{dV}{d\theta} \tag{3.6}$$

Rather than extracting $\theta(P)$, the twist angle as a function of pressure, from Equation (3.6), it is more straightforward to solve for P as a function of rotation

angle , as follows:

$$P(\theta) = \frac{\gamma\left(\frac{2A}{A_0} - 1\right)\frac{dA}{d\theta} + \kappa\theta}{\frac{dV}{d\theta}} \tag{3.7}$$

We can invert the measured rotation vs. pressure data and use it for fitting Equation (3.7). However, the area A and volume V still need to be defined in terms of .

3.2.2 Spherical Cap Approximation

Because an inflating membrane without embedded fibers takes on a spherical cap shape [62], we use the spherical cap as an approximate shape to connect the membrane area A and volume V to the rotation angle θ, so Equation (3.7) can be solved for pressure. Later (Section 4.2), we will validate this assumption using image analysis. The surface area of a spherical cap (Fig. 3.2) is

$$A = \pi(r_0^2 + h^2) \tag{3.8}$$

and its volume is

$$V = \frac{\pi h}{6}(3r_0^2 + h^2) \tag{3.9}$$

In the membrane system, r_0 is the fixed radius of the testing plate (0.038 m) and h is the height of the membrane center above the plate, which varies with pressure.

3.2.3 Spiral Mapping onto Spherical Cap

The spiral is projected onto the spherical cap using a method that preserves the relative radial distances between features [231]. We map the radial coordinate r of the flat spiral (Equation (3.1)) to an arc length along a meridian passing through the center of the sphere, $r > R\alpha$, where α is the zenith angle on the spherical cap ($\alpha = 0$ at the center) and R is the radius of the sphere (see Supplementary Fig. 3.9 for an example). The spiral must also untwist by θ to make its own arc length match its initial value, because the threads cannot stretch, and that gives the connection between h and θ. A zero-finding method is used to solve for the twist angle θ that makes the projected spiral arc length match up with the original flat arc length at a given center height h. The twist angle θ for a given center height h depends on the spiral pattern wrapping number k. With an array of h values calculated for the different values of , it is possible to numerically calculate $\frac{dh}{d}$. Equation (3.7) for the pressure was rewritten using derivatives with respect to h, and the terms A, $\frac{dA}{dh}$, and $\frac{dV}{dh}$ were computed using the spherical cap geometry in Equations (3.8) and (3.9) to obtain an expression for the pressure as a function of rotation angle, up to a few coefficients,

$$P(\theta) = \frac{\gamma\left(\frac{2A}{A_0} - 1\right)\frac{dA}{d\theta}\frac{dh}{d\theta} + \kappa\theta}{\frac{dV}{d\theta}\frac{dh}{d\theta}} \tag{3.10}$$

3.2.4 Strain Energy

The area term in the energy expression (Equation (3.5)) has a proportionality constant γ that connects the change in membrane surface area to an energy cost. In the Yeoh model [234], the energy density u in a strained material is

$$u = \sum_{i}^{n} = C_i(I_1 - 3)^i, \tag{3.11}$$

where C_i are the Yeoh coefficients, $I_1 = \lambda_{12} + \lambda_{22} + \lambda_{32}$, and $\lambda = \epsilon + 1$ is the principal stretch along each direction. Looking only at the first term in Equation (3.11), $u = C_1(I_13)$, one can write out the λ_2 terms as $(\frac{L_x}{L_{x0}})^2$ and $(\frac{L_y}{L_{y0}})^2$, or for equi-biaxial stretching, A/A0. Setting 3 to 1 means the membrane thickness does not change during inflation, a simplification made to get an estimate for the value of γ in the first-order energy balance model. Re-assembling the first term in Equation (3.11),

$$u = C_1\left(\left(\frac{2A}{A_0} - 1\right) + 1 - 3\right) = \frac{2C_1(A - A_0)}{A_0}. \tag{3.12}$$

The first Yeoh coefficient C1 for Ecoflex® 00−30 was measured by others [90] to be 1.2710^2 MPa; it is likely smaller for the softer Ecoflex® 00 − 10 silicone we used. The total strain energy in the membrane is estimated by multiplying the strain energy density in Equation (3.11) by the volume tA of the thin membrane material, where the thickness t is ≈ 3 mm and the surface area A is given by the spherical cap Equation (3.8),

$$u_{strain} = \frac{2C_1tA(A - A_0)}{A_0} \tag{3.13}$$

By comparing Equation (3.13) with the first term of the energy expression (Equation (3.5)), the coefficient γ should be in the neighborhood of $\approx 2C_1t$ or $76Jm^2$ if Ecoflex® 00 − 30 were used. However, a smaller γ value of $30Jm^2$ better matched the experimental data from the softer Ecoflex® 00 − 10 membranes.

3.2.5 Shear Energy

The torsional spring constant was found to be in the range of 0.06 N m rad1 in the torque measurements; experimental details are provided in Section 4.3.

3.3 Results and Discussion

The membranes were inflated and evaluated for their rotation angle, torque, shape, and fiber optic light transmission as a function of pressure, and results were compared with the spherical cap model.

3.3.1 Rotation Angle vs. Pressure

The columns in Fig. 3.3 show the spiral layout, a side view, and top view photos at increasing pressures for membranes with wrap numbers (k from Equation (3.2)) of 0.44, 0.88, and 1.32, respectively.

We were able to double the final rotation angle by increasing the wrap number k from 0.44 turns to 1.32 turns. However, increasing k reduces spacing be-

Table 3.1: Maximum rotation for three sets of design parameters.

k	n	Max Rotation	Max Pressure
0.44	32	80^o	2.1 psi
0.88	24	115^o	1.85 psi
1.32	18	176^o	2.75 psi

tween fibers, limiting n, the number of spiral arms that would fit in the membrane. At $n = 24$ spirals and $k = 1.32$, for example, the embroidery machine was not able to complete the process without sewing over the adjacent Kevlar™ fiber, so the number of spirals was decreased to 18 for these actuators. Rotating and shape-changing occurred even with the lower number of spirals.

The theoretical absolute maximum rotation in degrees occurs when the spirals become straight lines radiating from the center. For the three designs in Table 1, the maximum possible rotations are 158^o, 317^o, and 475^o in order of increasing k. Although the experimental results in Table 1 do not reach these absolute maximum angles, instead leveling off with pressure (Fig. 3.4) as the silicone resists stretching and shearing. To increase the maximum rotation angle, the silicone might be changed to a softer material, or the spacing between the fibers might be increased. These adjustments, however, reach a limit because with softer silicone and greater spacing, energy transfers to volumetric expansion of the silicone between the threads. The spherical cap model includes strain energy stored in the silicone, but does not account for the effects of fiber spacing. The three k,n combinations shown in Fig. 3.4 all have similar fiber spacing in the optimal region, between one and two times the membrane thickness, where fibers are dense enough to prevent the silicone from bulging between them, yet sparse enough to still allow twisting. Supplementary Fig. S3.10 can give some insight on the relationship between k,n, and fiber density.

In Fig. 3.4, for $\Delta P < 0.75$ psi, the rotation for all three membranes was similar, with a slope of 90° per psi. Above 0.75 psi, the $k = 0.44$ membrane diverged and its rotation angle began to level off, followed by the $k = 0.88$ membrane near 1 psi. At $\Delta P \geq 3$ psi, the clamping force at the edges was insufficient, and the

membranes began to slip out of the fixture.

The spherical cap model, plotted as lines through data points in Fig. 3.4, captures the general shape of the twist vs. pressure curves, as well as the increase in final twist angle with k-value. The least squares error-minimizing fits in Fig. 3.4 were obtained using smaller k-values (0.25, 0.37, and 0.50) than the pattern (0.44, 0.88, and 1.32, respectively). This discrepancy in actual vs. best-fit k-values could be caused by the dense threads in the middle reducing the number of usable wraps as the threads occupy a large portion (50%) of the membrane surface within $\approx$ 1cm of the center. Also, energy stored in lateral compression of silicone in front of the threads was not captured in the model, but at pressures greater than 1 psi, we observed air pockets opening behind the threads as the silicone resisted twisting (Supplementary Fig. 3.11); thicker threads might reduce this effect by providing a larger bonding surface. Making a reliable interface between soft, highly compressible materials like silicone and less-compressible materials like the Kevlar™ fibers in this paper is still one of the fundamental challenges in soft robotics fabrication [149]. Materials solutions, for example, using adhesives or a porous, loosely twisted fiber with greater bonding area, would likely increase the rotation angle, lifting the curves in Fig. 3.4 to match higher k-values by pulling on the silicone instead of opening the air gap behind it.

3.3.2 Actuator Shape Compared with Spherical Cap Model

In this section, the validity of the spherical cap model is evaluated from actuator images. Cross-sections of the measured shape in comparison with the ideal

spherical cap are shown in Supplementary Fig. 3.12. In Fig. 3.5, a polygon-based similarity metric (details in Supplementary Methods, Equation (3.14)) quantifies the departure from the spherical cap shape with increasing pressure. In this metric, a score of 1 indicates 100% overlap of the measured inflated shape with a spherical cap. Before inflation begins, the pressure differential between the inner bladder and atmosphere is $\Delta P = 0$ and the membranes are slack, making the surface non-spherical. After the onset of inflation, the observed shapes do resemble spherical caps (similarity coefficient > 0.9) for all three designs. As shown in Fig. 3.5, the spherical cap shape used in the model is an excellent match for the measured $k = 0.44$ membrane shape across its full actuation range, while the higher twist $k = 0.88$ and $k = 1.32$ designs take on a more conical appearance (Fig. 3.3l) above $\Delta P = 1$ psi.

3.3.3 Torque Exerted by Actuator

The maximum torque measured by the method of Supplementary Figure 3.8 was 0.016 N m, attained by the $k = 0.88$ actuator. This torque would be sufficient to push a typical 40 gm tactile switch, like those found on microwave ovens and other household appliances, with a 4 cm lever. In Fig. 3.6, the measured value for the torsional spring constant κ varies with angle, but it is in the 0.01–0.10$Nmrad^1$ neighborhood. For the model in Fig. 3.4, a good match to the experimental data was obtained with a torsional spring constant κ of 0.06$Nmrad^1$, consistent with the experimental results. At the higher end of the rotation range for the highest-twist actuator, the contact area between the actuator and the wooden stick began to decrease as the actuator took on a more cone-shaped profile (Fig. 3.3l); debonding may explain why the $k = 1.32$ actua-

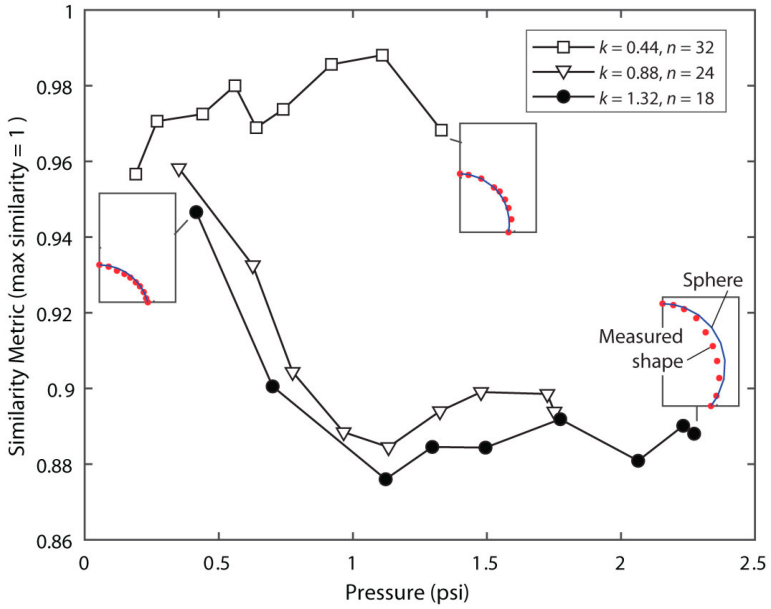

Figure 3.5: Sphere similarity metric vs. pressure, and measured vs. ideal spherical cap shape for three cases. A metric of 1 means the shape has 100% overlap with the spherical cap.

tor exerted a decreasing amount of torque at higher angles.

3.3.4 Optical Detection of Actuator State

Fig. 3.7 shows the intensity signal output versus angle when a membrane with embedded stretchable optical fiber is inflated; this signal is plotted versus pressure in Fig. 3.13.

At small angles, the fiber optic showed an increasing signal, likely because the membrane is still slack at very low pressures, causing bending losses from the fiber. As the pressure and rotation angle increase, the signal reaches a maximum. With further inflation, it begins to stretch, producing a monotonically decreasing signal between 15^o and 50^o. The inset in Fig. 3.7 shows that the polyurethane-core, silicone-clad fiber is soft enough to follow the bending and

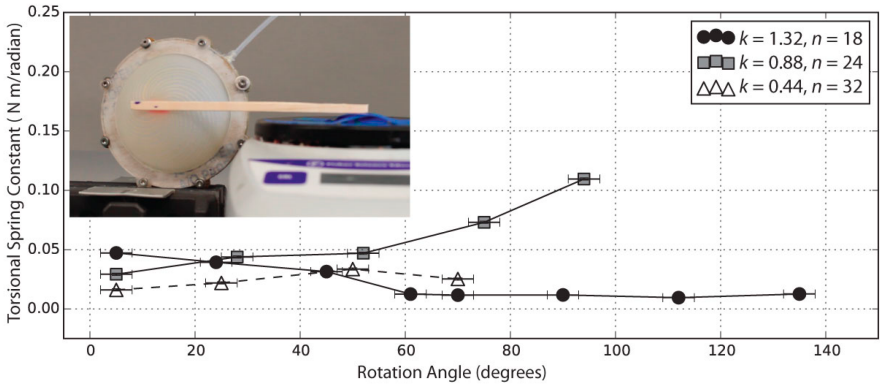

Figure 3.6: Torsional spring constant measured over the rotational range of three membranes with $k = 0.44$, $k = 0.88$, and $k = 1.32$.

stretching of the soft silicone surface, in contrast to the Kevlar™ threads that rotate in the opposite direction. Because the silicone is softer than the optical fiber, a small amount of distortion can be seen in the upper right inset of Fig. 3.7, where the optical fiber crosses the Kevlar™ threads, showing the potential for a single material to add both sensing and mechanical actuation capability. Stretchable constraining materials were not included in the spherical cap model, which assumed the constraining fibers were completely inextensible. To accommodate stretchable fibers, an arc length-dependent spring energy term ($\frac{1}{2}k_f\Delta s^2$, where Δs is the difference between the original and stretched arc length of the spiral arm, and k_f is the spring constant of the fiber) could be added to the energy balance in Equation (3.5); the stretched arc length would be obtained from the spherical cap radius that balances the equation. A stretchable constraining material would likely yield smaller rotation and more volumetric expansion, as in [232], where 2D stretchable fabric inserts in silicone membranes led to both texture changes and volumetric expansion during inflation.

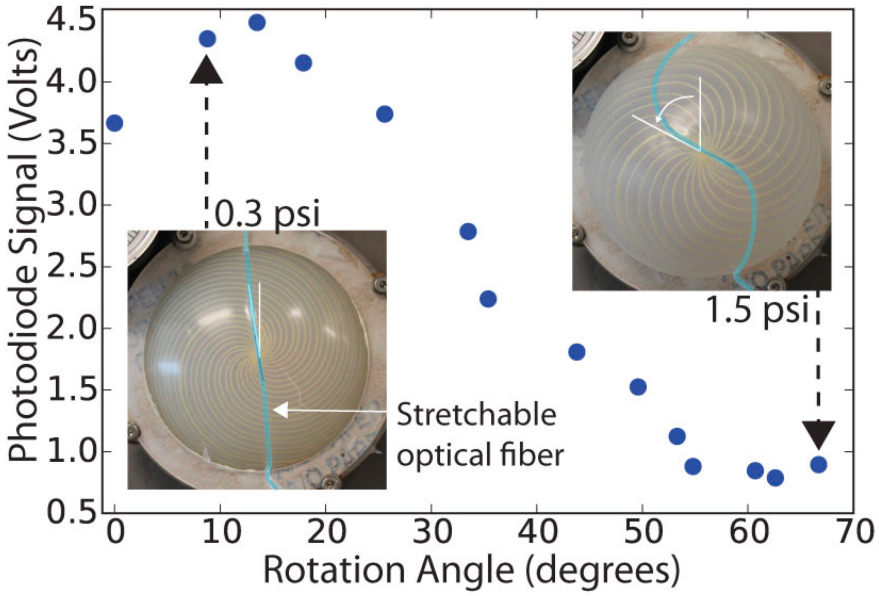

Figure 3.7: Optical signal as a function of rotation angle for a membrane with an embedded spiral pattern of $n = 24$ and $k = 0.88$.

3.4 Conclusion

We have developed a method for programming the shape and rotation of surfaces by embroidering inextensible Kevlar™ fibers into soft silicone sheets. These actuators could rotate nearly 180^o at 2.75 psi, adopt 3D axisymmetric shapes, and produce 0.016 N m torques. We developed a model that balanced the energy stored in the stretched and sheared silicone-fiber composite with the energy stored in compressed gas to predict the final actuator rotation angle. The embroidery-based fabrication process was simple, fast, and able to program complex patterns into silicone sheets using water soluble thread and stabilizer. In addition, we installed stretchable optical fiber sensors into the silicone sheets that detected the rotation angle, demonstrating the ability to embed fibers with different sensing and actuating functions. Improvements in the maximum composite material strain or in new fiber geometries would allow for higher rota-

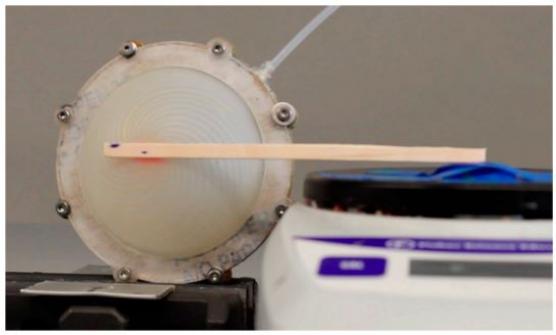

Figure 3.8: Method for measuring the torsional spring constant κ of pressurized fiber-embedded membranes. A glued-on stick (Loctite 404) exerted force on a scale. To measure the spring constant κ, the membrane was inflated to a fixed pressure, and was clamped so that the stick touched the scale (force = 0) at an angle 10 degrees below the horizontal. The scale was raised until the stick became horizontal, and the force F on the scale was measured. The torque = F $\times$ stick length. Torsional spring constant $\kappa = \tau/\Delta\theta = F sticklength/10^o$. We measured the value of κ at different pressures to check for variations across the rotation range.

tion angles and increased torque. Additionally, embedding active fibers would enable controlled transformation between shapes. In the biological world, oriented active fibers are responsible for motion over a wide range of scales, from separating genetic material during cell division, to organizing complex motions in human-scale muscular structures. The technological implications for this work are extensive and include the large area integration of textiles into soft synthetic skins for controlling the shape of intelligent catheters [84], improving aerodynamic efficiency in airplane wings [200], wearable sensors, soft robotic design [219, 36, 173, 153], and controllable surface actuators that rotate and manipulate compliant external shapes [179].

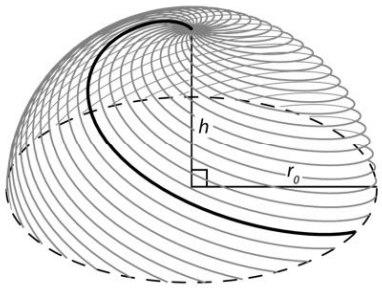

Figure 3.9: An example of a $n = 32$, $k = 0.44$ spiral mapped onto a spherical cap. During inflation, the center height of the cap increases from 0 to h, and the arc length of each spiral arm is preserved by rotating the cap by θ. This example is a hemisphere ($h = r0$).

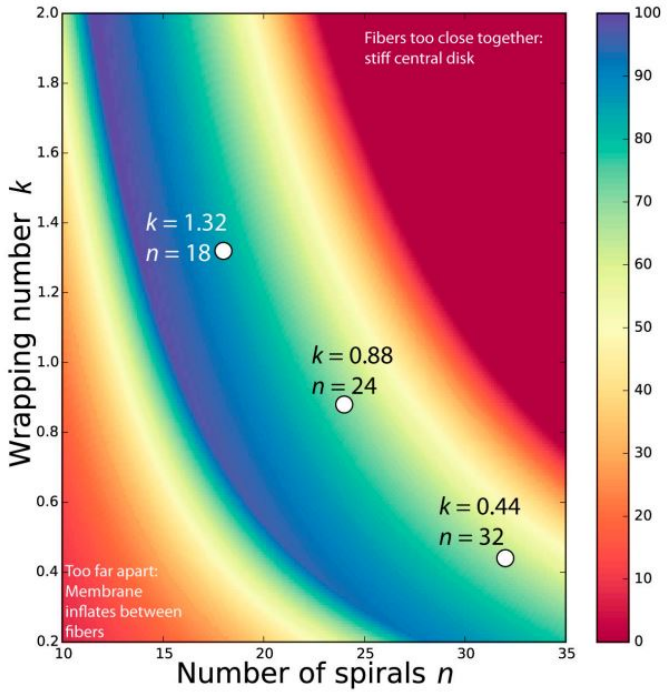

Figure 3.10: Percentage of membrane that has fiber spacing between one and two times the membrane thickness, for different values of wrap number k and number of spiral arms n. The three membranes pictured in Fig. 3.2 are marked on the plot, and have 60–70% of their surface area in this "optimal" region where fibers are close enough to constrain the silicone from bulging out between adjacent fibers, but not so close that the fibers stiffen the material. The optimal region always excludes a disk at the center, and sometimes excludes a ring around the edge where the fibers have the greatest separation distance.

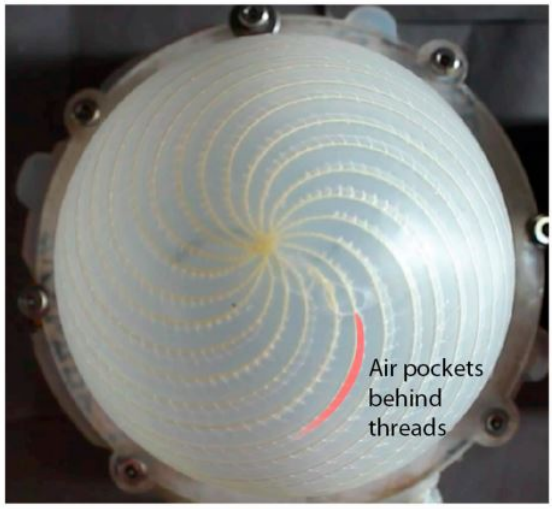

Figure 3.11: Example of air pockets opening behind threads at high pressures from k = 1.32, pressure = 1.5 psi, actuator at 132^o rotation.

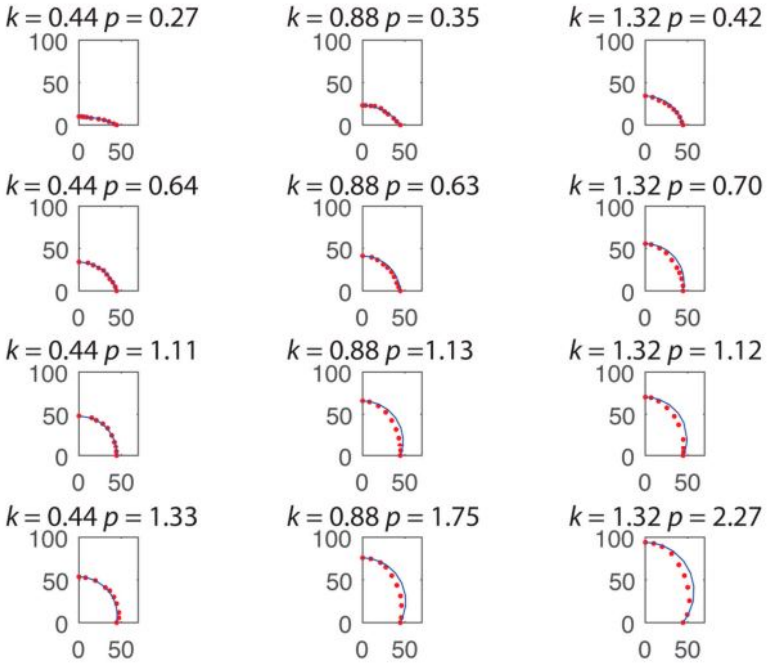

Figure 3.12: Measured and ideal spherical cap cross-sections of inflated membranes for three k-values at increasing pressures (p) in psi. The top row and bottom row sample the low-end and high-end pressures for each actuator's full range of motion, respectively, while the middle two rows show how the three different actuators look at similar pressures.

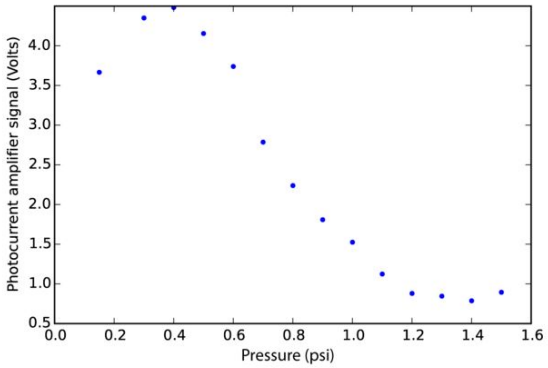

Figure 3.13: Fiber optic intensity signal vs. pressure for $k = 0.88$, $n = 24$ with straight stretchable optical fiber.

3.5 Supplementary Materials

3.5.1 Shape Similarity Metric

Actuator shapes were measured from side-view images and compared to the ideal spherical cap shape using a similarity metric. The similarity metric M for polygons P_1 (having area A_1) and polygon P_2 (having area A_2) is defined as:

$$M = 1 - \frac{(A_1 \cup A_2) - (A_1 \cap A_2)}{A_1 \cup A_2} \tag{3.14}$$

For example, if the polygons overlap perfectly, the area of their union and area of their intersection will be the same area $A_1 = A_2 = A$. The similarity metric becomes $1 - (A - A)/A = 1$. If there is no overlap, the similarity metric is $1 - ((A_1 + A_2) - 0)/(A_1 + A_2) = 0$. In this work, the measured shape P1 is typically smaller than the ideal spherical cap P_2 and fully contained inside (see Supplementary Figure 3.12). If a fraction f of the area of P_2 is filled by P_1, $M = 1 - (A_2 - fA_2)/A_2$ or $1 - (1 - f) = f$. The similarity metric gives a spherical cap's

2D cross-sectional area filled by the membrane.

CHAPTER 4

LEVERAGING FLUID RESISTANCE IN SOFT ROBOTS

Soft actuators enable complex motion with inexpensive material, rapid manufacturing techniques, and low level control [165, 71]. When applied to full-scale robots however, these mechanisms typically require several chambers and separate pumps or many valves, as well as real time embedded control to produce useful behaviors. These add-ons increase price, complexity, weight, and rigidity of the robot. Here, we introduce the use of fluid resistance to produce wave-like actuation of a single chamber without the need for complex manufacturing, expensive materials and components, or accurate real-time control. An embodied control mechanism, determined by the soft actuator's shape, material properties, and internal fluid resistance, is used to produce consecutive movements along the length of the actuator from bursts of fluid created by simple on-off control of a single pump (Fig. 4.1). We demonstrate this concept through designs that produce forward locomotion with traveling wave patterns, much like those exhibited by a range of natural organisms from flatfish to millipedes [63].

A traveling wave provides the necessary forward momentum for an object by lifting subsequent regions of a linear body in successive fashion [252]. Traveling waves for locomotion have been reproduced with a range of techniques including FEAs [136, 127], shape memory alloys embedded into tubular meshworms [171], ionic polymer actuators embedded along beams [196], central pattern generators in (rigid) modular robots [37], and more. Furthermore, many other researchers have sought inspiration from locomotion in natural systems, including inchworms [214], caterpillars [101], fish [40, 111], jellyfish [128], and octopuses [112]. Similar to the minimalistic approach presented in this paper,

researchers have demonstrated traveling wave locomotion using a single motor attached to a helix-shaped axle [246]. To the best of our knowledge, this is the first demonstration of locomotion by traveling waves in a soft robot, produced with only a single valve and pressure inlet.

In the following sections, we first describe design and fabrication of the poroelastic foam actuators (Sec. 4.1). We then characterize the tensile strength of the foam and three different actuator designs with respect to the force exerted, the maximum deflection of the chamber, and the forward speed of the actuator along a flat surface (Sec. 4.2). All three actuator designs have a spine-like structure with extruding segments, referred to as the ”legs”, along the length of the body. We show actuation with two fluids of different viscosity (air and water). Finally, we show simple locomotion by a robot with two sets of actuators coupled to a single source of pressure (Sec. 4.3) and conclude (Sec. 7.7).

4.1 Methods

To demonstrate the use of fluid resistance and traveling waves in soft actuators, we rely on FEAs and poroelastic foams. The following subsections briefly introduce the concept and fabrication of each.

4.1.1 Fluidic Elastomer Actuators

FEAs are a subset of soft actuators that use pressurization of elastomeric chambers to produce large deformations specific to localized strain patterns [166]. Strain-limiting layers on FEAs can be comprised of a wide set of materials,

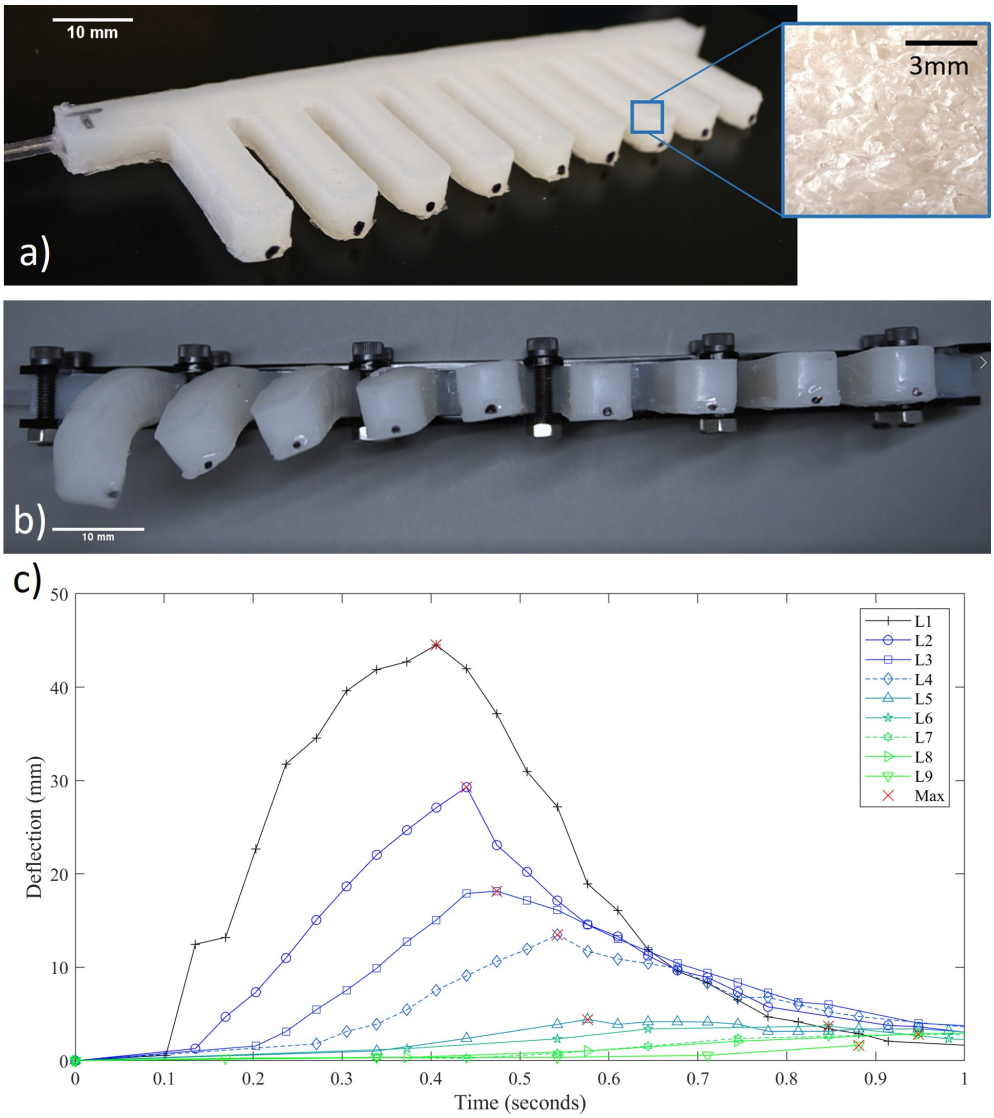

Figure 4.1: Demonstration of how fluid resistance may be leveraged to create complex motions. (a) The experimental platform consists of a poroelastic foam actuator with a spine and nine legs; the inset shows a close-up of the internal foam. (b) Side view of the same actuator 0.15s after an air pressure of 20 psi has been applied. The higher deflection in the left-most extruding segment (closest to the inlet) demonstrates that fluid is retained closer to the inlet for a longer period of time. (c) Deflection of each leg (L1-9) over time when a pressure of 20 psi is applied for about 325 ms. At the end of the pulse, a valve is opened and the actuator returns to atmospheric pressure. Due to the geometric layout of the actuator, the legs closer to the inlet inflate more than the subsequent legs. The point of maximum deflection in each leg is marked in red. As this curve indicates, the resistance of the foam causes a damped traveling wave through the legs.

including inextensible fibers, fabric, or variable elastomer thicknesses, which upon pressurization of the FEA, produce a strain gradient, resulting in programmed bending or twisting of the elastomer [108].

FEAs with prismatic elastomer chambers are accurately manufactured with one- or two-step molding processes [71]; however, as the chamber shape becomes more complex, the number of fabrication steps also often increases and the repeatability of the final product often suffers. Recently, poroelastic foams were developed as a new class of FEAs that offer greater complexity in soft, repeatable, smart 3D structures [108]. As opposed to elastomeric chambers where there is an internal volume of air, poroelastic foams contain minuscule, interconnected pockets of air spread throughout an elastomer. Pressurization of these actuators also results in programmed deformations; however, the period of time necessary for a foam chamber to reach pressure equilibrium across its volume drastically increases as a result of fluidic resistance which varies as a function of foam porosity, foam shape, and inflation pressure.

Fluidic resistance in poroelastic foams offers opportunities to design complex embodied control in soft robotic actuators, thus decreasing the need for external controllers. A traveling wave for instance can be created from multiple, neighboring chambers subsequently pressurized one right after the other; however, this requires external control and drivers to coordinate between the inflation and deflation of adjacent chambers. Instead, poroelastic foams offer an embodied control mechanism that can produce a traveling wave along the length of a single foam chamber.

4.1.2 Foam Fabrication

The poroelastic foams are fabricated with a lost- salt process, previously used in [108] and originally adapted from [100]. The matrix material is comprised of elastomer, and the porogen (the mass used to create the miniscule voids) comes from Himalayan salt. The foam is encapsulated into the spine-like Ecoflex 00-30 structure shown in Fig. 4.1 with 3, 5, and 9 legs respectively. The width of each leg is 16.26 mm; the gap between the legs are 93.73 mm, 38.86 mm, 11.43 mm respectively. In our design the foam serves two purposes. It enables an easy fabrication process as it automatically fills the void of the surrounding elastomer, and it provides added fluid resistance to create the traveling wave.

The fabrication process is split into two parts: foam sealing and strain sealing. All silicone used in this process was Ecoflex 00-30 (Smooth-On, Inc.), prepared as directed by the manufacturer. Other materials include: silicone adhesive (Silpoxy from Smooth-On, Inc.), non-woven nylon sheets (Soft 'n Sheer from Sulky of America), and Himalayan salt (Pure Himalayan Salt, 1-3mm). Table 4.1 shows the salt / Ecoflex 00-30 mixture ratios for the three actuators.

First, the foam is fabricated as indicated in Fig. 4.2A. The silicone and salt are mixed with corresponding mass amounts listed in Table 1, to reach 50.45% porosity, and cured in an acrylic laser cut mold at room temperature. The foam is then demolded and loosened by hand; the salt can be removed from dissolving in a sonicator or massaging the actuator by hand under running water.

Sealing the foam involves three steps (Fig. 4.2B). Layer 1 is cast using silicone and cured at room temperature. Layer 2 (Foam-to-EF Adhesive Layer), is cast

Table 4.1: The actuators are fabricated using EcoFlex 00-30 (EF), Himalayan Salt (HS), and Silpoxy silicone adhesive. The different steps are described in Fig. 4.2. This table specifies the mixture of materials in grams.

Process	3 Legs	5 Legs	9 Legs
Foam Fabrication	29.95 g (HS) / 14.5 g (EF)	36.96 g (HS) / 17.9 g (EF)	50.8 g (HS) / 24.6 g (EF)
Layer 1	16 g (EF)	22 g (EF)	30 g (EF)
Foam-to-EF Adhesive Layer	8 g (EF)	8 g (EF)	11 g (EF)
Foam Sealing Layer	35 g	43 g	60 g
Strain Sealing Layer	50 g	75 g	95 g
Final Silpoxy Layer	5.2 g	6 g	9 g

on top of Layer 1, with the desalted foam placed on top. This is cured in the oven (80^{o}C) to prevent the foam from soaking up an excessive amount of silicone and to allow it to become anchored to the first layer. This, in turn, prevents it from floating in the next step. The final layer (Foam Sealing Layer) seals the foam cavity; the silicone is poured on the foam and cured at room temperature. Any bubbles that form are popped manually.

The second part of the fabrication involves the strain-limiting layers for both the spine and the legs (Fig. 4.2C). These layers consist of a laser-cut non-woven nylon sheet to produce asymmetric bends upon inflation. Each leg and body is wrapped in an individual sheet, and attached to the sealed foam with silicone adhesive. To complete sealing of the strain-limiting layer to the sealed foam a final Strain Sealing Layer is casted. 50% of the layer's silicone is poured into the mold, and 40% is painted on all sides of the actuator. The painted actuator is placed top side down, and the last 10% of the silicone is poured on top of the mold. The mold is covered, weighted down, and allowed to cure in room

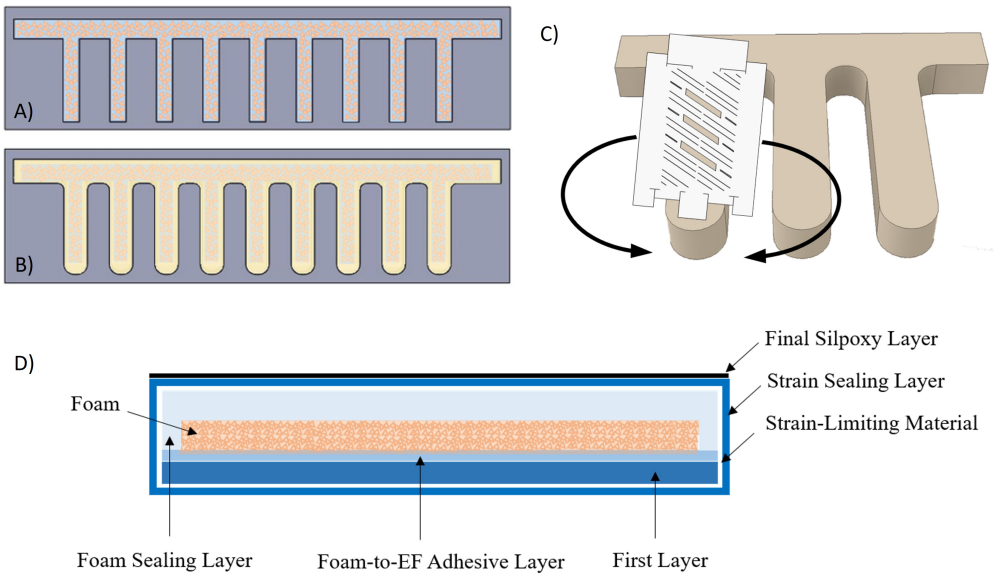

Figure 4.2: Sketches showing the process to mold a 9-legged actuator. A) Mold of laser cut acrylic to cast the poroelastic foam. B) Foam-sealing layer, also molded in the acrylic mold. C) Strain-limiting layer wrapped around each finger along the body of the foam actuator. D) Side view of a complete foam actuator. The foam is sandwiched between equal layers of silicone to avoid bulging out on one side of the actuator. The strain-limiting layer is wrapped completely around the actuator, and a final layer of silicone adhesive is applied to one side of the actuator.

temperature. Next, a 1/16" inlet tube is inserted 1" into the actuator, sealed with silicone adhesive, and cured in an oven at 80^{o}C for 10 minutes. Finally, a layer of silicone adhesive is added to the strained side of the mold and smoothed with a plastic (non-silicone) sheet. This is also allowed to cure in the oven at 80^{o}C for 20 minutes. Fig. 4.2D shows a side cross-sectional sketch of the assembled actuator.

4.2 Actuator Characterization

To characterize the actuators, we first compare the tensile strength of the foam and the silicone. We then examine the relationship between actuator design and the traveling wave produced upon application of pressure. As previously stated we test three, five, and nine-legged actuators; the number of legs signify the number of locations at which the pressure within the actuator is temporally split two ways, causing differential pressure across the length of the actuator. Each of the three actuators was pressurized with air and water and characterized with respect to the exhibited deflection and speed of each leg. Force measurements for each leg were recorded when the actuator was inflated by air. Throughout the results, the first leg (L1) refers to the perpendicularly extruding segment closest to the inlet of the foam actuator. The last leg (L9) refers to the segment farthest away from the inlet.

As expected, throughout the results we observe that the viscosity of the fluid is strongly correlated with the fluid resistance, and therefore a critical parameter in the design of the traveling wave. We encourage the reader to view the accompanying video to view how a traveling wave behaves differently when the actuator is inflated with air and when it is inflated with water.

4.2.1 Tensile Test

Using a Zwick Roell z010 instrument, we conducted tensile tests on five pieces of Ecoflex 00-30 and five pieces of the Ecoflex 00-30 foam to demonstrate the differences in the material properties (Fig. 4.3). The foam is simply a porous

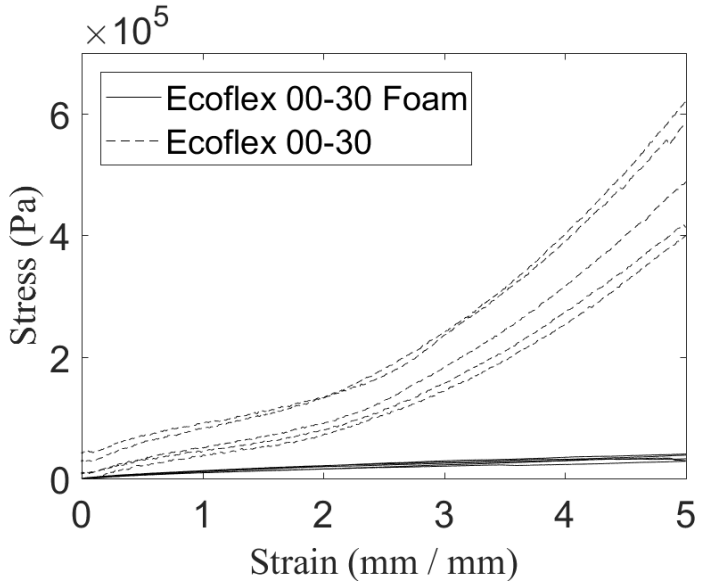

Figure 4.3: Tensile tests conducted on Ecoflex 00-30 (Width = 14 ± 1 mm, Thickness = 1 mm) and Ecoflex 00-30 Foam (Width = 30 mm, Thickness = 5 mm ± 1 mm).

medium of the Ecoflex 00-30 silicone, and as a result, the stiffness of the material is reduced by more than two times. The elastic modulus was found to be 50.894 ± 7.561 kPa for the Ecoflex and 19.805 ± 2.702 kPa for the foam. The strain of the two specimens is shown only up to 5 mm/mm, because the specimens started to slip at elongations greater than 600%. The tensile strength of Ecoflex is 1.379 MPa and the elongation at break is 900%. These tests verify that the Ecoflex 00-30 has a higher stiffness than the poroelastic foam. The Ecoflex 00-30 therefore serves as a semi-rigid encasing structure for the foam to expand within. The foam must expand at a higher rate than the Ecoflex, so that the pores inside can be filled as air travels along the length of the actuator. At high pressures, the foam may stretch to its breaking point, and leave an empty space within the actuator where the fluid aggregates temporarily.

Table 4.2: Force exerted at maximum deflection by the legs closest and furthest from the inlet, when actuated by air at 20 psi. Essentially no force was exerted by the last leg in the 5- and 9- legged foam actuators. ($\overline{x} \pm \sigma_x; n = 4$).

Actuator	First Leg [N]	Last Leg [N]
3-Finger Actuator	0.508±0.008	0.105±0.008
5-Finger Actuator	0.432±0.012	-
9-Finger Actuator	0.434±0.029	-

4.2.2 Actuator Force

We adopted a setup similar to that shown in Fig. 4.1b. A scale placed underneath the legs allowed us to measure the force exerted by each leg when pressurized by air. Table 4.2 shows the results of these tests. In the 3-legged actuator, the greatest amount of force produced by the first leg was 0.508±0.008 N, compared to 0.105±0.008 N by the last leg. Actuators with 5 and 9 legs have very small deflections at the last leg, below the resolution of our measurement techniques, and therefore are unlisted. We similarly tested the force application when the actuator was pressurized with water. However, due to the high viscosity of water, the legs expanded slowly and slipped over the scale of the actuator resulting in inaccurate data collection. Consequently, this data is not reported here.

4.2.3 Actuator Deflection

The individual leg deflection trajectory is controlled though a embedded custom strain layer. The strain layer is a non-woven nylon fabric cut to both wrap around the individual leg and direct the actuator's motion (Fig.4.1c). The strain

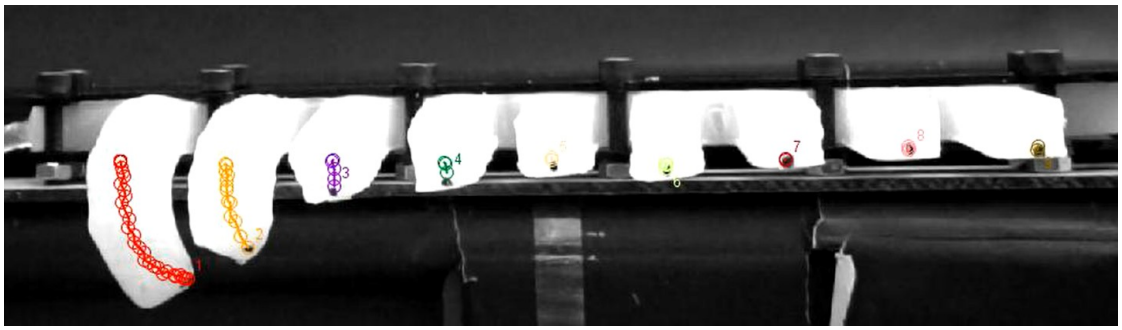

Figure 4.4: The motion of the legs consist of bending and twisting, controlled by the design of an embedded custom strain layer

layer was designed to produce bending and twisting, both necessary to achieve locomotion (Fig. 4.4). The angle of the slit controls twisting and the width of the slits control bending. These parameter can be further adjusted and tested to achieve faster locomotion.

The maximum vertical deflection of each leg in the three actuator designs is observed when inflated with air (Table 4.3) and when inflated with water (Table 4.4). Figs. 7.1, 4.5, and 4.6 show that the maximum deflection of the legs exhibit an exponential decay as a function of the leg's distance from the inlet. Fluidic resistance causes a decrease in pressure in each consecutive leg, therefore over limited-time pressurization, the back legs do not experience the same maximum pressure as the legs closer to the inlet. The vertical deflection, a result of the pressure within the individual leg, decreases in each leg from the inlet.

Discrepancies in the decay of the maximum vertical deflection for the 5-legged actuator is due in part to imperfections in the fabrication procedure. A difference in the layer thickness of the Ecoflex in any of the steps described in Sec. 5.1 can result in slightly higher straining on one side. At higher pressures, these imperfections can cause rips in the Ecoflex, rendering the actuator useless.

Notice also how the number of legs correlates with the time it takes legs

Table 4.3: Maximum deflection, d_{max}, and velocity, v_{max}, exhibited by each leg in the three actuators when inflated with air at 20 psi. L1 refers to the extruded segment closest to the inlet and L9 refers to the extruded segment farthest away from the inlet.

Leg no.	3		5		9	
	d_{max} [mm]	v_{max} [mm/s]	d_{max} [mm]	v_{max} [mm/s]	d_{max} [mm]	v_{max} [mm/s]
L1	41.28	563.22	49.00	363.73	40.69	352.35
L2	-	-	-	-	29.03	195.1
L3	-	-	25.45	128.42	18.14	84.18
L4	-	-	-	-	13.46	61.21
L5	27.36	140.06	22.23	125.88	4.42	22.96
L6	-	-	-	-	3.63	10.52
L7	-	-	9.58	52.00	2.87	9.19
L8	-	-	-	-	3.63	6.12
L9	12.95	72.49	6.30	42.88	1.57	7.65

Table 4.4: Maximum deflection, d_{max}, and velocity, v_{max}, exhibited by each leg in the three actuators when inflated with water at 3.24 ± 0.12 mL/s. L1 refers to the extruded segment closest to the inlet and L9 refers to the extruded segment farthest away from the inlet.

Leg no.	3		5		9	
	d_{max} [mm]	v_{max} [mm/s]	d_{max} [mm]	v_{max} [mm/s]	d_{max} [mm]	v_{max} [mm/s]
L1	34.01	22.96	35.26	14.287	32.61	17.91
L2	-	-	-	-	28.68	12.98
L3	-	-	20.84	3.90	24.46	3.81
L4	-	-	-	-	22.81	3.43
L5	16.56	5.64	17.191	3.33	21.18	2.31
L6	-	-	-	-	21.18	2.13
L7	-	-	18.74	2.49	17.91	1.50
L8	-	-	-	-	18.26	1.83
L9	23.57	7.98	17.86	1.25	18.59	1.80

further from the inlet to equalize to ambient pressure. In the 9-legged actuator all legs return to 0mm deflection in one second, shown in Fig. **??**; whereas the legs further from the inlet take longer to equalize pressure when more legs are present (Figs. 4.5 and 4.6). Again, this is due to the fact that the designs with less legs reached higher pressures within the 325ms applied pulse.

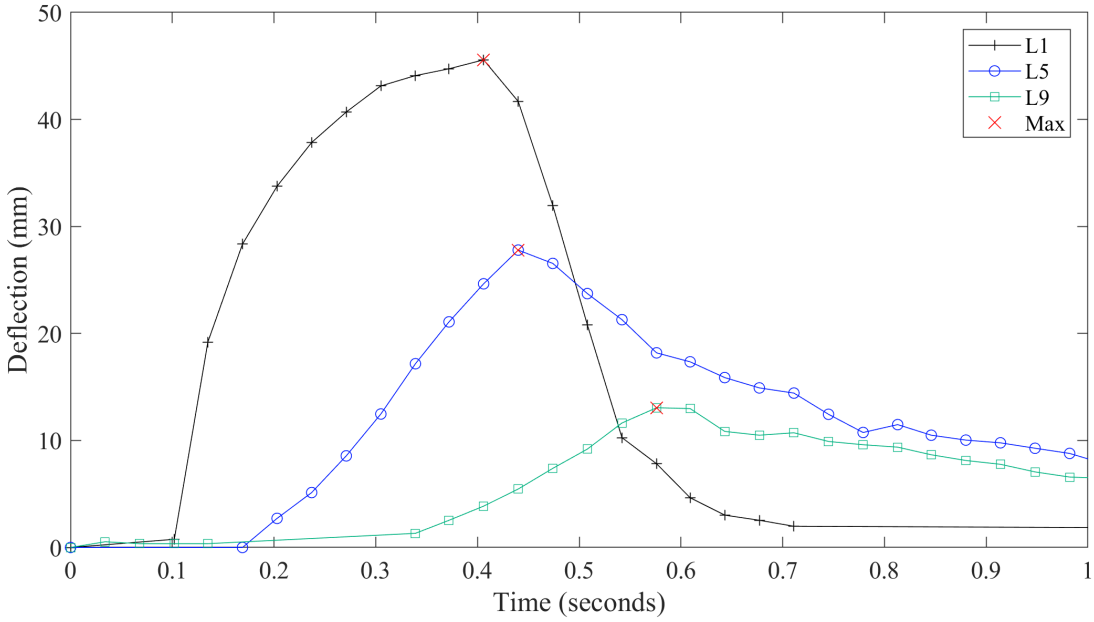

Figure 4.5: 3 legs, traveling wave.

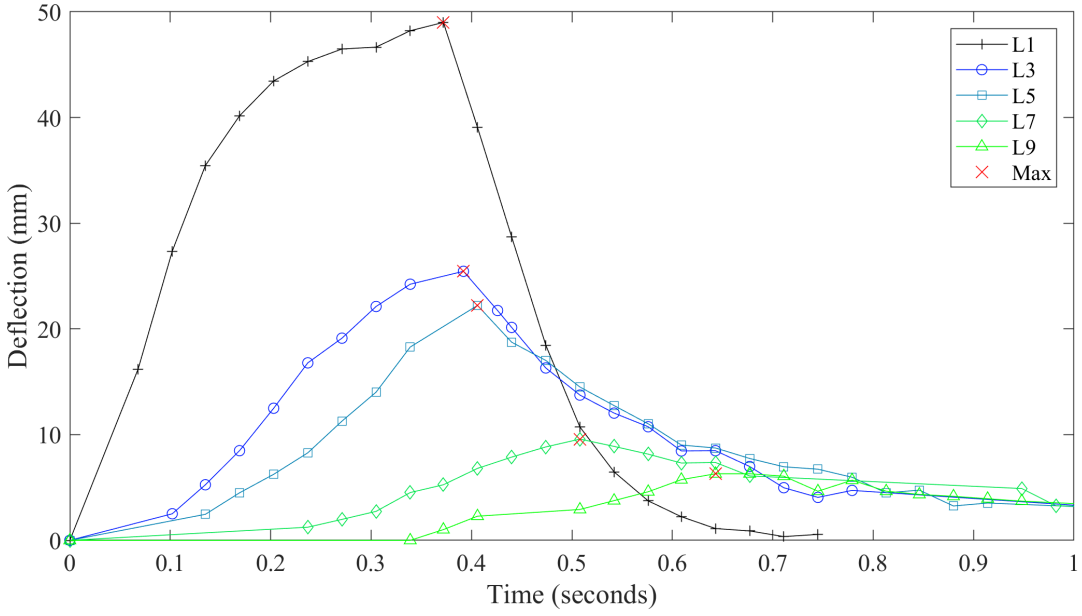

Figure 4.6: 5 legs, traveling wave.

4.3 Robot Demonstration

To demonstrate proof-of-concept locomotion, we added two 3-legged actuators to either side of a rigid backbone. We do not show locomotion with 5-and 9-legged actuators since only very minor forward locomotion is exhibited due in part to increased actuator weight and in part to exponentially decaying deflections. The 3-legged actuator were coupled through 1/16" tubes and pressurized with air through a pump at 16.5 psi. Each pulse of air lasts 325ms, separated by 1000ms deflation cycles. In this experiment the robot travels 39 mm over 6 min (Fig. 4.7). The traveling wave creates a frictional contact differential throughout the length of the actuators, allowing them to crawl forward (Fig. 4.8). Observe in Figure 4.5, how the leg closest to the inlet first exhibits maximum deflection (0.4s), bending down and backwards to drag the hind body along; then as the front leg deflates, the hind leg achieves maximum deflection (0.58s) which causes enough friction to keep the front stationary.

To test whether the motion was indeed caused by the traveling wave, and not just the asymmetric strain limiting layers incorporated into the legs, we created a separate actuator in which the foam was replaced with an empty chamber. In this version, all legs inflated simultaneously and by the same amount due to the negligible fluid resistance. Over five inflation/deflation cycles the robot did not produce any forward locomotion, compared to 7.3mm that the robot with foam walked.

Furthermore, we examined how much the inflation of the hind legs aid the locomotion speed of the robot. To do this, we added a zip tie around the actuator just after the first legs, cutting off all other legs from pressurization. This in

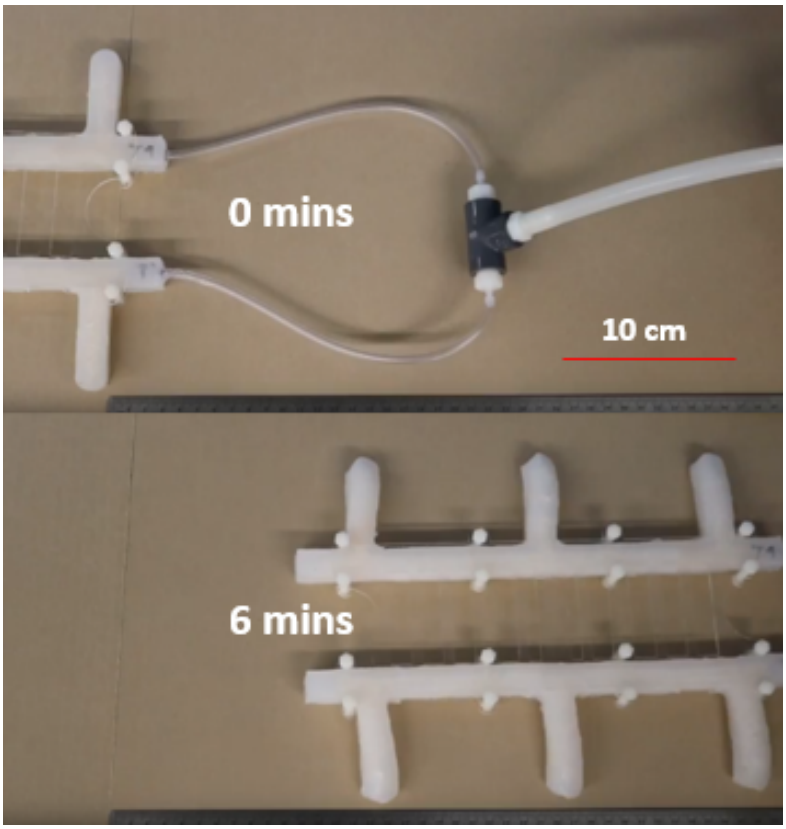

Figure 4.7: Two soft robotic actuators attached to a rigid backbone crawl forward at a rate of approximately 1.1 mm/s for a period of six minutes.

turn means that the majority of the actuator remains limp while the first legs provide force to move the robot forward. When inflated at 8 psi, the actuator moves forward a distance of 15 cm over three minutes, resulting in a velocity of approximately 0.83 mm/s. By comparing this number to the locomotion of the full robot (1.1 mm/s), we see that the last four legs increase the speed by 32.5%.

It should be noted that the undisturbed 3-legged actuators were inflated at 16.5 psi; however, due to foam resistance and splitting of the airway between the spine and the first leg, it can be assumed that at the beginning of the pulse the first leg is actually pressurized at 8.25 psi, half the inlet pressure. A number of parameters can be adjusted to improve the robot's locomotive speed including foam porosity, number of legs, and material strain. Another set of variables

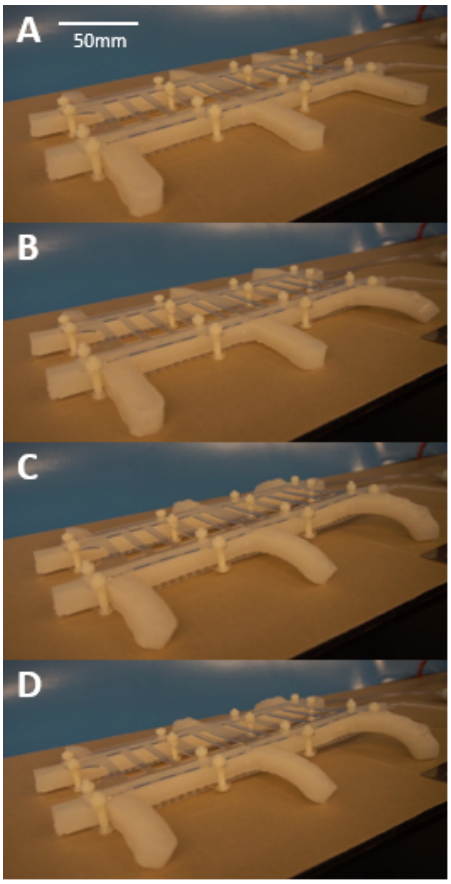

Figure 4.8: The undulating wave in four steps: A) $t = 0$. There is no actuation in any of the legs. B) $t = 166.7\ ms$. L1 is approaching peak actuation. C) $t = 333.3\ ms$. L1 is at peak actuation, L5 is approaching peak actuation, and L9 is starting to actuate. D) $t = 466.7\ ms$. L1 is approaching zero actuation, L5 is post peak actuation, L9 is at peak actuation.

that can be optimized are the inflation cycle parameters (i.e. pressure, inflation time, deflation time). It should be noted that a careful combination of these parameters is necessary to avoid failure from the build up of high pressures within the actuator.

4.4 Conclusions

Many robotic implementations can benefit from reduced complexity. Here, we have shown that poroelastic foams may be useful in reducing the number of additional components (pumps, valves, embedded controllers) necessary to produce intricate motions. Fluid resistance in the foams is exploited to produce traveling waves, even though only a single inlet pressure is applied to the actuator.

The determining factors in the flow rate of a fluid throughout the length of the foam include foam shape, foam porosity, number of extruding sections of foam, the inlet pressure, and fluid viscosity. In this paper we examined the effect of the volume of foam and the fluid viscosity. The optimal settings for the remaining parameters were manually estimated. We showed that with careful design considerations, it is possible to produce repeatable traveling wave motions along the length of the actuator. The length of the spine as well as position and number of extruding legs determine the velocity of the traveling wave, the maximum deflection and force exerted by individual legs, and, as a result, the forward velocity of the robot when used for locomotion.

The embodied control methodology proposed lends itself to a great variety of future applications. Next, we intend to focus on simpler fabrication methods and validated models to further enhance the design of embodied intelligent soft robots that can exhibit complex motions with simple drivers and control.

CHAPTER 5

SIMPLE LOW-COST FABRICATION OF SOFT SENSORS FOR SHAPE RECONSTRUCTION AND TOUCH LOCALIZATION

Soft sensors are an active area of research with diverse applications, many of which require repeatable interactions with fragile and irregular objects [7]. This has prompted demonstrations of materials with mechanical, chemical, and electrical response to changes in stretch, pressure and temperature [71] in search of durable, compliant and highly stretchable sensors. Materials like, e.g., polydimethylsiloxane [145] and silicone elastomers [9] have become popular choices, and a variety of fabrication techniques such as micro- and nano-contact patterning [121] and passivation techniques [52] are often applied to synthesize novel robotic sensors. The majority of these techniques, however, require prior knowledge and experience, which raises the barrier of entry to the field. To enable a greater number of researchers to customize soft sensors for their respective applications, it is important to minimize the cost of sensors and introduce fast, easily accessible fabrication.

Towards this end, we present a soft, low-cost sensor with a simple fabrication procedure that has high manufacturing tolerances; requires no advanced equipment, control sequences, or data processing; and can easily be customized for various applications.

We show that a specific ratio of inexpensive carbon black mixed by hand with an uncured silicone elastomer enables conductivity at high stretch. Furthermore, this gel has a high viscocity and is less prone to leakage compared to other popular conductive fluids such as Eutectic Gallium-Indium (EGaIn) [174]. We show how sensors using this composite can be made by non-experts in hours

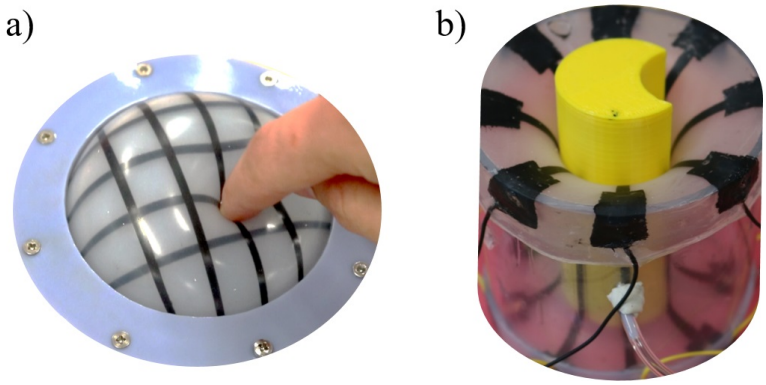

Figure 5.1: We aim to lower the barrier of entry to soft sensors through simple fabrication, control, and data processing. We demonstrate our concept in two devices: (a) a tactile interface for contact sensing, and (b) a sensitive, pneumatic gripper which can estimate the 2D shape of an encompassed object.

without expensive equipment. We demonstrate the customizability of the sensors through two devices: a passive sensor capable of detecting touch on the surface of an inflated membrane, as well as a sensitive pneumatic gripper that can encapsulate an object and stretch around its convex and concave features (Fig. 5.1). Using the latter, we show that object geometry can be estimated using a simple control sequence based on constant rate of inflation. To avoid issues with material buckling, we operate the gripper primarily in negative pressure such that the material is always experiencing stretch. Finally, despite the differences in the individual sensors, we further show that we can estimate the object shape, simply by normalizing the sensor response and identifying when the channels come into contact with the encompassed object.

Specifically, this paper presents the following contributions: 1) a widely accessible and low-cost fabrication procedure for a stretchable strain sensor composed of a carbon conductive filler embedded in a soft elastomeric matrix (Sec. 5.1); 2) characterization of the durability of sensor over the course of 15 days and repeatability over the course of 30 inflation cycles; 3) demonstra-

tion of a dynamic, soft tactile grid with multiple sensor channels (Sec. 5.2); 4) demonstration of 2D convex and concave shape reconstruction using a soft encompassing sensor, operating in negative and positive pressure with a simple control procedure (Sec. 5.3); and 5) a simple computational method for shape reconstruction that overcomes the individual differences between the low cost sensors. Through this work, we hope to make soft sensors and robots more widely accessible, enabling deployment in a broad range of applications.

5.1 Fabrication and Sensor Characterization

The following sections describe the design and fabrication procedures for the conductive composite and a single stretchable sensor. We further discuss two characterization tests of a sensor to demonstrate its resistive response to stretch.

5.1.1 Carbon Black Composite Preparation

Consumer demand is driving research to combine the flexibility of silicone materials and electrical properties of conductive filler materials for a variety of applications [32]. Silicone rubbers have great elongation and tensile strength, and offer good resistance to humidity and temperature. However, like most polymers, they are electrically insulating at low voltage due to the nonavailability of delocalized electrons. The majority of conductive composites are produced by adding conductive fillers, such as carbon black [192], carbon nanoparticles[88] and nanotubes [34], graphene sheets [184], graphene nanoplates [142] and silver nanoparticles [34].

One of the factors that determines a composite's conductivity and the percolation threshold is the concentration of the added conductive filler [192]. For expensive fillers such as silver nanoparticles and carbon nanotubes, concentrations that reach the percolation threshold are costly. In addition, achieving a homogeneous and stable dispersion of the filler is crucial to create the network for electrical transfer, and usually requires a polar aprotic solvent to assist the dispersion [244]. A variety of dispersion methods [192] and dispersing solvents have been developed [106] to improve this process. Unfortunately, these techniques can be time consuming and require expensive and high precision tools such as a ultrasonication bath and the Haake^{TM} torque rheometer.

To address these issues, we demonstrate a fast, simple, accessible, and inexpensive fabrication technique which yields adequate conductivity for stretch up to 135%. To lower cost, we chose to disperse low grade carbon black into Ecoflex^{TM} 00-30 Part A, and embed it into a support material of cured Ecoflex^{TM} 00-10. Such carbon composites have previously been demonstrated to have high conductivity at up to 500% stretch [175]. Because the conductive gel is not cured, it is possible that Ecoflex silicone with a different shore hardness would work equally well. We conducted a pilot experiment with a carbon black powder (VULCAN XC72R) to Ecoflex ^{TM} mass ratio of 1:7 based on the electrical conductivity reported in [233]. We mixed the carbon black powder into Ecoflex ^{TM} 00-30 Part A with ethyl acetate as the dispersing agent. To further aid the dispersion of conductive carbon black powder, we applied ~3 hours of continuous stirring at 100 rpm. No additional step is needed to remove the residual dispersing agent from the composite due to the low boiling point of ethyl acetate of 77.1 °C. To give an example, a volume of our composite the size of a quarter US coin costs 0.145 USD, as compared to 44.64 USD using EGaIn. Although EGaIn is a liquid

metal at room temperature and can be used in smaller quantities which lowers the cost of the sensor, our technique is inexpensive, fast, leak-proof, and requires no prior training because operating high-precision equipment is not needed.

In pursuit of an even simpler and faster fabrication technique, we eliminated the use of the dispersing solvent and compensated by increasing the filler concentration. We increased the carbon black to Ecoflex™ ratio to 1:6 and mixed it by hand for several minutes. Doing this resulted in an uncured conductive gel that can be spread onto a polymer surface in a thin layer, as discussed in Sec. 5.1.2. The cost of making a quarter coin-sized conductive composite with this technique is only 0.12 USD, saving an additional 18% compared to the pilot experiment. This simplified conductive composite fabrication technique requires no specialized equipment, takes only a few minutes, and is orders of magnitude faster than other common approaches.

5.1.2 Single Sensor Fabrication

Fig. 5.2 shows the process for embedding the carbon composite in Ecoflex™ gel to fabricate single sensors. First, we pour a 1 mm thick base layer Ecoflex™ rubber mixed 1A:1B by weight into a mold. To eliminate entrapped air, we vacuum degas the mixture before pouring. We cure the silicone for approximately 2 hours at room temperature, or speed up the process by using an oven at 70°C. After the silicone has cured, we cover it with a laser-cut stencil which is 0.8 mm in thickness. The stencil is 2 mm wide and corresponds to the width of the sensor. Note that the laser cutter was used for ease, but this stencil could easily have been cut by hand given its dimensions. Two copper electrodes (20 mm ×

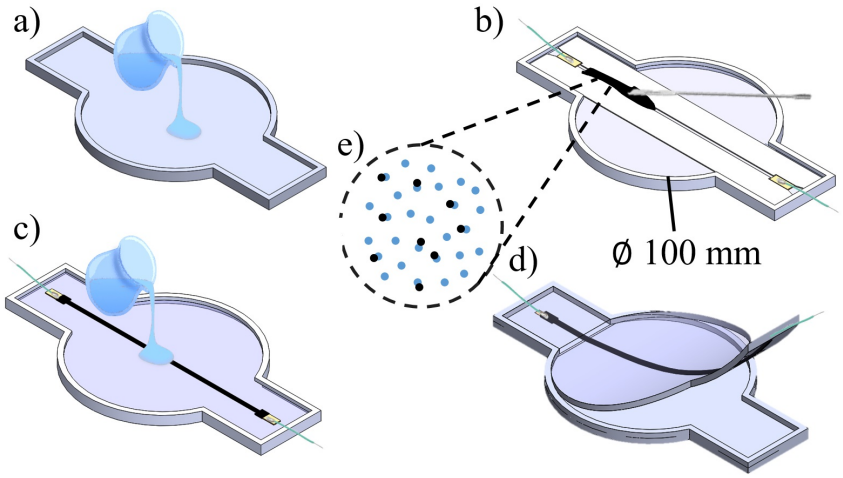

Figure 5.2: Fabrication of a single sensor: a) 15 g of Ecoflex™ 00-10 mixture is poured into a mold to form a layer of 1 mm thickness. b) The cured Ecoflex is covered with a mask and the Carbon Black composite is spread across the channel. c) The mask is peeled off leaving a conductive sensor channel and a second layer of 10 g of Ecoflex™ 00-10 mixture is poured. d) The membrane is slowly peeled from the mold. e) The carbon composite is composed of a 1:6 mass ratio of Carbon Black powder to Ecoflex™ 00-30.

5 mm) with wire leads are glued onto the base layer at the ends of the stencil using Sil-Poxy™ silicone adhesive. Next, using a micro-spatula, the conductive composite is spread over the stencil, connecting to the copper electrodes. The stencil is then peeled off and another layer of 1 mm thick Ecoflex™ rubber is poured on top. The end product is a single channel of conductive composite embedded in translucent support material. The entire fabrication process can be finished without the use of expensive equipment or advanced tools in less than 5 hours; 4 of which are curing time. Note that since the polymer is cured in a shallow mold, the vacuum chamber step can be skipped by simply pouring the silicone in a thin layer and popping remaining bubbles by hand with a sharp instrument.

5.1.3 Sensor Characterization

To demonstrate the robustness of the sensor, we first characterize its durability by inflating it once per day for 15 days, and then its repeatability over 30 inflation cycles. Both properties are important to long-term operation of the sensors which is critical in many applications.

The experimental setup for the sensor characterization tests is shown in Fig. 5.3a-c. We characterized the single sensor by placing it under a circular clamp with a diameter of 85 mm and inflating it into a dome structure at approximately 50 mL / s. We inflate the membrane for 2 s, hold the pressure for 5 s, and then deflate at the same rate for 2 s. We then wrote a Matlab®-program to automatically extract the outline of the inflating dome and in turn, the strain experienced by the sensor during inflation and deflation. The stretch of the membrane is calculated by dividing the length of the outline of the inflated dome over the initial length of the membrane, which peaks at 135%. The sensor responses were normalized by subtracting and dividing by the initial resistance value recorded before actuation, i.e. while the sensor is not pressurized and not experiencing stretch.

In Fig. 5.3d, we show the sensor response over an inflation-deflation cycle. We see that the resistance increases and decreases shortly before the 2 s inflation ends. When the pressure is held constant, the resistance decreases as the polymer relaxes (shaded in green). After the initial relaxation, the resistance remains constant as we hold the strain for 5 s. When we start deflation, the resistance increases (shaded in yellow) and then decreases as the strain on the sensor reduces. We have yet to determine the cause for the temporary increase in resistance, however, the effect is apparent and similar in all of our tests.

To characterize durability we tested 4 membranes once a day for 15 days (Fig. 5.3.e). The plot indicates several phenomena: 1) nonlinear increase in resistance with increasing stretch. We suspect that the non-linearity can be attributed to the relaxation effect combined with slight fluctuations in the inflation rate. 2) As the membrane deflates, the resistance first increases (largely due to the temporary increase in resistance discussed above), and then decreases with decreasing stretch. 3) Although the sensors generally behave the same, their raw response has significant variation. This occurs due to the manual and simple fabrication process; in Sec. 5.3.3 we show how to account for these differences to perform shape reconstruction. 4) Finally, we see that each sensor is fairly durable with a relatively low average standard deviation of 0.11 (Ω/Ω) across all days.

Fig. 5.3.f shows the signal response over 30 successive measurements, i.e. the repeatability of three sensors. Between each cycle we wait 2 min to mitigate effects from the visco-elastic relaxation. As the dome inflates, the resistance increases, reflecting the increase in stretch almost linearly. During deflation, the change in resistance is almost symmetric around the peak, and we use this symmetric property to identify the point of contact with objects as described in Sec. 5.3.3. Again, we see relatively low standard deviation over the 60 trials.

5.2 Tactile Grid

The fabrication of the tactile grid sensor is graphically represented in Fig. 5.4. Using the same method described in Sec. 5.1.2, we embed two perpendicular sets of 4 conductive channels in three layers of 160 mm $\times$ 160 mm $\times$ 1 mm sub-

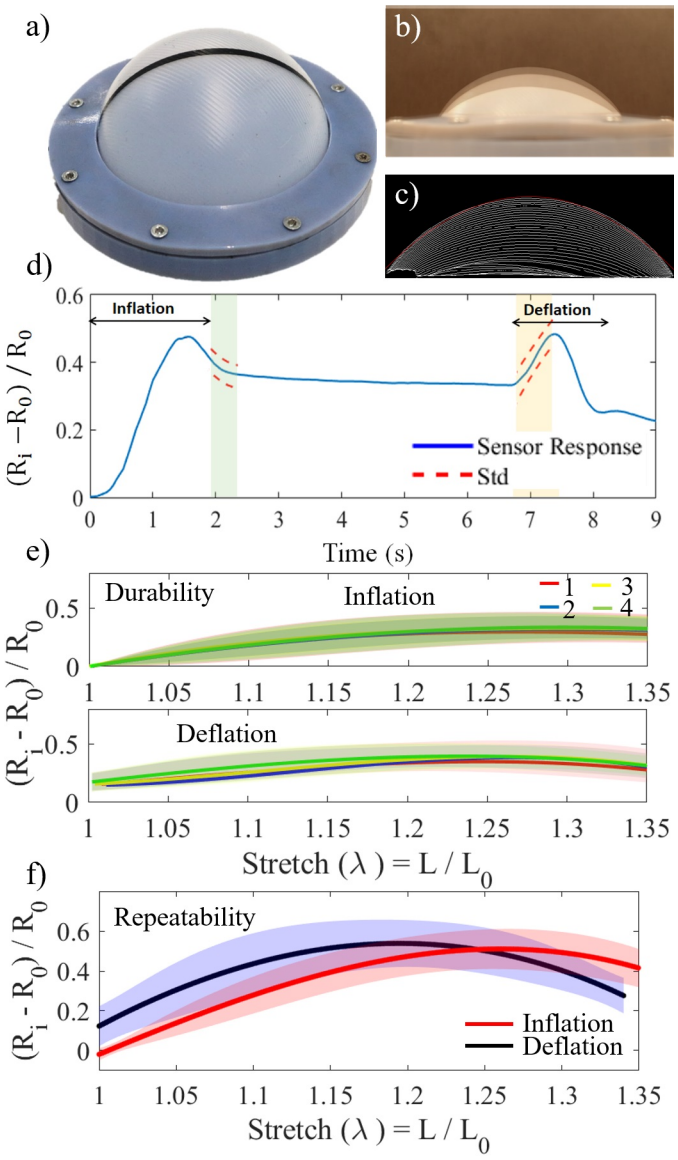

Figure 5.3: a) Setup used to characterize a single sensor. b) Overlaid snapshots of a sensor membrane during inflation. c) Matlab®-generated plot to detect the membrane outline, i.e. membrane stretch, during inflation. d) An example of the resistive response (blue) of a single sensor through one inflation-hold-deflation cycle. The red dashed line indicates the standard deviation over 15 days, during relaxation (green shaded region) and at the beginning of deflation (yellow shaded region). e) Durability test of four separate sensors over 15 days. f) Repeatability test of three sensors over 30 inflation cycles. The solid curve denotes the average resistance during inflation and deflation; the shaded regions are the standard deviations.

strate. We then constrain the membrane by an 85 mm-diameter circular clamp and inflate it with 50 mL of air. The entire process took less than 7 hours; 6 hours of which was for curing.

To demonstrate the use of the tactile grid, a user sequentially pressed on various regions of the inflated membrane. Specifically, we pressed on the six locations shown in Fig. 5.4a-b. Note that because of the simple fabrication procedure, all sensor channels experience different initial resistance and behaviors. We counteract this, simply by subtracting their resistance at rest and normalizing by this amount. Here, we automatically determine which grid cell is being perturbed by looking at the two sensor channels with the sharpest increase in electrical resistance. Obviously, both the sensor and the data processing can be optimized depending on the specific application, which may include soft user interfaces, wearable devices, and more.

5.3 Sensitive, Pneumatic Gripper

Although many recent papers discuss how soft robots may distinguish geometric shapes from one another [73], few touch on the challenge of actually measuring the object geometry [220]. The majority of these soft robots require active control and sophisticated analysis of the sensor so that it traces around the edge of the object. Other examples include soft sensors applied to augmented reality, where, e.g., haptic devices must give information about a virtual object's shape and texture [93]. Here, we describe a simple alternative to shape reconstruction.

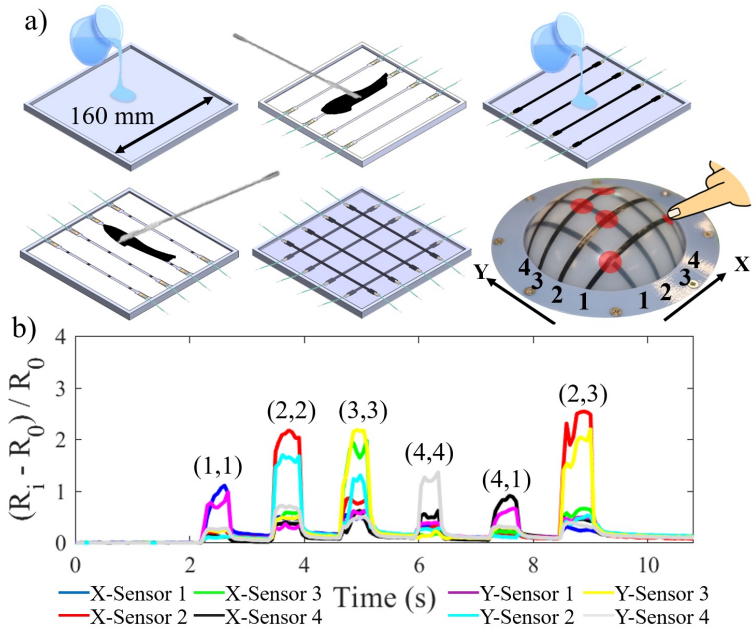

Figure 5.4: a) Fabrication procedure of a tactile grid. b) Resistive response to perturbations; touch location can be pinpointed simply by looking for the sharpest increases in resistance.

5.3.1 Fabrication

Fig. 5.5 shows the steps needed to fabricate the soft gripper. Using the same method as fabricating a single carbon composite stretchable sensor, we embed 8 channels in a 160 mm × 115 mm × 2 mm substrate. We fold it into a cylindrical envelope and seal the rim with Ecoflex™ 00-10 mixture. This envelope is wrapped onto an acrylic cylinder (100 mm in height and 50 mm radius) to form an airtight gripper. We then insert a flexible tube for pneumatic actuation. Note, that the syringe pump was used for experimental ease, but the inflation could also have been done by hand. The total fabrication time for the gripper array was no more than 5 hours from start to completion.

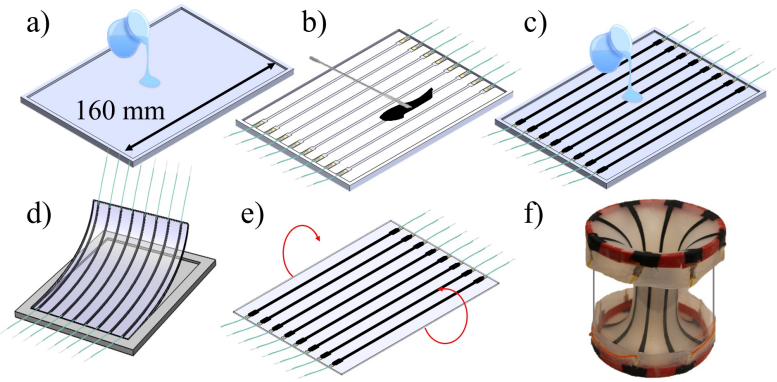

Figure 5.5: Fabrication of the encapsulating sensor. a) 25 g of Ecoflex™ 00-10 is poured into a rectangular mold to form a 1 mm thickness. b) After the silicone has set, we laser cut a stencil with sensor patterns and place it on top of the silicone. The Carbon composite is spread across the laser cut mask and over the electrodes. c) The mask is peeled off and a second layer of 25 g of Ecoflex™ 00-10 is poured. d) The membrane is peeled off from its mold. e) The membrane is folded along its long axis and 1 g of Ecoflex™ 00-10 is applied to join the two edges. f) The encapsulating sensor is made by wrapping the edges around a Plexiglass cylinder and attaching a tube for actuation.The gripper is resting at ambient pressure.

5.3.2 Operation

We use a syringe pump to actuate the pneumatic gripper at the speed of 50 mL / s, causing a change in stretch at the same order of that used in the characterization of the single sensor (Sec. 5.1.3). Note that using inflation alone would cause the material to buckle inwards, which would complicate sensor response and consequently the shape reconstruction (Fig. 5.6a). Instead, we avoid sensor buckling by only using the membrane under stretch. To sense the geometry of an encompassed object, we therefore conduct the following steps also shown in Fig. 5.6b-d: (1) we deflate the gripper for 5 s to reach negative pressure, dilating the center of the gripper; (2) we hold a negative pressure for 5 s, during which we insert the object to be measured; (3) we then inflate for 6 seconds, allowing the gripper to encompass the object fully. Pressure inside the gripper goes from

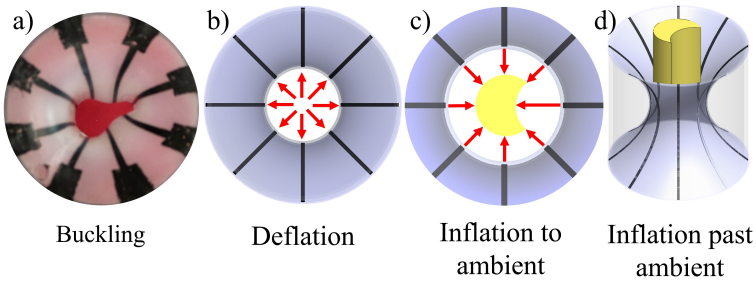

Figure 5.6: a) When the gripper is inflated past ambient, it risks buckling which complicates data processing. b-d) Top and isometric views of the gripper as it measures an extruded (yellow) shape with convex and concave features. The red arrows indicate direction of motion.

ambient to negative (deflation and hold), to ambient and then positive pressure (inflation) subsequently.

The inner diameter of the gripper is 42 mm when fully deflated and is 30 mm when it reaches ambient. The range of the diameter of objects we can measure is therefore 30 mm to 42 mm. Fig. 5.7 shows how the inner diameter of the gripper changes during a sensing cycle. The radius of the opening increases and decreases almost linearly with time during deflation ($v_d = \Delta R/t = 1.54$ mm / s) and inflation ($v_i = \Delta R/t = 2.12$ mm / s). We use this property later when we estimate the shape of the object.

5.3.3 Shape Estimation

Next, we demonstrate the ability of the gripper to measure convex cylinders of different diameters, as well as a cylinder with a concave feature similar to a crescent moon shape. We use a motor-actuated syringe to keep the speed of the inflation at 50 mL / s, the same as the sensor characterization tests, such that we can expect similar behaviour of the membrane.

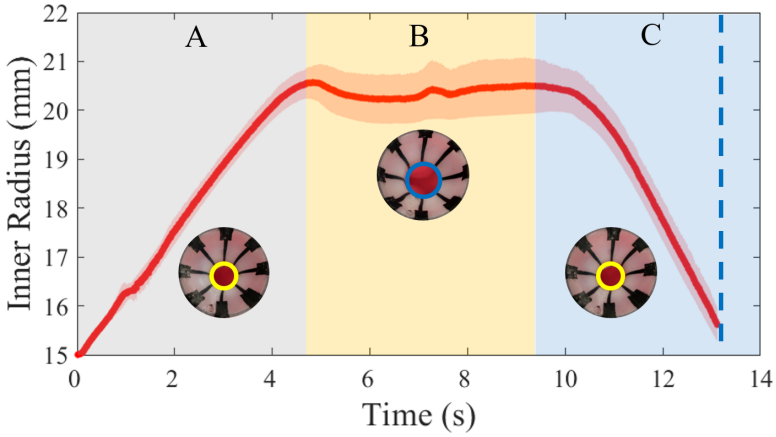

Figure 5.7: Measurement of the inner radius of the gripper during a deflation(A)-hold(B)-inflation(C) cycle. The red curve shows the average of five cycles; the shaded region the standard deviation. The blue dashed line represents the point at which the gripper begins to buckle as shown in Fig. 5.6a.

To measure the size of an encompassed cylinder, we simply measure the rate of change in resistance, ΔR, in each sensor channel at a rate of 136 samples per second. During ambient to inflation, the sensors experience increasing stretch which causes increasing resistance; however, as the sensors come into contact with the object, ΔR decreases significantly because the sensor no longer stretches and instead is compressed against the object surface. We automatically determine when ΔR changes. Specifically, we look at the readings during inflation (between 10 to 16 s), smooth the curve using a running average of nine samples, and then identify the peak in resistance, i.e. when the slopes of the smoothed resistance curves cross zero during inflation. We approximate the distance traveled by the sensor as the product of v_i and total inflation time. Using the speed of inflation estimated from the experiment in Fig 5.7, we can estimate the traversed distance of each channel. By focusing on when ΔR changes, rather than the actual resistance value, we bypass issues related to variations in sensor fabrication.

We tested this simple technique on three cylinders of diameter 30 mm, 35

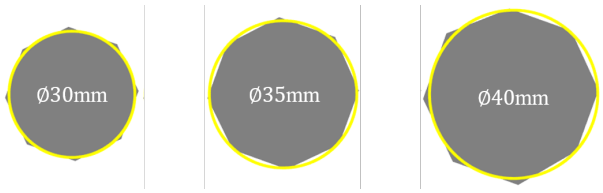

Figure 5.8: Real (yellow) and reconstructed (gray shape) outlines for circular objects with varying diameter.

mm and 40 mm. The results are shown in Fig. 5.8. In these experiments, the mean error of the sensors is 0.7 mm, with a standard deviation of 0.65 mm and a maximum error of 1.48 mm. Note, that part of this error could be caused by a slight off-center placement of the object.

To demonstrate the ability of the technique to identify concave features in the crescent moon shape, we overinflate the gripper past ambient and estimate the position of the concavity. Fig. 5.9a shows an example of the response of all eight sensors during a full deflation-hold-inflation cycle. The resistance first drops as the gripper is deflated; then remains constant as we hold the pressure; and finally increases as we inflate the gripper back to (and past) ambient pressure. During inflation, we notice two behaviors: the rate of resistance change drops in sensors that are in contact with the object; the rate of resistance change in sensors that have yet to reach the object exhibit a symmetric quadratic shape around its peak, which matches the rate of resistance change with stretch characterized in Sec. 5.1.3. To find the latter automatically, we fit second-order polynomials to the data 0.25 seconds before and after the peaks (shown in Fig. 5.9b), and identify the one with the highest symmetry.

Fig. 5.9.c shows the reconstructed shape of the crescent moon at 8 different orientations. The mean error of the sensors that are touching the crescent is 2.82 mm, with a standard deviation of 0.085 mm and a maximum error of 2.96 mm.

Note that these sensors all overestimate the size of the object, but have a small standard deviation. The sensor accuracy could therefore be improved simply by subtracting this offset. In all eight tests, we are able to correctly identify the position of the cavity, however, these sensors have a much higher mean error of 7.26 mm. This happens because at 13 s the membrane starts bulging and buckling at the top and the bottom, before the sensor positioned by the cavity comes into contact with the object. Because we can only extrapolate the dimension of the object by how far the sensor has travelled towards the object, this makes the calculation erroneous. This issue could potentially be fixed by changing the thickness across the membrane so that the bulging occurs later.

Finally, although we only focus on rigid objects here, we hypothesize that the sensors may also work for soft or compliant objects, if their effective stiffness coefficient is more than or equal to that of a fully inflated gripper. A high stiffness coefficient will ensure that the encompassing the membrane of sensor will inflate around the object's perimeter and conform to its circumferential geometry.

5.4 Conclusion

In this paper, we showed a shape reconstruction technique based on simple, accessible fabrication methods, supported by customized mechanical implementations for simple control and processing. We demonstrated that its characteristics persist over multiple inflation cycles and as the sensor ages. Finally, we showed how it could be easily customized to fit the need of the user through a passive tactile array and a gripper for active shape recognition. The main

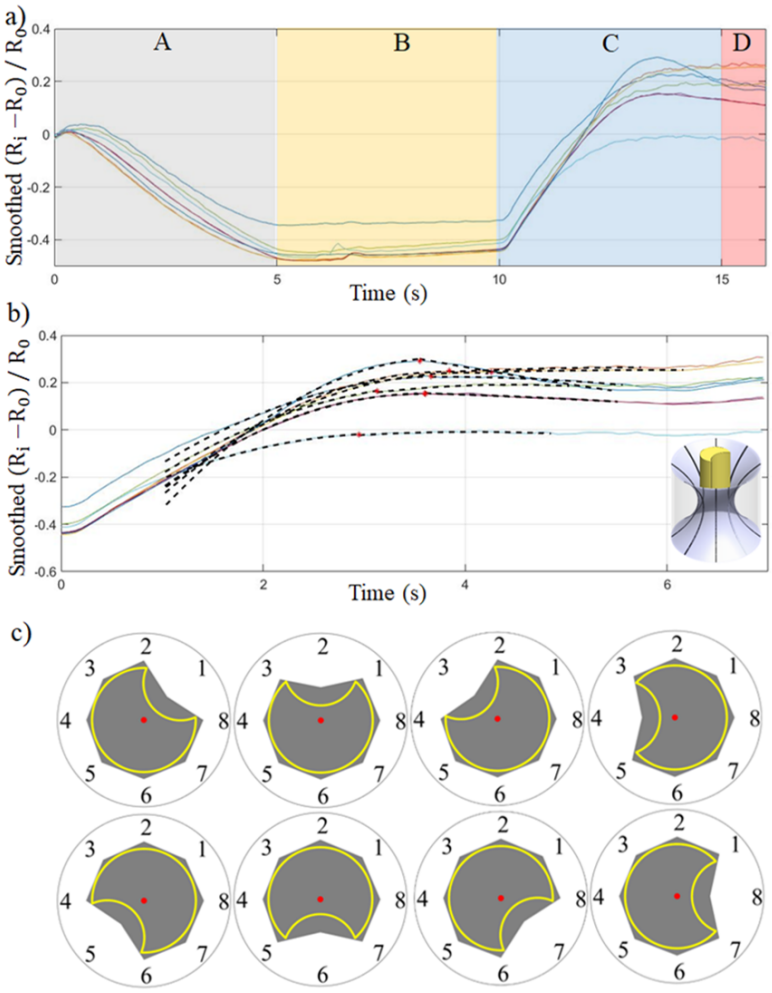

Figure 5.9: a) Sensor responses during a deflation (A) - hold (B) - inflation (C & D) cycle around a crescent moon shape. Membrane buckling occurs in (D) at the end of inflation. The object is inserted during the hold phase near 6 s. b) By looking at the symmetric tendency around the peaks in the curve (marked in red), we can identify which sensor is located by the cavity. c) Real (yellow) and reconstructed (gray shape) outlines of a concave object in eight different orientations.

contribution of our work is to make these sensors more easily adopted (and developed) by a wide range of researchers and users. The simple customized platforms we have shown, can be built upon to achieve better performance or behavior depending on the particular use case.

CHAPTER 6

COMPLIANT AND SELF-RECONFIGURABLE MODULAR ROBOTS

Modular self-reconfigurable robots are composed of active modules capable of rearranging their connection topology to adapt to dynamic environments, changing task settings, and partial failures ([236]). It is desirable to increase the number of modules to increase the potential for adaptability and redundancy, however, scaling up the collective size poses several challenges ([19]). Controllers must be capable of efficiently exploring the configuration space and providing introspection to cope with internal and external changes. The module hardware must be inexpensive and fast to produce, work reliably, and require little maintenance. Consequently, isolated efforts to develop scalable control and hardware do not necessarily result in system-level robustness. Rather, to facilitate large numbers of robots in the first place, we argue for the importance of incorporating robustness into all levels of design, and demonstrate how this approach leads to tightly co-dependent parameters across hardware and software. In this paper, we discuss our design approach, an early hardware prototype, and custom controllers. Our focus is explicitly on enabling long-term robustness of an autonomous, self-reconfigurable, modular robot through a hardware-software design cycle, with the idea that we can build on such a robust platform in the future to achieve more advanced behaviors.

Fig. 7.1A provides an overview of the measures we have taken to ensure system-level robustness, and how many of these design decisions carry over between fabrication, operation, and control. Related to the *design* itself, system robustness is mediated by 1) the simultaneous development of hardware and software; 2) ease of iterations, e.g. through realistic simulation environments

that let the designer focus on high level behaviors, as well as simple hardware that supports easy extensions; and 3) open access to permit a wide range of users and inputs. To support inexpensive, fast, and therefore *scalable fabrication* we focus on 1) simple designs with minimal components; 2) mechanical compliance to permit higher manufacturing tolerances; and 3) manufacturing rigs to support non-expert labor. These design parameters correlate with those of *scalable operation*, e.g. because 1) compliance lets modules interact safely with each other and with external objects; 2) compliance permits large scale connectivity despite poor manufacturing tolerances; and 3) hardware simplicity limits the risk of failure. Other operation-specific considerations include the ability of modules to operate, sense, and perceive independently from others; the ability to stay connected without continuous use of power; the ability of modules to move in a multitude of ways to overcome partial failures; and the potential to lower mechanical wear by omitting internally moving parts. All of these design choices warrant custom *controllers* and to support system robustness, we focus on 1) reactive (over deterministic) behaviors that could adapt to dynamic perturbations; 2) naive and simple control schemes that scale well with the number of robots; 3) minimum energy expenditure through efficient path planners; 4) connection redundancy to avoid single module failures from causing complete collective failure; and 5) enabling a large configuration space that facilitates system adaptability to unforeseen perturbations.

More specifically, we introduce a novel planar, modular robot composed of compliant modules moving in unison. We refer to the robotic modules as 'DONUts' (Deformable Self-Organizing Nomadic Units) for their visual kinship (Fig. 7.1B-D). To support simple and fast manufacturing, DONUt modules are composed of a single flexible printed circuit board (PCB) wrapped in a loop and

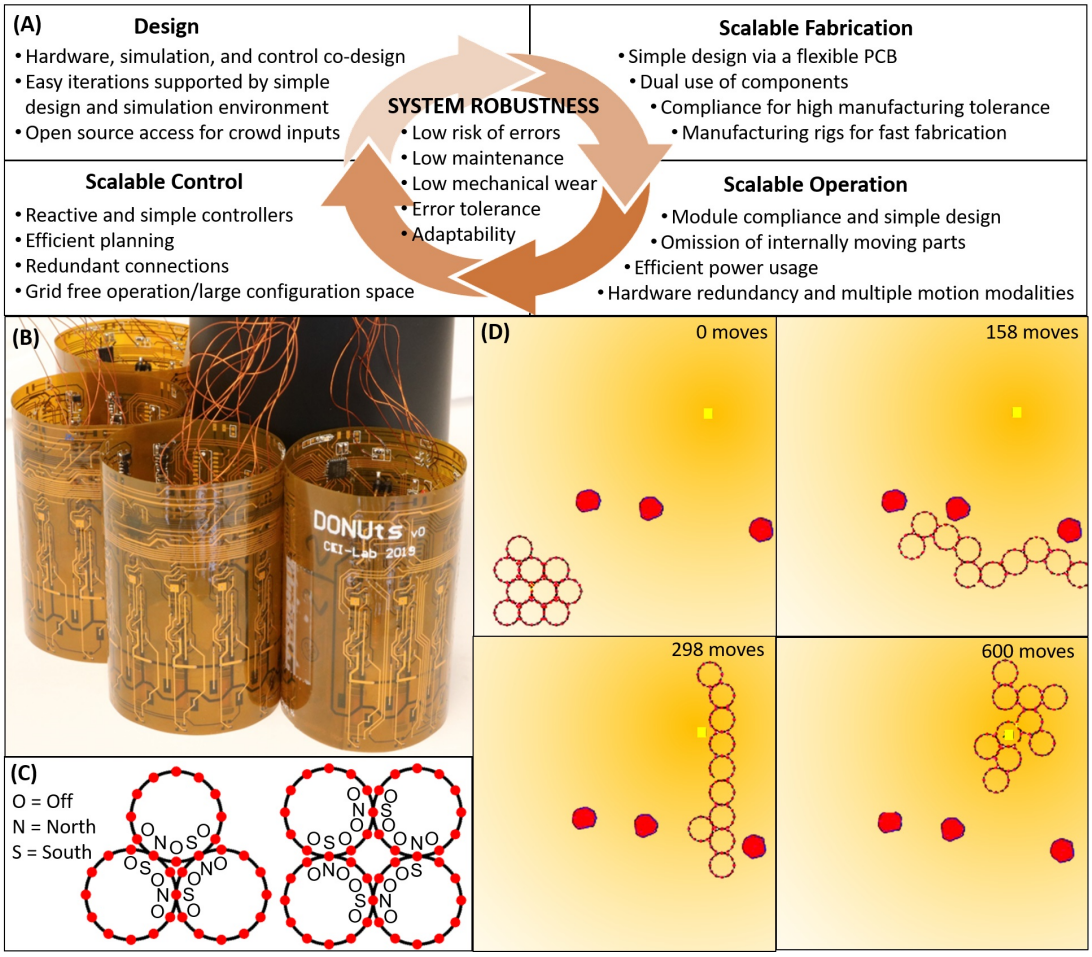

Figure 6.1: (A) Interdependent design guidelines centrally motivated by system level robustness. (B) Simulated DONUts moving along an environmental gradient, where the yellow square denotes the origin of the gradient, and the red polygons obstacles. (C) DONUt modules with onboard computation, sensing, and switchable magnets to facilitate collective communication and motion. (D) Magnets which can be switched to either polarity and off to permit a large range of configurations.

populated with sensors, actuators, processors, and room for batteries. To mitigate wear, the DONUts have no moving parts; rather, they move as a collective by activating and deactivating Simplified Electro-Permanent Magnets (SEPs) on their perimeter. These magnets can be polarized in either direction or turned off to enable a very large configuration space and consequently collective adaptability (Fig. 7.1C). Furthermore, they do not require continued application of

power to maintain polarization which saves energy. To lower fabrication cost and risk of errors, we minimize the number of components, e.g. by making double use of the PCB as a chassis and the SEPs for communication. The passive compliance introduced with the flexible PCB permits large lattice configurations despite rapid, imprecise manufacturing. The compliance and low driving voltages also enable the modules to interact safely with each other and with surrounding objects.

We further develop DONUt-specific coordination schemes, low-level primitives for module operation, as well as an open source simulation environment to support controller development. We refrain from imposing artificial constraints on module motion beyond what the hardware is capable of. This means that the modules operate in a grid-free environment and can achieve a much larger set of connection topologies to adapt to the task at hand. Towards real-world operation, we furthermore focus on reactive configurations, rather than predetermined shape transitions as is common for modular robots. Specifically, in a simulated energy harvesting scenario, we investigate how such modules may perform gradient tracking towards a light source in clutter-free and cluttered environments (Fig. 7.1D). We choose this specific task, because it supports reactive and scalable behavior and because it highlights the benefits of grid-free operation. To evaluate the performance, in terms of path efficiency, of our controllers, we compare them against paths generated by an all-knowing Oracle planner in clutter-free environments. We explore a locally optimal A* search-based controller and how we may incentivize redundant connection topologies for more error-tolerant operation. We compare this to a "naive" iterative control scheme that scales better with the number of modules in both computation and memory, finding comparable performance. We further discuss particular con-

nection topologies which may impede progress due to the hardware-specific motion constraints, and show how these may be circumvented using the naive controller. We also allude to how energy expenditure is used across modules in the collective, which is an interesting area for future work. In this paper, we focus only on centralized coordination, however, all of the methods may be adapted for decentralized coordination at the expense of communication.

Although more work is needed to demonstrate full-scale practical collective operation, the work in this paper illustrates the highly interdependent design choices that lay the foundation for a scalable and robust modular robot. The following sections detail 1) related work of both controllers and hardware; 2) a hardware prototype composed of compliant modules with individual computation, communication, sensing, and collective motion; 3) an inexpensive, quick manufacturing process for both modules and components, based on prepopulated, flexible PCBs and a rapid SEP winding mechanism; 4) a characterization of module deformation, mobility, sensing, and communication; 5) an open source kinematic simulation framework for the DONUts informed by low-level motion primitives and experimentally obtained sensor performance characteristics; and 6) a comparative study of two controllers for efficient and error-tolerant gradient tracking with the DONUts in environments without an occupancy grid.

6.1 Related Work

The framework described in this paper combines and builds on findings from many sources spanning both hardware and coordination. In the following sec-

tions, we describe these in turn.

6.1.1 Modular Robot Platforms

Past research on hardware for modular self-reconfigurable robots includes design of inexpensive and durable mechanisms for actuation, docking, communication, and power distribution ([19]). Low maintenance requirements are especially important for this class of robots, as they scale linearly with the number of modules required. Module cost and fabrication time are equally important factors, but are somewhat mitigated by the fact that unit price decreases significantly with mass fabrication. Additionally, the module weight and stiffness determines both structural stability and how many modules can be moved at once.

The majority of modular robots consist of rigid components assembled into either a fixed form factor ([41, 60, 80, 253]), or into modules which can actively deform to produce motion ([98, 81, 78, 167]). Recently, merging with soft robotics, pneumatically-driven modules with infinite degrees of (passive) freedom have also been shown ([207, 95]). These have the benefit of overcoming small manufacturing defects that otherwise scale poorly in large lattice-structures. The most successful demonstrations of these robots currently rely on traditional electro-mechanical actuators for reconfiguration, such as DC motors ([41]). However, researchers are also exploring designs that require fewer components and 1) have no internal moving parts which are prone to wear ([253, 207, 60]), 2) rely solely on collective motion over individual module mobility ([98, 60]), and 3) exploit non-mechanical latches, such as switchable magnets

([253, 57, 60]), electrostatics ([81]), and meltable plastic and alloys ([194, 130]). Note that the last two options are superior for connection strength, but require high voltage generation or power usage, respectively. The DONUts are intended for rapid reconfiguration, standalone operation, and will not experience high tensile force, therefore we base our design on switchable magnets.

Currently, the closest 'relatives' of the DONUts are the Catoms ([60]) and the RoboPebbles ([57]), both planar modular robots. In the former, round, rigid modules can move in six discrete steps around each other using switchable magnets. This is still an active research platform, especially in terms of controllers, power, connectors, and communication ([129, 151, 87, 21]). The DONUts rely on a similar means of locomotion, but are compliant, simpler to manufacture, and have the potential to be tetherless. The RoboPebbles are small form-factor cubes with switchable magnets used both for inter-module docking, power transfer, and communication; module movement comes from external forces. They involve a quick manufacturing procedure by wrapping a flexible PCB around a rigid frame, enabling deflections to overcome manufacturing defects.

It is worth noting our specific choice of an SEP docking mechanism. In the Catoms and RoboPebbles, the switchable magnets were electromagnets and electro-permanent magnets, respectively. The former has high power consumption when on, and the latter can only be switched off or on in one polarity. To limit power consumption and to permit a wider range of configurations (Fig. 7.1C), we instead leverage SEPs ([253]) which can switch polarities and be turned off. We further explore different SEP designs to lower module weight and enable stand-alone operation.

In summary, the design of the DONUts combines many of these past find-

ings, including: 1) passive module compliance to overcome manufacturing defects, 2) collective motion via switchable magnets to decrease mechanical wear, and 3) a very simple fabrication process to improve system scalability.

6.1.2 Coordination of Modular Robots

Path planners for modular, lattice-based robots typically focus on shape transition, i.e. how to plan admissible and energy efficient paths for all modules from one configuration to another ([211, 140]). Past literature on reactive reconfiguration to reach a goal in a cluttered environment is much more sparse, but has been shown with slime mold-inspired, crystalline, and prismatic modules ([98, 78, 167, 20, 89]), through coupled oscillators, traditional path planners, and cellular automata respectively. All of these were based on distributed controllers and hardware with active degrees of deformation to help the modules move.

In contrast, the DONUt modules briefly presented in [24], have only passive compliance. Although this passive compliance is not currently part of our simulation framework, the presented control algorithms are only dependent on the connection topology and sensed objects, not the actual robot morphology, and could therefore work on the real hardware. We reason further about the benefits of module deformability and strain sensing in [27].

The majority of research has focused on distributed controllers, e.g. through agent automata and globally imposed, or module-generated, gradients ([20, 187]). Centralized path planners for optimal shape transition become computationally intractable as the number of modules grow. This is typically overcome

through careful preplanning ([41, 212]) or sub-optimal planners dealing with hierarchical layers of modules ([16]). The planning is further simplified through discrete occupancy grids (triangles, squares/cubes, and hexagons/rhombic dodecahedrons). Controllers for the Catoms, for example, typically discretize the world into hexagonal cells([211, 16]). Although this approach is convenient mathematically, it also artificially limits the set of achievable configurations, which becomes especially critical in modules that are dependent on others to move.

Here, we explore centralized control schemes which adds no constraints on the module configuration beyond what the hardware is capable of. Similar to [98] and [78] we do not divide the world into a fixed occupancy grid, however, each module does have a finite set of connection points.

Also, similar to many past controllers, path admissibility is ensured through a globally connected topology and consecutive movement of modules. Centralized controllers can suffer from a single point of failure and requires the need of a global sensor (or global communication), however, the algorithms we present rely on knowledge and plans which could be computed locally to overcome such weaknesses, at the expense of added synchronized communication.

6.2 Module Design and Characterization

We start by describing the SEPs, as they dominate the module infrastructure, power consumption, weight, and assembly time. We then detail the remainder of the hardware (Fig. 6.2A), characterize the module ability to move, deform, communicate, and sense, and end with a discussion on scalability. As previ-

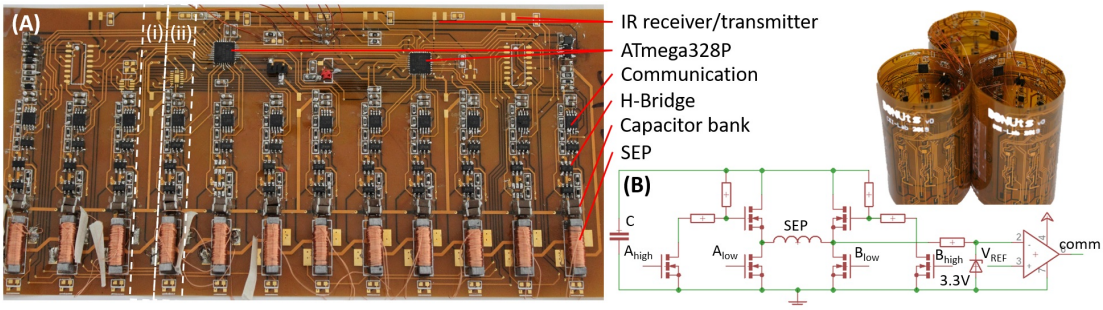

Figure 6.2: (A) A module PCB (unwrapped) and three modules (wrapped). The white dashed lines indicate (i) flexible and (ii) rigid regions due to the placement of components; IR sensors and amplifiers are not mounted in this photo, similarly, a few external wires appear only for initial debugging and powering purposes. (B) SEP driver and communication circuit.

ously mentioned, our design considerations are based on enabling long term, stand-alone operation.

6.2.1 Docking Mechanism

SEPs consist of a low coercivity magnet wound with a copper coil and finished with ferrous end caps to induce and guide the magnetic field, respectively. By sending a high current pulse through the coil we can orient all the dipoles in the core to change its overall polarity; by applying a pulse of lower current magnitude, we can effectively turn off the magnet (Fig. 6.3A inset). SEPs are advantageous for modular robots because 1) they have no internally moving parts which limit wear, 2) they remain polarized without continued supply of power which lowers maintenance, 3) they can be used for both movement and communication which minimizes the number of components, and 4) they can switch between opposite polarizations and off which supports a large range of module configurations. This section details our first SEP design and how it relates to the rest of the module design.

The SEP design considerations include part accessibility, the magnet geometry and coercivity, the geometry of the end cap, the number of turns in the coil, the wire gauge, and the amount of energy that can be transferred to the coil, which in turn is dependent on the supply voltage, series resistance, and pulse duration. These considerations come with trade-offs: a stronger SEP will facilitate better bonding strength and require fewer on-board SEPs needed for actuation, whereas a weaker SEP weighs less and can therefore work on a lower weight module that is easier to move. Our SEP design is based on a careful balance of these parameters. Small-scale, off-the-shelf, low coercivity magnets are rare and therefore the availability of these dominated our design. We decided on a magnet made of AlNiCo grade 5, with a length of 3/8" and a diameter of 1/8", available from Magnet Kingdom. The end caps are made of steel and manually cut to the dimensions 4×4×1.5mm.

A high energy pulse, and therefore a high supply voltage, is needed to flip the dipoles in the AlNiCo magnet. To keep the modules light weight, small, and mobile, we target a single cell Lithium Polymer on-board battery with a 3.7V output. To activate the SEPs, we boost the battery voltage from 3.7V to 26V, using an AP3012KTR boost converter with ~80% efficiency. To avoid damaging the battery, we first charge a capacitor bank $C = 1mF$ slowly (over 75ms), and then discharge rapidly from this bank into the coil. We choose ceramic capacitors to provide a low R_{ESR}. There are four $22uF$ capacitors in parallel placed next to each SEP. Our circuit design is modular, such that the capacitor bank can be discharged into any combination of SEPs simultaneously depending on the actuation sequence desired (Fig. 6.2B). The maximum charge, Q, that can be sourced from the bank is given by: $Q = CV = 27.5mC$. We used this circuit to help us find the remaining parameters of the SEPs experimentally.

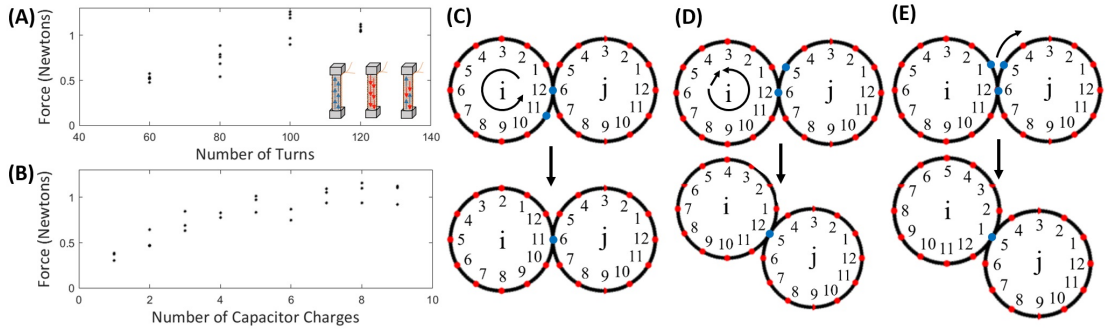

Figure 6.3: (A) SEP pull force when placed against a steel bar versus the number of coil turns (five trials each). All measurements were taken by polarizing the SEP in one orientation with a strong magnet, then depositing a constant charge to flip the polarization. The insets show how the SEPs work conceptually, by changing the orientation of dipoles in the AlNiCo-material. (B) Pull force for an SEP with 100 turns, 40 AWG wire, and 4 mm end caps. Each measurement was done by first orienting all dipoles in one direction (using 11 charges), and then depositing a number of charges in the opposite direction. (C-E) Conceptual movement by module i (red illustrates the position of the SEPs, blue those related to the move). (C) Rotating-motion, i.e. counterclockwise rotation of i. (D) Rotating-translating motion, i.e. counterclockwise rotation and translation by i to the adjacent SEP on j. (E) Gear-like motion, i.e. clockwise rotation by i along the perimeter of j.

Knowing the magnet material and dimensions as well as the available power, we next focus on the coil. Specifically, the achievable SEP pull force is directly dependent on the amount of current we can push through the coil, which in turn is dependent on the number of coil turns (or inductance) and the resistance in the coil:

$$I = V/R_{ESR}(1 - e^{-tR_{ESR}/L}) \tag{6.1}$$

where V is the SEP supply voltage, R_{ESR} is the series resistance in the supply R_C, plus that in the coil R_L, L is the inductance of the coil, and t is the time since the charge started. Thicker, longer wires however produce diminishing returns due to 1) the maximum steady state magnetization strength of the AlNiCo rod, 2) the limited power available, and 3) the fact that the copper adds to the weight of the module which in turn increases the necessary pull force to produce motion.

Through a number of experiments to evaluate weight versus magnet strength, we decided to settle for 40 AWG (American Wire Gauge) copper wire. Fig. 6.3A shows how the number of turns with this wire affects the SEP pull force. F_{max} was measured between an SEP charged with the circuit described above and a steel bar, using a micro load cell rated 0-780g from Phidgets Inc. As expected, F_{max} increases with an increasing number of turns, until R_L starts to limit I. With 100 turns, we found $F_{max} = 1.11 \pm 0.15N$. We then measured how the pull force was affected by the number of times an SEP (40 AWG, 100 turns) was charged after being fully polarized in the opposite direction, shown in Fig. 6.3B. We found that the SEP reaches maximum pull force after being charged approximately 5 times. These SEPs weigh 0.95g, with the coil and end caps contributing 0.15g and 0.30g, respectively. With 12 SEPs located around the perimeter of a 46mm diameter module, the weight of a full module is around 20.9g without a battery and 25.4g with one; i.e. the 12 SEPs make up approximately 45% of the full module weight. Based on the experiments above, we use 5 consecutive capacitor bank charges to flip the polarity of a SEP and 1 to simply turn it off. As part of future work, we hope to perform a model-based analysis to find more optimal parameters, with the aim of increasing the SEP strength, while decreasing the total module weight.

6.2.2 Actuation

To move the modules, we make two assumptions: First, the moving module moves only itself. Second, the module it is moving around is connected to many other modules keeping it relatively stationary. To move on a neighboring module, the moving module has to first inform the other about its desired move and

polarity. If the module is transitioning between two modules it needs to ask its neighbor to pass the message along to the following module. We target several types of motion including on-axis rotation, rotation-translation, and gear-like rotation, as shown in Fig. 6.3C-E, respectively. We imagine that the latter two modes are useful for general motion, and that the former is of use if a particular module sensor is broken, or if the collective wants to take more measurements from slightly different angles. We anticipate that a combination of these motion abilities will support system-level robustness.

We found that rotation around the module axis is possible through the following sequence: 1) [S-O-N-N; N-S-S-N], 2) [S-O-O-N; N-S-S-N], 3) [S-N-O-N; N-S-S-N]; and 4) [S-N-S-N; N-S-S-N], where N, S, and O corresponds to north, south, and off, respectively. When enabling these types of motions we used a total of 11 capacitor bank charges to make sure that an SEP was polarized to the desired state. We further found that rotation-translation is feasible by conducting the following sequence of polarity switches: 1) [X-N-S-X; X-S-S-X], 2) [X-N-N-X; X-S-S-X], 3) [X-S-N-X; X-S-S-X], where X corresponds to any state. In step 1, the modules are connected between locations 2 in the array, and in step 3 between locations 3 in the array. This type of motion requires a total of 10 capacitor bank charges. We conducted a reliability test of the translation motion, and found that the module was able to successfully move 48 out of 50 times when no external forces were applied (Fig. 6.4A). It should be noted that in these two experiments we used external power for experimental ease, but both tests were performed with the weight of a Li-Po battery on-board. It is also important to note that these moves require only one module to activate its SEPs. Therefore, although modules must first agree on the upcoming move with their neighbor, a movement does not require synchronous behavior.

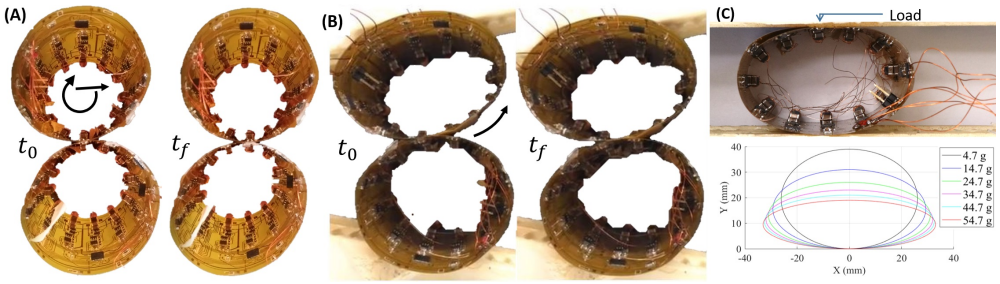

Figure 6.4: (A) Module moving about another module, with motions as described in Fig. 6.3C. (B) Motion of compressed modules, with rotation similar to that described in Fig. 6.3D. (C) Characterization of module deformation, conducted by placing weights on a module.

Finally, we found that the current hardware only facilitates gear-like rotation in two scenarios: either when external compressive loads are applied as shown in Fig. 6.4B, or when approximately half the weight is removed from the modules. More generally, we found that friction is an important factor in determining the motion that a module is capable of and that it is dominated by acceleration due to fast SEP switching. The acceleration, in turn, is determined by module inertia. According to Steiner's theorem, the inertia required for the module to move about a point on its perimeter is: $I = I_o + mr^2$, where I_o is the inertia for the module to rotate about its own axis, and m and r are the module mass and radius respectively. Therefore, if given the chance, the module will spin around its own axis, rather than travel along the perimeter of another. In future work, we hope to enable gear-like motion via the following approaches: 1) an in-depth study and optimization of SEP and module parameters, 2) synchronized SEP switching in neighboring modules, and 3) addition of friction tape along the module perimeters to make on-axis rotation more energy consuming than translational motion.

6.2.3 Passive Deformation

The passive module deformation is useful both to enable large-scale configurations beyond what manufacturing tolerances would allow with rigid modules, and to permit modules to interact safely with other modules and their environment. For completeness, we characterize the deformation modules are capable of.

The components on the flexible PCB are spaced to produce rigid zones, and flexible zones in between the SEPs (Fig. 6.2A). This means that when a static external load is applied to a DONUt module, it deforms by an amount proportional to the load. Beyond guiding the magnetic field, the SEP end caps also function as a mechanical stop which prevents pinching that could permanently deform the PCB. Therefore, when the load is released, the module reverts back to its original shape, exhibiting spring-like behavior. The effective spring constant of a DONUt module was experimentally obtained by applying increment amounts of weight on a flat surface lying on top of a sideways module. The constant is calculated from Hooke's law: $F = -k_s \Delta x$. The term k_s refers to the effective spring constant and Δx is the change in length when a force, F, is applied. We found $k_s = 28.01 \pm 2.85 N/m$ (Fig. 6.4C).

The looped PCB, of course, does not behave like a perfect spring, and the change in deformation between increment weights decreases slightly with increasing load. This is due to an increasing effect of the rigid zones on the deformation of the module as they are pressed closer to each other at the right- and left-most edges of the module, corresponding to the areas of highest curvature. It should be noted that if the load was dynamic with non-negligible momentum, impact, or vibrations, then the geometric response of the module would

be quite different, and it is possible that this effect may be exploited in future work.

6.2.4 Computation

Our choice of controller, ATmega328, coincides with those of the Arduino platforms which are very popular in the do-it-yourself community, again aligning with our philosophy of lowering the barriers to entry for diverse researchers and developers to help increase system robustness. To provide a sufficient number of control pins, each DONUt module has two ATmega328 microprocessors running on their internal 8MHz RC oscillator, with 2KB SRAM and 32KB EEPROM. The first processor controls SEPs 1-7 and three IR transceivers; the second, SEPs 8-12, one IR transceiver, and all SEP communication channels. The two processors communicate via UART. The software for low-level control of all peripheries take up just 2.3% of the SRAM and 6.5% of the EEPROM, leaving the majority of static and dynamic memory for the controllers described in Sec. 6.4.

6.2.5 Communication

As previously mentioned, we simplify the design by making double use of the SEPs for actuation and module-to-module communication. Restricting the communication range is a commonly used method to avoid bandwidth problems as many asynchronous modules try to communicate([164]). When two SEPs located on separate modules are in contact, they can communicate locally as fol-

lows. The capacitor bank is first charged to maximum capacity. Bits are then transmitted using electromagnetic induction; i.e. the transmitter encodes bits in pulses of current, which are received by the neighboring SEP via induced current in the coil. The receiver then decodes these (weaker) pulses into bits. The current communication protocol is able to send a packet of 4B at a rate of 5 kbps on a single capacitor bank charge.

We developed our own protocol to facilitate communication with bits encoded in pulse length: A '1' is approximately twice the length of a '0' (Fig. 6.5A top). This encoding simplifies synchronization because we can treat any bit like a clock signal, and use a simple schmitt-trigger coupled to a timer input comparator on the processor to decode the package. A transmission is started with a '1', and bits are sent from least to most significant. The main limitation in baud rate is the time it takes to charge the capacitor bank. Fig. 6.5A bottom shows the decrease in transmission voltage as a (worst case) package of all '1's sent, and the capacitor bank discharges.

To test communication reliability, we cycled through a transmission of all possible characters between two SEPs. We found the error rate to be 1 flipped bit per 1000 bits. This issue may be addressed by adding in one or more parity bits for a slight decrease in throughput.

6.2.6 Sensing

Sensors allow the modules to interact intelligently with their environment. Although we focus on simple IR sensors for gradient tracking and obstacle detection, it is relatively easy to modify the module design to fit different sensors

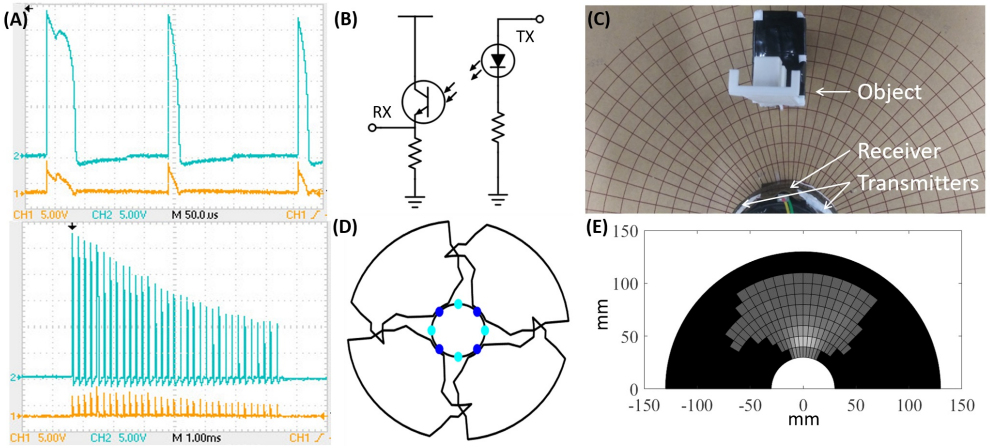

Figure 6.5: (A) Top: Communication packet between SEPs. Received (orange) and transmitted (blue) message of a start bit, '1', followed by two '0's. Bottom: Decrease in voltage over the capacitor bank as a package of all '1's is sent. (B) IR transceiver circuit. (C) Experimental setup to measure module field of view. (D) Top view of the experimentally measured sensor coverage in a module. (E) IR intensity map (bright values correspond to close objects and reach a maximum of 498 bits; dark values correspond to 0 and no measured signal).

because it only involves a slight re-routing of the PCB.

Currently, each module is equipped with four infrared emitters (OP140A) and four receivers (LTR-301) operating at 935-940nm (Fig. 6.5B). For full spatial coverage while keeping the number of components small, these 8 components are spaced equally around the perimeter of the module, and have a radial emission angle of 40^o and a relative sensitivity around 20^o, respectively. The outputs from the receivers are multiplexed into the analog to digital converters (ADC) on the processors. To measure the distance to an object for instance, we turn on the relevant emitter and multiplexed channel, and subsequently read the ADC value. We experimentally tested the distance sensors using the setup in Fig. 6.5C. Fig. 6.5D shows a top view of the module coverage pattern and Fig. 6.5E bottom shows the raw values from the sensor. Although every module will have a slightly different coverage dependent on the manual mounting of the sensors, even small objects should be visible before contact. In [27], we

discuss how to use this ability for object shape estimation.

6.2.7 Power

A DONUt module can fit up to three single cell 0.15Ah Li-Po batteries from E-flite, weighing 4.5g and measuring 45×12×8mm each. The module has the ability to measure its own battery level to support more intelligent collective behaviors as further discussed in Sec. 6.4. The vast majority of energy spent in a module is on actuation and communication. As a rough estimate, a single battery should be able to support $E_{batt}/(.5CV^2) = 6000$ capacitor bank charges. Given that a single gear-like move requires 11 capacitor bank charges, this corresponds to a full travel length of 12.9 m or 280 module diameters (with no communication). Beyond improved movement, future work will target integration of solar cells to support longer term operation.

6.2.8 Scalability

As argued in the introduction, a focus on individual module robustness supports large scale robot collectives, which in turn enables system-level robustness. Here, we discuss the current state of the modules in terms of cost, fabrication time, and maintenance, and how these may be improved to make large scale DONUt collectives feasible.

Cost

As we have yet to optimize for cost, a single module is priced around 587 USD. The biggest cost stems from the 2-layer flexible PCB (468 USD quote from Advanced PCB), the 48 ceramic capacitors (46 USD), the 12 MOSFET drivers (17 USD), and the 12 SEPs (12 USD). The remaining 44 USD stems from components, such as processors, LEDs, resistors, etc.

There are several ways to lower the price of low-volume module fabrication. The cost can be reduced drastically by picking a cheaper PCB manufacturer (the lowest quote was just 90 USD, but had a longer lead time), or by taking advantage of the recent progress in Inkjet printable flexible PCBs ([82]). The latter reports a drop in price to 10 USD per meter of film, which would leave the cost of the PCB to be negligible compared to the other parts in the module. There are also cheaper alternatives to the current capacitor banks; we could, e.g., use fewer, but larger OSCON capacitors similar to those used for flash in cameras. To give an idea of how the price scales with mass fabrication, the price of the current (non-optimized) component list drops from 119 USD/module to 52 USD/module when ordering for 1000 modules. We aim to produce a second version of these modules with a price point around 50 USD, placing them in a similar range to the cheaper modular robots in literature ([19]).

Fabrication

One of the key benefits of the DONUt module design, is the reliance on a single PCB which supports imprecise, rapid, and inexpensive manual assembly of both SEPs and wrapped PCBs. The largest time sink for the fabrication is com-

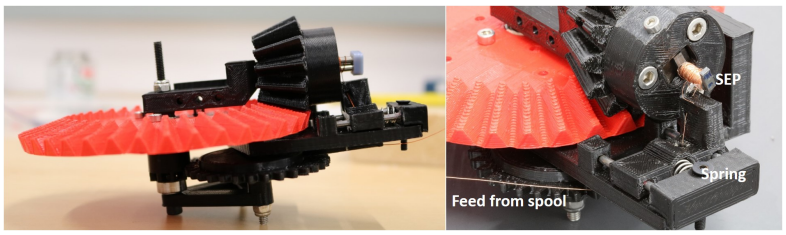

Figure 6.6: 3D printed, manual winding device for rapid production of SEPs. The SEP is mounted into the black piece with a screw; the spring keeps the wire from a spool taught during winding, similar to the mechanism on a sowing machine. A full turn of the red wheel adds roughly 100 turns to the SEP.

ponent soldering; currently, one PCB takes around 5 hours to solder by hand. In the future, we hope to have the majority of the PCB pre-populated at a manufacturing house. To get a rough estimate of how this would trade off cost for lowered assembly time, we requested a quote from Advanced PCB which came to 30 USD/module for an order of 1000 modules. We expect that this cost can be lowered with a more thorough search of vendors, a longer requested lead time, and the right choice of components. The current capacitor bank, for example, consists of many components in parallel; it would be beneficial to replace these with a few, larger capacitors.

If the PCB assembly is outsourced, that leaves the following steps for in-house assembly: 1) SEP manufacturing, 2) attachment of SEPs and batteries, and 3) flexing the PCB into a loop. Of these three, only the first two take any considerable amount of time. The process is as follows. First, the magnet is glued to the steel end caps with super glue; then the assembly is inserted into our winding rig shown in Fig. 6.6. The gears in the rig are dimensioned such that a single turn of the red wheel by hand adds 100 turns to the coil. This entire process, including PCB mounting, takes at most 4 minutes per SEP, i.e. 48 minutes per module.

Maintenance

The maintenance requirements of modular robots stem from mechanical wear, the ability of a user to operate (start, stop, and program) all modules with a global command, the module battery life time, and the reliability of individual components. We address each factor in sequence. 1) DONUt modules have no internally moving mechanical parts that can wear with use, and have no loose wires or connectors that may break over time which tend to be one of the bigger problems in small electro-mechanical devices. 2) In future versions, we may explore better parallel operation, enabling user control through a single IR source similar to past platforms ([164]). 3) In the future we may optimize the maximum possible travel distance per module through integration of solar panels on the PCBs. Although this type of power harvesting will be slow, it fits this particular style of robots well: only perimeter modules in large collectives are able to move which causes a spiraling migration pattern where the majority of modules at any one point in time remain stationary (further discussed in Sec. 6.4). 4) Although more thorough tests are needed, we tested 50 moves in a row without any component faults.

6.3 Simulation Environment

We have developed an open-source simulation platform in Matlab® to support general access to development and testing of control schemes for the DONUts modular self-reconfigurable robot (`https://github.com/njw68/DONUts_Simulation`). The framework permits programmers to easily test large numbers of modules operating in varying degrees of clutter, and perform structured

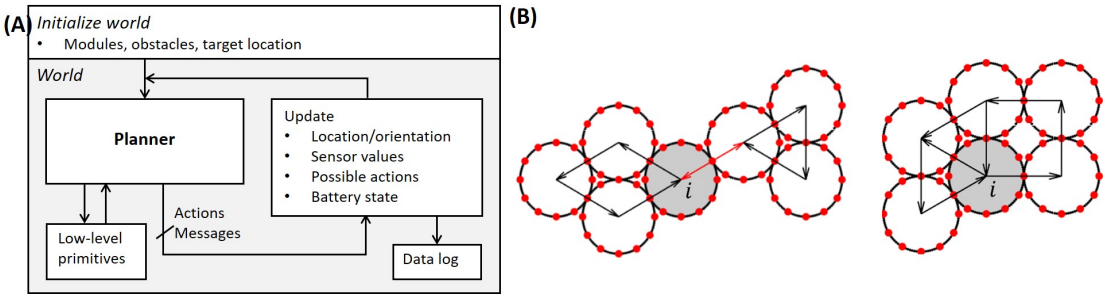

Figure 6.7: (A) DONUt simulation framework. The user specifies the high-level planner, which makes use of low-level primitives. When actions and messages are computed, the framework automatically reevaluates relevant variables, feeds these back to the controller, and logs the state of the world for later debugging. (B) Checking if a module (in grey) can move. Left: *i* satisfies props. 1 and 2, but violates 3. Right: *i* satisfies props. 1 and 3, but violates 2, as described in Sec. 6.3.1.

analysis of system resilience to signal noise and component failures. The simulation incorporates gear-like motion (Fig. 6.3D), connections, sensing range, and message passing. Module compliance, friction, and inter-module forces are not integrated at present. The software is written such that the user can focus on implementation of high-level control schemes, while lower-level primitives like those needed to identify obstacles, connections, and viable motions are abstracted away. An architecture overview is shown in Fig. 6.7.

A programmer can experiment with path planning in cluttered environments with their choice of the number of modules and the amount and complexity of the clutter. The simulation framework may be easily modified to support other task settings and distributed algorithms as well, similar to how we used it in [27]. Upon initialization, the programmer may specify the number of modules, the target location, and either pre-determined or randomly generated obstacles with a user-specified size. The software can generate either a rectangular or a random configuration of interconnected modules; it can also run a random initial configuration, where each of the aforementioned variables is

randomly generated.

6.3.1 Module Primitives

Next, we introduce several low-level behaviors to support operation of the DONUts.

Motion restrictions

To determine whether module i can physically move, we make three successive checks related to the following properties:

1. i is connected to at least one other module, such that at least one c_{ij} exists, where c_{ij} is the set of connection positions on i between i and j. j refers to the set of modules that are connected to module i and $c_{ij} \in [1, ..., 12]$.
2. Connections to other modules are contained within 180°, i.e. the module has five consecutive free connections.
3. Movement will not disrupt global connectivity of the modules.

The first property relates to the fact that modules cannot move on their own; the second to the fact that they need physical clearance to move; the third check ensures a cohesive collective (Fig. 6.7B). The latter is done by checking for loops in the connectivity graph; i.e. we pass a message to all neighboring modules to see if it can loop back to the origin without passing the same edge twice. After verifying these properties, we compute the possible movements (clock-

wise (CW) / counterclockwise (CCW) / both) taking into account the presence of other modules and obstacles in the environment.

Motion

To physically move a module, it must pass a message to the neighbor which it is rotating about to prepare the next connection (i.e. switch on the correct magnet with the correct polarity). The attraction of the two successive magnets, alongside the repulsion from the previous connection point will propel the module forward. The geometric movement of each module is a function of the center of the module about which they are moving (Fig. 6.3B). We can compute the center position (x, y) of a moving module by Eq. 6.2:

$$\begin{bmatrix} x_i \\ y_i \end{bmatrix} = \begin{bmatrix} x_j \\ y_j \end{bmatrix} + 2R \begin{bmatrix} cos(\theta_j + \frac{2\pi}{12}(c_{ji} + u)) \\ \\ sin(\theta_j + \frac{2\pi}{12}(c_{ji} + u)) \end{bmatrix} \tag{6.2}$$

The terms i and j refer to two adjacent modules; module i moves about the perimeter of stationary module j. R is the module radius, θ_j is the orientation of j with respect to the world reference frame, and c_{ji} is the magnet position of the connection between j and i on j, where $c_{ji} \in [1, ..., 12]$. The term u is the control input for i which determines whether i will move CW or CCW about j's reference frame, $u \in [-1, 0, 1]$. When $u = -1$, i moves CCW about j; when $u = 1$, i moves CW about j; and when $u = 0$, i remains static at its current location.

To keep track of modules and their orientations, we allocate specific IDs to every magnet on the perimeter, and map these to relative IDs as they rotate.

An array stores the position of the magnet ID with respect to the inertial frame of reference. Initially, all modules have magnets mapped one to one, such that magnet 1 is at position 1 ($c_1 = 1$), magnet 2 is at position 2 ($c_2 = 2$), etc. When a module moves CCW about another, the moving module's magnet positions are updated by -1, such that $c_k = c_k - 1$, $k \in \{1, ..., 12\}$. Similarly, CW movement results in updates by $+1$. A check ensures proper rollover when surpassing 1 and 12. The software updates all magnet positions, c_k, through the module's control input, u:

$$c_k(t + 1) = (c_k(t) + u) \tag{6.3}$$

After the movement has occurred, the module may find itself near new neighbors. To determine the presence of such neighboring modules, a module will briefly activate all connection points, transmit its ID, and await an acknowledge message. In general this sequence needs to be performed only by a module after movement. However, it is possible that occasional checks by all modules to verify their connectivity will improve system robustness.

6.4 Module Coordination

Translating algorithms developed in simulation to real hardware often requires considerable effort. However, such simplified simulations may still be used to quickly iterate the overall coordination methodology as well as to illuminate non-intuitive pitfalls related to the hardware design. In this section, we discuss important findings related to robust coordination of many DONUt modules for gradient tracking, introduced by the hardware-specific constraints. Gradient

tracking is a robust and potentially scalable basic behavior necessary for navigation in coordinate-free environments. This behavior may support applications such as identifying the source of chemical spills or simply navigating towards a source of light to harvest power. We introduce controllers for gradient tracking in clutter-free and cluttered environments, using the available sensors described in Sec. 6.2 and building on the simulation framework and the low level primitives introduced in Sec. 6.3.

Specifically, we introduce two types of controllers towards robust collective behavior: an A* search-based controller and a more naive, iterative controller. We discuss implementation details, and compare these in terms of complexity and optimality with respect to the number of module moves which directly impacts energy efficiency and maintenance. To produce a benchmark for 'optimal behavior', we also introduce an Oracle planner with complete knowledge of the world. Beyond control methodologies, we discover and discuss a type of connection topology that generally impedes progress along the gradient, and discuss how to avoid this with the naive controller.

Intuitively, sophisticated controllers should not be necessary for gradient tracking as every agent in the collective can simply navigate according to the local gradient. Here, however, we target controllers that advance the entire collective efficiently towards the gradient source. Note that, because 1) we enforce a globally connected collective, 2) modules cannot move on their own, and 3) only perimeter modules are capable of moving, this is not a simple problem. Were we, for example, to perform a naive graph-search across all possible moves of a state in which ten modules are configured in two adjoining rows, this state would have twenty children for a single module move. In other words, the

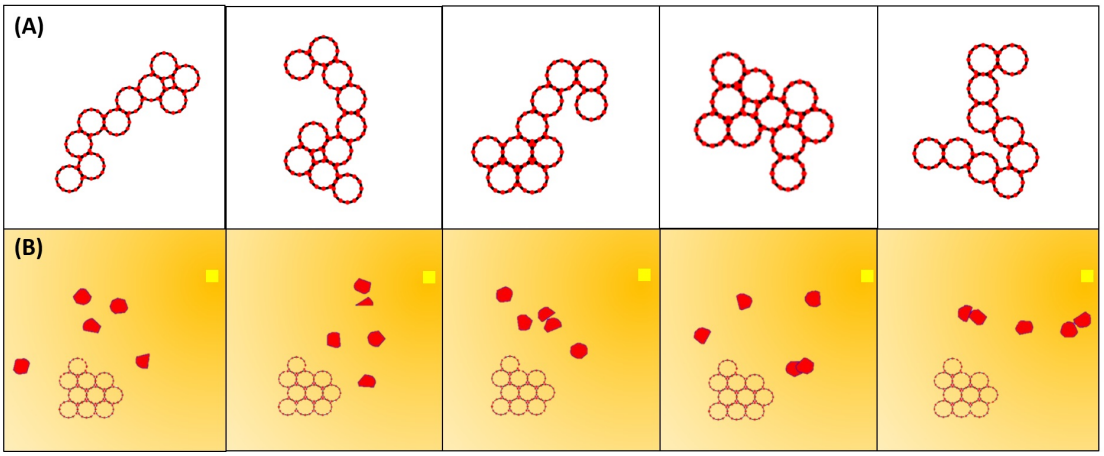

Figure 6.8: Five examples of the test scenarios for controller evaluation. (A) Randomly generated initial configurations (*TS2*). (B) 5 randomly generated obstacles with randomly generated positions in the path to the goal (*TS3*).

search space quickly becomes intractably large.

To evaluate our controllers, we use different subsets of the following three scenarios:

- *Test Scenario 1 (TS 1):* 10 modules starting in a cluster 10 module diameters (20*R*) from the goal in a clutter-free environment.
- *Test Scenario 2 (TS 2):* 10 modules starting from 10 random configurations 20*R* from the goal in a clutter-free environment (Fig. 6.8A).
- *Test Scenario 3 (TS 3):* 10 modules starting in a cluster 20*R* from the goal in an environment with 5 randomly generated and randomly placed obstacles (Fig. 6.8B).

Note that, unless otherwise noted, we abort runs which exceed ~7,000 states; furthermore, we limit the scope to sequential module movement.

6.4.1 Oracle Path Planning

To provide a baseline against which our centralized controllers can be compared, we implement an Oracle planner that computes an optimal path in terms of module moves to a global light source, given complete knowledge of its environment. This planner is based on A* graph-search, where the nodes in the graph correspond to the state of the robot (i.e. the location of all DONUt modules) and the edges correspond to module moves. The cost of a node, $cost_{state}$, is calculated as the number of moves it takes to get to that state. To search the state space efficiently, we compute an admissible search heuristic, h, expressed in module moves, and prioritize nodes with lower total cost: $cost_{total} = cost_{state} + h$. The combination of graph-search and an admissible heuristic allows us to prune the large search space and return globally optimal results ([168]). To ensure that the modules cluster around the light source, we complete the search when the distance from the collective center of mass (COM) to the goal is within two module radii, $2R$.

We examined two heuristics in terms of search space efficiency. The first heuristic, h_0, is based on the intuition that it is beneficial for the collective to quickly align their orientation with the highest gradient. To do this we make h_0 a function of the euclidean distance between the module with the highest measured light intensity (corresponding to the lowest distance to the goal, D_{min}). We compute the number of moves it would take one module to travel this distance and multiply by the total number of modules in the collective, N, i.e. $h_0 = ND_{min}$. The second heuristic, h_1, is more generally based on the intuition that all modules need to move towards the goal. We make h_1 dependent on the euclidean distance between the collective's COM and the goal ($h_1 = ND_{COM}$). Because

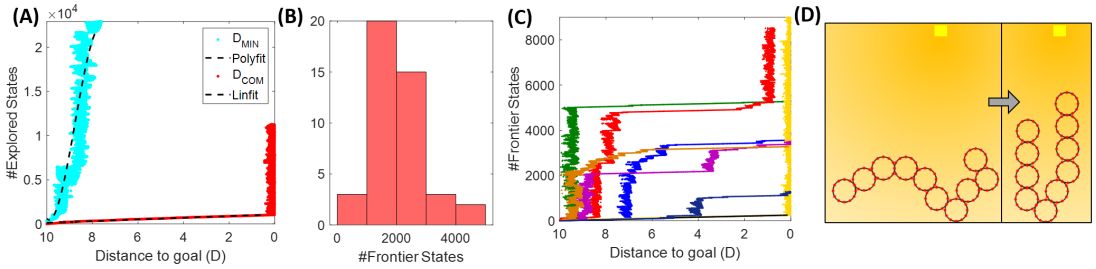

Figure 6.9: (A) Performance of Oracle planner in *TS1* with heuristics $h_0 = ND_{MIN}$ and $h_1 = ND_{COM}$. (B) Histogram showing the number of states in the graph-search frontier at convergence using h_1, with 55 random initial conditions. (C) Examples of the runs shown in (B). (D) Example condition that leads to slow search behavior.

modules actually have to travel around the perimeter of other modules to reach the goal, the straight line distance is an underestimate of the true distance and results in an admissible heuristic.

We found that h_1 far out-competes h_0 in terms of search space efficiency. An example of what happens is shown in Fig. 6.9A; the number of expanded states in the tree grows exponentially with h_0, and closer to linear with h_1. The intuition behind h_0's performance is that once a module has been moved as close as possible to the goal within a configuration, all other moves have an equal cost. That is, when a new module moves closer to the goal, but not enough to surpass the current closest module, D_{min} is the same as the scenario when that module moves away from the goal. In contrast, h_1 ensures that until the collective reaches the goal, we favor states that directly impact the progress of the entire collective. Once the COM gets within $2R$ of the goal, the frontier grows rapidly simply because the heuristic no longer supports closer clustering.

To reason about how well the h_1-heuristic worked, we calculated the effective branching factor, b^* in *TS1*. Briefly explained, the effective branching factor denotes how many branches every node would have on average if the solution

was recast as a breadth first search ($n = b^0 + b^1 + b^2 + ...b^a$, where n is the number of states, b is the number of branches, and a is the depth of the search tree). A b^* close to 1 indicates that we almost always guess the optimal move and therefore keep the search tree from branching excessively. We found that h_1 is a very efficient guess, with an average $b^* = 1.034 \pm 0.0054$, confirming that moving the module that advances the collective COM as much as possible towards the goal is preferred. Note that this result does not necessarily translate to cluttered environments or take into account the fact that extra connections between modules may improve their redundancy in case of failures.

Interestingly, we found that the search efficiency was heavily dependent on the initial configuration of the collective. To examine this phenomenon more, we ran 55 iterations of *TS2* and plotted the maximum number of states reached in the frontier before convergence. The results are shown in Fig. 6.9B. 47 out of 55 trials converged within the allotted number of expanded states. The fastest searches converged after evaluating about 500 states, but the majority required 2-4 times as many evaluated states. Fig. 6.9C-D illustrates why this occurred. We see that the number of states in the search frontier grows linearly over most of the path, but exhibits periods of exponential growth. These periods occur when the search reaches a state where the collective forms a single chain with the center point of the chain closest to the goal. In this state, moving either of the two end-modules forward is the fastest predicted way to reach the goal, eventually leading the search to a state in which the collective forms a U-shaped chain. Once this state is found, the search must explore all other higher cost states before it again finds a move that will bring the COM closer than when it was in the U-shape. We designed the following on-board controllers with this risk in mind, to support faster convergence.

6.4.2 A* Search-Based Controller

In a realistic scenario, the modules will not have access to the state of the world and must plan according to what they know; i.e. their connection topology, the measured light intensity, and nearby obstacles. We first implement an A* search-based controller for the modules similar to the Oracle planner with two exceptions. First, instead of planning towards the actual goal, we choose an intermediate goal location which corresponds to the module with the highest measured light intensity, i.e. the module closest to the goal. The modules plan their path to the temporary goal, execute this path, recalculate the new temporary goal, and re-plan. Second, based on the discussion of the effective branching factor, we calculate a new admissible heuristic based on the distance to the intermediate goal from the collective's COM, $h_2 = CND_{COM}$, where C is a constant scaling factor. Effectively, this means that the collective moves in stages (each locally optimal): first communicating and identifying which module is closest to the goal, then planning how to bring their COM to that location before reevaluating which module is now closer. They repeat this process until the collective COM is within $2R$ from the light source.

To find the optimal value of C, we did a parametric sweep from $C = 0.1 - 1.0$. We did this sweep with a square initial configuration (*TS1*), and found that $C \leq 0.5$ performed very poorly, rarely making progress beyond $2R$ towards the goal in the allotted number of states. Conversely, $C > 0.5$ yielded results that were too similar to draw a conclusion. We therefore ran an additional sweep from 0.6-1, using 10 configurations in *TS2*. The results are shown in Fig. 6.10A. We found that coefficients at the extremes (0.6 and 1) rarely converged in the allotted number of expanded states. The best results were with $C = 0.7$, which

converged in all cases and reached a collective COM within $4R$ and $2R$ from the goal more quickly than when using other values for C. Note that with $C = 0.7$, the heuristic is still admissible.

Based on these simulations, we further make the observation that the collective may enter live lock, i.e. an infinitely repeated movement pattern, before reaching the goal depending on the collective's angle to the gradient. An example of what causes this is shown in Fig. 6.10C; modules 10 and 5 oscillate back and forth leaving the collective within the temporary goal, but not the global goal. Because the collective has no memory from previous planning iterations these movement patterns will execute forever. To overcome this, we added a check to assess how much progress the collective has made within one planning iteration. If the collective converge on the temporary goal after moving just one module, no multi-iteration progress occurs. In this case, we move a random module (excluding the last moved module) 1 step. By adding a degree of randomness, we avoid local minima like these, and ensure that the collective will eventually converge at the goal.

In Fig. 6.10B, we next compare the performance of the A* search-based controller to the Oracle in *TS2*. As would be expected, the A* search-based controller is less than optimal. The performance especially degrades as the collective approaches the goal, because at this point the number of moves it takes to reconfigure the collective's COM to the temporary goal dominates the difference of which module is closer to the goal.

We further make the observation that the controller often generates chain-like configurations, where every module on average has only two neighbors. These are problematic because a single module failure can split the chain in two,

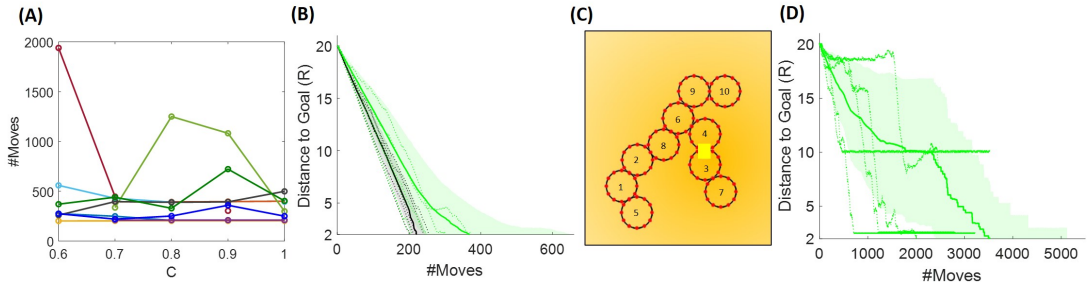

Figure 6.10: (A) Parametric sweep of C in *TS2*. (B) Comparison of 10 paths generated by the Oracle (black) and 50 paths generated by the A* search-based controller (green) in *TS2*. The solid lines denote mean, shaded regions the standard deviation, and dotted lines are 5 actual runs chosen at random. (C) Example of live lock near the goal in the A* search-based controller.(D) Paths generated by the A* search-based controller in *TS3*.

disrupting global performance. The heuristic-based control approach permits a simple way to deal with this issue: we simply add a penalty for a loosely connected graph. Note that this effectively makes the heuristic inadmissible and results in (locally) sub-optimal, but (globally) more robust plans. We used a coefficient α to change the severity of the calculated penalty, P, where x is the number of connections a module possesses:

$$p = \begin{cases} x_i > 2, 0 \\ x_i = 2, 1 \\ x_i = 1, 2 \end{cases} \tag{6.4}$$

$$P = \sum_{i=1}^{N} p(x_i)\alpha \tag{6.5}$$

In other words, we add a penalty of 2α for modules that are configured in a chain and only have two neighbors, and a penalty of α for modules that are at the end of a chain. The new cost per node comes to: $cost_{total} = cost_{state} + h_2 + P$. We ran this simulation in *TS2* using $\alpha = [0 \quad 2 \quad 4 \quad 6]$, and compared both the total number of moves needed for the collective's COM to reach the goal within $4R$

and the average number of connections in each step along the way (Fig. 6.11A-B). Again, we see that the initial configuration has a big impact on performance, and that, as expected, with increasing penalty, the modules stay more clustered. The choice of α relates both to the desired redundancy and the number of modules in the collective. For example, with ten modules configured in a double-row the average number of connections per module corresponds to 3.4. We see that the graph levels out at $\alpha = 2$, i.e. at 2.8 connections per module which is reasonable given that some modules have to deviate from the double row for the collective to move. This experiment is a repeated measures, correlated samples test, thus we perform a one-way ANOVA for correlated samples and find that α has a statistically significant effect on the average number of module connections ($F(3,57) = 663$, $p < .0001$). Conversely, α does not have a statistically significant effect on the number of module moves ($F(3,57) = 1.32$, $p = 0.28$). The average number of moves between the α's vary by ~30 . To explain this, we examine the simulations at $\alpha = 0$ and $\alpha = [2 \quad 4 \quad 6]$. We find that while with a value of $C = 0.7$ and $\alpha = 0$ is an admissible heuristic for local optimization, it results in chain-like configurations, which are more susceptible to temporary live lock. These instances of temporary live lock require modules to move sub-optimally to break out of temporary live lock and resume regular planning. This causes an increase in the number of modules moves to reach the goal. In the cases of $\alpha = [2 \quad 4]$, we observe that clustered configurations lead to sub-optimal local planning, but more robust global planning, thus fewer temporary live lock instances occur, and the average number of module moves is less than with $\alpha = 0$. An example of the path taken given $\alpha = 6$ is shown in Fig. 6.11C. This brief study indicates that adding a clustering penalty is a viable and simple way to ensure higher collective redundancy.

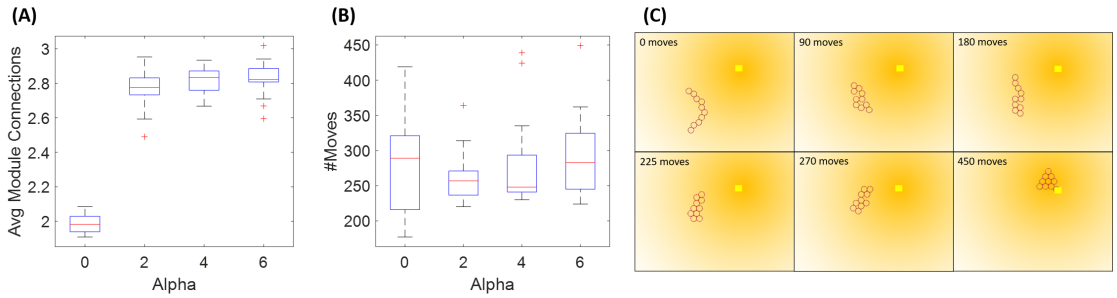

Figure 6.11: Enforcing a penalty for sparsely connected modules improves the redundancy of the system and is independent of the time to reach the goal. (A-B) Number of module moves and connections as a function of clustering penalty α. Each box plot shows the median, standard deviation, outliers, and the 25th and 75th percentiles based on 20 runs in *TS2*. (C) Example path generated with an $\alpha = 6$.

Finally, we tested the A* search-based controller in cluttered environments (*TS3*). The results, shown in Fig. 6.10D, indicate live lock near obstacles. By studying the actual runs closely, we find that this happens because the number of modules which can move randomly is severely limited by either their connection topology (chain-like configuration) or their proximity to obstacles. We may deal with this by adding either a higher degree of randomness or memory between planner iterations. The former comes at the cost of planner efficiency and without guarantees that live lock can be avoided in all situations. The latter is complicated because the collective may enter configurations that appear similar to previous ones, but at geographically different locations. Modules may compute their trajectory to overcome this problem, however, this would require perfect dead reckoning skills which is not practically feasible with the hardware.

We can further discuss the ability of this planner to operate on the actual hardware processor, i.e. the 2KB of RAM in the ATmega328P ([24]). The state space of the planner grows somewhere between linear and exponential with the number of modules, depending on 1) the optimality of the heuristic and 2) the

configuration of the collective, i.e. the number of modules that are capable of movement. Every node in the search tree contains the collective's connection topology and a reference to the parent and child nodes. For 10 modules in a perfect cluster this would correspond to 19 connections and 1 parent node, i.e. a memory footprint of 20B. In this state, 8 modules are capable of moving CW, CCW, or staying, therefore the node has 24 children; i.e. just two levels in, the search would take up 500B of memory. Alternatively, we could trade off memory for computation by storing only the move and recomputing the configuration for every explored node. In this case we spend 20B on the first node, and 1B per node moving forward. With a good heuristic, the memory would then grow close to linear as in a depth-first search. To improve memory, we could further explore how this search could be distributed to over the two on-board processors ([35]). Given the current hardware constraints, however, we are unlikely to be able to support planning for more than a few tens of modules. In the next section, we instead focus on more naive, iterative planners that require less memory and computation altogether and are inspired by what we learned from the graph-based controllers.

6.4.3 Naive, Iterative Controllers

To produce an algorithm that scales well in memory and computation with near-optimal control, we next examine a naive, iterative controller for gradient tracking. In this controller, we simply prioritize moves of modules that are farthest from the light source, hence we name this type farthest-first or 'faf-controllers'. As before, we identify the module with the highest light intensity, i.e. the one closest to the light source, and treat it as an intermediate goal. We then iden-

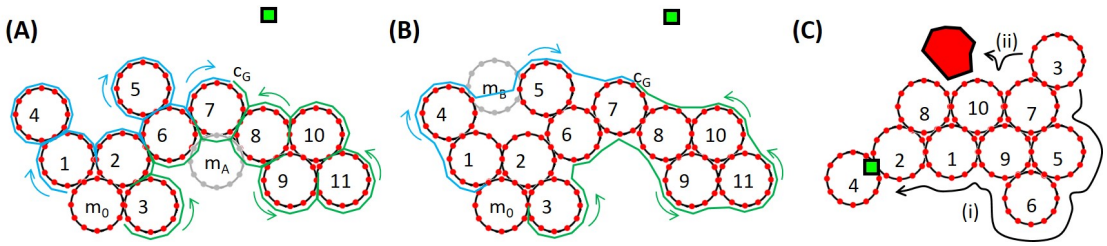

Figure 6.12: (A-B) Example configuration in which module m_0 plans a path, either *CW* (blue) or *CCW* (green), to the location with the highest brightness, c_G. (C) Illustration of the two versions of the faf1 controller. In faf1$_i$ m_3 chooses the only viable path towards the goal; in faf1$_{ii}$ it follows the shortest path to the goal and stops when it sees an obstacle.

tify a movable module with the lowest brightness, and move it towards the intermediate goal along the shortest path around the collective perimeter. This process repeats until all modules are clustered around the goal location. We explore two versions of this controller. In the first, we move the darkest module one step before searching for a new darker module ('faf0'). Intuitively, this approach works well for highly dynamic environments where information quickly becomes stale. In more static environments, or when communication between modules or between modules and the centralized controller is costly, the update rate can be lowered by only re-planning when the moving module reaches its intermediate goal ('faf1').

The following list details how this controller works, using the example shown in Fig. 6.12.

1. *Initialize:* We first identify the intermediate goal, i.e. the brightest module, m_7; and the darkest module which is capable of moving, m_0. We also identify which connection on m_7 is closest to the light source, c_G.
2. *Generate viable paths and identify external obstacles:* We next decide which direction (*CW* or *CCW*) around the collective will yield the most efficient

path. We construct two candidate sequences, S_{CW} and S_{CCW}, along the perimeter modules from c_G to the closest connection on m_0, c_0. To construct S_{CCW}, we first append c_G ($S_{CCW} = [m_7(c_G)]$) and then continue appending connections on m_7 in a CCW direction until the neighboring module, m_6, is reached ($S_{CCW} = [m_7(c_1 : c_G)]$). We continue this process until we reach the m_0 ($S_{CCW} = [m_1(c1 : c7)]...m_6(c_1 : c_4)m_7(c_1 : c_G)]$). These steps unambiguously define the sequence of connection points that m_0 must go through to reach the goal. In other words, by using connection points rather than module center points, we avoid confusing any connection on the closest module (e.g. m_A in Fig. 6.12A) with the goal location. Every time we encounter a new module, we check for obstacles seen by that module to indicate whether or not the sequence is tenable.

3. *Optimize viable paths and identify geometrically incompatible modules:* The second step overestimates the number of moves needed to reach the goal, because it does not take into account locations like m_B illustrated in Fig. 6.12B, where the module can connect directly between two non-neighboring modules, m_4 and m_5. To prevent this overestimate, we loop through each tenable sequence, projecting m_0 along the sequence generated above, checking for physical proximity of connectors that would reveal new potential neighbors. By iterating forward through the sequence and for each projection checking backwards from the goal we ensure that m_0 always identifies the connection that is closest to the goal. If one exists, we delete all of the intermediate entries and produce new sequences, CW' and CCW'. If at any point the m_0 projection overlaps with another module we label the sequence untenable. Note again, that overlap is possible because we are not operating in a discrete occupancy grid. On the real

hardware, overlap could also occur because of module deformation.

4. *Move module along shorter path:* Finally, we simply compare the length of the sequences and move the module in the direction of the shortest path.

Fig. 6.13A shows the performance of faf0 and faf1 in *TS2*. Because the test is performed in a static, clutter-free environment faf1 outperforms faf0, here by a factor of ~4. The oscillations in faf0 occur when the collective, similar to what we saw with the Oracle planner, finds itself in a U-shaped chain where it greedily moves the darkest module up the gradient at each cycle, effectively making the collective gather at one extreme of the connection topology, then the other, until it finally reaches the global goal. We see that faf1 performs almost as well as the Oracle planner, but that the performance is still dependent on the initial configuration.

For operation in cluttered environments, we explored three variations of faf1, also illustrated in Fig. 6.12C. In $faf1_i$, if the shortest path which the darkest module must take to the intermediate goal is intercepted by an obstacle, we instead move the module in the opposite direction; if obstacles are detected in both directions, we move another module. In $faf1_{ii}$, when an obstacle is encountered we simply move the darkest module as close to the obstacle as possible. In faf1, when an obstacle is encountered, we choose according to $faf1_i$ and $faf1_{ii}$ with 50% likelihood, and, with 20% likelihood move a random movable module one step in a *CW* direction. Fig. 6.13B compares the performance of these three variations in *TS3*. Generally, $faf1_{ii}$ outperforms the others, however, it may enter livelock. Similar to our previous observations, we find that this happens in U-shaped chain configurations where the two ends point towards the goal and are near obstacles that hinder further movement. At this point each end mod-

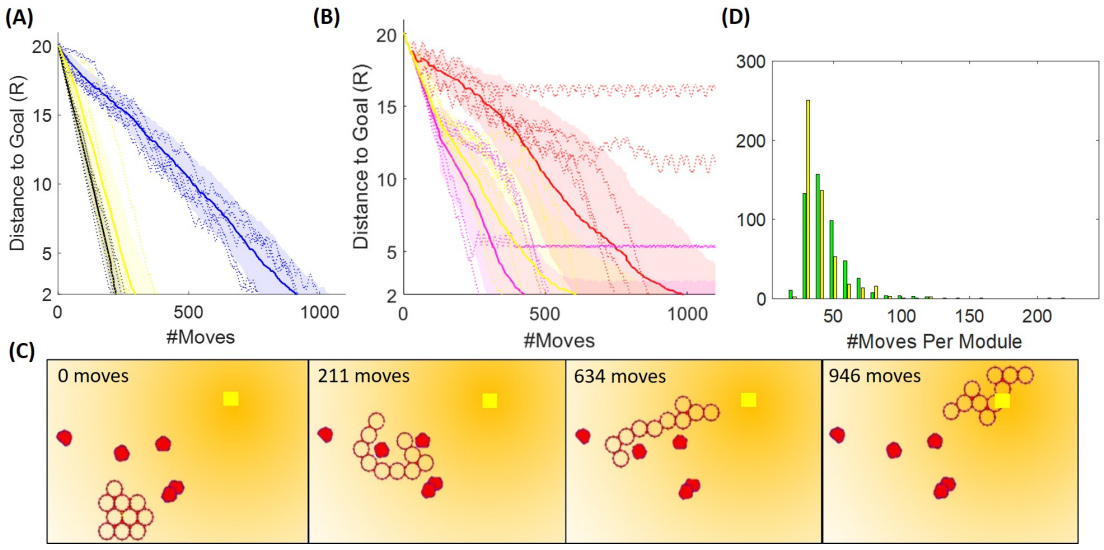

Figure 6.13: (A) 10 paths generated by the Oracle planner, and 50 paths generated each by the faf0 (blue) and faf1 (yellow) controllers in *TS2*. (B) 50 paths generated by the faf1$_i$ (red), faf1$_{ii}$ (magenta), and faf1 (yellow) controllers in *TS3*. The solid lines denote mean, shaded regions the standard deviation, and dotted lines are 5 actual runs. (C) Snapshots of a path generated by the faf1 planner. (D) Histogram showing the number of moves per module. To compute this plot, we counted all moves per module from 50 runs in *TS2* with the A* search-based and the faf1 controller. Note that we discounted runs that reached live lock near the goal.

ule simply moves back and forth along the collective, without making actual progress. faf1$_i$ does not show issues with live lock, but takes nearly twice as long to reach the goal. faf1 overcomes issues with live lock due to stochasticity, at the cost of ~1.5 times more module moves.

Deriving the exact scaling behavior for this planner is complicated due to the motion restrictions discussed in Sec. 6.3.1. In the algorithm, most operations scale constant or linear with the number of modules; however, optimizing the path along the collective, i.e. step number 3 in the description above, approximates polynomial time. Intuitively explained, in the worst-case scenario where the collective is spaced out in a single file line and not in the presence of obstacles, the darkest module has to be projected along every other module to check

for short-cuts. This step is an interesting point for future work. Another obvious direction for improving the scalability of this algorithm is to outsource computations. In [27] we, for example, detail how the connection topology can be computed in a distributed manner. To extend the current planners to a completely distributed system, one can imagine combining these algorithms with a consensus-based scheme to identify the modules with highest and lowest brightness.

6.4.4 Discussion

In summary, in the context of gradient tracking in clutter-free environments, our 10-module simulations indicate that both controllers may perform nearly optimal despite the lack of global knowledge. The locally-optimal A* search-based controller performed well in terms of the number of modules moves for clutter-free environments, but additional measures must be taken to overcome potential live lock near obstacles. We also find that even with a good search heuristic, the algorithm scales poorly in terms of memory and will not support more than a few tens of modules if implemented on the two on-board ATmega328 processors. The naive, farthest-first controller performed equally well and had the ability to deal with live lock near obstacles via a small degree of randomness. This controller is simple and may support more scalable behavior.

Through simulations, we further found that both types of controllers generally create chain-like, rather than clustered, configurations. Chain-like configurations are bad for the DONUts, because 1) they severely limit the amount of modules that are capable of moving, 2) simulations show that chains often end

up creating U-shaped configurations that impede general progress towards the goal, and 3) they leave the collective at risk of complete failure if just a single module breaks. We showed that encouraging redundant connection topologies in the A* search-based controller was fairly simple; encouraging these in the farthest-first controllers will be an important area of study in future work.

Finally, system energy consumption warrants explicit discussion because it is a major contributor to system autonomy and robustness, affecting the strategy of exploration versus exploitation as the modules traverse an environment. The DONUt hardware, for example, was designed around SEPs which keep their polarization without continued supply of power, the number of power consuming components was minimized, and the modules were designed as light weight as possible (25.4g). In Fig. 6.13D, we compare the A* search-based and the faf1 controller in terms of how well they distribute energy consumption among the modules. As we have yet to consider energy spent on communication in our centralized controller, the energy we can estimate is directly correlated with the number of moves a module has to make. The plot shows that the faf1 controller inherently distributes power usage more evenly, whereas a few modules in the A* search-based controller moves many times further than the others. Evening out power consumption will also be an interesting future extension to our work.

6.5 Conclusion

In summary, we have introduced a new planar, modular, self-reconfigurable robot. Although more work is needed before practical large-scale demonstrations are feasible, this initial hardware-software design cycle has contributed

several concepts that may translate to other platforms. Most importantly, by basing our design on a single flexible PCB without mechanically moving parts, we were able to achieve simple, fast manufacturing, and support low maintenance in terms of breakage and wear. By creating an open source simulation platform with realistic movement and sensing, we explored two control schemes and non-intuitive challenges that arose because of the module-specific motion constraints. We explicitly focused on enabling a large configuration space to enable operation in dynamic environments, and explored a range of challenges related to collective efficiency, scalability, redundancy, and adaptability. More generally, we showed that enabling scalability and system-level robustness, rely on tightly integrated design decisions that span fabrication, operation, and control with an explicit focus on constituent robustness.

We have several agendas moving ahead. On the hardware side, we will focus on decreasing cost, increasing battery life, and improving motion reliability before pursuing a large-scale collective. So far, we have depended only on the passive compliance for added robustness, however, long term, we hope to investigate novel collective behaviors enabled by the compliance, including their ability to generate macroscopic materials with different density and tensile strength. Similarly, their spring-like properties promises interesting dynamic behaviors which may be leveraged for both communication and motion. Finally, the fact that every single module weighs only 25.4g also indicates a new set of potential applications beyond those seen with previous platforms. On the control side, we are exploring several avenues. The most near-term is to combine centralized and decentralized algorithms for better scaling properties. Longer term, we hope to better investigate the trade-off between control redundancy and efficiency.

CHAPTER 7

COMPARATIVE ANALYSIS OF SENSORS IN RIGID AND DEFORMABLE MODULAR ROBOTS FOR SHAPE ESTIMATION

Modular self-reconfigurable (MSR) robots have the potential to adapt their overall shape to suit a particular task or environment [19]. To support intelligent autonomous behavior in these systems, it is critical that they are able to reason about both their own state and the state of the world. To perform optimal shape transitions for instance, the robot must know the location and connection topology of all its modules. This is especially true in realistic, large-scale systems where hardware may fail, inadvertently changing the robot configuration. To further perform useful tasks, the robot could, e.g., measure environmental gradients or the shape of an object to be circumnavigated or contained. In past work, many researchers have shown the ability of traditional rigid modular robots to identify their own connection topology. Here, we extend on that work by introducing distributed algorithms for external 2D shape estimation by rigid MSR robots given two typical sensor modalities, as well as 2D shape estimation by passively compliant modules equipped with strain sensors.

This work is performed in simulation, based on a representative example of a planar MSR robot composed of circular modules with peripheral sensors and the ability to move along their neighbors in discrete steps. In general, the simple algorithms presented here apply to lattice-based planar modular robots, and can easily be extended to non-circular shapes or modules with an arbitrary number of connections. Examples of existing platforms that work with these assumptions include the DONUts [23], Catoms [60], Atron [80], Soft Cubes [207], and Metamorphic [139].

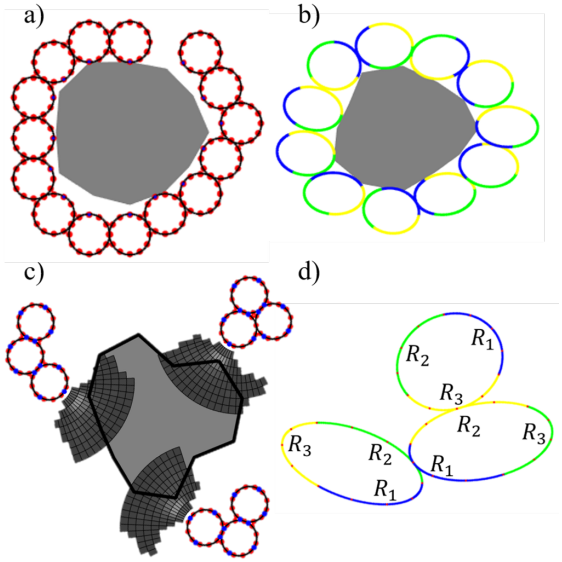

Figure 7.1: MSR robot sensing modalities examined in this paper. a-b) Rigid and deformable modules encapsulate an object and use connection topology to estimate its shape. c) Modules circle an object, using IR transceivers to measure its shape. d) Deformable modules are simulated with three strain sensors covering the perimeter of each module.

This paper presents the following contributions: 1) a simple distributed algorithm for encompassing arbitrary planar objects with rigid and deformable modules, 2) distributed shape estimation with connectivity sensors (topology estimation, Fig. 7.1a), 3) distributed shape estimation by deformable modules equipped with strain sensors (Fig. 7.1.b), using experimentally obtained strain sensor data, 4) distributed shape estimation with infrared (IR) sensors (Fig. 7.1.c), using experimentally obtained data, 5) a method of generating random 2D objects with a specified size and degree of convexity, and 6) comparison of the accuracy of these methods for increasing object size and degree of convexity. To ground this work in realistic numbers, we base the evaluation and experimental results on a MSR platform in our lab, 'the DONUts', introduced in [23] and [223]; however, the insights generalize to other modular robots.

The paper is structured as follows. Sec. 7.1 presents the related work on MSR

robots and their sensing mechanisms. Sec. 7.2 details how sensing modalities are compared, including a kinematic model, a brief introduction of the DONUts, and how we generate arbitrary objects with a degree of convexity. Sec. 7.3- 7.5 detail algorithms for shape estimation and experimental sensor characterization. Sec. 7.6 compares all sensor modalities, and Sec. 7.7 concludes and describes potential extensions.

7.1 Related Work

Research in MSR robots spans both hardware design and controllers. Platforms include chain-, strut-, or lattice-connected modules, typically made of rigid elements with one or more controllable degrees of freedom for reconfiguration [236, 31]. Modules with deformable properties are more sparsely represented, and include rigid elements which can actively extend [78, 167, 20, 89], as well as inherently soft elements that actuate by inflation [207, 95]. Some platforms support single-module locomotion [41], but many are restricted to collaborative movement with other modules similar to the ones used here [98, 61, 78].

Table 7.1 lists examples of sensing modalities on existing MSR platforms. Most MSR robot designs are limited to proprioception (e.g. knowing the position of motors through encoders, or the presence of connected modules); but a few have also shown the use of exteroceptive sensors ranging from pressure sensors for contact measurements, IR transceivers to help them localize other modules or external gradients, and more advanced sensors like RGB-D cameras mounted on a subset of modules. Here, we compare the ability of MSR robots to wrap around and detect the shape of an enveloped object through

the use of common proprioceptive and exteroceptive sensors in rigid modules, connectivity and IR, respectively; and proprioceptive strain sensors in passively compliant modules.

This research falls in between topology determination in modular robots [143, 141], self-replication [58, 150] and sensor fusion for object recognition in multi-robot systems [120, 189]. However, as opposed to the majority of past MSR robotic papers, we do not limit module configurations to discrete world occupancy grids. The modules also cannot move freely in space, and are therefore more limited in their sensor range than freely roaming multi-robot systems. Finally, we explore the use of distributed strain sensors to measure both topology and external shapes.

Table 7.1: Example of sensing modalities in modular robots.

Robotic Platforms	**Sensors**
Atron [33]	IR, tilt, connectivity
Catoms [61]	Connectivity
CKbot [144]	IR, connectivity
Crystalline [167]	Expansion, connectivity
DONUts [23]	IR, strain, connectivity
Morpho [240, 239]	IR, expansion, pressure
Particle Swarm [98]	IR, expansion
SMORES [41]	Connectivity, camera

7.2 Comparison Framework

To reason about module motion and sensing, we introduce the following comparison framework which is easily extendable to any planar, modular robot with a discrete set of connectors and sensors. Each module has the following properties: a pose in the world reference frame, a connection topology, a control input, a desired direction of travel, sensor measurements, and a degree of

deformation.

7.2.1 Kinematic Model

We simplify the simulated movement of a module by a single control input that specifies the desired direction of travel (clockwise or counterclockwise) about a neighboring module. The kinematic constraints dictate that modules cannot physically overlap with other modules or objects. Furthermore, the simulation framework considers the sensor measurements for each of the modules as determined by experimental characterization.

The reference frames for a stationary module j and a moving module i are defined by $\mathcal{F}_{Aj}$ and $\mathcal{F}_{Ai}$, respectively. The orientation of the connection c_{ji} between these two modules with respect to the world reference frame $\mathcal{F}_W$ is given by:

$$\theta_{W/c_{ji}}(t) = c_{ji}\frac{2\pi}{N}, \tag{7.1}$$

where $c_{ji} \in \{1, 2, ..., N\}$ is the position of the connection between j and i scaled by the angular distance between connections, and N is the number of connectors on each module (Fig. 7.2). When module i moves, $\theta_{W/cji}$ can be updated by a control input u, where $u_i \in \{-1, 1\}$ for the moving module i and $u_j = 0$ for the stationary module j.

$$\theta_{W/c_{ji}}(t+1) = \theta_{W/c_{ji}}(t) + 2u_i\frac{2\pi}{N} \tag{7.2}$$

Since module i is moving about the center of module j, module i defines the (x,y)-position of its center by $\mathcal{F}_{Aj}$ and rotates about module j's periphery.

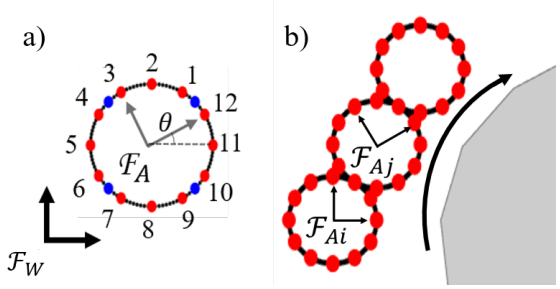

Figure 7.2: a) Definition of a module's reference frame $\mathcal{F}_A$, with respect to the world reference frame $\mathcal{F}_W$. (b) Reference frame $\mathcal{F}_{Ai}$ refers to moving module i and $\mathcal{F}_{Aj}$ refers to stationary module j.

7.2.2 DONUt Modules

To ground this work in real numbers, we base our assessment on the DONUt MSR robot from our lab, shown in Fig. 7.3 and detailed in [23]. These modules have onboard computation, IR sensing, communication, and $N = 12$ connectors. They are based on a single flexible PCB wrapped in a loop, which permits modules to deform ensuring safe physical interaction with other modules and objects in the environment. Modules move about other modules by switching the polarity of their magnetic connectors to repel and attract, resulting in a gear-like motion, where one module rolls about the surface of the other. Connected modules communicate with each other through near-field magnetic induction and may transmit their state, information about the local environment, or pass on messages from other modules located further away in the collective.

7.2.3 Object Generation

To assess the accuracy of different sensing modalities for shape estimation, we introduce a methodical approach to generate arbitrary 2D objects. Our simulation framework defines an object by a user-specified number of vertices N_k, a

Figure 7.3: Four DONUt modules encapsulating an obstacle. Modules have onboard actuation, sensing, communication, and computation.

maximum radial size R_{max}, and the object convexity factor α. The set β, is defined by a list of N_k angles evenly spaced from $2\pi/N_k$ to 2π. Each element in β is the angle of the corresponding vertex k, where $r(k)$ is the vertex radius. $r(k)$ is given by:

$$r(k) = (\alpha + (1 - \alpha)X)R_{max} \tag{7.3}$$

where $\alpha \in (0, 1]$ and $X \in (0, 1]$ as a randomly generated value. As α increases, objects become more convex, and at $\alpha = 1$ the object is a regular polygon. To determine how the accuracy of the shape estimation with different sensors scales with the size of the object, we randomly generate object vertices using Eq. 7.4:

$$\begin{bmatrix} x_{object}(k) \\ y_{object}(k) \end{bmatrix} = r(k) \begin{bmatrix} cos(\beta(k)) \\ sin(\beta(k)) \end{bmatrix}, \tag{7.4}$$

where $k \in \{1, 2, ..., N_k\}$, R_{max} refers to the maximum $r(k)$ possible when generating the arbitrary object, and R_{module} is the module radius.

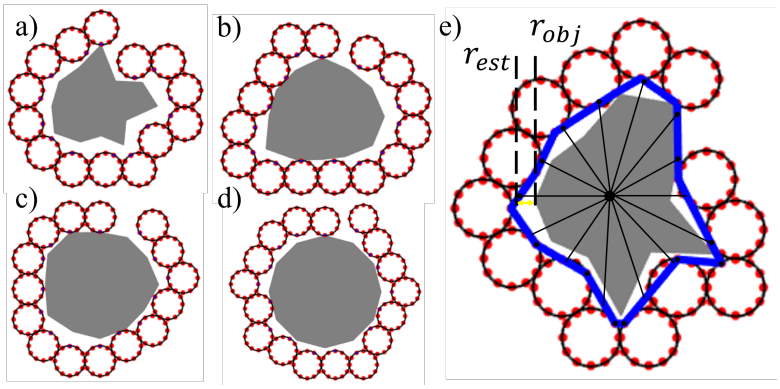

Figure 7.4: a-d) Modules encapsulating randomly generated 2D objects with $R_{max} = 4R$ and α corresponding to 0.4, 0.6, 0.8, and 1.0, respectively. e) Shape estimation error; the blue line is the reconstructed shape.

7.3 Shape Estimation Based on Connections

We first demonstrate an approach by which a collective of round, rigid modules with N connection points can determine the shape of an object. The modules encapsulate the object by first placing a seed module immediately next to the object and then placing the following modules as close as possible to the object perimeter, while remaining globally connected. This process continues until no more modules fit tightly against the perimeter of the object (Fig. 7.4).

Given knowledge of their relative connections and orientations, rigid modules can accurately determine their connection topology and therefore the approximate area of the shape they encompass. We assume the seed module knows its pose in $\mathcal{F}_W$. The seed starts by computing Eq. (7.5) for its neighbor:

$$\begin{bmatrix} x \\ y \\ \theta \end{bmatrix}_{W/i} = \begin{bmatrix} 2R_{module}cos(\frac{2\pi}{12}c_{ji}) \\ 2R_{module}sin(\frac{2\pi}{12}c_{ji}) \\ \theta_{W/j} + \frac{2\pi}{12}c_{ji} + \pi - \frac{2\pi}{12}c_{ij} \end{bmatrix} \tag{7.5}$$

The seed module transmits the result to its neighbor and prompts the neighbor to do the same to the following module. This process continues in an iterative

manner through all of the modules. Each module passes a message with the information of its neighbor's position and all modules' positions before then. In order for all of modules to know all other modules' locations and thus the shape of the object they encapsulate, the final message must be passed through the group back around to the seed module. The communication overhead for a distributed system is $O(2n - 1)$, where n is the number of modules encapsulating the object. This same method is useful for a collective in a chain-type configuration or a tree-like branching lattice structure.

7.4 Shape Estimation Based on IR Sensors

We demonstrate how rigid modules can make use of IR transceivers to estimate the shape of an object. To do this, we place three clustered modules such that the nearest is within sensing range of the object. We then iterate through the three modules, letting them move clockwise around the perimeter of their neighbors to a set of way points around the edge of the object. The starting point and way points are defined by the vertices of a virtually scaled up version of the object. The modules navigate to each of the way points until they have rotated all the way around the object, and then combine all sensor measurements (Fig. 7.5) to determine its shape.

To ground this assessment in real data, we integrate into our simulation framework the DONUt IR transceiver response to nearby objects, as shown in Fig. 7.6. By comparing readings at ambient light to readings when the emitter is on, we can accurately detect objects in the surrounding environment. Since IR transceiver readings are dependent on a number of factors including object

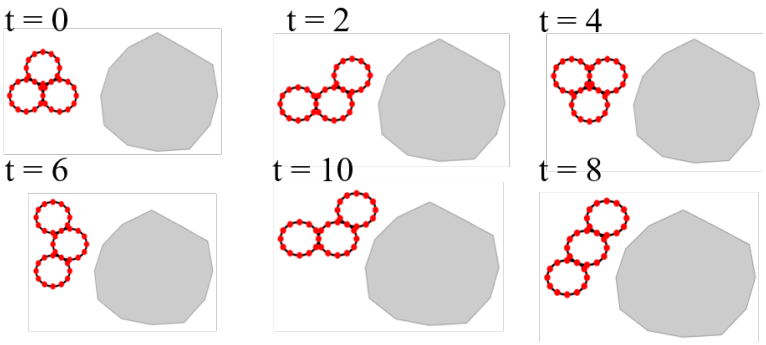

Figure 7.5: Sequence of movements for three modules moving clockwise (u = -1) about the perimeter of an object.

material, distance, angle of incidence, and lighting conditions, it is difficult to predict the resultant value when a module is in a given position with respect to an object. Therefore, we discretize the sensor field-of-view into an array of arced cells that each represent an experimentally obtained value when a small rectangular object is placed at a location equivalent to the inner edge of each cell. We estimate the sensor response to an object, by adding up the intensity response of each arced cell intersecting with the object. A plot of the summed values is shown in Fig. 7.6. The total sum value is compared against the values shown in the graph and these are interpolated to find a point at a specified distance from the module perimeter along the mid-line of the sensor field-of-view, which corresponds to an estimated object vertex.

7.5 Shape Estimation with Compliant Modules

An increasing number of researchers have started merging soft and modular robots, producing modules with infinite (passive) degrees of freedom. On the positive side, these can safely interact with physical objects in the environment, and therefore also reason about external shapes in new ways. On the negative

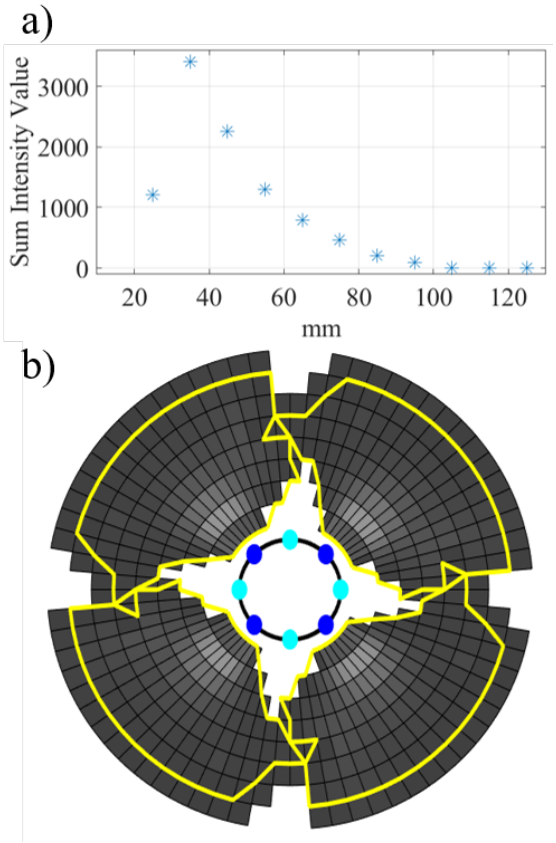

Figure 7.6: DONUt IR transceiver response to objects in the environment. Light gray values show a response of 495, dark grey a response of 2. White show a response similar to ambient. Blue and cyan dots on the module perimeter represent the position of photo-transistors and emitters respectively.

side, they require added reasoning to determine the overall shape of the collective. Here, we examine how such deformable modules may leverage distributed strain sensors to reason about the surrounding environment.

To measure the shape of objects, we execute a similar algorithm as that described in Sec. 7.3. We place a round module immediately next to the object, and then place the next module as close as possible to the object while staying globally connected to the other modules. Because modules have the ability to deform, we try this placement with a deformation corresponding to a minor axis of $2R_{module}$, $3R_{module}/4$, $5R_{module}/8$, and $R_{module}/2$. This process continues until no

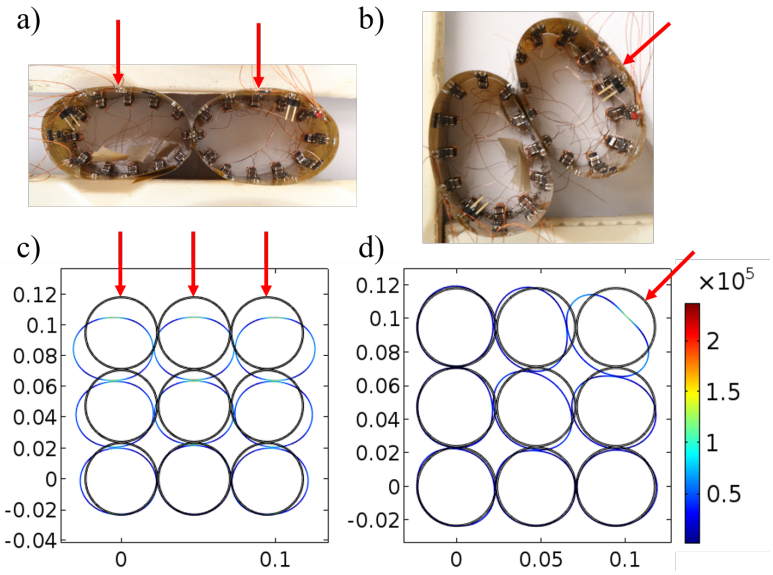

Figure 7.7: a-b) Experiments with deformation of DONUt modules under static load. c) Nine simulated modules in a lattice configuration with three static point loads (0.3 N) applied downwards. d) Static point load (0.3 N) applied to the same configuration at the upper right-hand corner at an angle of 45^o. The color legend refers to the von Mises stress in N/m^2.

more modules fit around the object perimeter. We ground our observations in the DONUt platform through measurements of modules' compliance and the response of resistive strain sensors that can be scaled down and placed along the perimeter of the module.

7.5.1 Characterization of DONUt Compliance

DONUt modules are compliant and deform under external load. They also exhibit a spring-like behavior, i.e. they revert back to their original, circular shape after an external load is removed, with an effective spring constant of 28.01±2.85 N/m. In the following, we assume that modules move so slow that we can consider static loads only. For simplicity, we also assume that modules deform in an ellipsoidal manner upon application of a load.

COMSOL Multiphysics software simulations were performed on several DONUt lattice configurations with a static load applied vertically down or at an angle. Care was taken to keep the static load below the yield point of the PCB material to avoid irreversible plastic deformation. Fig. 7.7.a-b illustrate experimental test cases where DONUt modules deform very close to ellipses. The COMSOL output is shown in Fig. 7.7c-d, where the deformed version of each simulated DONUt is displayed in the color corresponding to the von Mises stress experienced in that region. Fig. 7.7d shows a simulated nine-module lattice structure with a load applied to the upper right corner. In this case, all modules have essentially zero deformation, except for the one experiencing the load which does not deform as a near-perfect ellipse. However, in both Fig. 7.7c and Fig. 7.7d major axes and minor axes can still be identified, and therefore we argue that in most cases, the modules will approximately deform as an ellipse when pressed upon by an external force.

7.5.2 Characterization of Strain Sensors

To ground our simulations in a realistic output, we acquired a resistive flex sensor (77 mm length from Adafruit). We show that three such sensors located on the perimeter of a module can help uniquely identify the amount and orientation of ellipsoidal compression.

The output of the sensor is dependent on the length of the major and minor axes of the ellipse and the placement of the sensor on the perimeter. To measure the sensor output dependent on its perimeter placement, we 3D printed 4 rigid ellipses with different minor axes and a constant circumference of 222 mm

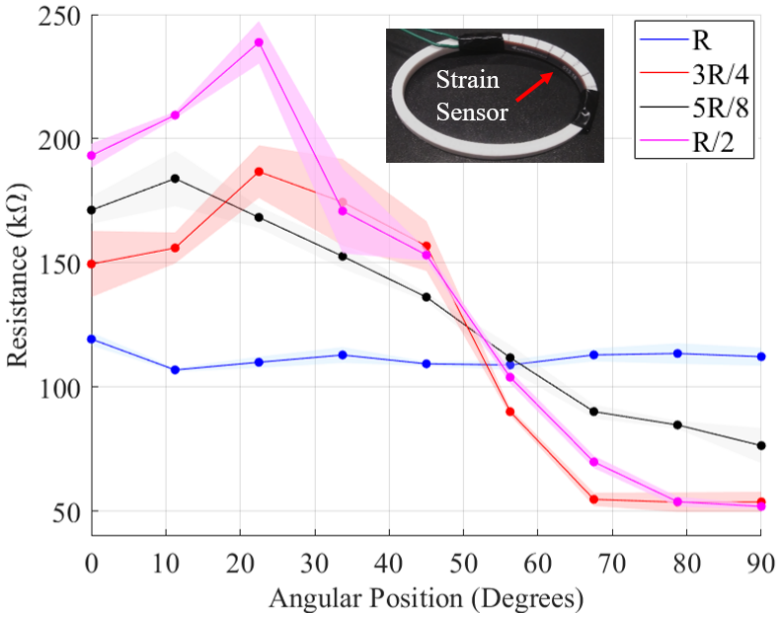

Figure 7.8: Strain sensor resistance when placed at different angular positions along the perimeter of an ellipse (between 0^o and 90^o). The x-axis denotes the position of the sensor's midpoint. Four ellipses with a fixed circumference and different minor axes were tested.

corresponding to three strain sensor lengths. We then placed the sensor with 11.25^o intervals on the perimeter and measured the output nine times (Fig. 7.8). A perfectly circular module results in a constant resistance reading (111.78 $k\Omega$) at all placements along the perimeter. With a single sensor, however, there is no unique mapping from sensor output to module deflection and orientation (illustrated best by Fig. 7.8.bottom). This is the reason why three strain sensors are spaced at equal intervals along the circumference.

7.6 Results and Discussion

To evaluate the accuracy of the methodology portrayed in Fig. 7.4e, we calculated the relative mean error ($\bar{\epsilon}$) between the estimated shape and the true object

shape for each of the sensing modalities:

$$\overline{\epsilon} = \frac{\sum_{p=1}^{N_{kest}} |\hat{r_{obj}} - \hat{r_{est}}|}{N_{kest}} \tag{7.6}$$

To do this, virtual lines were drawn radially extending from the centroid of the object at equal angular spacing designated by the number of vertices on the estimated object. Each of the virtual lines intersects with the edges of the estimated object and the real object outline, for which the corresponding distances from the centroid are denoted as $\hat{r_{est}}$ and $\hat{r_{obj}}$, respectively. The number of vertices on the estimated object is determined by N_{kest}. In the test cases where modules are simply equipped with connectivity sensors, $N_{kest} = n$. In these tests, the closest connection point to the object's edge is a vertex of the estimated object shape. This condition is also true when the shape is estimated by deformable modules equipped with strain sensors. In the test cases where modules are equipped with IR sensors, however, N_{kest} is equal to the number of times the modules' IR sensors detected the object while circumnavigating the object.

Fig. 7.9 shows the results of all shape estimations. Notice that the standard deviation seen on the $\alpha = 1$ graph occurs because we place the seed module at slightly random starting configurations. Both rigid and deformable modules with connectivity sensors exhibit higher errors with smaller objects. We credit this to the fact that for small objects, the error is dominated by the minimum step size of a module. As would be expected, when the objects increase in size, this number settles at a constant value of around $0.5R_{module}$. The deformable modules perform approximately as well (and at lower object sizes better) as the rigid modules.

Observing the error generated by rigid modules with IR sensors circumnavigating the objects, it is clear that our sensor model is introducing additional

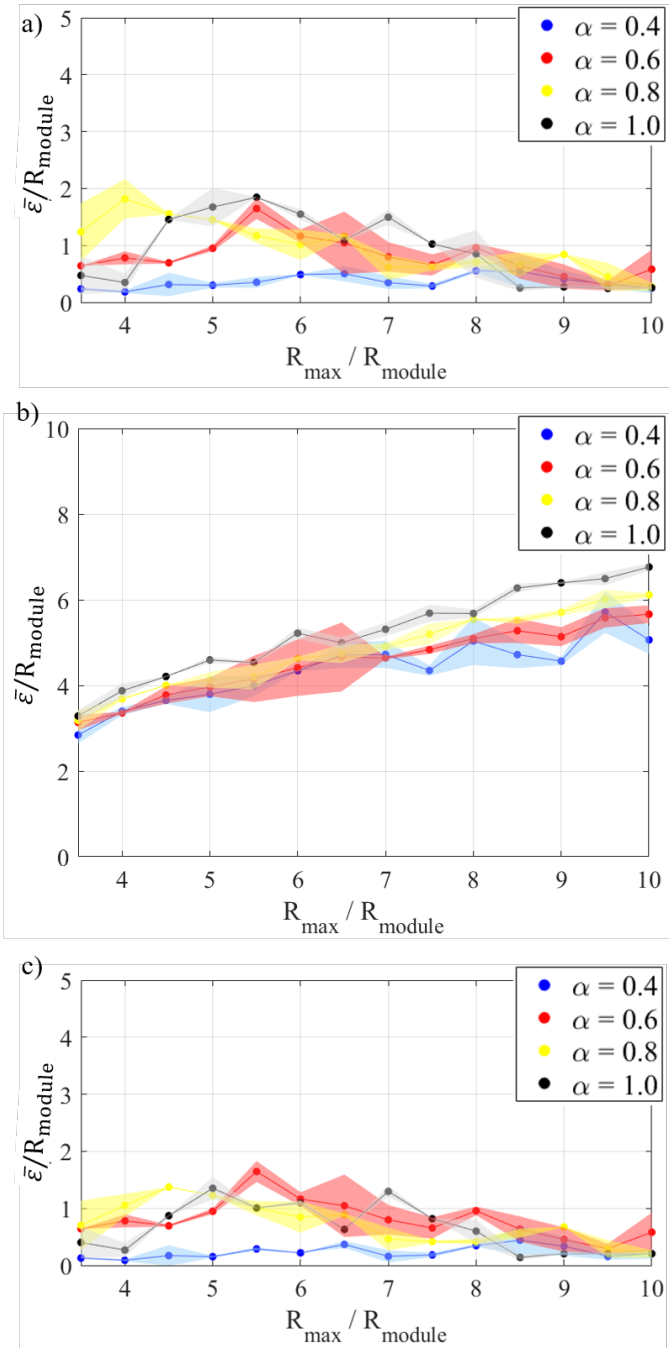

Figure 7.9: Shape estimation error with increasing object size and convexity, performed by rigid modules with connectivity sensors encapsulating an object (a), rigid modules with IR sensors circumnavigating an object (b), and deformable modules equipped with strain sensors closely encapsulating an object (c). Shaded regions represent the standard deviation of 10 simulations for each test case.

error in the shape estimation. This may be improved in future work, but we can still use this graph to reason about data trends and we see that the error increases with larger object size independent of the degree of convexity. With even larger objects, we would expect this value to level out.

In comparing all the graphs, we can draw no definitive conclusion on which sensor methodology is better, although the deformable modules seem to slightly outperform rigid modules at smaller object sizes. Note however, that each sensor modality has other advantages and disadvantages that should be taken into consideration. For example, the topology estimation requires no additional parts; the IR sensors are affected by object color and ambient light settings; and passively compliant modules may operate safely in close vicinity to objects. In the future, there are many avenues to better estimate the object shape. Modules could, e.g., circle the object more than once, iteratively adapting their path to improve sampling.

7.7 Conclusion

We compared shape estimation accuracy for three sensing modalities on a representative rigid and deformable MSR platform, and found that each of the sensing modalities tend to perform better at different object sizes. Modules with IR sensors performed best when the object size was smallest, while rigid and deformable modules performed best with larger object sizes. In general, we found that deformable modules with embedded strain sensors may have advantages over the others for shape estimation. In the future, we aim to extend these algorithms to 3D modular robots, which would allow for even more inter-

esting studies of 3D object shape estimation in future work. Additionally, there is much we could learn from practical implementations of these algorithms on the physical DONUt hardware. This work brings us a step closer to autonomous modular robots capable of perceiving their surroundings through embodied interactions.

CHAPTER 8

SOFT ROBOTIC OSCILLATORS WITH STRAIN-BASED COORDINATION

At the microscale, multicellular organisms often use coupled oscillations to synchronize, disperse, aggregate, and locomote. Popular examples include *Dictyosteliida*, a slime mold where cells coordinate by inducing chemical waves in response to food deprivation [85], and *Trichoplax Adhaerens*, an epitheloid where cells modulate contraction degree and rate to collectively locomote and regulate harmful mechanical stresses [8]. These microorganisms are proof that robustness without global information is possible through a combination of collective physical interactions and local, information-lean signaling. Future robot swarms with limited situational awareness operating in stressful and dynamic environments ranging from the micro- to macro-scale can benefit from studying such emergent behaviors in living collectives, and the mechanisms needed to translate them to simulated and physical robotic hardware.

To enable such studies, we introduce the Foambots platform consisting of soft, robotic modules capable of coordinating, communicating, and moving by sensing and inducing perturbations and strain in the collective (Fig. 8.1a). The modules couple loosely through 6 magnets embedded in their perimeter. Similar to the *Trichoplax Adhaerens*, the Foambots contract and expand in a 2D plane through fluidic actuation, and use strain sensors on their perimeter to reason about their own state and the actions of their neighbors (Fig. 8.1b-d). Beyond accommodating strain-based coordination, the soft modules hold several key advantages over their rigid counterparts. They consist of fewer mechanical parts, and are simple and easy to produce without advanced infrastructure. Compli-

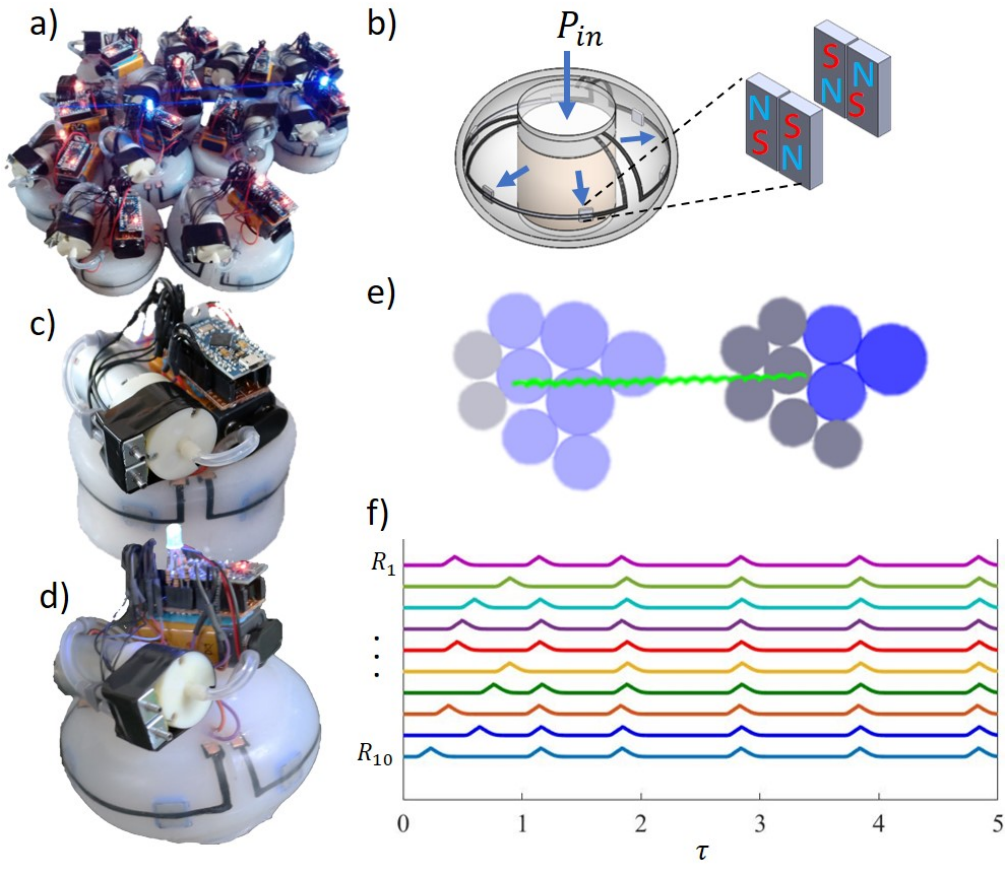

Figure 8.1: a) 12-module Foambot collective. b) Illustration of an expanded module with 6 magnets and 3 strain sensors able to loosely couple with neighbors, sense its own state and state transitions in neighboring modules. c-d) Module in contracted and expanded state. e) Simulated modules locomote as a result of traveling waves of expansion and contraction. f) Module radius over time as 10 out of a 100-module simulated collective synchronize.

ance facilitates large aggregations with low mechanical tolerance in fabrication. It furthermore ensures safe physical interactions between modules and between modules and external objects. Soft modules may also be used for a wider range of tasks. The soft module membrane can deform to fill gaps, and the collective can change its overall stiffness both as a function of module density and as a function of module expansion state. We have prioritized these design features as a first step toward applications such as active bio-medical stents or mobile retaining structures, such as temporary dams.

The remainder of this article discusses related work and details hardware design, fabrication, characterization, and exploratory experiments, alongside a coupled oscillator algorithm to produce emergent behaviors in a custom simulator (Fig. 8.1e-f). We hope this platform will further research on and serve as a low-barrier of entry to the study of physical interactions in the collective robotics realm.

8.1 Related Work

The Foambots platform is related to two, largely separate bodies of work in literature. The first is *active matter*, where simple oscillating robots leverage statistical mechanics to produce global behaviors from local physical interactions, such as motion or synchrony [98, 251, 176]. Most notably, the Particle robots used rigid components and statistical mechanics demonstrating directed motion by phase locking their oscillations to a global signal [98]. In contrast to these robots, the Foambots are designed for studies of local coordination via strain, and additionally benefit from soft material properties as described earlier.

The second body of work is *modular robots*, where physically connected agents reason deliberately about how to produce collective behavior. Modular robots inspired by natural cells was first proposed by Fukuda [54], and has since the introduction of soft robots been followed up by a wealth of examples of soft modular cubes in rectilinear lattice formations, [238, 190] just to name a few. These studies often focus on producing peristaltic locomotion or conveyor belt transport of other objects. As is true for most soft robots, the ma-

jority still rely on external power or pressure, and none have coupled sensing and actuation. They typically rely on either manual assembly leading to fixed topologies, or loose magnetic coupling which can be cumbersome as connecting tubes and wires tangle. As alternatives to pneumatics, [223] leveraged passive deformations in flexible PCBs, and switchable magnets to produce collective motion. [245] demonstrated magnetically coupled tensegrity modules capable of collective motion with a specific focus on ease of assembly and pre-emptive stiffness tuning. Finally, although some robot collectives have shown coordination through physically transmitted vibrations [118, 110], none have the coupled strain actuation and sensing which is key to coordination in e.g. *Trichoplax Adhearens*.

8.2 Foambot Fabrication

A Foambot module consists of a rigid electronic core resting on top of a poro-elastic foam which is surrounded by a polymer pocket that can expand radially upon pressurization. The hardware was designed with accessibility in mind: fabrication requires little know-how or specialized equipment beyond a soldering station and a well-ventilated space. Each Foambot module can be fabricated with ~3 hours of active time and ~5 hours of curing time. In our case, we molded four modules simultaneously with only a marginal increase in production time.

The poro-elastic foam core gives the soft robot structural integrity, while allowing fluid to flow throughout its volume to the outer cavity. The core is created through a salt-loss process (Fig. 8.2a), where Himalayan salt (grain diame-

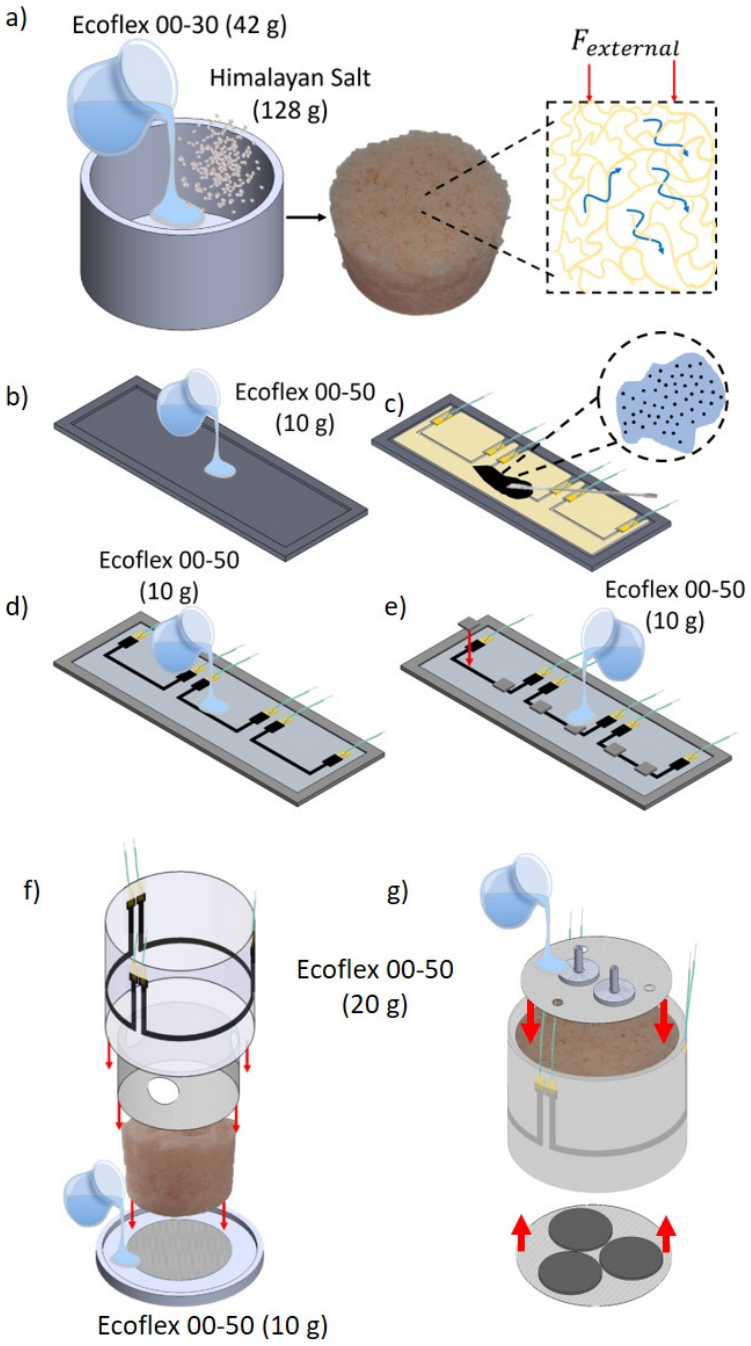

Figure 8.2: Module fabrication. a) Poro-elastic foam with 65% porosity. b-e) Carbon composite sensor with embedded magnets on the outer membrane. f) Poro-elastic foam wrapped in an inner strain-limiting layer and an outer membrane. g) Top strain-limiting layer and bottom 3D-printed sliders.

ter = 1 - 3 mm) is mixed with Ecoflex™ 00-50 before setting and is then dissolved after the silicone has set. The salt grains are well-packed such that the resulting pores are interconnected, thus allowing fluid to flow through its volume. Once cured, the core is wrapped by a strain-limiting layer that creates a barrier between the internal porous pocket and the outer cavity. The strain-limiting layer is fabricated by pouring Ecoflex 00-50™ into a mold with a piece of laser-cut fabric. The holes along the length of the strain-limiting layer allow air to flow to the external cavity.

The stretchable outer membrane encompasses 6 magnet pairs and 3 resistive strain sensors (Fig. 8.1b). The magnets enable modules to aggregate loosely. The sensors enable sensing of three event types: modules can sense the extent of their own expansion; they can sense when new neighbor attachments form; and they can detect when attached neighbors start to expand. By including three separate strain sensors, modules have a coarse sense of directionality.

The outer membrane is fabricated by first pouring a 1 mm thick layer of Ecoflex™ 00-50 into a rectangular mold. After the first layer has set, a stencil paper is placed on top of it. Copper-taped electrodes are soldered to silicone wires and adhered to the Ecoflex™ 00-50 surface using Silpoxy™. A hand-mixed Carbon composite is spread across the surface of the stencil. The Carbon composite is composed of Carbon Black powder and Ecoflex™ 00-30, part A, with a mass ratio of 1:6 [107]. A second 1 mm thick layer of Ecoflex™ 00-50 is added on top. When the second layer has set, we adhere the six magnet pairs with equal spacing using Silpoxy™, and firmly embed the magnets in the membrane through another thin layer of Ecoflex™ 00-50. The pairs consist of two magnets oriented in opposite directions to ensure that modules can attach

in any orientation. Each magnet is made of NdFeB (Grade N52) material with a surface field of 3114 Gauss. Upon completion, the membrane is wrapped around on itself to form a cylinder. The membrane is positioned such that the gap between its two ends can be filled by Ecoflex™ 00-50 (Fig. 8.2b-e).

Finally, the outer membrane is positioned around the poro-elastic foam (Fig. 8.2f-g). The inner strain-limiting layer and the outer membrane are placed flush with the bottom of the foam, wrapped around it, and the ends are glued with Silpoxy™. Ecoflex™ 00-50 is poured into a mold to form a 2 mm thick layer at the bottom of the module. The upper edge of the outer membrane is then folded inward and glued against the inside of the strain-limiting layer with SilPoxy™. A circular strain-limiting layer (embedded in Ecoflex™ 00-50) is placed on top of the foam and glued to the folded membrane sides. After the SilPoxy™ sets, Ecoflex™ 00-50 is poured on the top to create a 15 mm layer that restricts upward expansion. The bottom strain-limiting layer and sliders (printed in Veroblue with a Stratasys Objet 3D printer with 300 μm resolution) are glued to the bottom of the module. The sliders reduce friction, enabling easy testing of the collective on a variety of surfaces.

To control the Foambots, the core electronics consist of an Arduino Pro Micro, an Uxcell 6V miniature air pump, two Uxcell 5V mini solenoid valves coupled in parallel, an RGB LED for debugging, and a 9V battery (Fig. 8.3a).

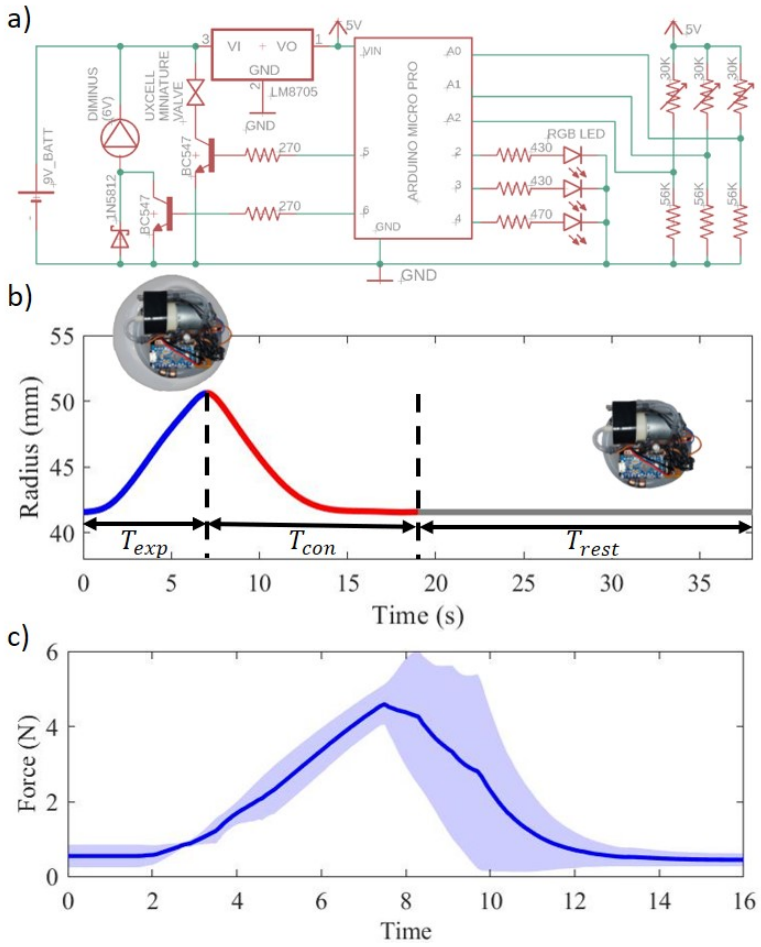

Figure 8.3: a) Module driver schematic. b) The oscillatory cycle of a module with T_{exp} = 7 s, T_{con} = 12 s, and T_{rest} = 19 s. The inserts show the module top view at full expansion/contraction. c) Pushing force exerted on a strain gauge by a module with T_{exp} = 6 s and T_{con} = 10 s.

8.3 Foambot Characterization

8.3.1 Actuation

The Foambot modules actuate through expansion and contraction of their outer membrane. During inflation, the outer membrane exhibits an approximately linear increase in radius; this behavior is mirrored during depressurization (Fig. 8.3b). The full actuation cycle consists of an expansion period, a contrac-

tion period, and a rest period. Given the particular pump and membrane elastic modulus, we found the following parameters to provide significant changes in properties, while limiting adverse material effects: By running the pump for T_{exp} = 7 s, we see 21% increase in radius from R = 42 mm to 51 mm, a notable amount of strain amongst soft sensors and actuators. From a fully inflated state, in isolation, it takes T_{con} = 12 s for the module to deflate to ambient pressure. Further, to enhance sensor signal to noise ratio as discussed in the following section, we normally add a rest period after an expansion and contraction cycle where the module remains passive (T_{rest} = 19 s). Note that the radial expansion creates pressure distribution on the surroundings, which allows the module to perform work on itself or on others, depending on the balance between its own pushing force and the static friction force of its neighbors.

8.3.2 Acting Forces

Three forces dominate movement in a Foambot collective - magnetic attraction, pushing forces, and frictional forces with the floor. A module will slide across a surface making or breaking connections with neighboring modules if the combined magnetic and pushing forces acting on it are greater than its frictional force. Note that the relative magnitude of each of these forces is an interesting line of study that we leave for future investigations.

We measured the magnetic holding force between two magnet pairs embedded in Ecoflex™ 00-50 to be 2.38 ± 0.33 N (n = 10). This was measured by fixating one to a load cell (Adafruit, 5 kg), while pulling the other away with a linear actuator. Fig. 8.3c shows the pushing force during module expansion.

Note that the contraction cycle shows more variation due to slight differences in the valves and membrane thicknesses. When measured for a module with T_{exp} = 6 s, with a maximum radial expansion of 13% the force reached 4.6 ± 0.54 N. We performed this experiment by placing the module at rest between two walls, one fixed, another connected to the aforementioned load cell.

Due to their slow movement, module friction with the floor is largely static. The static coefficient of friction between a module's sliders and different surfaces was found by connecting a module to one end of a string on a pulley and adding load to the other end until the module began to move. These experiments were done with five different modules (each weighing approximately 250 g) for a wooden table surface, a Styrofoam surface, and a white board plane; the resulting static coefficients of friction were determined to be 0.27 ± 0.01, 0.52 ± 0.11, and 0.29 ± 0.03, respectively. Each of these surfaces is common to research labs where algorithms for planar, modular robots can easily be tested across different terrains.

8.3.3 Deformation

As previously discussed, the softness of the modules paves the way for a range of interesting studies. Interestingly, as the modules inflate, their elastic modulus decreases. When at ambient pressure, modules have an elastic modulus given by the internal poro-elastic foam wrapped by membranes of Ecoflex™ 00-50. As the module expands, it effectively creates more open space in the outer cavity decreasing the effective elastic modulus, similar to the way poro-elastic foams with increasing porosities reduce their effective elastic modulus. To character-

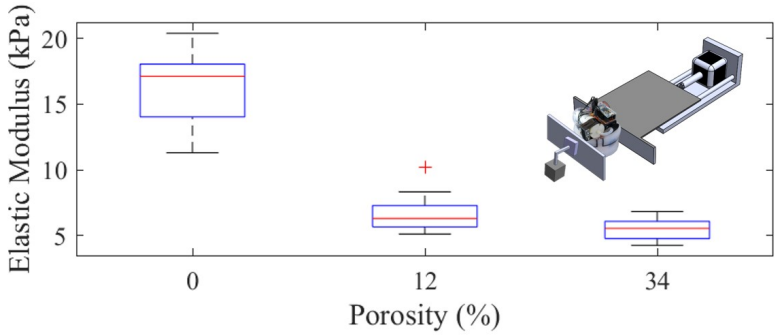

Figure 8.4: Compression tests of a single module (n = 15).

ize this property we performed compression tests on a single module located between one plate connected to a linear actuator and another mounted with a load cell (Adafruit, 5 kg) to determine the applied force. We assumed a constant area for determining stress, equal to the cross-sectional area given at the module's center. Although the area of interest changes with applied stress, we found that this approximation matched the general profile found in poro-elastic foams compressed using an Instron machine.

8.3.4 Sensing

The three sensors on the Foambots facilitate strain-based coordination. These sensors exhibit greater electrical resistance as their length increases and when they are squeezed. The former is most pronounced when modules expand; the latter depends on the acting forces between neighboring modules, e.g. during expansion, and any magnetic connections. To measure their value, each strain sensor is connected in a half-bridge Wheatstone configuration. We characterized the sensor performance in terms of repeatability, consistency over time, and the mechanical coupling between them on both passive and active modules.

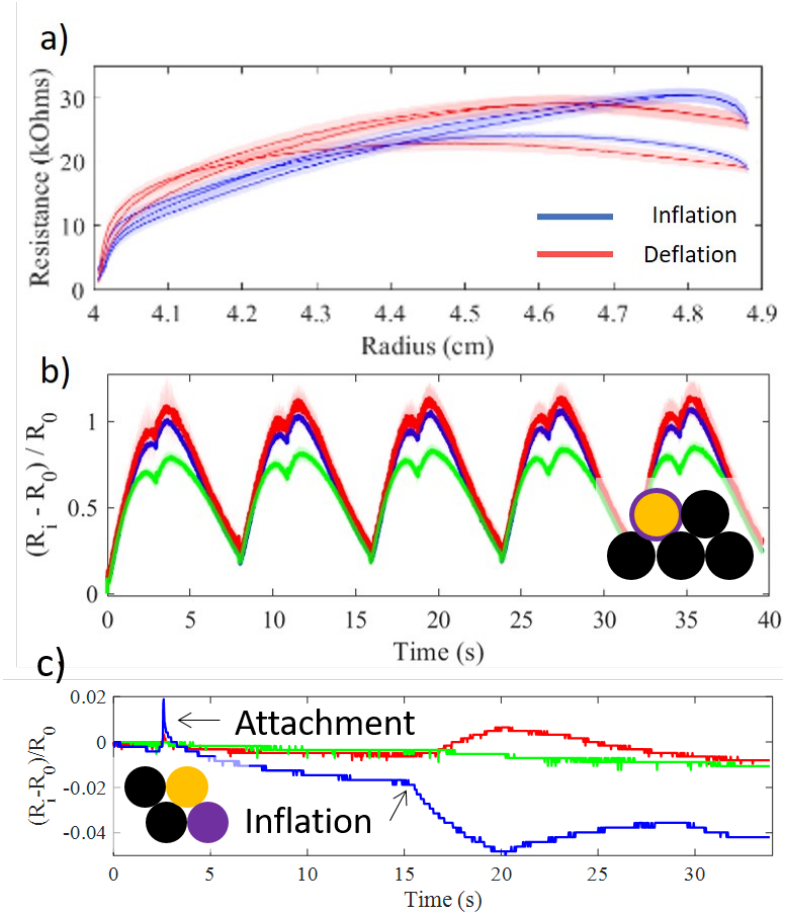

Figure 8.5: a) Output from two sensors embedded on a module oscillating 10 times. b) Normalized sensor outputs from an oscillating module (yellow) with four neighbors (black). In a) and b), solid lines and shaded regions represent mean and standard deviation respectively. c) Normalized sensor outputs from a passive module (yellow) with two passive neighbors (black), and one module (purple) attaching and oscillating.

Fig. 8.5a shows the raw resistance versus module radius over 10 expansion/contraction cycles for two sensors. While the absolute value and range of resistance varies due to the inexpensive, manual fabrication process, the general profile is qualitatively similar.

Fig. 8.5b shows the normalized sensor output for all three sensors on an active module with four passive neighbors arranged as shown in the insert. This data demonstrates the repeatability of the resistance-strain relationship over

time. Again, we note that the range varies between sensors, but the qualitative behavior is similar and stays constant over multiple oscillation cycles. Specifically, the signal dips toward the end of the expansion period, a feature that is apparent at approximately the same strain (~1.2 mm / mm) across all sensors, and is mirrored at the beginning of the deflation period (~1.3 mm / mm). This could be attributed to the gel-like nature of the Carbon composite: a lower strain value might break up some of the electrical pathways and increase resistance; a strain higher than a given threshold might cause the gel to move around slightly within the Ecoflex™ membrane and repair electrical pathways and decrease resistance. Further tests exploring these sensors would be needed to confirm this.

We tested the ability of a module to detect new module attachments and neighboring expansions (Fig. 8.5c). Because of sensor variability, and because their signal changes depending on whether one or two modules are connected over their length, we distinguish between the two events as follows. Attachments were detected by checking if the change in raw sensor output over 100 ms was greater than 4 bits. Inflations were detected by doing a complementary low pass filter on the change in raw sensor output (alpha = 0.5), and checking for a change greater than 3.2 bits over 1 s. To eliminate multiple detections triggering in a row, we omit detections occurring up to 5 s after an inflation has been triggered. Normally, at this time, the sensing module would itself be inflating and consequently ignore new events anyway. We tested this method with three sensors over 30 attachments and 30 expansion cycles, in a three and six consecutive neighbor configuration. All attachments were detected with a 0.14 s ±0.08 s delay. 27 out of 30 inflations were detected with a 1.08 s ±0.56 s, as well as 5 false positives and 1 false negative. Four of the false positives occurred on sensors that were not connected to the expanding module.

We further found that the sensors have a low signal to noise ratio while the onboard pump is running. This is due to both direct noise coupling in the shared power supply, and because the loop configuration of the strain sensors pick up electromagnetic interference. Therefore, modules can effectively only sense strain when the module is not expanding. Although this is limiting, this concept has precedence in natural collectives, where, e.g. large networks of neurons can create emergent behavior in spite of refractory periods occurring after individual action potentials.

8.4 Foambot Collectives

The advantage of a single Foambot stems from coupled sensing and actuation and its ability to elastically deform. An aggregate of modules can collectively leverage these simple functionalities to produce emergent collective behaviors such as collective force exertion, locomotion, and fracture (Fig. 8.7). Using up to 9 modules, we demonstrate that each of these behaviors are feasible with the current hardware and encourage the reader to look at the accompanying video. Note that we leave it to future work to incorporate full feedback behavior on the hardware, and that these videos represent hard-coded cycles. In the next section, we expand on how decentralized algorithms for these robots might work through a quasi-static simulation framework.

Fig. 8.6 demonstrates how synchronized modules may push in unison to achieve greater force exertion. Using the same 5 kg load cell setup mentioned in Sec. 8.3.2, we found that three modules connected in parallel could exert more than three times the force feasible when out of phase.

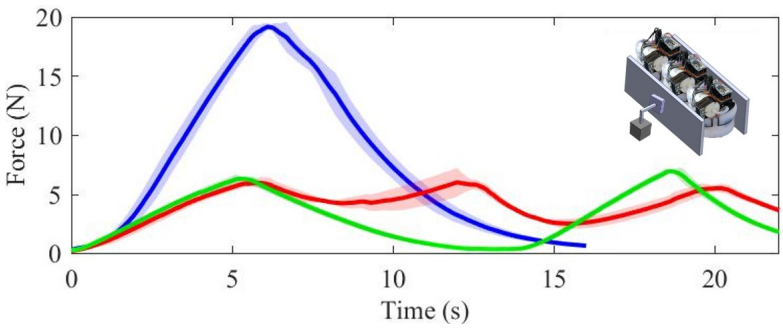

Figure 8.6: Force exertion by three modules (T_{exp} = 6 s, T_{con} = 10 s, T_{rest} = 0 s), when they are synchronized (blue), and out of phase by ~ 70 (red) and 135 (green), respectively.

Collective motion appears when the following conditions on the module pushing force are satisfied: it must be greater than its static friction force and less than the summed static friction force of the modules that actuate after this module. Figs. 8.7a-b show the ability of Foambots to locomote collectively through waves of expansion and contraction traveling opposite the module motion. We found that 3 modules move ~0.1 robot radii per cycle, and 9 modules move ~0.125 robot radii per cycle. Note that in the latter experiment, the top left module is left behind. This is caused by the combined pushing force of several modules along the diagonal expanding together; the module is pushed out such that it breaks a connection with one of the modules and can then not join back with the collective as the group moves away, severing its second connection. This example highlights 1) that the aggregate is robust to loss of individuals and 2) the need to carefully couple neighboring oscillations to avoid unwanted fractures.

As previously indicated, the choice of Foambot magnets will affect the collective behavior. Strong magnets allow experiments without fracture; however, weak magnets facilitate loose magnetic coupling and reconfiguration which may be used advantageously to overcome environmental geometric constraints or to converge on more stable collective morphologies (tight circle packing).

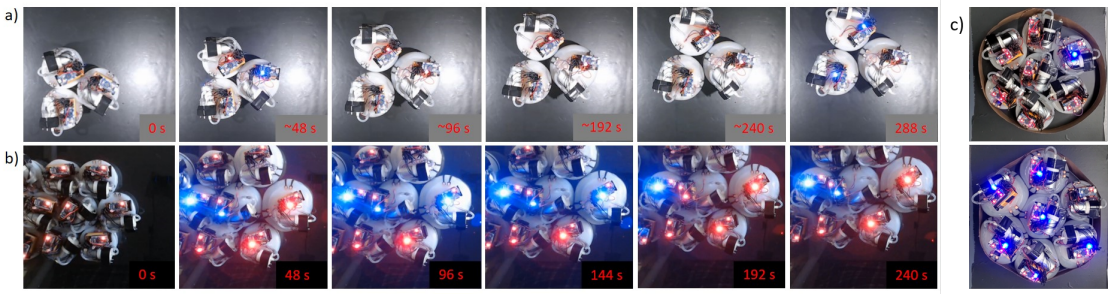

Figure 8.7: a-b) Snapshots from movie showing locomotion in the uper right direction of 3 and 9 modules when there are traveling waves in the opposite direction. c) 7 synchronized modules expand and fill the space in a constraining membrane. Blue light signifies expansion, red contraction, and blank rest.

Emergent behaviors based on these low-level physical interactions are predominantly dependent on the number of modules, the starting configuration of the collective, the balance between attractive and frictional forces, and the amplitude and synchrony of radial expansion. As shown throughout the videos summarized in Fig. 8.7, the slow movement of these modules enables most broken connections to be repaired. In cases where different sections of the collective are moving in opposing directions, the appearance of larger fractures may be reduced with greater connection density and appropriate actuation patterns.

8.5 Simulation and Metrics

To support algorithmic development, we wrote a custom simulation framework based on Matlab® and / or the free alternative Octave Online. The simulation includes the ability of modules to expand and contract radially and detect when neighboring modules transition between states. It also includes collision checking, pushing forces, static friction, and magnetic forces. Informed by experiments and COMSOL simulations, the latter was incorporated as a decaying

function with a maximum force capped at 2.4 N at separation distances ≤ 0.38 module radii, and a minimum of 0 N at a distance greater than 1 module radii. Incorporation of module deformations is left for future work.

Inspired by the rich literature on coupled oscillators dating back to the basic Winfree model [224], we suggest three metrics to evaluate the emergent behavior of the collectives:

Global coherence: the average coherence of phases amongst all modules. This is a dimensionless value between 0 and 1:

$$Z_G = \frac{1}{N}\left|\sum_{j=1}^{N} e^{i\theta_j}\right| \tag{8.1}$$

Local coherence: the average coherence of phases amongst neighboring modules. This is a dimensional value between 0 and 1, where m is the iterative counter for the total number of modules and n is the number of neighbors around a given module:

$$Z_L = \frac{1}{N}\sum_{m=1}^{N}\left[\frac{1}{n}\left|\sum_{\langle j\rangle}^{n} e^{i\theta_j}\right|\right] \tag{8.2}$$

Linear momentum: the collective motion:

$$P = \frac{1}{N}\left|\sum_{i=1}^{N} \dot{x}_i\right| \tag{8.3}$$

Throughout these metrics, N is the total number of modules in the collective, θ_j is the phase of a given module, and $\dot{x}_i$ is the change in module position.

A high global coherence means all modules share the same phase; however, it is much more common to encounter scenarios where there is low global coherence and high local coherence due to fractures appearing in the collective.

Along the same track, a high linear momentum means that the collective moves in the same direction, which implies that the collective most likely remains connected. A low linear momentum could also mean that the collective has broken into multiple clusters, each possibly moving in a different direction.

8.6 Coupled Oscillator Algorithm

To demonstrate how modules may achieve emergent behavior, we took inspiration from past work on static coupled oscillators [224, 46]. Specifically, we modified the original model, such that modules maintain equal natural frequency, and a constant T_{exp} and T_{con}, adjusting only their T_{rest} to achieve collective oscillatory patterns. More specifically, modules map their actuation cycle to a phase value as shown in line 2 of Algorithm 1. Here, τ_i is the time since the cycle of module i began, A_i is the actuation state (-1 for contraction, 1 for expansion, and 0 for rest).

Algorithm 1 describes how modules adjust their cycles, and the behavior is further illustrated in Fig. 8.8, through radial profiles of two interacting modules. The algorithm uses a coupling factor, $K \in (0, 1)$, as a "knob" to control the behavior of the collective. When a neighboring activation is detected, an agent at rest will update its phase value by an amount proportional to the phase difference between itself and the activating neighbor, scaled by K. See line three of Algorithm 1 for the exact expression.

When a neighbor inflates, the "listening" module calculates a new phase value $\theta_i(\tau_i)$ as a function of the coupling factor and its phase difference with module j. Our algorithm allows for two possible cases: if the new phase is over

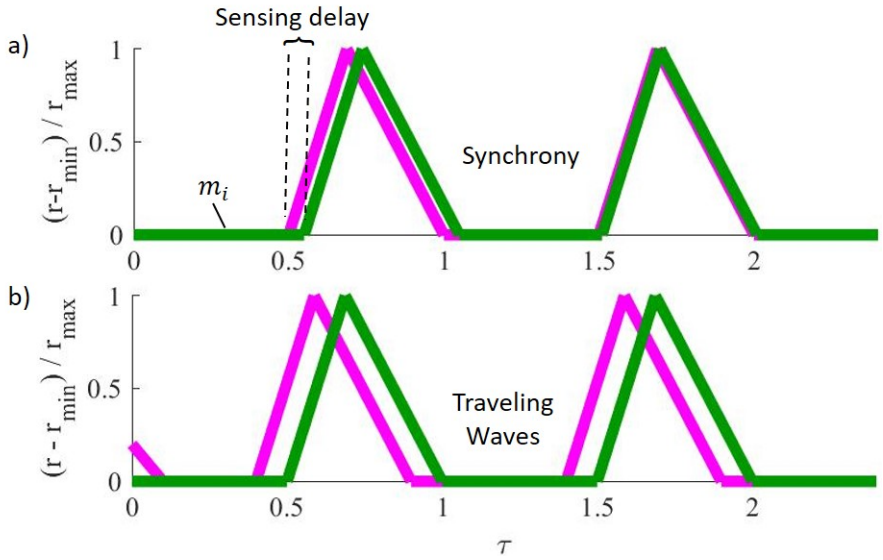

Figure 8.8: Graphical representation of modules' behavior when a sensing module (green) responds to a neighboring module's (purple) expansion. a) The coupling factor K is sufficiently high that it brings two modules to synchrony within one cycle. b) The sensing module maintains a phase offset with its neighbor, enabling traveling waves of actuation.

the expansion threshold, the module at rest immediately begins to expand and sets $\theta_i(\tau_i) = 0$. In the second case, the phase update does not yet require expansion, but the resting module still shortens the amount of time it stays at rest. Intuitively, increasing K increases synchrony by causing the jump in phase to increase, bringing modules closer in phase to their neighbors during an inflation event.

To demonstrate the range of behaviors that can emerge from this algorithm, we evaluated our metrics over a range of values of K and the number of modules in a rectangular 10-module tall configuration. Fig. 8.9a-b demonstrate synchronization as the global and local order parameters increase with increasing K. A snapshot of 10 modules within a 100 module collective synchronizing is also shown in Fig. 8.1f. Fig. 8.9c demonstrates locomotion, caused by asynchronous patterns of activation leading to higher linear momementum for lower

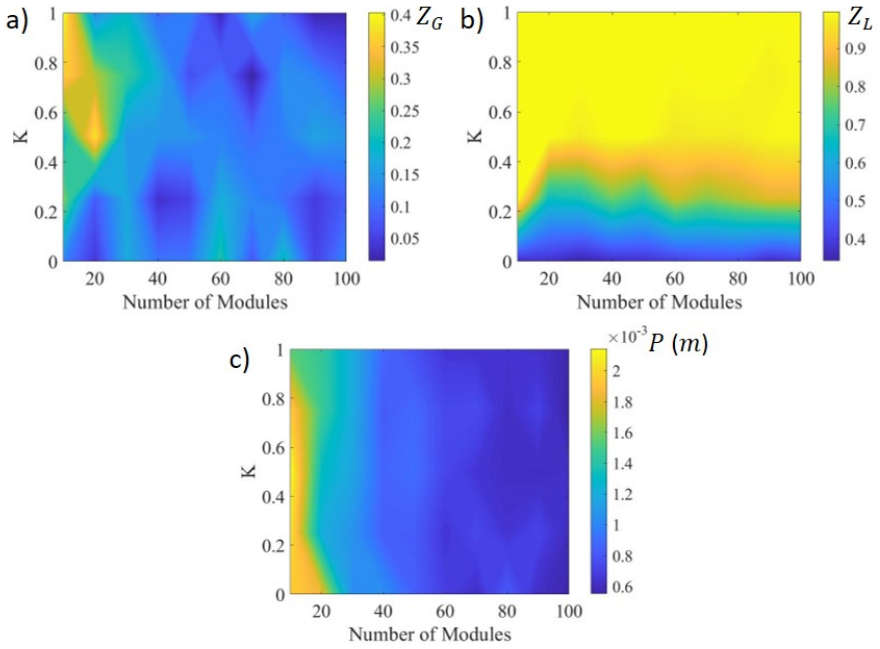

Figure 8.9: Algorithm 1 applied to 10 - 100 module collectives in a rectangular configuration. Results are averaged over 20 simulations. a) Global Coherence (Z_G). b) Local coherence (Z_L). c) Linear momentum (P)

values of K and smaller collectives. Fig. 8.9a and b show higher local than global coherence, indicating fracture. At high numbers of modules, the collective may form fracture lines that split the modules into multiple groups and thus lead to high local coherence but low global coherence.

Algorithm 1 Coupled Oscillator Algorithm

if $A_j = 1$ and $r_j \sim r_{min}$ **then**
  $\theta_i(\tau_i) = \frac{\tau_i}{T_{exp}+T_{con}+T_{rest}}$
  $\theta_i(\tau_i + dt) = \theta_i(\tau_i) + K(\theta_i(\tau_i) - \theta_j(\tau_i))dt$
end if
if $t_i^s \neq 0$ **then**
  if $A_i = 0$ and $\theta_i(\tau_i)T/(2\pi) < T_{exp} + T_{con}$ **then**
    $A_i = 1$, $\tau_i = 0$
  else if $A_i = 1$ and $\tau_i = T_{exp}$ **then**
    $A_i = -1$
  else if $A_i = -1$ and $\tau_i = T_{exp} + T_{con}$ **then**
    $A_i = 0$
  end if
end if

8.7 Summary

We introduced a soft robot to enable studies on strain-based coordination of robot collectives, following inspiration from natural systems. This system is unique in that modules directly couple actuation and signaling to coordinate locally. We demonstrated the effects of synchrony, locomotion, and fracture in 9 real modules and up to 100 simulated modules as coupled oscillators. In the future, we intend to leverage this platform to demonstrate robust emergent behaviors through local interactions on the real robots. Given the extreme simplicity of these robots and the strain-based coordination mechanism, insights from these studies may pave the way for robust emergent behavior in robot swarms interacting physically at the micro- to macro-scale.

CHAPTER 9

MICROROBOT COLLECTIVES WITH RECONFIGURABLE BEHAVIORS, FUNCTIONS, AND MORPHOLOGIES

Collectives in nature often make use of reconfiguration, altering the group's morphology to carry out complex functions in various environments [209, 53, 85, 116, 155, 218, 222]. At small scales, reconfiguration enables organisms to adapt to environmental disturbances and complete diverse functions. Inspired by the robustness and adaptability of these systems, engineers have mimicked naturally occurring behaviors through robot collectives that are programmable and interact with their environment to enable robust reconfiguration. For example, at the macro-scale, Kilobot collectives use programmed interactions to create different formations [164, 178, 181] and reconfigure to manipulate objects based on global signal inputs [14]. Other macro-scale robot collectives demonstrate how environmental interactions like contact-based coupling [98, 170, 25, 39] can enable collectives to change their shape [161, 41, 172], function, and mode of locomotion [15, 137, 169]. At the micron-scale, reconfiguration in artificial systems is rare and it has the potential to open up possibilities in biomedicine, environmental remediation, and other applications [125, 3]. At this scale, collectives interact through physical and chemical interactions to organize global responses beyond the reach of individuals [216, 235, 228, 113, 217]. The main paths for reconfiguration at the microscale include self-driven systems with active particles, and externally driven systems with particles controlled by one or more global signals [177]. In self-driven systems, local stimuli dominate a particle's behavior; particles react to their neighbor's actions to produce collective behaviors [160, 13, 126, 213, 138]. Externally driven microrobot collectives may be driven by magnetic fields [215], light [94, 250], acoustics [2], or any other

global stimulus that can alter the motion of one or more particles in the system. Given the high permeability of magnetic fields in many biological and non-biological materials used in biomedical applications, many researchers have focused on developing particle collectives2 [235] and soft materials [249, 76] that are responsive to one or more quasistatic [44] or time-varying [50] magnetic fields. Therefore, a system that can utilize the mutual interactions between its constituents and respond to a global magnetic field stimuli to exhibit different behaviors would help realize a versatile reconfigurable robot collective.

One of the first magnetically actuated self-organizing systems was demonstrated by Grzybowski et al. [65, 66], where millimeter-sized magnetic disks at the fluid-air interface spun in response to an external rotating magnet and assembled into hexatic patterns as a result of their hydrodynamic interactions. Manually changing the shapes of the magnetic particles [67] enabled the system to reconfigure by exploiting hydrodynamic interactions and a permanent magnet's potential well confinement to create self-organized collectives. Other systems, like the one used in this study, use capillary interactions by patterning edge corrugations on micro-disks so that the micro-disk collectives self-organize into square lattices [216] and rotating collectives [215]. Other microrobotic systems have demonstrated ribbon, chain or vortex formations [235, 228, 113, 227, 242, 241], locomotion [44, 225], and object manipulation [148, 114]. One study shows impressive locomotion of two microrobotic swarms that can navigate through various mediums and complex environments; however, each swarm demonstrates a single mode, one creates ribbon-like formations while the other creates vortex-like formation [241]. Another experimental system produces four emergent modes (liquid, chains, vortices, and ribbons) [228], and it relies on a solid substrate for symmetry breaking to en-

able the formations and locomotion. Although this system exhibits four modes, the relative strength of different mutual interactions in the system is not clearly tunable; this limits the control of the collective's size, inter-particle separation, and each mode's local order. An ideal system should enable an external control parameter, like the magnetic field frequency, to dynamically program relative dominance among different particle-particle and particle-environment interactions to reconfigure between several tunable modes and their functions. Moreover, a system that can transition on-demand from globally driven behaviors to a mutual interactions - dominated self-propelling behavior (like self-propelling Janus particles [160, 13]) is yet to be realized. Such a system would not only be useful for robotics applications but also for fundamental studies to explore the link between globally driven and active systems.

Here, we present a micro-disk collective, consisting of around 120 micro-disks, at the fluid-air interface externally driven by time-varying magnetic fields that enable the collective to rotate, oscillate, remain static although individual micro-disks are dynamic, form chains, locomote through magnetic field gradients, perform contact-based and flow-based object translation and rotation, and explore an open space through gas-like self-propelling micro-disk pairs (Fig. 1). Each behavior is enabled by several particle-particle and particle-fluid interactions (e.g., hydrodynamic, capillary, and magnetic dipole-dipole interactions) that are controlled by external magnetic fields. Some of these behaviors are unique to our system and have no counterpart in other systems. Morover, our system shows both isotropic (rotating collectives) and anisotropic (chains) behaviors, and it also transitions from such globally driven behaviors to mutual interactions - dominated self-propelling behavior (like self-propelling Janus particles). The system's versatility and the micro-disks' ability to remain at the

fluid-air interface is well-suited for practical applications like manipulating cells within a microfluidic chip, guiding development of micromachines, acting as a model system for exploring self-organization in soft matter, and studying collective behaviors that could finally translate to three dimensions and be used for microscale packaging [125] and medical applications, such as targeted active drug or other cargo delivery [6, 28, 49].

9.1 Modes of Collective Behavior

All of the collective behavior modes in this study are produced by collectives of magnetic micro-disks at the air-water interface controlled by a biaxial oscillating unifiorm magnetic field (Supplementary Fig. 1). Micro-disks are driven by the global magnetic stimuli and locally interact through three pairwise forces: capillary, hydrodynamic, and magnetic dipole-dipole interactions. Each micro-disk is circular and has a six-fold symmetry given by six cosinuisoidal profiles along the disk's perimeter; the corrugations along each disk's boundary enables capillary interactions that can be attractive or repulsive depending on the relative disk orientations. The micro-disks' hexatic characteristic causes capillary interactions with six-fold symmetry. The number of symmetrically-placed cosinuisoidal profiles (between 2-6) would not significantly affect the behaviors presented in this work, however, the six-fold symmetry and circular shape are used because of simplicity in modeling the mutual interactions between such disks.When the corrugations on two micro-disks align, they attract; when they misalign above a threshold (8°) they repel each other. A uniform ferromagnetic nanofilm of cobalt on each micro-disk's surface enables orientation-dependent magnetic dipole-dipole interactions. The hydrodynamic interactions are depen-

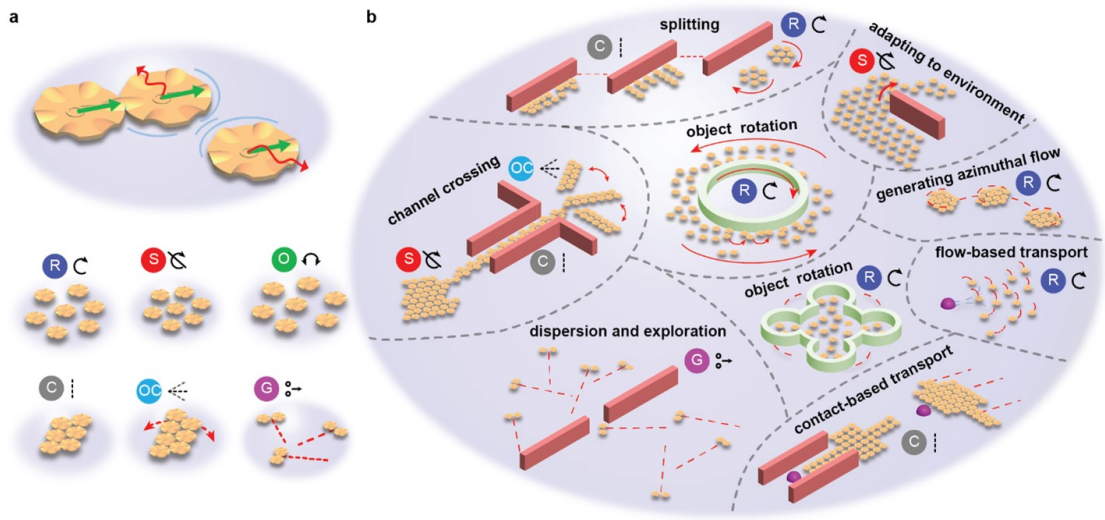

Figure 9.1: Microrobot collective reconfigurable behaviors and functions. (a) Three micro-disks driven by external magnetic fields exhibit magnetic dipole-dipole attraction, capillary attraction, and hydrodynamic repulsion (top). Six collective modes are possible: rotation (R), oscillation (O), static (S), chains (C), oscillating chains (OC), and gas-like mode containing self-propelling pairs (G) (bottom). (b) Schematic of collective transitioning between the possible modes to perform various functions. Starting on the left side and continuing clockwise along the edge: the collective starts out in static mode and transitions to a chain to locomote through a narrow channel and exit the channel to form oscillating chains (channel crossing). At the top, the collective lines itself up against a wall and uses the physical interactions with the wall to separate into two clusters when it transitions to rotation mode (splitting). The collective can then pass around an obstacle more easily by adapting inter-disk distance through its static mode at high magnetic field frequencies (adapting to environment). The collective can then rotate and locomote at the same time (generating azimuthal flow) and induce motion on surrounding objects through its azimuthal flow field (object rotation and flow-based transport). At the bottom, the collective forms chains and pushes on an object (contact-based transport) and then disperses through a gas-like mode (dispersion and exploration). The center images show the collective can rotate objects through the azimuthal flow field when the micro-disks are within the object as well as encapsulating it.

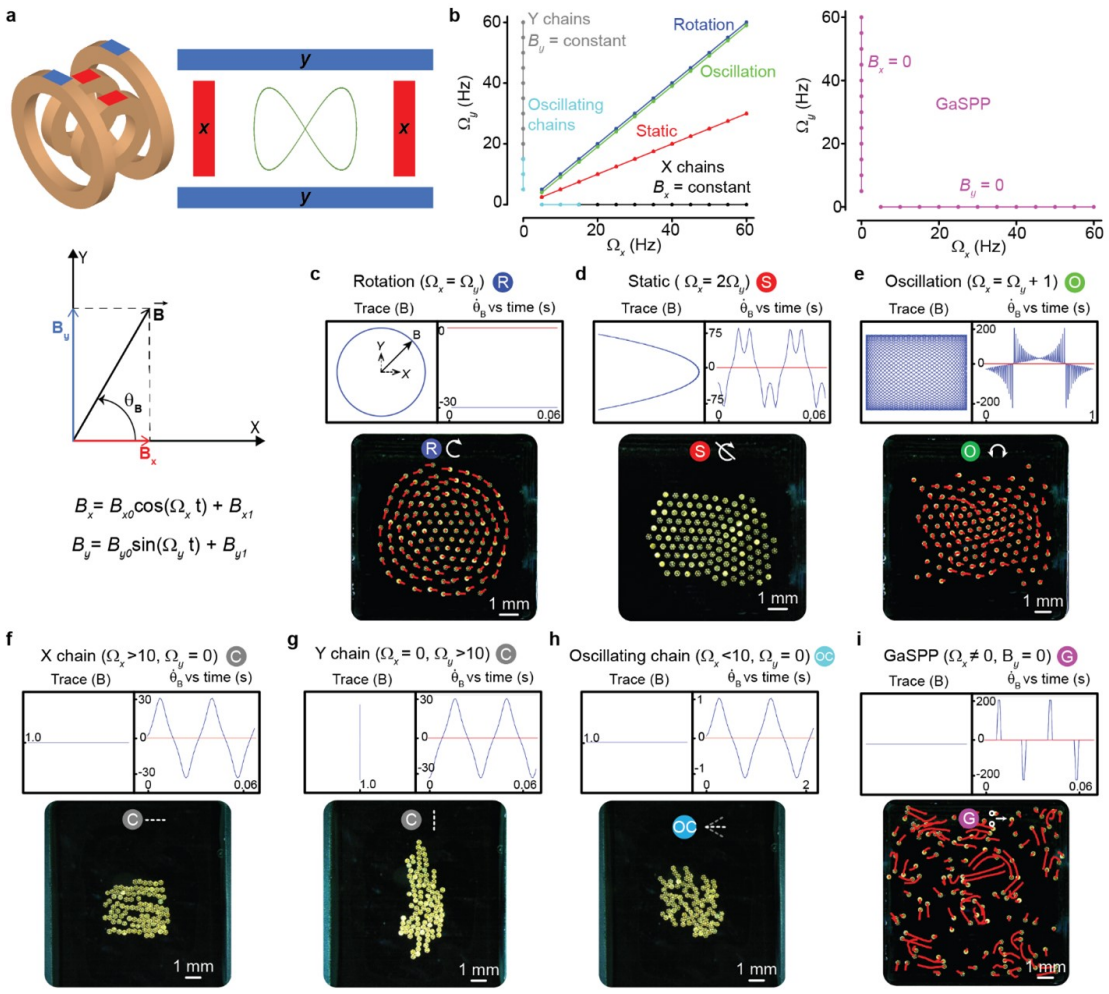

Figure 9.2: Demonstration of different collective modes. (a) The external magnetic field **B** modulated in 2D space by the axial magnetic oscillation frequencies, where θ_B is the orientation of **B** with respect to the x-axis. (b) Specific linear relationships between the two axial magnetic oscillation frequencies enables the different collective behaviors: Rotation (blue), static (red), oscillation (green), X chains (black), Y chains (gray), oscillating chains (cyan), GaSPP (magenta). (c-i) Summary of collective modes: Curve traced by the magnetic field vector Trace(B) (top left), the derivative of the orientation of magnetic field vector $\dot{\theta}_B$ (blue) with respect to the x-axis (red) (top right), representative experimental images of the collective exhibiting respective behaviors (bottom). The brightness of the images in (c-i) is enhanced using photoshop for better visualization. The symbols on top of the experimental images in (c-i) represent the mode that collective exhibits. These symbols correspond to those shown in Fig. 1a.

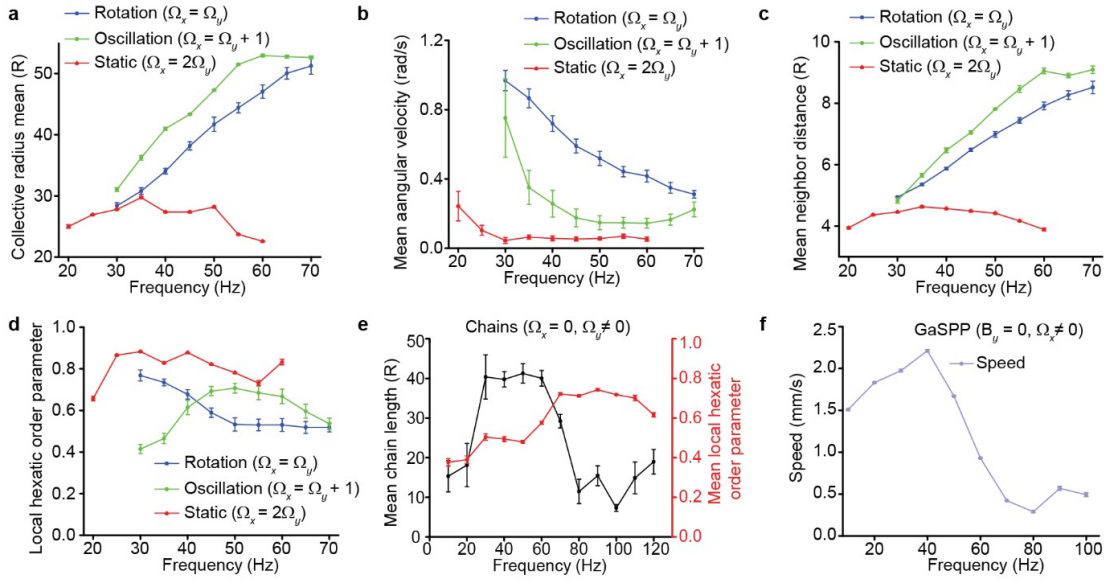

Figure 9.3: Characterization plots for the microrobot collectives of 120 micro-disks in different modes. (a) Collective radius, (b) mean angular velocity, (c) mean neighbor spacing, and (d) mean local hexatic order parameter for the rotation, static and oscillation modes. (e) Mean chain length and mean local hexatic order parameter for the chain mode. (f) Mean speed for the GaSPP mode. Error bars represent standard deviations over 10 s.

dent on micro-disks' instantaneous spin speeds; faster spinning micro-disks exert greater hydrodynamic repulsion and create larger azimuthal flow fields that cause the collective to spread out. Our system differs from those reported earlier [215] in that it exploits two independent oscillating magnetic fields (eq 1), each along one of the axes on a horizontal plane, as compared to a rotating magnetic field used in the previous studies, to drive the ferromagnetic micro-disks. Therefore, the behaviors shown by the previous systems are a subset of those exhibited by the current system. Specifically, our system shows the same behaviors as the system reported earlier when the oscillation frequencies along both axes are equal, i.e., $\Omega_y = \Omega_x$, which produces a rotating magnetic field. The use of two independent oscillating magnetic fields enables a richer set of behaviors, some of which are isotropic (e.g., hexatic-like circular collectives) while some

are anisotropic (e.g., chains). Moreover, our system can transition from globally driven behaviors to mutual interactions-dominated self-propelling behavior and vice-versa. The magnetic field profiles are explained in Fig. 2, and the behaviors are characterized in Fig. 3. The external magnetic field exerts a torque on the micro-disks, trying to align the micro-disks with external magnetic field vector. The relative strength of the three pairwise interactions changes as the global magnetic field oscillates at different frequencies, which allows the collective to exhibit different modes and functionalities dependent on the relationship between the oscillation frequencies of the two orthogonal magnetic fields, Ω_x and Ω_y, as shown in the line plots in Fig. 2a-b and the state map in Supplementary Fig. 2. Each colored line in Fig. 2b represents a different global behavior and is only one instance of several linear relationships that lead to that behavior. For instance, collective oscillation happens when the frequencies fulfill $\Omega_y = \Omega_x - 1$; however, the same general behavior could be found with $\Omega_y = \Omega_x - 2$ and $\Omega_y = \Omega_x - 3$. In this study, we do not exhaust all possible linear combinations that lead to particular behaviors, but instead focus on several distinct modes that enable useful functions and examine the collective's properties at one linear relationship for each mode. The magnetic field vector **B** is defined as:

$$\mathbf{B} = \begin{bmatrix} B_{x0} cos\,(2\pi\Omega_x t) + B_{x1} \\ B_{y0} sin\,(2\pi\Omega_x t) + B_{y1} \end{bmatrix} \tag{9.1}$$

where B_{x0} and B_{y0} are the amplitudes of the axial time-varying fields (10 mT), B_{x1} and B_{y1} are the constant axial fields (B_{x1} and $B_{(y1}$ are 0 for all modes except the X-chains where (B_{x1},B_{y1}) = (0, 10) mT, and t is time. As illustrated at the top of each subfigure in Fig. 2c-i, the axial frequencies affect the trace of **B**

along the two-dimensional (2D) workspace and the time-dependent behavior of $\dot{\theta}_B$; B drives the orientation of each micro-disk as it aligns its magnetic dipole axis with the external field, and $\dot{\theta}_B$ indicates the rate at which the external field changes its orientation. For example, $\Omega_y = \Omega_x = \Omega$ produces a rotating magnetic field, the trace of **B** is a circle and $\dot{\theta}_B$ is constant and equal to Ω. This rotating magnetic field exerts a torque on the micro-disks such that each disk spins about its own center of mass. The linear relationship between Ω_x and Ω_y changes each micro-disk's angular velocity and its axial oscillation over time. These variations along with the capillary, magnetic, and hydrodynamic interactions enable the global formations and functions described in the following sections.

9.1.1 Rotation Mode

For $\Omega_y = \Omega_x$ (blue line in Fig. 2a), **B** traces a circle, resulting in a rotating magnetic field that exerts a torque on the micro-disks (Fig. 2c (top)). Consequently, each micro-disk spins about its own axis at same angular velocity as the external magnetic field, below the step-out frequency ($\sim 65 - 75$ Hz), where the external magnetic torque is insufficient for synchronized disk rotation. Each spinning micro-disk creates an azimuthal flow field, which enables the collective to orbit around a common center of mass. Each disk's spin speed and the inter-disk hydrodynamic repulsion increases with frequency while the local hexatic order parameter decreases. This increased repulsion causes the collective to spread out and orbit more slowly (Fig. 3a-c). Also, the micro-disks further away from the collective's center of mass revolve faster than those closer to it (the red trajectory lines in the image in Fig. 2c) (see Materials and Methods subsection on experimental protocol). We reproduce the rotation behavior in simulations

using a numerical model constructed using the pairwise interactions (Supplementary Fig. 3). The agreement between the experiments and simulations suggests that the numerical model contains the right ingredients responsible for the behaviors of our system (for more details see the Materials and Methods subsection model for simulations). Above 60 Hz, the collective expands and conforms to the physical boundary's shape, however, the simulations retain the collective's circular shape across all frequencies. Although this affects the experimental evaluation of the collective radius, it exemplifies how confinement forces the collective to adapt its morphology. This mode's remarkable feature is the collective azimuthal flow field, which is used for various functions as demonstrated later.

9.1.2 Static Mode

The static mode is a novel behavior composed of individually dynamic micro-disks where each disk's center of mass remains static with respect to the global reference frame, but the disk oscillates about its own center axis. This mode is characterized for Ω_x and Ω_y lying on the $\Omega_y = \frac{\Omega_x}{2}$ line (red line in Fig. 2b and Supplementary Fig. 2). This linear relationship between Ω_x and Ω_y produces a parabolic trace of $\mathbf{B}$, which enables a time-varying profie for $\dot{\theta}_B$ (Fig. 2d). The oscillations of $\dot{\theta}_B$ across the x-axis indicate that micro-disks change their direction of oscillation and angular velocity over time, oscillating while fixed in place and interacting with their neighbors via time-varying pairwise interactions, which cancels out any fluid motion in the short term and keeps the collective static. Increasing the oscillation frequency increases micro-disks' effective hydrodynamic repulsion, which increases their mean neighbor separation distance until

the disks start to step-out around $\Omega_y = 50$ Hz (Fig. 3c). The distance between neighbors within the collective allows it to encapsulate objects while maintaining a high local and global hexatic order across all frequencies (Fig. 3d and Supplementary Fig. 4). Regardless of the object's size, the collective remains cohesive much more easily in this mode; in contrast, during the collective rotation, all micro-disks exhibit higher hydrodynamic repulsion on each other, which enables dispersion in the presence of non-uniform external forces like repulsion from boundaries and objects.

9.1.3 Oscillation Mode

Oscillating collectives are characterized for $\Omega_y = \Omega_x - 1$, with frequencies in the same range as rotating collectives. For this mode, $\dot{\theta}_B$ oscillates for several periods either below or above the x-axis (Fig. 2e), meaning disks keep a constant spin direction in the short term but with angular speed fluctuations. This driving signal enables the whole collective to periodically switch between clockwise and counter-clockwise rotations with a time-varying angular speed. The key difference between the static and oscillation modes is that **B** has a much longer period for the oscillation mode. This causes uniform collective rotation in one direction for short-time observation, while the mean long-time angular speed of this mode is still smaller than that of the rotation mode. The characterization experiments show that the neighbor separation distance increases with higher frequencies, and the average angular speed of the oscillating collective is smaller than that of the rotating collectives (Fig. 3a-c). The local hexatic order for this mode is lower than for the static mode, but higher than the rotation mode. This mode enables the collective to remain robust against unfavorable system con-

ditions like defective particle corrugations or irregularities in the fluid medium and surrounding boundaries.

9.1.4 Chain Mode

Magnetic fields oscillating about a fixed mean-axis of oscillation create chain formations aligned along the x or y axis, or any vector between the two. Chains along the x or y axis only require a frequency along the alignment axis while the other axis frequency is zero (Fig. 2f-h). Chains along any direction in 2D can be formed as shown in Supplementary Fig. 2b (see Materials and Methods subsection on experimental protocol for more details).

Throughout the experimental characterizations and demonstrations, the chains were kept either in the x or y direction. At low frequencies ($\Omega_{x,y} < 50$ Hz) the attractive forces surpass the repulsive ones and the micro-disks align and attach along edge corrugations forming connected chains. For even lower frequencies ($\Omega_{x,y} < 10$ Hz), the collective oscillates about its center of mass while following **B**, resulting in oscillating chains. At higher frequencies ($\Omega_{x,y} > 50$ Hz), the micro-disks separate due to greater hydrodynamic repulsion, thereby forming chains with separated micro-disks, whose neighbor separation distance increases with frequency (Fig. 3e). At these higher frequencies, the collective resembles formations given by similar frequencies in the static mode with high hexatic order (Fig. 3e). Although the two modes seem similar in spatial configuration, the orientation of the chains can be controlled more reliably than that of the static configuration.

It is worth noting that although intuitively it seems that a static magnetic

field could be used to create chains, this system indeed requires an oscillating magnetic field. The chain formations are formed as a result of the synchronous orientation oscillation throughout the collective, the flow generated by each micro-disk, and its effect on neighboring constituents. If a static magnetic field is applied, the micro-disks would cease to oscillate about their axes and the capillary interactions would dominate, which would result in formation of hexagonal clusters.

9.1.5 Gas-like self-propelling pairs (GaSPP) mode

One-dimensional (1D) oscillating magnetic fields (like in eq. 2) produce a gas-like formation in which the collective breaks into several micro-disk pairs that randomly disperse, similar to the way active self-propelling Janus particles behave when they are stimulated30,31. The key difference here is that the micro-disks' collective behaviors are determined by controllable global stimuli, whereas active Janus particles are mainly driven by local stimuli. The micro-disk pairs translate perpendicularly to the line joining their two respective centers (Fig. 2i); their translation speed increases with frequency and drops to zero as soon as the pair collides with a boundary or other micro-disks, both points at which the pair permanently or temporarily break apart. The micro-disks translate in a new direction if they rejoin or become pairs with other micro-disks. Interestingly, two pairs frequently collide and exchange partners before moving off in new directions. Tight clusters and single micro-disks far away from others remain at a location until other micro-disk pairs collide with them. The average velocity of the pairs in this mode increases with frequency until a threshold ($\sim$ 50 Hz) when the collisions of the pairs with the physical boundary becomes

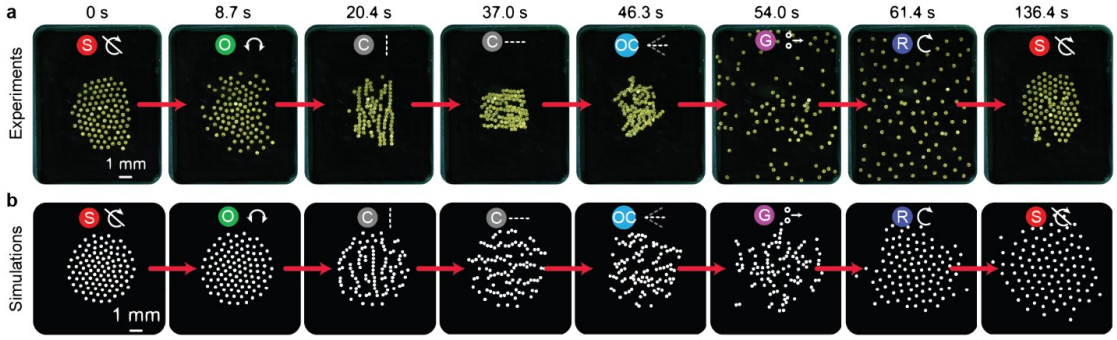

Figure 9.4: Collective mode transitions between different collective formations defined by the value for Ω_x and Ω_y. (a) Experimental transitions (from left to right): static (Ω_x = 60 Hz, Ω_y = 30 Hz), oscillation (Ω_x = 31 Hz, Ω_y = 30 Hz), Y chains (Ω_x = 0 Hz, Ω_y = 30 Hz), X chains (Ω_x = 30 Hz, Ω_y = 0 Hz, B_y = 10 mT), oscillating chains (Ω_x = 1 Hz, Ω_y = 0 Hz, B_y = 10 mT), GaSSP (Ω_x = 70 Hz, Ω_y = 0 Hz, B_y = 0 mT), Rotation (Ω_x,Ω_y = 70 Hz), Static (Ω_x = 60 Hz, Ω_y = 30 Hz). (b) Simulated mode transitions corresponding to the experiments in (A). The last frame of a mode in the simulations is used as the first frame in the simulation of a subsequent mode. The brightness of the images in (a-b) is enhanced using photoshop for better visualization. The symbols on top of the sub-images in (a-b) represent the mode that collective exhibits. These symbols correspond to those shown in Fig. 1a.

more frequent, thereby reducing their average velocity (Fig. 3f). This mode enables collectives to disperse and fill open areas at different speeds. An example of the magnetic field profile that enables GaSPP mode is the following:

$$\mathbf{B} = \begin{bmatrix} 10cos\,(40t) \\ 0 \end{bmatrix} \tag{9.2}$$

Supplementary Figs. 5-6 shows that the collectives exhibit all the above mentioned behaviors even with a low number of micro-disks.

9.1.6 Transition Between Modes

The mode transitions are demonstrated via experiments and simulations (Fig. 4 and Supplementary Fig. 2c). A rotating collective of around 120 micro-disks starts out at $\Omega_{x,y}$ = 70 Hz and transitions to a rotation mode at $\Omega_{x,y}$ = 20 Hz, this increases the collective's average angular velocity and decreases its size. The collective then transitions from the rotation mode to a static collective, followed by a transition to the oscillation mode. Further, the system transitions from isotropic oscillation mode to anisotroic Y chains. The Y chains transition to X chains by changing the alignment axis; the collective then switches to oscillating chains, where each chain oscillates about the x-axis. Thereafter, the collective transitions from the globally driven chains to self-propelling mode, where the disks disperse through the GaSPP mode and transition to rotation mode at higher frequencies. Finally, the static mode collapses the collective back to the center and forms a stationary hexatic-like structure. The transition sequence was simulated using a numerical model where the collective starts with rotation mode ($\Omega_{x,y}$ = 20 Hz) and transitions through the whole sequence and ends with the static mode (Fig. 4b). The qualitative agreement between the experiments and simulations indicates that our system's behaviors can be explained using the main pairwise interactions between the micro-disks and external magnetic fields (for more details on the numerical model see Materials and Methods subsection on model for simulations and model for GaSPP simulations). Note that there are some discrepancies between experiments and simulations in the final formations for the rotation mode (x, y = 70 Hz) and static mode (x = 60 Hz, y = 70 Hz). These discrepancies arise because we do not consider the hydrodynamic drag from the arena boundary, which remains insignificant in most cases but becomes significant at higher frequencies of the external magnetic

field. The main reason for slight differences in the experiments and simulations for the chain motions could be due to the simplified model used for the capillary interactions between the disks in simulations. The capillary interactions are simplified to be pairwise in simulations, however, in experiments the capillary interactions could also include a many-body term. The capillary interactions significantly affect the assembling of the micro-disks and the absence of the many-body term could explain the presence of unattached micro-disks in the simulations for chains. Because the modeling of the many-body capillary term and the drag from the arena boundary is highly non-trivial and because the absence of these terms does not influence the simulation results significantly, these terms were not included in our numerical model. Additionally, a concave air-water interface can drive the disks towards the center of the arena, creating an effective attraction between the disks. The simulations assume a flat air-water interface and each experiment approximates this; however, even a small concavity in the interface lowers neighbor spacing between micro-disks in the experiments, constraining the motion of individual disks. This difference is most clearly evident in the simulations of the chain mode.

9.2 Mode-Enabled Robotic Functionalities

Next, we demonstrate diverse functions using different collective modes and quantitatively characterize several key parameters, including locomotion and dispersion speed under various external field parameters and angular velocities of the manipulated objects. These demonstrations begin with magnetic field gradient-based mechanisms that enable collective locomotion and navigation through complex environments and enable contact-based object transport

(Figs. 5). Figs. 6-7 demonstrate the collective's ability to manipulate itself and the surrounding environment through the fluid medium; this includes flow-induced locomotion, object transport, object rotation and orientation control. Finally, we show the useful functions available through the GaSPP mode: dispersion and space-filling with directional flows, and splitting by using the environment boundaries (Fig. 8). Most of the demonstrations in this section make use of multiple modes to achieve different functions. For example, to demonstrate object transport, the collective can simply start near the object that is to be transported, however, that may not always be the case in realistic situations. Therefore, to present a complete picture, we present demonstrations where the collective starts farther from the object and needs to locomote to get near the object and make the transport possible. Such demonstrations better highlight the advantage of using multiple modes even to achieve a single function.

9.2.1 Gradient-based locomotion and navigation through intricate environments

We use 2D external magnetic field gradients to enable collective locomotion. We characterize around 120 micro-disks' average locomotion speed as a function of their collective mode, field gradient along the x and y axes, and field frequency (Figs. 5a-b) and collective size (Supplementary Figs. 7-8). The chain mode with alignment along the gradient's axis exhibits the highest speed among the four tested modes. Note that the chains slow down when they approach the arena's boundary as a result of the confinement effect; this results in higher standard deviations (Fig. 5a-c). The collective moves on desired trajectories to form the

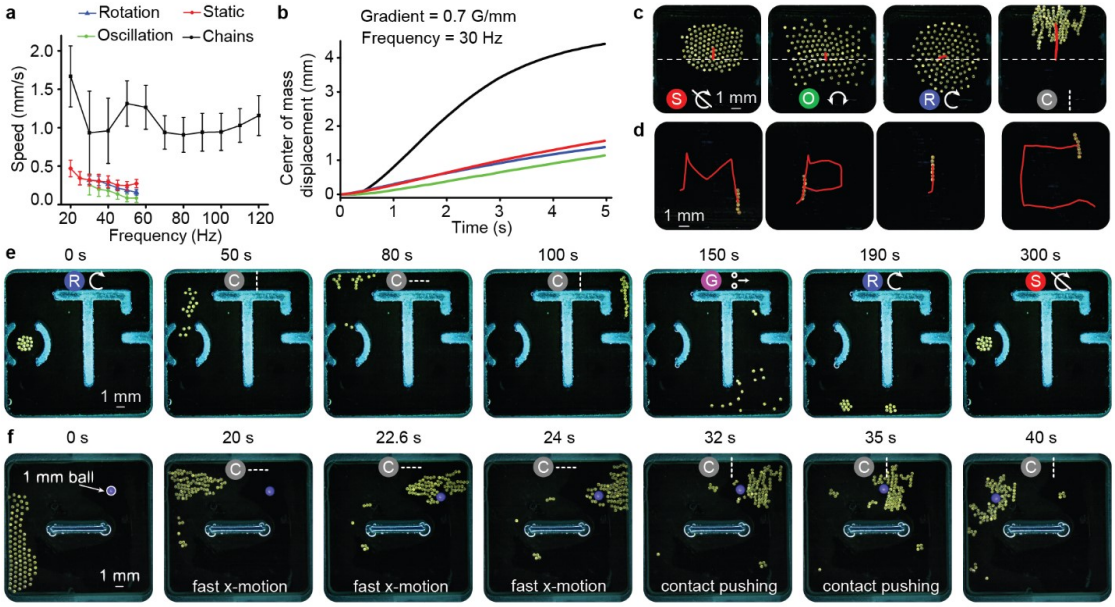

Figure 9.5: Magnetic gradient-assisted collective navigation through confined environments and contact-based object transport. (a) Locomotion speed comparison for the rotation, static, oscillation, and chain modes with N = 126 micro-disks driven at different frequencies when the gradient is F = 0.7 Gauss / mm. The chains move faster than other modes. The error bars represent standard deviations over 5 s. (b) Displacement of each mode over time when Hz. The chains move faster and get slowed down due to the physical boundary around 2.5 s. This contributes to large standard deviations in chain speed in (a). (c) Representative images showing the trajectories of static (left), oscillating (middle left), rotating (middle right), and chain (right) collectives under the influence of a magnetic field gradient along the y axis. (d) Y chain of seven micro-disks driven with magnetic field gradients to produce MPI and C trajectories. (e) 17 micro-disks transition between different modes to navigate through narrow passages. (f) The collective switches between the modes static, X chains, and Y chains to locomote and push an object. The brightness of the images in (c-f) is enhanced using photoshop for better visualization. The symbols on the sub-images at the bottom, in (c), and top, in (e-f), represent the mode the collective exhibits. These symbols correspond to those shown in Fig. 1a. The sub-images in (f) are labeled at the bottom with the function that the collective performs.

letters ”MPI” and ”C”, while maintaining a chain formation (Fig. 5d). Next, we demonstrate the system’s ability to switch between collective modes that enable it to navigate through a complex environment (Fig. 5e). Throughout this environment, the collective passes through narrow passages that require it to switch between X- or Y-chains in order to keep all micro-disks together. Additionally, the collective moves quickest as a chain, when the chain is aligned along the direction of the magnetic field gradient. After about 150 s, we switch the collective to the GaSPP mode, demonstrating that the collective can disperse within a complex arena and coalesce afterwards through the rotation mode.

9.2.2 Contact-Based Object Transport

We also show object transport using physical contact (Fig. 5f) through a collective that must navigate towards and around an object and then reconfigure to push it in the desired direction. The collective starts out at the arena’s left side in static mode and passes the spherical object (1 mm-diameter polystyrene bead) as X-chains, driven by a magnetic field gradient (0.7 Gauss/mm). It is important that the collective exhibits the X-chain mode when moving to the right side of the arena since this allows it to maximize its speed and minimize the contact surface area to prevent pushing the bead to the right side. Then the collective switches to Y-chains and pushes the bead to move left. The Y-chains ensure that the collective has a large surface contact area along which it can push the object from the right side of the arena to the left.

9.2.3 Flow-Induced Locomotion

Flow-induced locomotion enables a collective to move around by taking advantage of the generated fluid flows and surrounding environmental boundaries. When the collective reaches the arena's bottom right corner (after 190 s in Fig. 5e) it transitions into a clockwise rotation mode with a constant downward field gradient and moves towards the left, opposite to how a wheel rolls on a boundary. We speculate that this counter-intuitive leftward movement is caused by a combination of the clockwise flow and the symmetry breaking due to the presence of a fixed boundary on one side of the collective. A detailed study will give insight into the specific mechanisms that enable this collective behavior; however, this is beyond the scope of this paper. The complex interplay between parameters like magnetic field gradient, boundary conditions, and bi-axial magnetic field frequencies opens up many avenues for researchers to explore optimal control methods for transporting a collective within complex and/or dynamic environments.

9.2.4 Azimuthal Flow Fields

The emergence of flow-induced locomotion results from the azimuthal flow generated by each spinning micro-disk in rotation mode. Fig. 6a shows a fluorescent dye that is introduced to the left of a clockwise-rotating collective and spreads through a combination of its own diffusion and the azimuthal flows generated by the collective. A close look at the images shows that the dye circles around individual micro-disks' edges and is swept by azimuthal flows onto other nearby micro-disks.

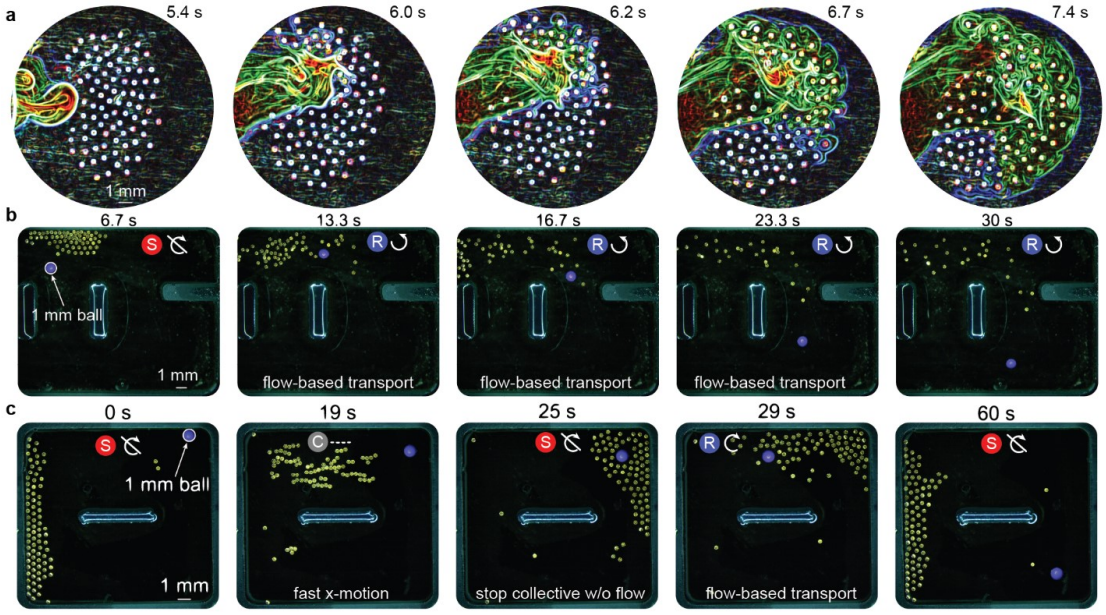

Figure 9.6: Flow-assisted contact-free object transport. (a) Qualitative demonstration of flow around micro-disks when the collective is rotating. Green and blue lines were extracted using edge detection. (b) Collective rotates to guide a purple ball to the bottom right-hand corner. (c) Collective rotation guides a ball around the perimeter of the arena by using the arena design. The brightness of the images in (a-c) is enhanced using photoshop for better visualization. The symbols on top of the sub-images in (b-c) represent the mode the collective exhibits. These symbols correspond to those shown in Fig. 1a. The sub-images in (b-c) are labeled at the bottom with the function that the collective performs.

9.2.5 Contact-Free Object Transport

Contact-free object transport is achieved through the rotation mode. First, a collective of 120 micro-disks rotates to move a polystyrene ball (1 mm) from the top center of the arena to the lower right corner (Fig. 6b). The collective rotates in the counter- clockwise direction to generate a flow that drags the ball along, thus transporting it into the greater open space in the lower right corner of the arena. Similarly, the ball can be transported to the arena's left side using a clockwise rotation (Supplementary Fig. 9).

The second demonstration of contact-free object transport is shown in Fig. 6c

where the goal is to move the ball to the arena's bottom right corner. Similarly to the experiments in Fig. 5f, the collective navigates to the right side of the arena and around the bead. As opposed to the demonstration in Fig. 5f where the collective must be aligned adjacent to the bead to transport it, here the collective must encapsulate the bead so there is a significant density of micro-disks around it in all directions. After locomoting to the arena's right side at a high speed through X-chains, the collective switches to static mode so that micro-disks can evenly distribute throughout the bead's perimeter without transferring torque that might send the bead in an undesired direction. The micro-disks begin to spin clockwise to generate a flow that moves the ball towards the left. Because the arena has a center barrier with fluid all around it (rectangular loop design), the ball makes its way to the left side, downward, and then back to the right side where it finishes below its starting point. The cumulative effects of the boundary, the size of the collective, their direction of rotation, and the general arena design dictate the ball's trajectory. This experiment demonstrates the capability of our system to use external factors, like boundaries, to achieve otherwise difficult tasks. Although it is beyond the scope of this paper, the complex interplay between these different parameters offers great opportunities to develop robust, efficient, and real-time control strategies for targeted manipulation of one or multiple objects.

9.2.6 Flow-induced object manipulation (rotation and orientation control)

We have shown the collective can transport large spherical objects through contact-based and contact-free mechanisms; however, it is also useful if these collectives control single or multiple objects that encapsulate the collective, or that the collective itself encapsulates. Fig. 7 demonstrates the various flow-induced object manipulation behaviors possible.

The azimuthal flow fields from the individually spinning micro-disks, placed inside a ring, creates a larger circular flow around the collective's perimeter; the viscous drag on a ring's inner boundary enables it to rotate (Fig. 7a). Fig. 7b shows that the collective can also control the motion of an object externally, as would be needed for solid objects. In these cases, a ring's direction of rotation is opposite the individual micro-disks' spin direction. The strength of the azimuthal flows generated by the collective can be changed in three ways: by using different numbers of micro-disks (varying the area density), by using rings of different sizes while keeping the number of micro-disks constant, and by changing the rotation speed of the collective. These experiments were performed for three ring objects of different sizes and with different numbers of micro-disks inside or outside the structure in each case. Their characterization demonstrates that increasing the frequency of the external magnetic field decreases the collective's angular speed (Fig. 7a-c and Supplementary Figs. 10-11). Interestingly, at low frequencies several micro-disks forms pairs and rolls along the outer perimeter of the rings in several instances. The rotational manipulation is not restricted to objects of circular shapes; Figs. 7d-e show rod- and star-like shapes encapsulating collectives, rotating about their center axis

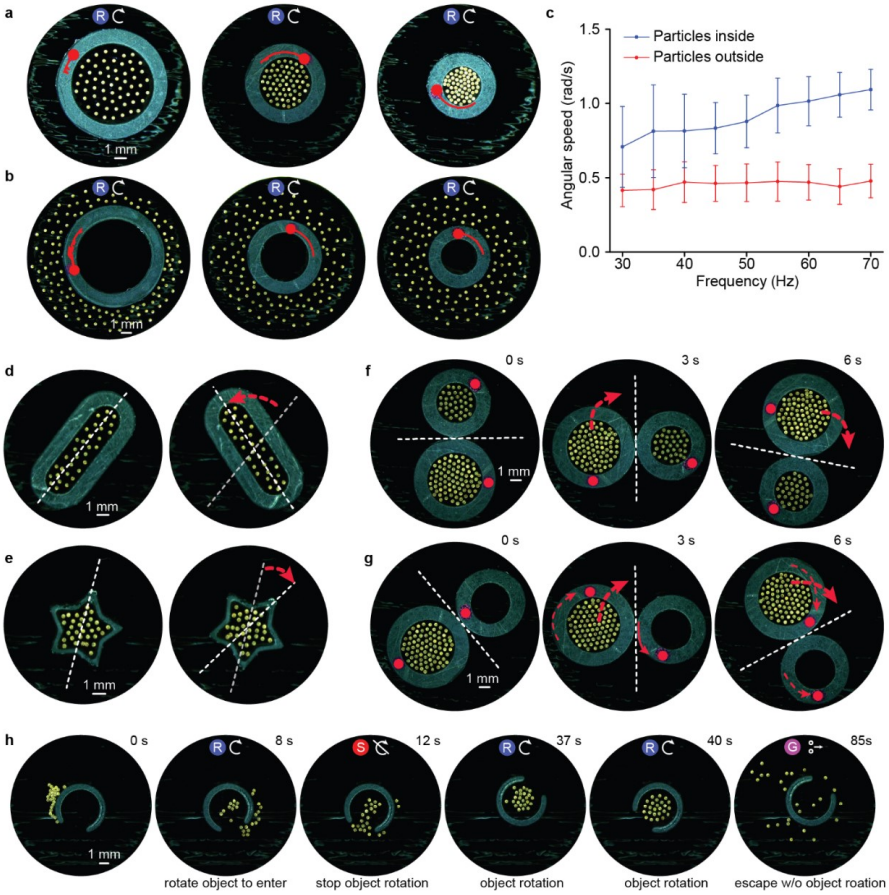

Figure 9.7: Flow-assisted object rotation and orientation control. (a) Micro-disk collectives within ring-shaped objects of different sizes; the object rotates in the same direction as the collective. (b) Collectives encapsulate and rotate ring-shaped objects; the object rotates in the opposite direction as the collective. Red line in (a-b) shows the rotational trajectory of the rings. The same rings are used for (a) and (b). (c) Angular velocity of a ring-like object (ID 3.4 mm and OD 6.5 mm) when there are 60 micro-disks inside or outside the structure. Error bars represent standard deviations over 10 s. (d) Collective rotates a rod-shaped object and (e) a star-shaped object. (f) Two collectives within adjacent objects enable coupled object rotation. (g) A collective within one of two adjacent ring-like objects rotates the structure it is in and exerts a torque on the neighboring object to enable gear-like motion. (h) A collective enters a C-shaped object, rotates it, and exits the structure. A red circle is added to highlight the orientation of the rings (a-b) and (g-f). The red dashed arrows in (d-g) show the direction of rotation of the individual objects (thin arrows) and their center of mass (thick arrows). The brightness of the images in (a-b) and (d-h) is enhanced using photoshop for better visualization. The symbols on top of the sub-images in (a-b) and (h) represent the mode that the collective exhibits. These symbols correspond to those shown in Fig. 1a. The sub-images in (h) are labeled at the bottom with the function that the collective performs.

as a result of the azimuthal flows. The next set of demonstrations address dual object manipulation when there are collectives within one or both of the objects (Fig. 7f-g). Two rings of different sizes, each encapsulating different numbers of micro-disks (34 in a small and 60 in a large ring, respectively), rotate in the same direction, but since they touch each other's boundary, their motion becomes coupled due to capillary torque and the two rotate about their common center of mass. However, when only one of the rings encapsulates a collective, the torque is exerted from the driven ring to the passive one, like gears, and as a result they rotate in opposite directions (Fig. 7g). This way the collective is used to demonstrate torque transfer between two rings, one ring actuated by the collective, while the other ring rotates either indirectly about its own axis or about a common center of mass with the first ring. Using the experiments discussed above, we finally demonstrate that the collective can switch between different modes to manipulate a C-shaped object with a small opening, stop it at a desired orientation to enter it, rotate it from the inside, and then exit (Fig. 7h).

9.2.7 Dispersion and Splitting

Finally, we show that the propulsion behavior in the GaSPP mode can be useful to disperse the collective (Fig. 8a). More specifically, this mode enables small collectives to disperse across large areas, within an object without transferring a significant amount of torque, as well as escape a free-floating structure without changing its orientation. We show that the mean velocity of the pairs increases with oscillation frequency (Ω_x) of the 1D magnetic field (Fig. 3f). We compare the dispersion of micro-disks when using the expanded rotating collec-

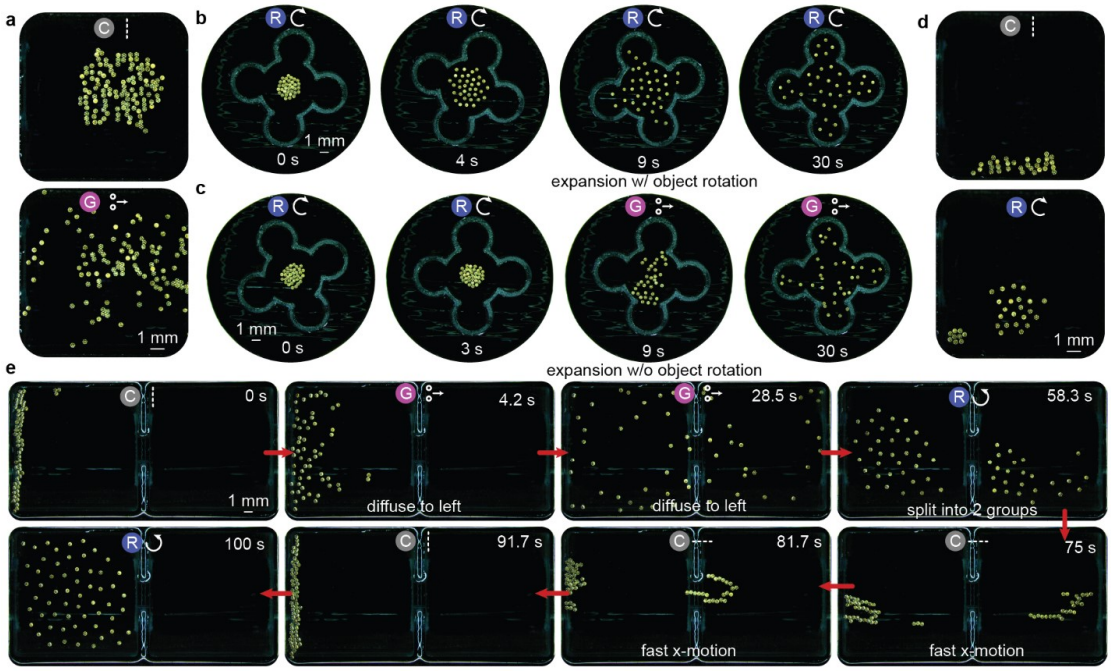

Figure 9.8: Dispersion and splitting of the microrobot collective. (a) Representative images of a collective transitioning from Y chains to GaSPP to explore the available area. (b) Collective disperses using the rotation mode (70 Hz) within a quadrotor-shaped object; the collective expands and rotates the object about its center. (c) transition from rotation mode to GaSPP mode; the collective expands but does not rotate the object. (d) Collective splits into two groups by forming chains along a boundary and then transitioning to rotation mode. (e) Demonstration of a collective splitting between two sides through GaSPP and then returning to the same side through gradient-assisted X chain locomotion. The brightness of the images in (a-e) is enhanced using photoshop for better visualization. The symbols on top of the sub-images in (a-e) represent the mode the collective exhibits. These symbols correspond to those shown in Fig. 1a. The sub-images in (b-c) and (e) are labeled at the bottom with the function that the collective performs.

tive and the GaSPP mode (Fig. 8b-c). In Fig. 8b, we place the rotating collective ($\Omega_{x,y}$ = 20 Hz) inside an arbitrary shape and then transition to the rotating collective at $\Omega_{x,y}$ = 70 Hz, and in Fig. 8c the collective transitions to a GaSPP mode at Ω_x = 70 Hz. We find that a rotating collective rotates the whole boundary while uniformly spreading across the whole available area, whereas the collective in GaSPP mode expands less uniformly, much faster, and without rotating

the boundary. Finally, we demonstrate two different ways to split up the collective. We first show the temporary splitting of the collective using reconfiguration into other modes and the physical boundary (Fig. 8d and Supplementary Fig. 12). In this case, the collectives split into two circular, rotating collectives for a short time until the inter-disk attraction takes over and they merge into a single collective. Then we demonstrate the use of GaSPP to split the collective and then merge the two small collectives using the chains, aided by magnetic field gradients, to navigate through a narrow opening (Fig. 8e). Specifically, we place the micro-disks inside a rectangular arena that is divided into two squares by a wall. The only way for the micro-disks to go from one side of the arena to the other is via a small ($\sim$ 1 mm) opening at the center of the dividing wall. We start by placing the collective in the left square, forming Y-chains, and then changing to GaSPP mode (Ω_x = 70 Hz). This mode enables fast dispersal of the micro-disks to the right side of the arena and on switching to the rotation mode ($\Omega_{x,y}$ = 50 Hz), the collective forms two rotating groups, one on each side of the arena. The two groups then merge by transporting the group on the right side using the X-chains to go back to the left side through the narrow opening at the center, when assisted by a magnetic field gradient. This experiment highlights the capability of our system to adapt to and explore diverse environments by reconfiguring into different formations. Aside from an application perspective, this novel mode has great potential in carrying out fundamental studies on self-propelling particles; although the behavior is enabled by mutual interactions between particle pairs, their speed is tuneable through a global magnetic field frequency. Studying the fundamental behaviors of this mode more closely could give insight into the possibilities of self-propelling collectives like those composed of Janus particles.

9.2.8 Discussion

In summary, we present a microrobot collective system that can reconfigure into six different behaviors, each of which is capable of diverse tasks. First, we show the different behaviors our system exhibits, both via experiments and simulations. These behaviors include globally rotating, static and oscillating formations composed of dynamic micro-disks, static and oscillatory chains, and a novel gas-like mode composed of self-propelling pairs. Our system exhibits various formations, each possessesing further tunability of collective size, angular velocity, and locomotion speed. We further characterize each behavior at different frequencies and demonstrate inter-mode transitions. Finally, by exploiting the reconfiguration capabilities of our system, we realize several functions like collective navigation through confined environments, contact-based and contact-free object transport, flow-induced object rotation, and collective dispersal to explore available areas and to split into smaller groups. These behaviors are possible due to the intricate balance between the mutual interactions between the micro-disks and the arena, and the judicious choice of the external magnetic field's form to drive the collective.

Although we explore two orthogonal oscillating magnetic fields in this study, we keep several parameters constant, like the phase difference between the two oscillating magnetic fields and the magnetic field intensity. Further variation of such parameters could uncover new behaviors in our system. One limitation of our system in its present state is its low force-bearing capacity, which limits the size of the object that can be pushed (via contact) using the chains. However, this problem could be solved either by increasing the collective size or through stronger magnetic field gradients. Moreover, the numerical model

for GaSPP mode contains a noise term and its physical origin is fundamentally intriguing. Further studies on the physical origin of this noise is out of the scope of this study and will be reported separately.

To the best of our knowledge, our system is more versatile and demonstrates more behaviors and functions than any other system at this scale and at the fluid-air interface. In addition, two of the presented behaviors are novel and unique to our system, i.e., the static collective composed of dynamic micro-disks and the gas-like formation composed of self-propelling pairs. Unlike any other system in the literature, our system transitions from globally driven to mutual interactions-dominated self-propelling behavior. Moreover, our system enables the use of traditional mechanical coupling at the millimeter scale for torque transfer, paving a way for the transfer of knowledge of traditional mechanical systems to build machines at smaller length scales. One feature of our system is that even an incredibly small number of micro-disks, as small as 7, can exhibit all the formations demonstrated in this study. This capability could be very advantageous in scenarios when the collective needs to be broken into smaller groups while still retaining the ability to reconfigure. We envision that our system would be useful in performing several tasks applicable to microscale self-assembly and packaging22, and its use as reconfigurable micromachines in biomedical and environmental applications.

9.3 Materials and Methods

9.3.1 Fabrication of the Microrobots

Microrobots were printed using two-photon polymerization-based 3D micro-printing (Nanoscribe Photonic Professional GT) and nanofilms of 500 nm cobalt and 60 nm gold were then sputtered onto them using Kurt J. Lesker NANO 36.

9.3.2 Video Acquisition and Analysis

The experiments were performed under Leica manual zoom microscope Z16 APO and they were recorded using Basler acA2500-60uc camera. LED light source SugarCUBE Ultra illuminator connected to a ring light guide (0.83" ID, Edmund Optics 54-176) and was used to illuminate the micro-robots. A Python script was developed using the OpenCV library to process the experimental videos and extract the positions of the micro-robots. The analysis of the processed data was done using MATLAB. The raw images were used without any enhancements for the processing.

9.3.3 Experiment Protocol

The characterization experiments (Fig. 3) were done in a square arena with a 12 mm side length. These experiments were perfomed using 120 micro-disks. For the rotation and oscillation mode, the experiments were performed for $\Omega_{x,y}$ above the frequency range that results in aggregation (> 10 Hz) and below the

step-out frequency (~ 65 – 75 Hz), where the external magnetic torque is insufficient for synchronized disk rotation. The experiments for static mode were performed for up to Ω_y = 60 Hz with a step size of 5 Hz, since the disks start to step out at higher oscillation frequencies. At low frequencies ($\Omega_{x,y}$ < 10 Hz), the capillary and magnetic dipole-dipole torques exceed the external magnetic field torque, while the attractive forces dominate over the repulsive hydrodynamic lift force, causing the micro-disks to align and connect along their corrugations, thereby forming aggregated clusters.

The experiments demonstrating the chain formations along any orientation (θ_{chain} with respect to the x axis), the frequencies can be set to the linear relationship needed for a static collective ($\Omega_x = 2\Omega_y$) while B_{x1} and B_{y1} are varied according to the function $\theta_{chain} = arctan(fracB_{y1}B_{x1})$. For example, if θ_{chain} should be 45^o below the x-axis, like the example shown in Supplementary Fig. 2b, then **B** could have the following parameters:

$$B = \begin{bmatrix} 10cos\,(40t) + 5 \\ 10sin\,(20t) - 5 \end{bmatrix} \tag{9.3}$$

The gear-like configuration (Fig. 7 f-g) was tested multiple times with the rings in physical contact and the result was the two rings rotating about their center of mass because of the increased capillary torque between the two rings.

9.3.4 Simulations

The numerical model developed by Wang et al.35 was modified to simulate the different formations. In the simulations, the initial positions of the micro-disks

were chosen to be on a hexagonal lattice centered at the center of the frame. The distances between the neighboring microrobots were 600 μm. The behaviors were simulated for a total time of 10 s with 1 ms steps. The equations described in the supplementary section of the simulation model were solved using the Explicit Runge-Kutta method of order 5(4) in the SciPy integration and ODEs library (see section on Model for simulations for more details on simulations).

9.3.5 Model for Simulations

9.3.6 Model for GaSPP Simulations

9.3.7 Calculation of hexatic order parameter

The local hexatic order parameter was calculated as:

$$\psi_{6Local} = \frac{\sum_k \left| e^{i6\theta_k} \right|}{K} \tag{9.4}$$

where K is the total number of neighbors of all micro-disks; k is neighbor index, θ_k is the polar angle of the vector from each micro-disk to the th neighbor. Calculation of global hexatic order parameter. The global hexatic order parameter was calculated as:

$$\psi_{6Global} = \left| \frac{\sum_k e^{i6\theta_k}}{K} \right| \tag{9.5}$$

9.3.8 Dye for Flow Visualization Experiments

Fluorescein sodium (C20H10Na2O5) dye from Fischer scientific (code: F/1300/48) was used to visualize the azimuthal flow around the rotating collective.

9.4 Supplementary Materials

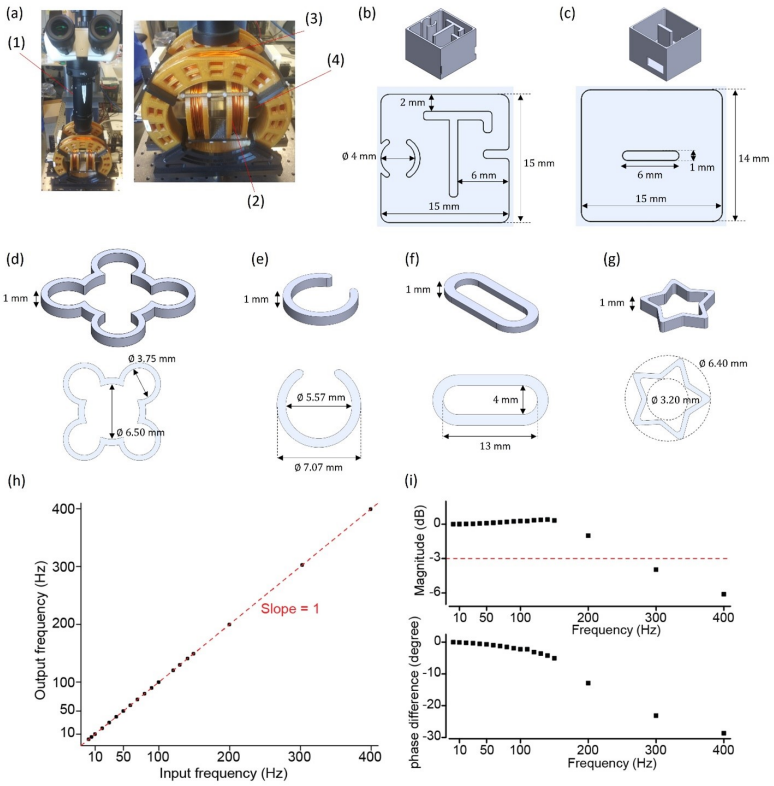

Figure 9.9: Experimental setup. (a) Two-axis Helmholtz coils and imaging setup: (1) Manual and computer view onto stage; (2) X-coils; (3) Y-coils; (4) Stage. (b-g) Arena designs for experimental demonstrations: (b) Maze arena. (c) Ball Motion Arena. (d) Quadrotor object. (e) C-shape object. (f) Rod-like object. (g) Star-like object. (h) Plot of frequency of output coil current vs input signal to generate the magnetic field. The output current has the same frequency as the input signal. (i) Bode plot of magnitude and phase of the coil current. The magnitude of the output current falls below the 3dB line after 200 Hz.

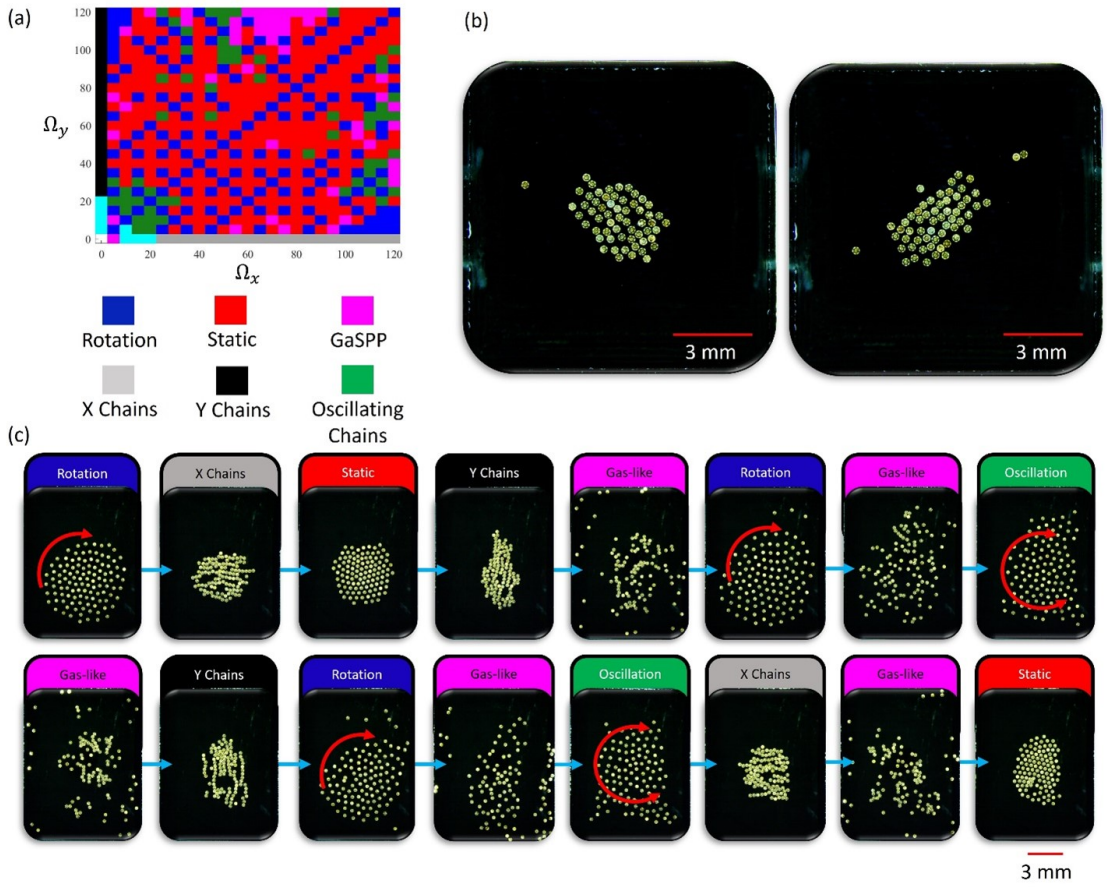

Figure 9.10: Additional collective behavior analysis. (a) State diagram across Ω_x,Ω_y space at 5 Hz increments. (b) Chain formation at two orientations not along the magnetic frequency axes (Ω_x = 40 Hz, Ω_y = 20 Hz: (left) 45^o below the x axis, (right) 45^o above the x axis. (c) Mode Transitions: (Top) Rotation ($\Omega_{x,y}$ = 40 Hz); X-Chains (Ω_x = 30 Hz); Static (Ω_x = 60 Hz); Y-Chains (Ω_y = 30 Hz); GaSPP (Ω_y = 70 Hz); Rotation ($\Omega_{x,y}$ = 50 Hz); GaSPP (Ω_y = 70 Hz); Oscillation (Ω_y = 40 Hz). (Bottom) GaSPP (Ω_y = 70 Hz); Y-Chains (Ω_y = 30 Hz); Rotation ($\Omega_{x,y}$ = 40 Hz); GaSPP (Ω_y = 30 Hz); Oscillation (Ω_y = 30 Hz); X-Chain (Ω_x = 50 Hz); GaSPP (Ω_y = 70 Hz); Static (Ω_x = 140 Hz).

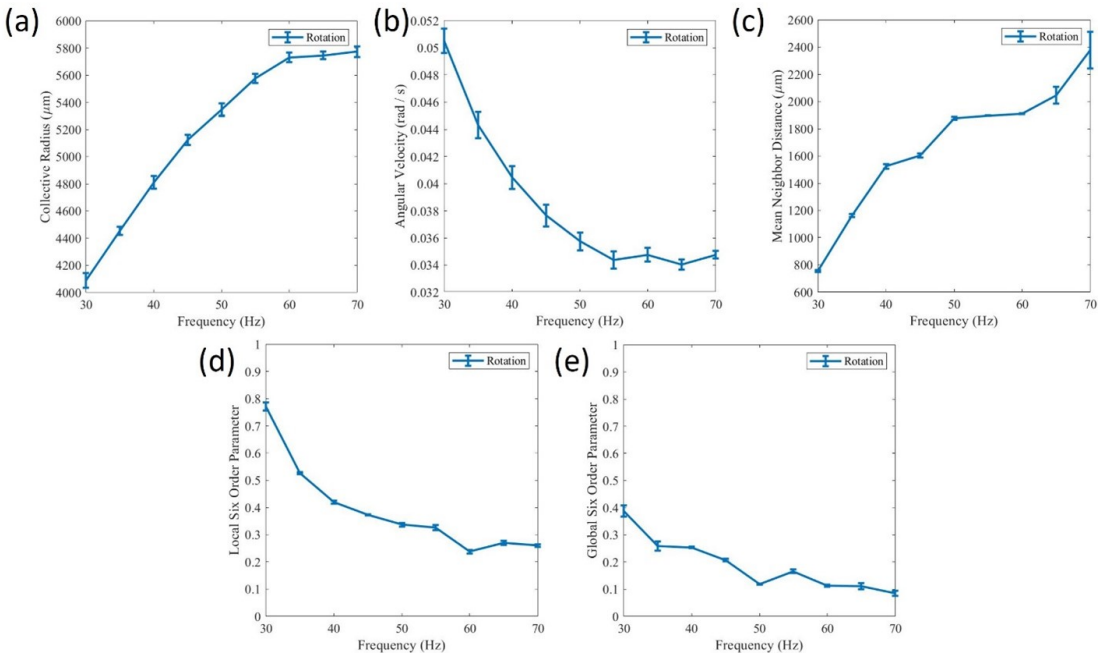

Figure 9.11: Characterization of the simulated rotating collectives with 120 micro-disks. (a) Collective radius; (b) mean angular velocity; (c) mean neighbor distance; (d) local hexatic order; (e) global hexatic order. The error bars represent standard deviation over 10 s.

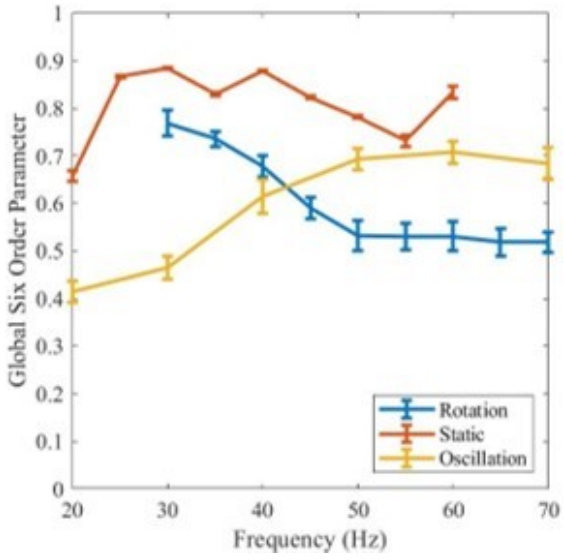

Figure 9.12: Global hexatic order parameter for 126 micro-disks in the rotating, static, and oscillating modes. The error bars represent standard deviation over 10 s.

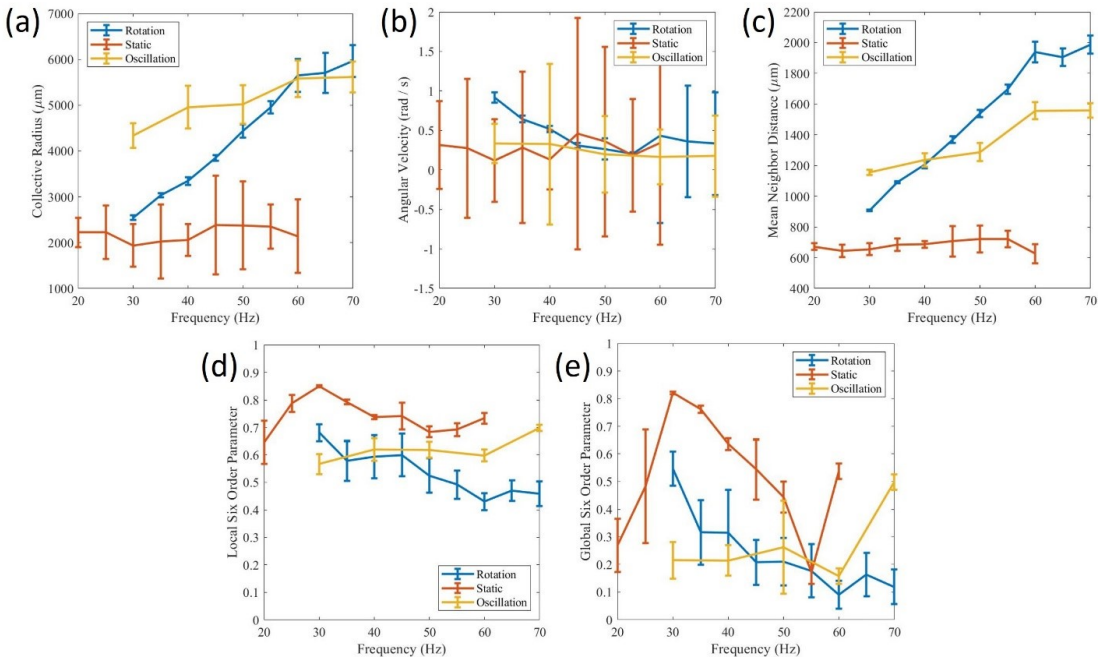

Figure 9.13: Experimental characterization of 34 micro-disks in the rotating, oscillating, and static modes. (a) Collective radius; (b) mean angular velocity; (c) mean neighbor distance; (d) local hexatic order parameter; (e) global hexatic order parameter. The error bars represent standard deviation over 10 s.

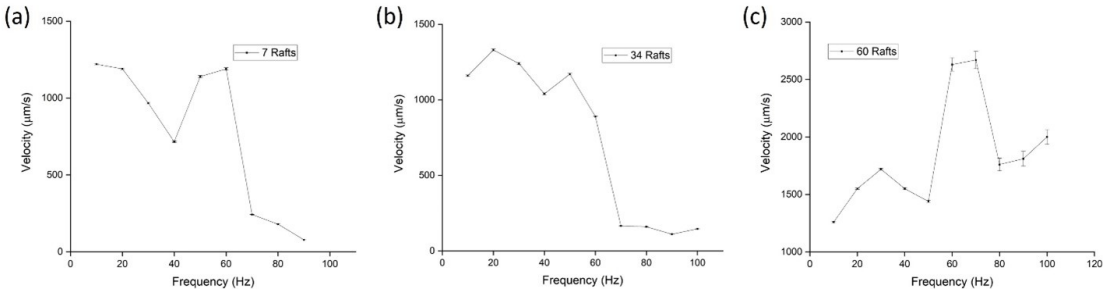

Figure 9.14: Velocity characterization of collectives with 7, 34, and 60 micro-disks exhibiting the GaSPP mode. Mean velocity of collective with (a) 7, (b) 34 and (c) 60 micro-disks, respectively. The error bars represent standard deviation over 10 s.

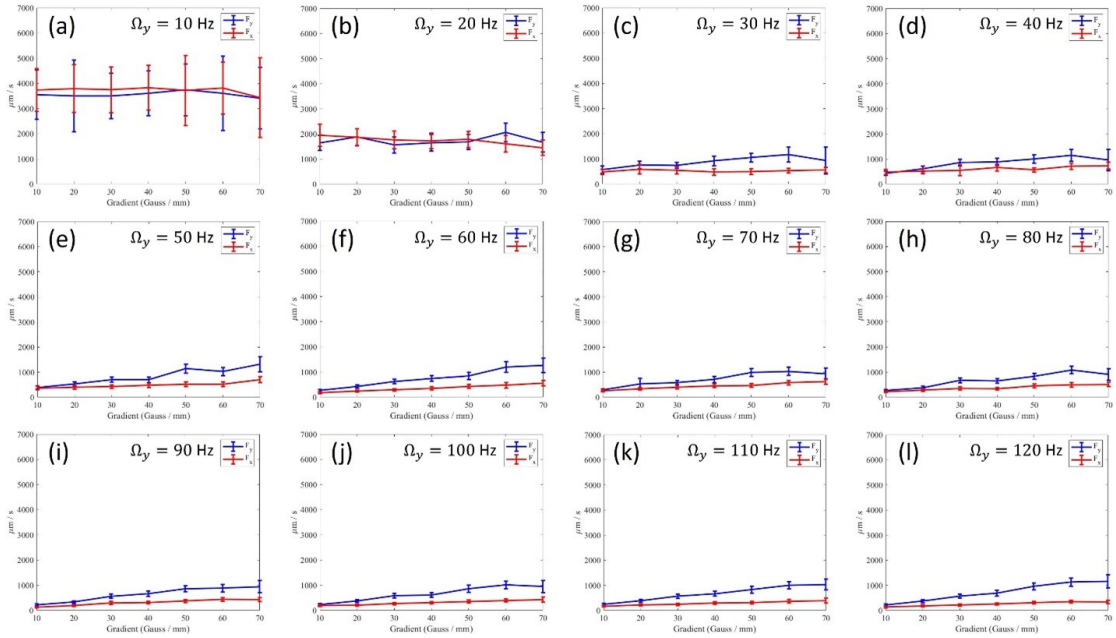

Figure 9.15: Chain locomotion speeds for different frequencies when there are x and y gradients of 0.7 Gauss/mm. (a-l) 10 – 120 Hz at 10 Hz increments. The error bars represent standard deviation over 5 s.

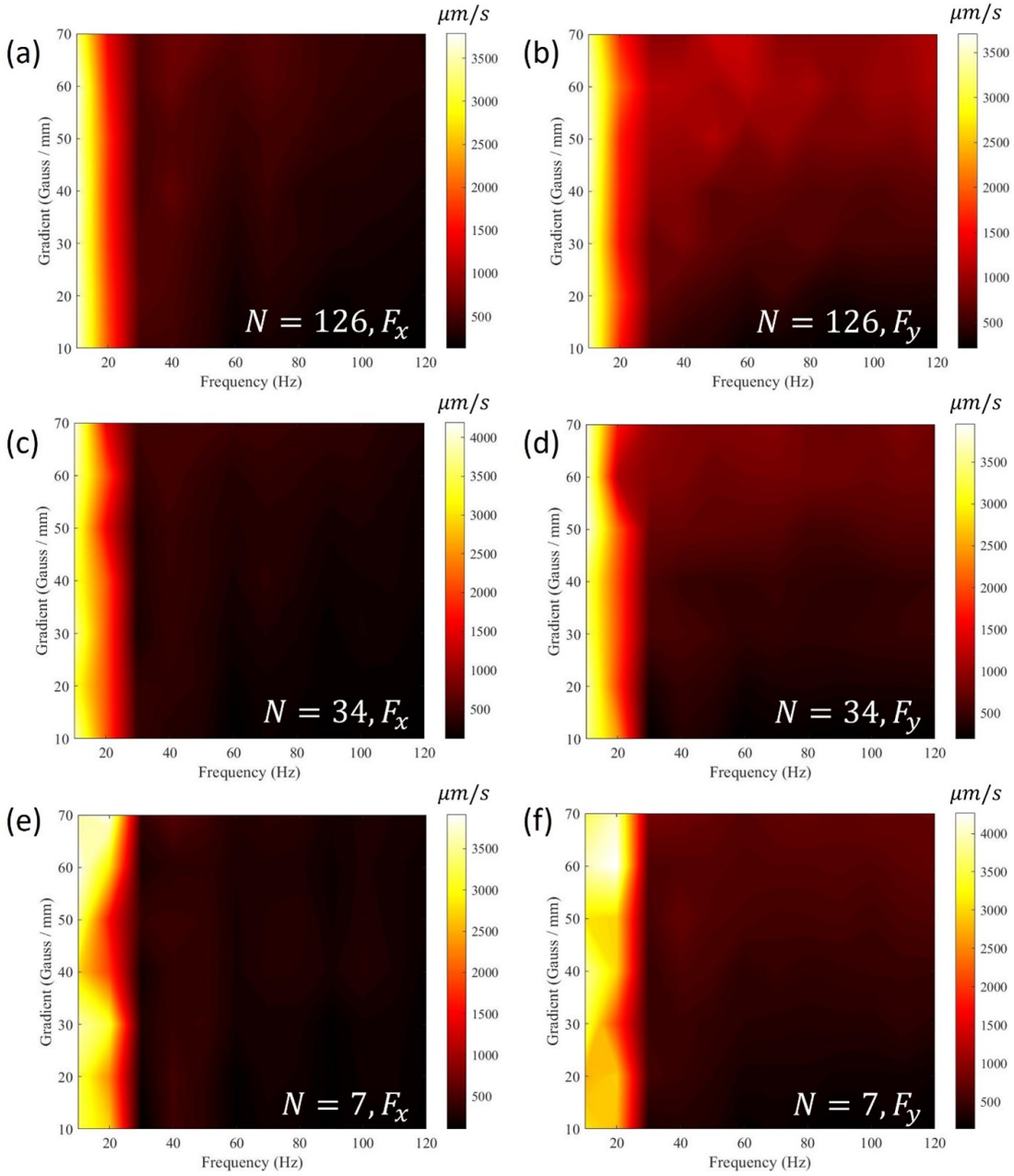

Figure 9.16: Locomotion speeds across various gradients and frequencies for chains aligned along the y direction. (a) Results for when there are 126 micro-disks and a gradient is acting on them in the (i) x direction and (ii) y direction. (b) 34 micro-disks. (c) Seven micro-disks. The error bars represent standard deviation over 5 s.

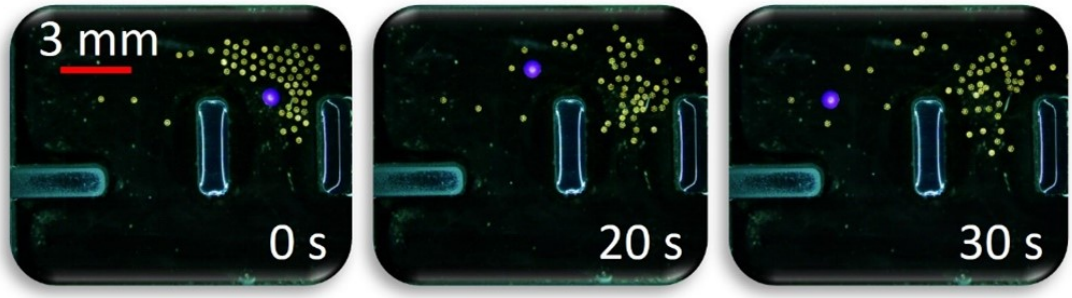

Figure 9.17: Flow-induced collective object manipulation in the rotation mode. Video snapshots of the collective in the rotation mode inducing flow that propels a ball in the left direction.

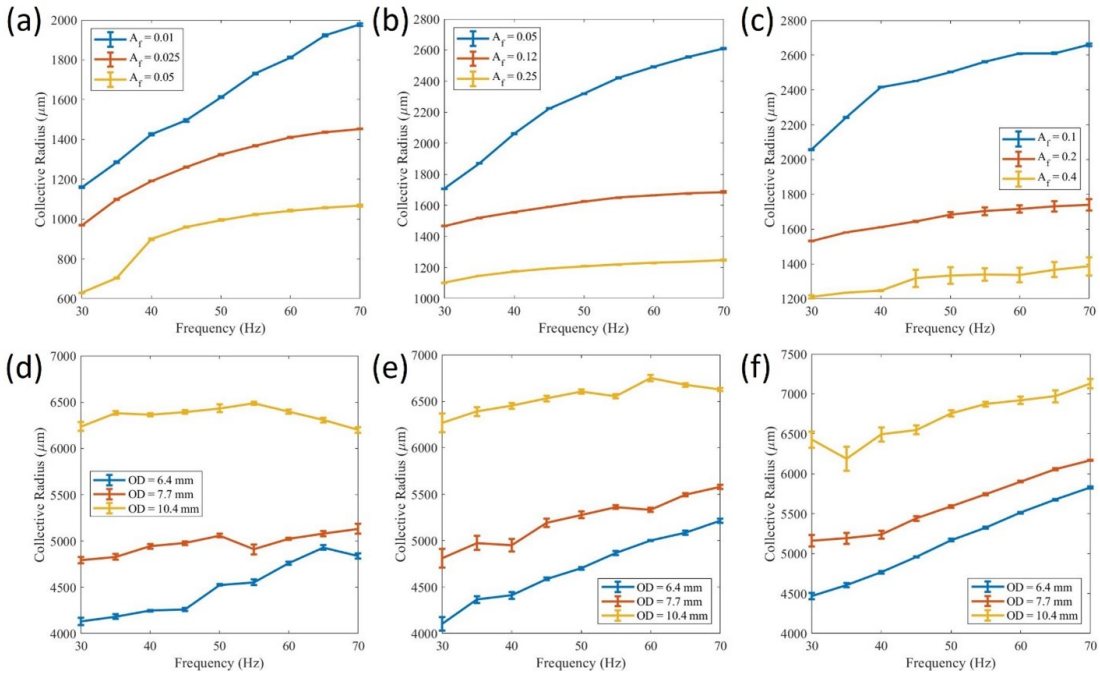

Figure 9.18: Collective radius when the micro-disks are within ring-like structures packed at various area fractions. (a-c): (a) 7 micro-disks, (b) 34 micro-disks, (c) 60 micro-disks. Collective radius when the micro-disks encapsulate ring-like structures with various OD (outer diameters) (d-f): (d) 34 micro-disks, (e) 60 micro-disks, (f) 120 micro-disks. The error bars represent standard deviation over 10 s.

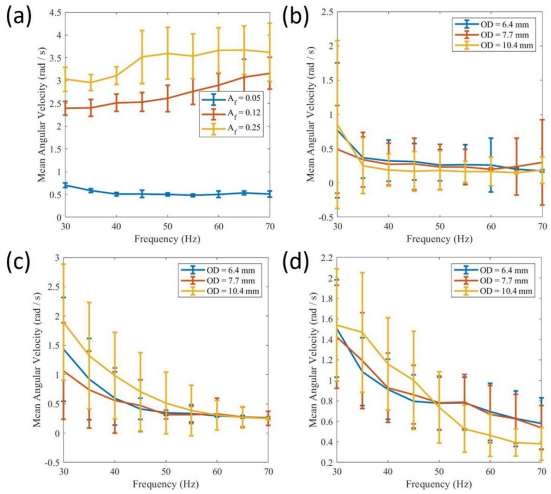

Figure 9.19: Mean angular velocity of micro-disks when they are within a ring-like structure. (a) 60 micro-disks. Mean angular velocity when the micro-disks encapsulate ring-like structures with various OD (outer diameters) (b-d): (b) 34 micro-disks, (c) 60 micro-disks, (d) 120 micro-disks. The error bars represent standard deviation over 10 s.

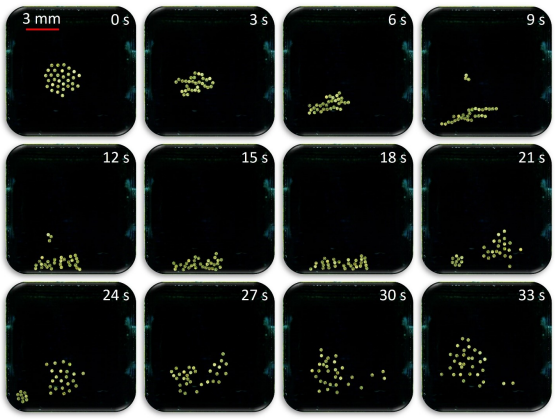

Figure 9.20: The collective separates into two clusters by using the arena boundary and then reforms a single cluster.

CHAPTER 10

SUMMARY & CONCLUSIONS

In this dissertation, I have discussed my work on robot collectives at the macro and micro length scales. I am interested in all aspects of collective systems that demonstrate emergent behaviors, ranging from the mechanical design of macro-scale agents to the algorithms and coordination mechanisms used to implement the behaviors at the different scales.

Through the branch of cross-scale coordination mechanisms, I expanded on a swarming coupled oscillator model to reveal many new emergent behaviors that can replicate the collective behaviors of several natural and artificial collectives. I also demonstrated that the environment could be designed to enable different emergent time-varying collective formations. The abstract mathematical frameworks I studied have strong potential in characterizing many different types of collective systems as well as providing simple control mechanisms to enable many different static and time-varying behaviors in collectives composed of agents with limited capabilities.

At the macro-scale, I developed soft actuators that use fluidic actuation to enable rotational motion and traveling waves. I also developed a stretchable strain sensor that can be used for different applications like tactile grid localization, and implemented it on a soft robotic oscillator to demonstrate how strain could be used to enable various emergent behaviors in a collective of expanding and contracting soft robots. I also developed the algorithms and simulations to study the different emergent behaviors on these robots. At the macro-scale, I also worked on the self-reconfigurable modular robots, the Donuts, to demonstrate proof-of-concept motion and docking. I developed several simu-

lation platforms for these robots to study their various sensing methodologies, including touch sensors, IR transceivers, and strain sensors.

At the micro-scale, I worked on a ferromagnetic microrobot collective system to demonstrate various emergent behaviors tunable through an external bi-axially oscillating magnetic field. I demonstrated that a micro-disk collective can reconfigure on-demand between several different collective modes to navigate through a complex arena, push an object, generate flows to transport an object to a desired location, and manipulate objects much larger than the individual agents. I also demonstrated that a heterogeneous collective composed of small and large micro-disks can spatially self-organize by size under an external magnetic field, can tune the local spacing / stiffness, and that this behavior can be replicated through a simple swarming coupled oscillator model. I also demonstrated that the rotational collective mode can be used to manipulate large and small objects when the collective has a small number of micro-disks, like ~ 35, and when it has a large number, like ~ 1000. I showed that a collective could also be used as a large set of micro-actuators to create more complex small-scale machines.

I hope that my work at the different length scales and with the cross-scale coordination mechanisms will lead to more studies on emergent collective behaviors. In my work, I have demonstrated many interesting collective behaviors and have shown in some cases how they can be used to manipulate objects, navigate through a complex environment, and exert forces on the surroundings. There is still a lot of room for high-impact exploration with the macro-scale robots, micro-robots, and cross-scale coordination mechanisms I used and I hope many more people expand on each of these avenues so that the fields

may further develop in the coming years and find practical uses for biomedical applications, small-scale manufacturing, and environmental remediation.

BIBLIOGRAPHY

[1] Juan A. Acebrón, L. L. Bonilla, Conrad J.Pérez Vicente, Félix Ritort, and Renato Spigler. The Kuramoto model: A simple paradigm for synchronization phenomena. *Reviews of Modern Physics*, 77(1):137–185, 2005.

[2] Amirreza Aghakhani, Oncay Yasa, Paul Wrede, and Metin Sitti. Acoustically powered surface-slipping mobile microrobots. *Proceedings of the National Academy of Sciences of the United States of America*, 117(7):3469–3477, 2020.

[3] Daniel Ahmed, Thierry Baasch, Nicolas Blondel, Nino Läubli, Jürg Dual, and Bradley J. Nelson. Neutrophil-inspired propulsion in a combined acoustic and magnetic field. *Nature Communications*, 8(1):1–8, 2017.

[4] Ikkyu Aihara. Modeling synchronized calling behavior of Japanese tree frogs. *Physical Review E - Statistical, Nonlinear, and Soft Matter Physics*, 80(1):1–7, 2009.

[5] A. Ainla, M.S. Verma, D. Yang, and G.M. Whitesides. Soft, rotating pneumatic actuator. *Soft Robotics*, 4:297–304, 2017.

[6] Yunus Alapan, Ugur Bozuyuk, Pelin Erkoc, Alp Can Karacakol, and Metin Sitti. Multifunctional surface microrollers for targeted cargo delivery in physiological blood flow. *Science Robotics*, 5(42):1–11, 2020.

[7] Morteza Amjadi, Ki Uk Kyung, Inkyu Park, and Metin Sitti. Stretchable, Skin-Mountable, and Wearable Strain Sensors and Their Potential Applications: A Review, 2016.

[8] Shahaf Armon, Matthew Storm, Andres Aranda-diaz, and Manu Prakash. Ultrafast epithelial contractions provide insights into contraction speed limits and tissue integrity. *Proceedings of National Academy of Sciences (PNAS)*, 115(44), 2018.

[9] Ozgur Atalay, Asli Atalay, Joshua Gafford, and Conor Walsh. A Highly Sensitive Capacitive-Based Soft Pressure Sensor Based on a Conductive Fabric and a Microporous Dielectric Layer. *Advanced Materials Technologies*, 2018.

[10] Cameron A Aubin, Snehashis Choudhury, Rhiannon Jerch, Lynden A

Archer, James H Pikul, and Robert F Shepherd. Electrolytic vascular systems for energy-dense robots. *Nature*, 571(7763):51–57, 2019.

[11] Agata Barcis and Christian Bettstetter. Sandsbots: Robots That Sync and Swarm. *IEEE Access*, 8:218752–218764, 2020.

[12] Ana Elisa D Barioni and Marcus AM de Aguiar. Complexity reduction in the 3d kuramoto model. *Chaos, Solitons & Fractals*, 149:111090, 2021.

[13] Clemens Bechinger, Roberto Di Leonardo, Hartmut Löwen, Charles Reichhardt, Giorgio Volpe, and Giovanni Volpe. Active particles in complex and crowded environments. *Reviews of Modern Physics*, 88(4), 2016.

[14] Aaron Becker, Golnaz Habibi, Justin Werfel, Michael Rubenstein, and James McLurkin. Massive uniform manipulation: Controlling large populations of simple robots with a common input signal. *IEEE International Conference on Intelligent Robots and Systems*, pages 520–527, 2013.

[15] Florian Berlinger, Melvin Gauci, and Radhika Nagpal. Implicit coordination for 3D underwater collective behaviors in a fish-inspired robot swarm. *Science Robotics*, 6(50):1–15, 2021.

[16] Preethi Bhat, James Kuffner, Seth Goldstein, and Siddhartha Srinivasa. Hierarchical motion planning for self-reconfigurable modular robots. In *2006 IEEE/RSJ International Conference on Intelligent Robots and Systems*, pages 886–891. IEEE, 2006.

[17] William Bialek, Andrea Cavagna, Irene Giardina, Thierry Mora, Edmondo Silvestri, Massimiliano Viale, and Aleksandra M. Walczak. Statistical mechanics for natural flocks of birds. *Proceedings of the National Academy of Sciences of the United States of America*, 109(13):4786–4791, 2012.

[18] Michael Breakspear, Stewart Heitmann, and Andreas Daffertshofer. Generative models of cortical oscillations: Neurobiological implications of the Kuramoto model. *Frontiers in Human Neuroscience*, 4(November):1–14, 2010.

[19] Alberto Brunete, Avinash Ranganath, Sergio Segovia, Javier Perez de Frutos, Miguel Hernando, and Ernesto Gambao. Current trends in reconfigurable modular robots design. *International Journal of Advanced Robotic Systems*, 14(3):1729881417710457, 2017.

[20] Zack Butler, Keith Kotay, Daniela Rus, and Kohji Tomita. Generic decentralized control for lattice-based self-reconfigurable robots. *The International Journal of Robotics Research*, 23(9):919–937, 2004.

[21] Jason Campbell, Padmanabhan Pillai, and Seth Copen Goldstein. The robot is the tether: active, adaptive power routing modular robots with unary inter-robot connectors. In *2005 IEEE/RSJ International Conference on Intelligent Robots and Systems*, pages 4108–4115. IEEE, 2005.

[22] Steven Ceron, Itai Cohen, Robert F Shepherd, James H Pikul, and Cindy Harnett. Fiber embroidery of self-sensing soft actuators. *Biomimetics*, 3(3):24, 2018.

[23] Steven Ceron, Logan Horowitz, Nialah Wilson, Claire Chen, Daniel Kim, and Kirstin Petersen. Towards a scalable, self-reconfigurable robot with compliant modules. In *2019 International Symposium on Multi-Robot and Multi-Agent Systems (MRS)*, pages 47–49. IEEE, 2019.

[24] Steven Ceron, Logan Horowitz, Nialah Wilson, Jenae, Claire Chen, Daniel Kim, and Kirstin Petersen. DONUts: A Scalable, Self-Reconfigurable Robot with Compliant Modules. In *International Symposium on Multi-Robot and Multi-Agent Systems*, 2019.

[25] Steven Ceron, Marta An Kimmel, Alexandra Nilles, and Kirstin Hagelskjaer Petersen. Soft robotic oscillators with strain-based coordination. *IEEE Robotics and Automation Letters*, 2021.

[26] Steven Ceron, Aleena Kurumunda, Eashan Garg, Mira Kim, Tosin Yeku, and Kirstin Pctersen. Popcorn-driven robotic actuators. In *2018 IEEE International Conference on Robotics and Automation (ICRA)*, pages 4271–4276. IEEE, 2018.

[27] Steven Ceron, Nialah Wilson, Logan Horowitz, and Kirstin Petersen. Comparative analysis of sensors in rigid and deformable modular robots for shape estimation. In *2019 International Symposium on Multi-Robot and Multi-Agent Systems (MRS)*, pages 252–258. IEEE, 2019.

[28] Hakan Ceylan, Immihan Ceren Yasa, Oncay Yasa, Ahmet Fatih Tabak, Joshua Giltinan, and Metin Sitti. 3D-Printed Biodegradable Microswimmer for Theranostic Cargo Delivery and Release. *ACS Nano*, 13(3):3353–3362, 2019.

[29] Hugues Chaté, Francesco Ginelli, Guillaume Grégoire, Fernando Peruani, and Franck Raynaud. Modeling collective motion: variations on the vicsek model. *The European Physical Journal B*, 64(3):451–456, 2008.

[30] Yuanhao Chen, Jiajia Yang, Xuan Zhang, Yiyu Feng, Hao Zeng, Ling Wang, and Wei Feng. Light-driven bimorph soft actuators: design, fabrication, and properties. *Materials Horizons*, 8(3):728–757, 2021.

[31] S. Sankhar Reddy Chennareddy, Anita Agrawal, and Anupama Karuppiah. Modular Self-Reconfigurable Robotic Systems: A Survey on Hardware Architectures. *Journal of Robotics*, 2017, 2017.

[32] Hyun Jung Choi, Moo Sung Kim, Damiro Ahn, Sang Young Yeo, and Sohee Lee. Electrical percolation threshold of carbon black in a polymer matrix and its application to antistatic fibre. *Scientific Reports*, 2019.

[33] David Johan Christensen, Ulrik Pagh Schultz, and Kasper Stoy. A distributed and morphology-independent strategy for adaptive locomotion in self-reconfigurable modular robots. *Robotics and Autonomous Systems*, 61(9):1021–1035, 2013.

[34] Kyoung Yong Chun, Youngseok Oh, Jonghyun Rho, Jong Hyun Ahn, Young Jin Kim, Hyouk Ryeol Choi, and Seunghyun Baik. Highly conductive, printable and stretchable composite films of carbon nanotubes and silver. *Nature Nanotechnology*, 2010.

[35] A Colbrook and C Smythe. Efficient implementations of search trees on parallel distributed memory architectures. *IEE Proceedings E (Computers and Digital Techniques)*, 137(5):394–400, 1990.

[36] Fionnuala Connolly, Panagiotis Polygerinos, Conor J. Walsh, and Katia Bertoldi. Mechanical programming of soft actuators by varying fiber angle. *Soft Robotics*, 2(1):26–32, 2015.

[37] Jorg Conradt. Distributed central pattern generator control for a serpentine robot. 03 2004.

[38] Alejandro J Cortese, Conrad L Smart, Tianyu Wang, Michael F Reynolds, Samantha L Norris, Yanxin Ji, Sunwoo Lee, Aaron Mok, Chunyan Wu, Fei Xia, et al. Microscopic sensors using optical wireless integrated circuits. *Proceedings of the National Academy of Sciences*, 117(17):9173–9179, 2020.

[39] Utku Culha, Zoey S. Davidson, Massimo Mastrangeli, and Metin Sitti. Statistical reprogramming of macroscopic self-assembly with dynamic boundaries. *Proceedings of the National Academy of Sciences of the United States of America*, 117(21), 2020.

[40] Hadi El Daou, Taavi Salumäe, Lily D. Chambers, William M. Megill, and Maarja Kruusmaa. Modelling of a biologically inspired robotic fish driven by compliant parts. *Bioinspiration & biomimetics*, 9 1:016010, 2014.

[41] Jonathan Daudelin, Gangyuan Jing, Tarik Tosun, Mark Yim, Hadas Kress-Gazit, and Mark Campbell. An integrated system for perception-driven autonomy with modular robots. *Science Robotics*, 3(23):eaat4983, 2018.

[42] Jay Davey, Ngai Kwok, and Mark Yim. Emulating self-reconfigurable robots-design of the smores system. In *2012 IEEE/RSJ International Conference on Intelligent Robots and Systems*, pages 4464–4469. IEEE, 2012.

[43] Carrick Detweiler, Marsette Vona, Yeoreum Yoon, Seung-kook Yun, and Daniela Rus. Self-assembling mobile linkages. *IEEE robotics & automation magazine*, 14(4):45–55, 2007.

[44] Xiaoguang Dong and Metin Sitti. Controlling two-dimensional collective formation and cooperative behavior of magnetic microrobot swarms. *International Journal of Robotics Research*, 39(5):617–638, 2020.

[45] D Dormann, Cornelis Weijer, and Florian Siegert. Twisted scroll waves organize dictyostelium mucoroides slugs. *Journal of cell science*, 110 (Pt 16):1831–7, 09 1997.

[46] Mirollo R. E. and Strogatz S. H. Synchronization of Pulse-Coupled Biological Oscillators. *SIAM Journal of Applied Mathematics*, 50(6), 1990.

[47] Nafiseh Ebrahimi, Chenghao Bi, David J Cappelleri, Gastone Ciuti, Andrew T Conn, Damien Faivre, Neda Habibi, Alexander Hošovskỳ, Veronica Iacovacci, Islam SM Khalil, et al. Magnetic actuation methods in bio/soft robotics. *Advanced Functional Materials*, 31(11):2005137, 2021.

[48] Nazek El-Atab, Rishabh B Mishra, Fhad Al-Modaf, Lana Joharji, Aljohara A Alsharif, Haneen Alamoudi, Marlon Diaz, Nadeem Qaiser, and Muhammad Mustafa Hussain. Soft actuators for soft robotic applications: a review. *Advanced Intelligent Systems*, 2(10):2000128, 2020.

[49] Pelin Erkoc, Immihan C. Yasa, Hakan Ceylan, Oncay Yasa, Yunus Alapan, and Metin Sitti. Mobile Microrobots for Active Therapeutic Delivery. *Advanced Therapeutics*, 2(1):1–18, 2019.

[50] Xinjian Fan, Xiaoguang Dong, Alp C. Karacakol, Hui Xie, and Metin Sitti. Reconfigurable multifunctional ferrofluid droplet robots. *Proceedings of the National Academy of Sciences of the United States of America*, 117(45):27916–27926, 2020.

[51] Chuhuan Feng, Qi Li, Yangjian Zeng, Xin Su, and Hongbin Yu. 2d to 3d convertible terahertz chiral metamaterial with integrated pneumatic actuator. *Opt. Express*, 26(11):14421–14432, May 2018.

[52] Stephen R. Forrest and Mark E. Thompson. Introduction: Organic electronics and optoelectronics. *Chemical Reviews*, pages 923–925, 04 2007.

[53] Peter Friedl and Darren Gilmour. Collective cell migration in morphogenesis, regeneration and cancer. *Nature Reviews Molecular Cell Biology*, 10(7):445–457, 2009.

[54] Toshio Fukuda. Self organizing robots based on cell structures-cebot. In *Proc. IEEE Int. Workshop on Intelligent Robots and Systems (IROS'88)*, pages 145–150, 1988.

[55] Chaim C Futran, Steven Ceron, Benjamin C Mac Murray, Robert F Shepherd, and Kirstin H Petersen. Leveraging fluid resistance in soft robots. In *2018 IEEE International Conference on Soft Robotics (RoboSoft)*, pages 473–478. IEEE, 2018.

[56] Gaurav Gardi, Steven Ceron, Wendong Wang, Kirstin Petersen, and Metin Sitti. Microrobot collectives with reconfigurable morphologies, behaviors, and functions. *Nature communications*, 13(1):1–14, 2022.

[57] Kyle Gilpin and Daniela Rus. Modular robot systems. *Robotics and Automation Magazine, IEEE*, 17(3):38–55, 2010.

[58] Kyle Gilpin and Daniela Rus. A distributed algorithm for 2D shape duplication with smart pebble robots. In *2012 IEEE International Conference on Robotics and Automation*, pages 3285–3292. IEEE, 2012.

[59] Francesco Ginelli. The physics of the vicsek model. *The European Physical Journal Special Topics*, 225(11):2099–2117, 2016.

[60] S.C. Goldstein, J.D. Campbell, and T.C. Mowry. Programmable matter. *Computer*, 38(6):99–101, 2005.

[61] Seth Copen Goldstein, Jason D Campbell, and Todd C Mowry. Programmable matter. *Computer*, 38(6):99–101, 2005.

[62] N.C. Goulbourne, E.M. Mockensturm, and M.I. Frecker. Electroelastomers: Large deformation analysis of silicone membranes. *International Journal of Solids and Structures*, 44(9):2609–2626, 2007.

[63] Sten Grillner. *Control of Locomotion in Bipeds, Tetrapods, and Fish*, pages 1179–1236. John Wiley Sons, Ltd, 2011.

[64] Jurriaan H. De Groot, Johan L. Van Leeuwen, and William M. Kier. Evolutionary mechanics of protrusible tentacles and tongues. *Netherlands Journal of Zoology*, 50(2):113 – 139, 2000.

[65] Bartosz A. Grzybowski, Howard A. Stone, and George M. Whitesides. Dynamic self-assembly of magnetized, millimetre-sized objects rotating at a liquid-air interface. *Nature*, 405(6790):1033–1036, 2000.

[66] Bartosz A. Grzybowski, Howard A. Stone, and George M. Whitesides. Dynamics of self assembly of magnetized disks rotating at the liquid-air interface. *Proceedings of the National Academy of Sciences of the United States of America*, 99(7):4147–4151, 2002.

[67] Bartosz A. Grzybowski and George M. Whitesides. Dynamic aggregation of chiral spinners. *Science*, 296(5568):718–721, 2002.

[68] Koohee Han, Gašper Kokot, Oleh Tovkach, Andreas Glatz, Igor S. Aranson, and Alexey Snezhko. Emergence of self-organized multivortex states in flocks of active rollers. *Proceedings of the National Academy of Sciences of the United States of America*, 117(18):9706–9711, 2020.

[69] Cindy K. Harnett, Huichan Zhao, and Robert F. Shepherd. Stretchable optical fibers: Threads for strain-sensitive textiles. *Advanced Materials Technologies*, 2(9):1700087, 2017.

[70] Jason Hindes, Victoria Edwards, M. Ani Hsieh, and Ira B. Schwartz. Critical transition for colliding swarms. *Phys. Rev. E*, 103:062602, Jun 2021.

[71] Lindsey Hines, Kirstin Petersen, Guo Zhan Lum, and Metin Sitti. Soft actuators for small-scale robotics. *Advanced materials*, 29(13):1603483, 2017.

[72] Lindsey Hines, Kirstin Petersen, and Metin Sitti. Inflated Soft Actuators with Reversible Stable Deformations. *Advanced Materials*, 28(19):3690–3696, 2016.

[73] Bianca S. Homberg, Robert K. Katzschmann, Mehmet R. Dogar, and Daniela Rus. Haptic identification of objects using a modular soft robotic gripper. In *IEEE International Conference on Intelligent Robots and Systems*, 2015.

[74] Hyunsuk Hong. Active phase wave in the system of swarmalators with attractive phase coupling. *Chaos: An Interdisciplinary Journal of Nonlinear Science*, 28(10):103112, 2018.

[75] Aleš Hrabec, Viola Křižáková, Stefania Pizzini, João Sampaio, André Thiaville, Stanislas Rohart, and Jan Vogel. Velocity enhancement by synchronization of magnetic domain walls. *Physical review letters*, 120(22):227204, 2018.

[76] Xinghao Hu, Immihan C. Yasa, Ziyu Ren, Sandhya R. Goudu, Hakan Ceylan, Wenqi Hu, and Metin Sitti. Magnetic soft micromachines made of linked microactuator networks. *Science Advances*, 7(23):1–10, 2021.

[77] Oleg A. Igoshin, Alex Mogilner, Roy D. Welch, Dale Kaiser, and George Oster. Pattern formation and traveling waves in myxobacteria: Theory and modeling. *Proceedings of the National Academy of Sciences of the United States of America*, 98(26):14913–14918, 2001.

[78] Akio Ishiguro, Masahiro Shimizu, and Toshihiro Kawakatsu. A modular robot that exhibits amoebic locomotion. *Robotics and Autonomous Systems*, 54(8):641–650, 2006.

[79] M. Iwasa, K. Iida, and D. Tanaka. Various collective behavior in swarm oscillator model. *Physics Letters, Section A: General, Atomic and Solid State Physics*, 376(30-31):2117–2121, 2012.

[80] M W Jorgensen, E H Ostergaard, and H H Lund. Modular ATRON: modules for a self-reconfigurable robot. In *2004 IEEE/RSJ International Conference on Intelligent Robots and Systems (IROS) (IEEE Cat. No.04CH37566)*, volume 2, pages 2068–2073 vol.2, 2004.

[81] Mustafa Emre Karagozler, Jason D Campbell, Gary K Fedder, Seth Copen Goldstein, Michael Philetus Weller, and Byung Woo Yoon. Electrostatic latching for inter-module adhesion, power transfer, and communication in modular robots. In *2007 IEEE/RSJ International Conference on Intelligent Robots and Systems*, pages 2779–2786. IEEE, 2007.

[82] Yoshihiro Kawahara, Steve Hodges, Benjamin S Cook, Cheng Zhang, and Gregory D Abowd. Instant inkjet circuits: lab-based inkjet printing to support rapid prototyping of UbiComp devices. In *Proceedings of the 2013 ACM international joint conference on Pervasive and ubiquitous computing*, pages 363–372. ACM, 2013.

[83] W. Kier and J. Leeuwen. A kinematic analysis of tentacle extension in the squid loligo pealei. *Journal of Experimental Biology*, Pt 1(200):41–53, 1997.

[84] Dae-Hyeong Kim, Nanshu Lu, Roozbeh Ghaffari, Yun-Soung Kim, Stephen P. Lee, Lizhi Xu, Jian Wu, Rak-Hwan Kim, Jizhou Song, Zhuangjian Liu, Jonathan Viventi, Bassel de Graff, Brian Elolampi, Moussa Mansour, Marvin J. Slepian, Sukwon Hwang, Joshua D. Moss, Sang-Min Won, Younggang Huang, Brian Litt, and John A. Rogers. Materials for multifunctional balloon catheters with capabilities in cardiac electrophysiological mapping and ablation therapy. *Nature Materials*, 10:316–323, 2011.

[85] Jongrae Kim, Pat Heslop-Harrison, Ian Postlethwaite, and Declan G Bates. Stochastic noise and synchronisation during dictyostelium aggregation make camp oscillations robust. *PLoS Comput Biol*, 3(11):e218, 2007.

[86] Brian Kirby, Jason Campbell, Burak Aksak, Padmanabhan Pillai, James Hoburg, Todd C Mowry, and Seth Copen Goldstein. Catoms: Moving robots without moving parts. In *Proceedings of the national conference on artificial intelligence*, volume 20, page 1730. Menlo Park, CA; Cambridge, MA; London; AAAI Press; MIT Press; 1999, 2005.

[87] Brian T. Kirby, Burak Aksak, Jason D. Campbell, James F. Hoburg, Todd C. Mowry, Padmanabhan Pillai, and Seth Copen Goldstein. A modular robotic system using magnetic force effectors. *IEEE International Conference on Intelligent Robots and Systems*, pages 2787–2793, 2007.

[88] Jeong Ho Kong, Nam Su Jang, Soo Hyung Kim, and Jong Man Kim. Simple and rapid micropatterning of conductive carbon composites and its application to elastic strain sensors. *Carbon*, 2014.

[89] Jeremy Kubica, Arancha Casal, and Tad Hogg. Complex behaviors from local rules in modular self-reconfigurable robots. In *Proceedings 2001 ICRA. IEEE International Conference on Robotics and Automation (Cat. No. 01CH37164)*, volume 1, pages 360–367. IEEE, 2001.

[90] P. Kulkarni. Centrifugal Forming and Mechanical Properties of Silicone-Based Elastomers for Soft Robotic Actuators. Master's Thesis: Rutgers University Graduate School, New Brunswick, NJ, USA. page 26, 2015.

[91] Yoshiki Kuramoto. *Chemical oscillations, waves, and turbulence*. Courier Corporation, 2003.

[92] Van Leeuwen J. L. and Kier W. M. Functional design of tentacles in squid: linking sarcomere ultrastructure to gross morphological dynamics. *Transactions of the Royal Society of London*, B(352):551–571, 1997.

[93] Chris Larson, Josef Spjut, Ross Knepper, and Robert Shepherd. A Deformable Interface for Human Touch Recognition Using Stretchable Carbon Nanotube Dielectric Elastomer Sensors and Deep Neural Networks. *Soft Robotics*, 2019.

[94] François A. Lavergne, Hugo Wendehenne, Tobias Bäuerle, and Clemens Bechinger. Group formation and cohesion of active particles with visual perception–dependent motility. *Science*, 364(6435):70–74, 2019.

[95] Jun Young Lee, Woong Bae Kim, Woo Young Choi, and Kyu Jin Cho. Soft Robotic Blocks: Introducing SoBL, a Fast-Build Modularized Design Block. *IEEE Robotics and Automation Magazine*, 23(3):30–41, 2016.

[96] Demian Levis and Benno Liebchen. Simultaneous phase separation and pattern formation in chiral active mixtures. *Physical Review E*, 100(1):1–8, 2019.

[97] Demian Levis, Ignacio Pagonabarraga, and Benno Liebchen. Activity induced synchronization: Mutual flocking and chiral self-sorting. *Physical Review Research*, 1(2):023026, 2019.

[98] Shuguang Li, Richa Batra, David Brown, Hyun-Dong Chang, Nikhil Ranganathan, Chuck Hoberman, Daniela Rus, and Hod Lipson. Particle robotics based on statistical mechanics of loosely coupled components. *Nature*, 567(7748):361–365, 2019.

[99] Xinquan Liang, Hong Kai Yap, Jin Guo, Raye Chen Hua Yeow, Yi Sun, and Chee Kong Chui. Design and characterization of a novel fabric-based robotic arm for future wearable robot application. In *2017 IEEE International Conference on Robotics and Biomimetics (ROBIO)*, pages 367–372, 2017.

[100] Hong-Ru Lin, Chun-Jung Kuo, C. Y. Yang, Shyh-Yu Shaw, and Yu-Jun Wu. Preparation of macroporous biodegradable plga scaffolds for cell attachment with the use of mixed salts as porogen additives. *Journal of Biomedical Materials Research*, 63(3):271–279, 2002.

[101] Huai-Ti Lin, Gary Leisk, and Barry Trimmer. Goqbot: A caterpillar-inspired soft-bodied rolling robot. *Bioinspiration biomimetics*, 6:026007, 06 2011.

[102] Qingkun Liu, Wei Wang, Michael F Reynolds, Michael C Cao, Marc Z Miskin, Tomas A Arias, David A Muller, Paul L McEuen, and Itai Cohen. Micrometer-sized electrically programmable shape-memory actuators for low-power microrobotics. *Science Robotics*, 6(52):eabe6663, 2021.

[103] Yue Liu and Yuxiao Guo. Synchronization in a kuramoto model with delay-dependent couplings. *AIP Advances*, 9(2):025026, 2019.

[104] Zeng Tao Liu, Yan Shi, Yongfeng Zhao, Hugues Chaté, Xia-qing Shi, and Tian Hui Zhang. Activity waves and freestanding vortices in populations of subcritical quincke rollers. *Proceedings of the National Academy of Sciences*, 118(40), 2021.

[105] Joao U.F. Lizarraga and Marcus A.M. De Aguiar. Synchronization and spatial patterns in forced swarmalators. *Chaos*, 30(5), 2020.

[106] M. R. Loos, J. Yang, D. L. Feke, and I. Manas-Zloczower. Effect of block-copolymer dispersants on properties of carbon nanotube/epoxy systems. *Composites Science and Technology*, 2012.

[107] Danna Ma, Steven Ceron, Gregory Kaiser, and Kirstin Petersen. Simple low-cost fabrication of soft sensors for feature reconstruction. *IEEE Robotics and Automation Letters*, 5(3):4049 – 4054, 2020.

[108] Benjamin C. Mac Murray, Xintong An, Sanlin S. Robinson, Ilse M. Van Meerbeek, Kevin W. O'Brien, Huichan Zhao, and Robert F. Shepherd. Poroelastic Foams for Simple Fabrication of Complex Soft Robots. *Advanced Materials*, 2015.

[109] A Mackay. William A. MacKay. 513646613(13646613), 1997.

[110] Melinda Malley, Bahar Haghighat, Lucie Houe, and Radhika Nagpal. Eciton robotica: Design and algorithms for an adaptive self-assembling soft robot collective. In *2020 IEEE International Conference on Robotics and Automation (ICRA)*, pages 4565–4571. IEEE, 2020.

[111] Andrew D. Marchese, Cagdas D. Onal, and Daniela Rus. Autonomous soft robotic fish capable of escape maneuvers using fluidic elastomer actuators. *Soft Robotics*, 1(1):75–87, 2014. PMID: 27625912.

[112] Ramses V Martinez, Jamie L Branch, Carina R Fish, Lihua Jin, Robert F Shepherd, Rui Nunes, Zhigang Suo, and George M Whitesides. Robotic tentacles with three-dimensional mobility based on flexible elastomers. *Advanced Materials*, 25(2):205–212, 2013.

[113] Fernando Martínez-Pedrero, Andrés González-Banciella, Alba Camino, Ana Mateos-Maroto, Francisco Ortega, Ramón G. Rubio, Ignacio Pagonabarraga, and Carles Calero. Static and Dynamic Self-Assembly of Pearl-Like-Chains of Magnetic Colloids Confined at Fluid Interfaces. *Small*, 17(25), 2021.

[114] Fernando Martinez-Pedrero and Pietro Tierno. Magnetic Propulsion of Self-Assembled Colloidal Carpets: Efficient Cargo Transport via a Conveyor-Belt Effect. *Physical Review Applied*, 3(5):1–6, 2015.

[115] Ali Maziz, Alessandro Concas, Alexandre Khaldi, Jonas Stlhand, Nils-Krister Persson, and Edwin W. H. Jager. Knitting and weaving artificial muscles. *Science Advances*, 3(1):e1600327, 2017.

[116] Colin P. McCann, Paul W. Kriebel, Carole A. Parent, and Wolfgang Losert. Cell speed, persistence and information transmission during signal relay and collective migration. *Journal of Cell Science*, 123(10):1724–1731, 2010.

[117] James E McClure and Nicole Abaid. Effect of topology and geometric structure on collective motion in the vicsek model. *Frontiers in Applied Mathematics and Statistics*, 8:829005, 2022.

[118] Ross M McKenzie, Mohammed E Sayed, Markus P Nemitz, Brian W Flynn, and Adam A Stokes. Linbots: Soft modular robots utilizing voice coils. *Soft robotics*, 6(2):195–205, 2019.

[119] Timothy A. McLennan-Smith, Dale O. Roberts, and Harvinder S. Sidhu. Emergent behavior in an adversarial synchronization and swarming model. *Physical Review E*, 102(3):32607, 2020.

[120] James McLurkin and Erik D Demaine. A distributed boundary detection algorithm for multi-robot systems. In *2009 IEEE/RSJ International Conference on Intelligent Robots and Systems*, pages 4791–4798. IEEE, 2009.

[121] Etienne Menard, Matthew A. Meitl, Yugang Sun, Jang-Ung Park, Daniel Jay-Lee Shir, Yun-Suk Nam, Seokwoo Jeon, and John A. Rogers. Micro- and nanopatterning techniques for organic electronic and optoelectronic systems. *Chemical Reviews*, 107:1117–1160, 2007.

[122] D. C. Michaels, E. P. Matyas, and J. Jalife. Dynamic interactions and mutual synchronization of sinoatrial node pacemaker cells: A mathematical model. *Circulation Research*, 58(5):706–720, 1986.

[123] Marc Z Miskin, Alejandro J Cortese, Kyle Dorsey, Edward P Esposito, Michael F Reynolds, Qingkun Liu, Michael Cao, David A Muller, Paul L McEuen, and Itai Cohen. Electronically integrated, mass-manufactured, microscopic robots. *Nature*, 584(7822):557–561, 2020.

[124] Andrew Moiseff and Jonathan Copeland. Firefly synchrony: A behavioral strategy to minimize visual clutter. *Science*, 329(5988):181, 2010.

[125] Christopher J. Morris, Sean A. Stauth, and Babak A. Parviz. Self-assembly for microscale and nanoscale packaging: Steps toward self-packaging. *IEEE Transactions on Advanced Packaging*, 28(4):600–611, 2005.

[126] Fangzhi Mou, Jianhua Zhang, Zhen Wu, Sinan Du, Zexin Zhang, Leilei Xu, and Jianguo Guan. Phototactic flocking of photochemical micromotors. *Iscience*, 19:415–424, 2019.

[127] Yuichi Nakazato, Yukihiro Sonobe, and Shigeki Toyama. Development of an in-pipe micro mobile robot using peristalsis motion. *Journal of Mechanical Science and Technology*, 24:51–54, 02 2010.

[128] Janna Nawroth, Hyungsuk Lee, Adam Feinberg, Crystal Ripplinger, Megan McCain, Anna Grosberg, John Dabiri, and Kevin Parker. A tissue-engineered jellyfish with biomimetic propulsion. *Nature biotechnology*, 30:792–7, 07 2012.

[129] André Naz, Beno\^\it Piranda, Thadeu Tucci, Seth Copen Goldstein, and Julien Bourgeois. Network Characterization of Lattice-Based Modular Robots with Neighbor-to-Neighbor Communications. In *Distributed Autonomous Robotic Systems*, pages 415–429. Springer, 2018.

[130] Jonas Neubert, Arne Rost, and Hod Lipson. Self-soldering connectors for modular robots. *IEEE Transactions on Robotics*, 30(6):1344–1357, 2014.

[131] Pham Huy Nguyen and Wenlong Zhang. Design and computational modeling of fabric soft pneumatic actuators for wearable assistive devices. *Scientific reports*, 10(1):1–13, 2020.

[132] Alexandra Nilles, Steven Ceron, Nils Napp, and Kirstin Petersen. Strain-based consensus in soft, inflatable robots. In *2022 IEEE 5th International Conference on Soft Robotics (RoboSoft)*, pages 789–794. IEEE, 2022.

[133] Géza Ódor, Jeffrey Kelling, and Gustavo Deco. The effect of noise on the synchronization dynamics of the kuramoto model on a large human connectome graph. *Neurocomputing*, 461:696–704, 2021.

[134] Kevin O'Keeffe, Steven Ceron, and Kirstin Petersen. Collective behavior of swarmalators on a ring. *Phys. Rev. E*, 105:014211, Jan 2022.

[135] Kevin P. O'Keeffe, Joep H.M. Evers, and Theodore Kolokolnikov. Ring states in swarmalator systems. *Physical Review E*, 98(2):1–14, 2018.

[136] C.D. Onal and Daniela Rus. Autonomous undulatory serpentine locomotion utilizing body dynamics of a fluidic soft robot. *Bioinspiration biomimetics*, 8:026003, 03 2013.

[137] Yasemin Ozkan-Aydin and Daniel I. Goldman. Self-reconfigurable multilegged robot swarms collectively accomplish challenging terradynamic tasks. *Science Robotics*, 6(56):1–13, 2021.

[138] Kevin P O'Keeffe, Hyunsuk Hong, and Steven H Strogatz. Oscillators that sync and swarm. *Nature communications*, 8(1):1–13, 2017.

[139] Amit Pamecha, Chih-Jung Chiang, David Stein, and Gregory Chirikjian. Design and implementation of metamorphic robots. In *Proceedings of the 1996 ASME Design Engineering Technical Conference and Computers in Engineering Conference*, volume 10. Irvine, California, USA: ASME, 1996.

[140] Amit Pamecha, Imme Ebert-Uphoff, and Gregory S Chirikjian. Useful metrics for modular robot motion planning. *IEEE Transactions on Robotics and Automation*, 13(4):531–545, 1997.

[141] Xinan Pan, Hongguang Wang, Yong Jiang, Neng He, and Cen Yu. Research of topological analysis of modular reconfigurable robots. In *2010 IEEE International Conference on Robotics and Biomimetics*, pages 327–332. IEEE, 2010.

[142] Huan Pang, Tao Chen, Gangming Zhang, Baoqing Zeng, and Zhong Ming Li. An electrically conducting polymer/graphene composite with a very low percolation threshold. *Materials Letters*, 2010.

[143] Michael Park, Sachin Chitta, Alex Teichman, and Mark Yim. Automatic configuration recognition methods in modular robots. *The International Journal of Robotics Research*, 27(3-4):403–421, 2008.

[144] Michael Park and Mark Yim. Distributed control and communication fault tolerance for the ckbot. In *2009 ASME/IFToMM International Conference on Reconfigurable Mechanisms and Robots*, pages 682–688. IEEE, 2009.

[145] Yong-Lae Park, Carmel Majidi, Rebecca Kramer, Phillipe Berard, and Robert J. Wood. Hyperelastic pressure sensing with a liquid embedded elastomer. *Journal of Micromechanics and Microengineering*, 20(12), November 2010.

[146] Dmitrii Pavlov and A. Kasumyan. Patterns and mechanisms of schooling behavior in fish: A review. *Journal of Ichthyology*, 40:S163–S231, 12 2000.

[147] Kirstin H Petersen, Nils Napp, Robert Stuart-Smith, Daniela Rus, and Mirko Kovac. A review of collective robotic construction. *Science Robotics*, 4(28):eaau8479, 2019.

[148] Franco N. Piñan Basualdo, A. Bolopion, M. Gauthier, and P. Lambert. A microrobotic platform actuated by thermocapillary flows for manipulation at the air-water interface. *Science Robotics*, 6(52):1–8, 2021.

[149] J. H. Pikul, S. Li, H. Bai, R. T. Hanlon, I. Cohen, and R. F. Shepherd. Stretchable surfaces with programmable 3d texture morphing for synthetic camouflaging skins. *Science*, 358(6360):210–214, 2017.

[150] Padmanabhan Pillai, Jason Campbell, Gautam Kedia, Shishir Moudgal,

and Kaushik Sheth. A 3d fax machine based on claytronics. In *2006 IEEE/RSJ International Conference on Intelligent Robots and Systems*, pages 4728–4735. IEEE, 2006.

[151] Benoit Piranda and Julien Bourgeois. Designing a quasi-spherical module for a huge modular robot to create programmable matter. *Autonomous Robots*, 42(8):1619–1633, 2018.

[152] AC Quillen, A Peshkov, Esteban Wright, and Sonia McGaffigan. Metachronal waves in concentrations of swimming turbatrix aceti nematodes and an oscillator chain model for their coordinated motions. *arXiv preprint arXiv:2101.06809*, 2021.

[153] Ahmad Rafsanjani, Yuerou Zhang, Bangyuan Liu, Shmuel M. Rubinstein, and Katia Bertoldi. Kirigami skins make a simple soft actuator crawl. *Science Robotics*, 3(15):eaar7555, 2018.

[154] Rahim Rahimi, Manuel Ochoa, Wuyang Yu, and Babak Ziaie. A sewing-enabled stitch-and-transfer method for robust, ultra-stretchable, conductive interconnects. *Journal of Micromechanics and Microengineering*, 24(9):095018, aug 2014.

[155] Wouter Jan Rappel, Alastair Nicol, Armand Sarkissian, Herbert Levine, and William F. Loomis. Self-organized vortex state in two-dimensional dictyostelium dynamics. *Physical Review Letters*, 83(6):1247–1250, 1999.

[156] Craig W. Reynolds. Flocks, herds, and schools: A distributed behavioral model. *Proceedings of the 14th Annual Conference on Computer Graphics and Interactive Techniques, SIGGRAPH 1987*, 21(4):25–34, 1987.

[157] Ingmar H. Riedel, Karsten Kruse, and Jonathon Howard. Biophysics: A self-organized vortex array of hydrodynamically entrained sperm cells. *Science*, 309(5732):300–303, 2005.

[158] Ellen T. Roche, Robert Wohlfarth, Johannes T. B. Overvelde, Nikolay V. Vasilyev, Frank A. Pigula, David J. Mooney, Katia Bertoldi, and Conor J. Walsh. A bioinspired soft actuated material. *Advanced Materials*, 26(8):1200–1206, 2014.

[159] Francisco A Rodrigues, Thomas K DM Peron, Peng Ji, and Jürgen Kurths. The kuramoto model in complex networks. *Physics Reports*, 610:1–98, 2016.

[160] P. Romanczuk, M. Bär, W. Ebeling, B. Lindner, and L. Schimansky-Geier. Active Brownian particles: From individual to collective stochastic dynamics: From individual to collective stochastic dynamics. *European Physical Journal: Special Topics*, 202(1):1–162, 2012.

[161] John W. Romanishin, John Mamish, and Daniela Rus. Decentralized Control for 3D M-Blocks for Path Following, Line Formation, and Light Gradient Aggregation. *IEEE International Conference on Intelligent Robots and Systems*, pages 4862–4868, 2019.

[162] Michael Rubenstein, Adrian Cabrera, Justin Werfel, Golnaz Habibi, James McLurkin, and Radhika Nagpal. Collective transport of complex objects by simple robots: theory and experiments. In *Proceedings of the 2013 international conference on Autonomous agents and multi-agent systems*, pages 47–54, 2013.

[163] Michael Rubenstein, Alejandro Cornejo, and Radhika Nagpal. Programmable self-assembly in a thousand-robot swarm. *Science*, 345(6198):795–799, 2014.

[164] Michael Rubenstein, Alejandro Cornejo, and Radhika Nagpal. Programmable self-assembly in a thousand-robot swarm. *Science*, 345(6198):795–799, 2014.

[165] D. Rus and M. Tolley. Design, fabrication and control of soft robots. *Nature*, 521:467–475, 2015.

[166] Daniela Rus and Michael T Tolley. Design, fabrication and control of soft robots. *Nature*, 521(7553):467–475, 2015.

[167] Daniela Rus and Marsette Vona. Crystalline robots: Self-reconfiguration with compressible unit modules. *Autonomous Robots*, 10(1):107–124, 2001.

[168] Stuart J Russell and Peter Norvig. *Artificial intelligence: a modern approach*. Malaysia; Pearson Education Limited,, 2016.

[169] David Saldana, Bruno Gabrich, Guanrui Li, Mark Yim, and Vijay Kumar. ModQuad: The flying modular structure that self-assembles in Midair. *Proceedings - IEEE International Conference on Robotics and Automation*, pages 691–698, 2018.

[170] William Savoie, Thomas A. Berrueta, Zachary Jackson, Ana Pervan, Ross

Warkentin, Shengkai Li, Todd D. Murphey, Kurt Wiesenfeld, and Daniel I. Goldman. A robot made of robots: Emergent transport and control of a smarticle ensemble. *Science robotics*, 4(34), 2019.

[171] Sangok Seok, Cagdas Denizel Onal, Kyu-Jin Cho, Robert J. Wood, Daniela Rus, and Sangbae Kim. Meshworm: A peristaltic soft robot with antagonistic nickel titanium coil actuators. *IEEE/ASME Transactions on Mechatronics*, 18(5):1485–1497, 2013.

[172] Wei Min Shen, Maks Krivokon, Harris Chiu, Jacob Everist, Michael Rubenstein, and Jagadesh Venkatesh. Multimode locomotion via SuperBot reconfigurable robots. *Autonomous Robots*, 20(2):165–177, 2006.

[173] Robert F. Shepherd, Filip Ilievski, Wonjae Choi, Stephen A. Morin, Adam A. Stokes, Aaron D. Mazzeo, Xin Chen, Michael Wang, and George M. Whitesides. Multigait soft robot. *Proceedings of the National Academy of Sciences*, 108(51):20400–20403, 2011.

[174] Xiaomei Shi, Ching-hsiang Cheng, and Yongping Zheng. An EGaIn-based flexible piezoresistive shear and normal force sensor with hysteresis analysis in normal force direction. *Journal of Micromechanics and Microengineering*, 2016.

[175] Jun Shintake, Vito Cacucciolo, Dario Floreano, and Herbert Shea. Soft Robotic Grippers, 2018.

[176] Siddharth Shrivastava, Andras Karsai, Yasemin Ozkan Aydin, Ross Pettinger, William Bluethmann, Robert O Ambrose, and Daniel I Goldman. Material remodeling and unconventional gaits facilitate locomotion of a robophysical rover over granular terrain. *Science Robotics*, 5(42), 2020.

[177] Metin Sitti. Mobile Microrobotics. *The MIT Press*, 2017.

[178] I. Slavkov, D. Carrillo-Zapata, N. Carranza, X. Diego, F. Jansson, J. Kaandorp, S. Hauert, and J. Sharpe. Morphogenesis in robot swarms. *Science Robotics*, 3(25):1–17, 2018.

[179] M.L. Smith, G.M. Yanega, and A. Ruina. Elastic instability model of rapid beak closure in hummingbirds. *Journal of Theoretical Biology*, 282(1):41–51, 2011.

[180] Loling Song, Sharvari M. Nadkarni, Hendrik U. Bödeker, Carsten Beta,

Albert Bae, Carl Franck, Wouter Jan Rappel, William F. Loomis, and Eberhard Bodenschatz. Dictyostelium discoideum chemotaxis: Threshold for directed motion. *European Journal of Cell Biology*, 85(9-10):981–989, 2006.

[181] Mohammad Divband Soorati, Mary Katherine Heinrich, Javad Ghofrani, Payam Zahadat, and Heiko Hamann. Photomorphogenesis for robot self-assembly :. 2019.

[182] Enrica Soria, Fabrizio Schiano, and Dario Floreano. Predictive control of aerial swarms in cluttered environments. *Nature Machine Intelligence*, 3:545–554, 2021.

[183] Varun Sridhar, Filip Podjaski, Yunus Alapan, Julia Kröger, Lars Grunenberg, Vimal Kishore, Bettina V. Lotsch, and Metin Sitti. Light-driven carbon nitride microswimmers with propulsion in biological and ionic media and responsive on-demand drug delivery. *Science Robotics*, 7(62):eabm1421, 2022.

[184] Sasha Stankovich, Dmitriy A. Dikin, Geoffrey H.B. Dommett, Kevin M. Kohlhaas, Eric J. Zimney, Eric A. Stach, Richard D. Piner, Son Binh T. Nguyen, and Rodney S. Ruoff. Graphene-based composite materials. *Nature*, 2006.

[185] A. Stilli, H. A. Wurdemann, and K. Althoefer. A novel concept for safe, stiffness-controllable robot links. *Soft Robotics*, 4:16–22, 2017.

[186] Agostino Stilli, Luca Grattarola, Hauke Feldmann, Helge A. Wurdemann, and Kaspar Althoefer. Variable stiffness link (vsl): Toward inherently safe robotic manipulators. In *2017 IEEE International Conference on Robotics and Automation (ICRA)*, pages 4971–4976, 2017.

[187] Kasper Stoy and Radhika Nagpal. Self-repair through scale independent self-reconfiguration. In *2004 IEEE/RSJ International Conference on Intelligent Robots and Systems (IROS)(IEEE Cat. No. 04CH37566)*, volume 2, pages 2062–2067. IEEE, 2004.

[188] Steven H. Strogatz. From kuramoto to crawford: exploring the onset of synchronization in populations of coupled oscillators. *Physica D: Nonlinear Phenomena*, 143(1-4):1–20, 2000.

[189] Ashley W Stroupe, Martin C Martin, and Tucker Balch. Distributed sensor fusion for object position estimation by multi-robot systems. In *Proceed-*

ings 2001 ICRA. IEEE international conference on robotics and automation (Cat. No. 01CH37164), volume 2, pages 1092–1098. IEEE, 2001.

[190] Xin Sui, Hegao Cai, Dongyang Bie, Yu Zhang, Jie Zhao, and Yanhe Zhu. Automatic generation of locomotion patterns for soft modular reconfigurable robots. *Applied Sciences*, 10(1):294, 2020.

[191] Yutaka Sumino, Ken H. Nagai, Yuji Shitaka, Dan Tanaka, Kenichi Yoshikawa, Hugues Chaté, and Kazuhiro Oiwa. Large-scale vortex lattice emerging from collectively moving microtubules. *Nature*, 483:448–452, 2012.

[192] Masao Sumita, Kazuya Sakata, Shigeo Asai, Keizo Miyasaka, and Hideaki Nakagawa. Dispersion of fillers and the electrical conductivity of polymer blends filled with carbon black. *Polymer Bulletin*, 1991.

[193] Jean Marie Swiecicki, Olesksii Sliusarenko, and Douglas B. Weibel. From swimming to swarming: Escherichia coli cell motility in two-dimensions. *Integrative Biology (United Kingdom)*, 5(12):1490–1494, 2013.

[194] Petras Swissler and Michael Rubenstein. FireAnt: A Modular Robot with Full-Body Continuous Docks. In *ICRA 2018-IEEE International Conference on Robotics and Automation*, 2018.

[195] Petras Swissler and Michael Rubenstein. Fireant3d: a 3d self-climbing robot towards non-latticed robotic self-assembly. In *2020 IEEE/RSJ International Conference on Intelligent Robots and Systems (IROS)*, pages 3340–3347. IEEE, 2020.

[196] Kentaro Takagi, Masanori Yamamura, Zhi Luo, Masaki Onishi, Shinya Hirano, Kinji Asaka, and Yoshikazu Hayakawa. Development of a rajiform swimming robot using ionic polymer artificial muscles. pages 1861–1866, 10 2006.

[197] Naotomo Takemura, Kenta Takata, Masato Takiguchi, and Masaya Notomi. Emulating the local kuramoto model with an injection-locked photonic crystal laser array. *Scientific reports*, 11(1):1–11, 2021.

[198] Dan Tanaka. General chemotactic model of oscillators. *Physical Review Letters*, 99(13):1–4, 2007.

[199] Yichao Tang and Jie Yin. Design of multifunctional soft doming actuator for soft machines. *Advanced Materials Technologies*, 3(7):1800069, 2018.

[200] C. Thill, J. Etches, I. Bond, K. Potter, and P. Weaver. Morphing skins. *The Aeronautical Journal (1968)*, 112(1129):117–139, 2008.

[201] Bertrand Tondu. Modelling of the mckibben artificial muscle: A review. *Journal of Intelligent Material Systems and Structures*, 23(3):225–253, 2012.

[202] J. C. Tsai, Fangfu Ye, Juan Rodriguez, J. P. Gollub, and T. C. Lubensky. A chiral granular gas. *Physical Review Letters*, 94(21):1–4, 2005.

[203] Charisios D Tsiairis and Alexander Aulehla. Self-organization of embryonic genetic oscillators into spatiotemporal wave patterns. *Cell*, 164(4):656–667, 2016.

[204] Koichiro Uriu and Luis G Morelli. Collective cell movement promotes synchronization of coupled genetic oscillators. *Biophysical journal*, 107(2):514–526, 2014.

[205] Koichiro Uriu and Luis G Morelli. Determining the impact of cell mixing on signaling during development. *Development, growth & differentiation*, 59(5):351–368, 2017.

[206] Bruno Ventejou, Hugues Chaté, Raul Montagne, and Xia-qing Shi. Susceptibility of orientationally ordered active matter to chirality disorder. *Phys. Rev. Lett.*, 127:238001, Nov 2021.

[207] Andrea Vergara, Yi-sheng Lau, Ricardo-Franco Mendoza-Garcia, and Juan Cristóbal Zagal. Soft modular robotic cubes: toward replicating morphogenetic movements of the embryo. *PloS one*, 12(1):e0169179, 2017.

[208] Tamás Vicsek, András Czirók, Eshel Ben-Jacob, Inon Cohen, and Ofer Shochet. Novel type of phase transition in a system of self-driven particles. *Physical review letters*, 75(6):1226, 1995.

[209] Tamás Vicsek and Anna Zafeiris. Collective motion. *Physics Reports*, 517(3-4):71–140, 2012.

[210] S. Voisembert, A. Riwan, N. Mechbal, and A. Barraco. A novel inflatable robot with constant and continuous volume. In *2011 IEEE International Conference on Robotics and Automation*, pages 5843–5848, 2011.

[211] Jennifer E Walter, Elizabeth M Tsai, and Nancy M Amato. Algorithms for fast concurrent reconfiguration of hexagonal metamorphic robots. *IEEE transactions on Robotics*, 21(4):621–631, 2005.

[212] Jennifer E Walter, Jennifer L Welch, and Nancy M Amato. Concurrent metamorphosis of hexagonal robot chains into simple connected configurations. *IEEE Transactions on Robotics and Automation*, 18(6):945–956, 2002.

[213] Qizhang Wang, Chao Zhou, Luyang Huang, and Wei Wang. "Ballistic" waves among chemically oscillating micromotors. *Chemical Communications*, 57(68):8492–8495, 2021.

[214] Wei Wang, Jang-Yeob Lee, Hugo Rodrigue, Sung-Hyuk Song, Won-Shik Chu, and Sung-Hoon Ahn. Locomotion of inchworm-inspired robot made of smart soft composite (ssc). *Bioinspiration Biomimetics*, 9:046006, 10 2014.

[215] Wendong Wang, Gaurav Gardi, Paolo Malgaretti, Vimal Kishore, Lyndon Koens, Donghoon Son, Hunter Gilbert, Zongyuan Wu, Palak Harwani, Eric Lauga, Christian Holm, and Metin Sitti. Order and information in the patterns of spinning magnetic micro-disks at the air-water interface. *Science Advances*, 8(2):1–15, 2022.

[216] Wendong Wang, Joshua Giltinan, Svetlana Zakharchenko, and Metin Sitti. Dynamic and programmable self-assembly of micro-rafts at the air-water interface. *Science Advances*, 3(5):1–10, 2017.

[217] Wendong Wang, Vimal Kishore, Lyndon Koens, Eric Lauga, and Metin Sitti. Collectives of Spinning Mobile Microrobots for Navigation and Object Manipulation at the Air-Water Interface. *IEEE International Conference on Intelligent Robots and Systems*, pages 6186–6192, 2018.

[218] Xiaoling Wang, Stephan A. Koehler, James N. Wilking, Naveen N. Sinha, Matthew T. Cabeen, Siddarth Srinivasan, Agnese Seminara, Shmuel Rubinstein, Qingping Sun, Michael P. Brenner, and David A. Weitz. Probing phenotypic growth in expanding Bacillus subtilis biofilms. *Applied Microbiology and Biotechnology*, 100(10):4607–4615, 2016.

[219] Zheng Wang, Panagiotis Polygerinos, Johannes T. B. Overvelde, Kevin C. Galloway, Katia Bertoldi, and Conor J. Walsh. Interaction forces of soft fiber reinforced bending actuators. *IEEE/ASME Transactions on Mechatronics*, 22(2):717–727, 2017.

[220] Benjamin Ward-Cherrier, Nicholas Pestell, Luke Cramphorn, Benjamin Winstone, Maria Elena Giannaccini, Jonathan Rossiter, and Nathan F. Lepora. The TacTip Family: Soft Optical Tactile Sensors with 3D-Printed Biomimetic Morphologies. *Soft Robotics*, 2018.

[221] Justin Werfel, Kirstin Petersen, and Radhika Nagpal. Designing collective behavior in a termite-inspired robot construction team. *Science*, 343(6172):754–758, 2014.

[222] James N. Wilking, Thomas E. Angelini, Agnese Seminara, Michael P. Brenner, and David A. Weitz. Biofilms as complex fluids. *MRS Bulletin*, 36(5):385–391, 2011.

[223] Nialah Jenae Wilson, Steven Ceron, Logan Horowitz, and Kirstin Petersen. Scalable and robust fabrication, operation, and control of compliant modular robots. *Frontiers in Robotics and AI*, 7:44, 2020.

[224] A. T. Winfree. Biological rhythms and the behavior of populations of coupled oscillators. *Journal of Theoretical Biology*.

[225] Sukyoung Won, Sanha Kim, Jeong Eun Park, Jisoo Jeon, and Jeong Jae Wie. On-demand orbital maneuver of multiple soft robots via hierarchical magnetomotility. *Nature Communications*, 10(1):1–8, 2019.

[226] Shuang Wu, Gregory Langston Baker, Jie Yin, and Yong Zhu. Fast thermal actuators for soft robotics. *Soft Robotics*, 2021.

[227] Zuyao Xiao, Mengshi Wei, and Wei Wang. A Review of Micromotors in Confinements: Pores, Channels, Grooves, Steps, Interfaces, Chains, and Swimming in the Bulk. *ACS Applied Materials and Interfaces*, 11(7):6667–6684, 2019.

[228] Hui Xie, Mengmeng Sun, Xinjian Fan, Zhihua Lin, Weinan Chen, Lei Wang, Lixin Dong, and Qiang He. Reconfigurable magnetic microrobot swarm: Multimode transformation, locomotion, and manipulation. *Science Robotics*, 4(28), 2019.

[229] J. Yan, S. C. Bae, and S. Granick. Rotating crystals of magnetic Janus colloids. *Soft Matter*, 11(1):147–153, 2015.

[230] D. Yang, B. Mosadegh, A. Ainla, B. Lee, F. Khashai, Z. Suo, K. Bertoldi,

and G.M. Whitesides. Buckling of elastomeric beams enables actuation of soft machines. *Advanced Materials*, 27, 2015.

[231] W. H. Yang and W. W. Feng. On Axisymmetrical Deformations of Nonlinear Membranes. *Journal of Applied Mechanics*, 37(4):1002–1011, 12 1970.

[232] Lining Yao, Ryuma Niiyama, Jifei Ou, Sean Follmer, Clark Della Silva, and Hiroshi Ishii. Pneui: Pneumatically actuated soft composite materials for shape changing interfaces. In *Proceedings of the 26th Annual ACM Symposium on User Interface Software and Technology*, UIST '13, page 13–22, New York, NY, USA, 2013. Association for Computing Machinery.

[233] Yun Sheng Ye, Hong Xia Zeng, Jun Wu, Li Yun Dong, Jin Tao Zhu, Zhi Gang Xue, Xing Ping Zhou, Xiao Lin Xie, and Yiu Wing Mai. Biocompatible reduced graphene oxide sheets with superior water dispersibility stabilized by cellulose nanocrystals and their polyethylene oxide composites. *Green Chemistry*, 2016.

[234] O. H. Yeoh. Some Forms of the Strain Energy Function for Rubber. *Rubber Chemistry and Technology*, 66(5):754–771, 11 1993.

[235] Berk Yigit, Yunus Alapan, and Metin Sitti. Programmable collective behavior in dynamically self-assembled mobile microrobotic swarms. *Advanced Science*, 6(6):1801837, 2019.

[236] Mark Yim, Wei-Min Shen, Behnam Salemi, Daniela Rus, Mark Moll, Hod Lipson, Eric Klavins, and Gregory S Chirikjian. Modular self-reconfigurable robot systems [grand challenges of robotics]. *Robotics & Automation Magazine, IEEE*, 14(1):43–52, 2007.

[237] Mark Yim, Ying Zhang, and David Duff. Modular robots. *IEEE Spectrum*, 39(2):30–34, 2002.

[238] Sehyuk Yim and Metin Sitti. Softcubes: towards a soft modular matter. In *2013 IEEE International Conference on Robotics and Automation*, pages 530–536. IEEE, 2013.

[239] Chih-Han Yu, Kristina Haller, Donald Ingber, and Radhika Nagpal. Morpho: A self-deformable modular robot inspired by cellular structure. In *Intelligent Robots and Systems, 2008. IROS 2008. IEEE/RSJ International Conference on*, pages 3571–3578. IEEE, 2008.

[240] Chih-Han Yu and Radhika Nagpal. Self-adapting modular robotics: A generalized distributed consensus framework. In *2009 IEEE International Conference on Robotics and Automation*, pages 1881–1888. IEEE, 2009.

[241] Jiangfan Yu, Ben Wang, Xingzhou Du, Qianqian Wang, and Li Zhang. Ultra-extensible ribbon-like magnetic microswarm. *Nature Communications*, 9(1):1–9, 2018.

[242] Jiangfan Yu, Lidong Yang, and Li Zhang. Pattern generation and motion control of a vortex-like paramagnetic nanoparticle swarm. *International Journal of Robotics Research*, 37(8):912–930, 2018.

[243] Xi Yu, M. Ani Hsieh, Cong Wei, and Hebert G. Tanner. Synchronous rendezvous for networks of marine robots in large scale ocean monitoring. *Frontiers in Robotics and AI*, 6, 2019.

[244] Liang Yue, Gholamreza Pircheraghi, Seyed Ali Monemian, and Ica Manas-Zloczower. Epoxy composites with carbon nanotubes and graphene nanoplatelets - Dispersion and synergy effects. *Carbon*, 2014.

[245] Davide Zappetti, Stefano Mintchev, Jun Shintake, and Dario Floreano. Bio-inspired tensegrity soft modular robots. In *Conference on Biomimetic and Biohybrid Systems*, pages 497–508. Springer, 2017.

[246] David Zarrouk, Moshe Mann, Nir Degani, Tal Yehuda, Nissan Jarbi, and Amotz Hess. Single actuator wave-like robot (saw): Design, modeling, and experiments. *Bioinspiration biomimetics*, 11:046004, 07 2016.

[247] Bo Zhang, Andrey Sokolov, and Alexey Snezhko. Reconfigurable emergent patterns in active chiral fluids. *Nature communications*, 11(1):1–9, 2020.

[248] Bo Zhang, Hang Yuan, Andrey Sokolov, Monica Olvera de la Cruz, and Alexey Snezhko. Polar state reversal in active fluids. *Nature Physics*, 18(2):154–159, 2022.

[249] Jiachen Zhang, Ziyu Ren, Wenqi Hu, Ren Hao Soon, Immihan Ceren Yasa, Zemin Liu, and Metin Sitti. Voxelated three-dimensional miniature magnetic soft machines via multimaterial heterogeneous assembly. *Science Robotics*, 6(53):1–15, 2021.

[250] Jianhua Zhang, Fangzhi Mou, Zhen Wu, Jiaqi Song, Joshua E. Kauffman,

Ayusman Sen, and Jianguo Guan. Cooperative transport by flocking phototactic micromotors. *Nanoscale Advances*, 3(21):6157–6163, 2021.

[251] Wei Zhou and Nick Gravish. Density dependent synchronization in contact-coupled oscillators. *arXiv preprint arXiv:2012.07124*, 2020.

[252] X. Zhou, C. Majidi, and O.M. O'Reilly. Flexing into motion: A locomotion mechanism for soft robots. 2015.

[253] Li Zhu and Didier El Baz. A programmable actuator for combined motion and connection and its application to modular robot. *Mechatronics*, 58:9–19, 2019.